

Luminescent Planar Single and Dual Optodes for Time-Resolved Imaging of pH, pCO₂ and pO₂ in Marine Systems

Dissertation zur Erlangung des Doktorgrades der Naturwissenschaften

(Dr. rer. nat.)

an der Fakultät für Chemie und Pharmazie

der Universität Regensburg



vorgelegt von

Claudia R. Schröder

aus Pirmasens

Oktober 2006

Diese Doktorarbeit entstand in der Zeit von Oktober 2000 bis September 2006 am Institut für Analytische Chemie, Chemo- und Biosensorik an der Universität Regensburg.

Die Arbeit wurde angeleitet von Prof. Dr. Otto S. Wolfbeis.

Promotionsgesuch eingereicht am 21.09.2006

Kolloquiumstermin: 10.10.2006

Prüfungsausschuß:	Vorsitzender:	Prof. Dr. Georg Schmeer
	Erstgutachter:	Prof. Dr. Otto S. Wolfbeis
	Zweitgutachter:	Prof. Dr. Ingo Klimant
	Drittprüfer:	Prof. Dr. Werner Kunz

Danksagung

Mein erster Dank gilt **Prof. Dr. Otto S. Wolfbeis** für die Vergabe des interessanten Themas, die Unterstützung während der Arbeit und die sehr guten Arbeitsbedingungen am Institut.

Besonderer Dank gebührt **Prof. Dr. Ingo Klimant** aus Graz für die trotz räumlicher Distanz immer sehr gute und umfassende Betreuung meiner Arbeit und für seine vielen, unverzichtbaren Ideen und Tipps, die zum Gelingen dieser Arbeit beigetragen haben.

Ganz herzlich bedanke ich mich bei **Dr. Sarina Arain** für die sehr schöne und lustige gemeinsame Laborzeit, in der wir im 4. Stock die Stellung gehalten haben, für gemütliche Abendessen bei Pizza und Tiramisu, wenn die "schnelle Messung" mal wieder länger dauerte und für die Rosenmontage, an denen wir (als rheinische Fraktion) die übrigen Mitglieder des Lehrstuhls mit Farbstiften bewaffnet zum Faschingfeiern animierten.

Ein großes Dankeschön möchte ich **Dr. Gregor Liebsch** aussprechen, der mich besonders am Anfang dieser Arbeit in die Geheimnisse des Imaging einweichte und für seine Hilfe bei kleineren und größeren Problemen mit dem Imaging Messsystem und IDL.

Ein weiteres großes Dankeschön geht an **Dr. Christian Krause** von der Firma Presens, der mir die neueste Generation seiner PD Referenzpartikel zur Verfügung stellte, ohne die es keine DLR Sensoren gegeben hätte und der immer ein kompetenter Ansprechpartner für alle meine Fragen zur optisch-chemischen Sensorik war.

Weiterhin bedanke ich mich ganz herzlich bei den derzeitigen und ehemaligen Mitgliedern unseres Institutes, insbesondere **Matthias Stich, Anna Vasilevskaya, Dr. Sergey Borisov, Doris Burger, Petra Suchomel, Edeltraud Schmied, Dr. Athanasios Apostolidis, Gisela Hierlmeier, Dr. Bianca Höfelschweiger, Dr. Bernhard Weidgans, Stefan Nagl und Dr. Michael Schäferling** für die wissenschaftlichen und nichtwissenschaftlichen Diskussionen, die gemeinsamen Kaffeerunden und die sehr gute Atmosphäre am Lehrstuhl.

Dr. Ulrich Franke, Dr. Lubos Polerecky und Dr. Björn Grunwald (MPI für Marine Mikrobiologie in Bremen) danke ich für die sehr gute Zusammenarbeit, für ihre Gastfreundschaft (inklusive Stadtführung) während meiner Aufenthalte in Bremen und für

ihre Hilfe bei diversen technischen Problemen. Dr. Lubos Polerecky danke ich insbesondere für die Durchführung der Messungen in natürlichen Sedimentproben mit pH/pO₂ Dualsensoren (Kapitel 4).

Des Weiteren danke ich *Dr. Henrik Staahl und Dr. Ronnie Glud* (Marine Biological Laboratory in Helsingor) für die ebenfalls sehr gute Zusammenarbeit und für die Bereitstellung ihrer Messergebnisse in natürlichen Sedimentproben mit planaren pH Sensoren (Kapitel 3).

Dem Bundesministerium für Bildung und Forschung (BMBF) danke ich für die finanzielle Unterstützung während dieser Arbeit.

Mein größter Dank gilt meinen Eltern *Lisa und Klaus Schröder* für ihre beständige Unterstützung während meines Studiums und meiner Doktorarbeit und meinem Lebensgefährten *Claude Robold* dafür, dass er immer für mich da ist und mir auch in stressigen Zeiten Rückhalt gibt.

Table of Contents

1. INTRODUCTION	1
1.1. Motivation	1
1.2. The role of pH, Carbon Dioxide and Oxygen in Marine Systems	2
1.3. pH, pCO ₂ and pO ₂ Sensors – State of the Art	5
1.3.1. pH Sensors.....	5
1.3.2. pCO ₂ Sensors.....	7
1.3.3. pO ₂ Sensors	9
1.4. Methods for biogeochemical studies in marine sediments	11
1.4.1. Electrochemical and optical chemical microsensors.....	11
1.4.2. Planar luminescent optical chemical sensor.....	12
1.5. Referencing Methods for Measurements with Luminescent Optical pH, pCO ₂ and pO ₂ Sensors	13
1.5.1. Time domain and frequency domain lifetime measurements	13
1.5.2. Referencing via Ratiometric Measurements	15
1.5.3. Frequency domain dual lifetime referencing	16
1.6. Time-Resolved Luminescence Imaging Methods Using Planar Optodes	17
1.6.1. Rapid lifetime determination.....	18
1.6.2. Time domain dual lifetime referencing	19
1.7. Luminescent dual sensors	20
1.8. References	21
2. INSTRUMENTS AND METHODS.....	35
2.1. pH Meter	35
2.2. Knife-coating device	35
2.3. Absorbance measurements.....	36
2.4. Luminescence measurements.....	36
2.5. Frequency-domain lifetime measurements	37
2.6. Chemical analysis of synthesised ion pairs and indicators	38

2.7. Time-resolved lifetime imaging.....	38
2.7.1. System components and set-up.....	38
2.7.2. Characterisation of the chip LED excitation light sources.....	40
2.7.3. Data acquisition and processing.....	42
2.8. References.....	44
3. pH FLUOROSENSORS FOR USE IN MARINE SEDIMENTS.....	45
3.1. Introduction.....	45
3.2. Experimental.....	47
3.2.1. Materials.....	47
3.2.2. Buffer preparation.....	48
3.2.3. Apparatus.....	48
3.2.4. Sensor fabrication.....	49
3.2.5. Preparation of sediment measurements.....	50
3.3. Synthesis.....	50
3.3.1. Synthesis of 5(6)-carboxy-2',7'-dihexylfluorescein (DHCF).....	51
3.3.2. Synthesis of 2',7'-dihexyl-5(6)-N-octadecyl-carboxamidofluorescein (DHFA).....	51
3.3.3. Synthesis of 2',7'-dihexyl-5(6)-N-octadecyl-carboxamidofluorescein ethyl ester (DHFAE).....	52
3.4. Results and discussion.....	52
3.4.1. Synthesis and characterisation of the lipophilic pH indicators.....	52
3.4.2. Characterisation of the intensity-based pH sensors.....	54
3.4.3. Cross-sensitivity towards ionic strength.....	58
3.4.4. Temperature effect.....	61
3.4.5. pH sensors for DLR-based referencing schemes.....	63
3.4.6. pH measurements in natural marine sediment using the M2_DHFAE sensor.....	67
3.5. Conclusion.....	70
3.6. References.....	71

4. TIME-RESOLVED MAPPING OF pH AND pO₂ WITH LUMINESCENT DUAL SENSORS.....	75
4.1. Introduction	75
4.2. Experimental	77
4.2.1. Materials	77
4.2.2. Sensor preparation.....	78
4.2.3. Instruments.....	79
4.3. Results and Discussion.....	81
4.3.1. Membrane design	81
4.3.2. Choice of indicators and optical components	83
4.3.3. Characteristics of the single parameter sensors	85
4.3.4. Characterisation of the DHFA/Pt(PFPP) dual sensor	86
4.3.4.1. Spectral interactions between the two indicator dyes	86
4.3.4.2. <i>td</i> -DLR/RLD measurement scheme	87
4.3.4.3. Considerations on the correction functions C_1 and C_2	91
4.3.4.4. Influence of RET and inner filter effect	95
4.3.4.5. Iteration procedure	95
4.3.4.6. Sensor stability - leaching and photodecomposition of the indicators.....	96
4.3.4.7. Cross-sensitivity towards ionic strength	97
4.3.4.8. Temperature effect.....	98
4.3.5. Imaging of pH and pO ₂ in natural marine sediment.....	100
4.4. Conclusion	100
4.5. References	102
5. LUMINESCENT DUAL SENSOR FOR TIME-RESOLVED IMAGING OF pCO₂ AND pO₂ IN AQUATIC SYSTEMS.....	106
5.1. Introduction	106
5.2. Experimental	108
5.2.1. Materials	108
5.2.2. Synthesis of the (TOA) ₃ HPTS ion pair	109

5.2.3. Sensor preparation	109
5.2.4. Instrumentation	110
5.3. Results and Discussion.....	112
5.3.1. Choice of indicators and sensor polymer.....	112
5.3.2. Characterisation of the sensor membranes for single parameter $p\text{CO}_2$ and $p\text{O}_2$ detection	114
5.3.3. Method.....	117
5.3.4. Characterisation of the $p\text{CO}_2$ - $p\text{O}_2$ dual sensor.....	119
5.4. Conclusion	126
5.5. References	127
6. EFFECT OF THE LIPOPHILIC BASE IN SOLID STATE OPTICAL $p\text{CO}_2$ SENSORS	131
6.1. Preliminary remarks	131
6.2. Introduction	132
6.3. Experimental	133
6.3.1. Materials	133
6.3.2. Synthesis of the XB-DTMA ion pair	133
6.3.3. Preparation of the sensor membranes	134
6.3.4. Apparatus	134
6.4. Results and Discussion.....	135
6.4.1. Lipophilic organic bases	135
6.4.2. Sensitivity towards $p\text{CO}_2$ with different amounts of organic base.....	137
6.4.3. Temperature dependence	139
6.4.4. Effect of relative humidity	141
6.4.5. Use of other neutral organic bases	144
6.4.6. Possible utilisation of PBO-containing $p\text{CO}_2$ sensors as humidity sensors.....	144
6.5. Conclusion	145
6.6. References	145
7. SUMMARY	147

8. ABBREVIATIONS, ACRONYMS AND SYMBOLS.....	149
9. CURRICULUM VITAE	152
10. LIST OF PUBLICATIONS	154
11. APPENDIX	156
11.1. Partial pressure - concentration conversion table for carbon dioxide and oxygen	156
11.2. List of Suppliers	157
11.3. Source code examples of the VBA applications used for the evaluation of the dual sensor measurements	158
11.3.1. <i>Extraction of the image data matrix from the IDL raw data file</i>	<i>158</i>
11.3.2. <i>Number of iteration steps required for the evaluation of the pH-pO₂ dual sensor measurements (Chapter 4.3.4.4).....</i>	<i>159</i>
11.3.3. <i>Evaluation of the pH-pO₂ dual sensor images of a natural sediment sample (Chapter 4.3.5).....</i>	<i>161</i>
11.3.4. <i>Number of iteration steps required for the evaluation of the pCO₂- pO₂ dual sensor measurements (Chapter 5.3.4)</i>	<i>164</i>
11.4. References	167

1. Introduction

1.1. Motivation

The oceans play an important role in the global ecological system. Covering more than two thirds of the earth's surface, ca. 46 % of the net primary production occurs in marine environment^{1,2}. Mainly phytoplankton (e. g., diatoms, cyanobacteria) in surface seawater produces organic compounds and oxygen from inorganic carbon dioxide and water via photosynthesis. Autotrophic organisms are the first link in the marine food web feeding directly and indirectly heterotrophs such as bacterioplankton, zooplankton or fish. Dead organisms and biogenic particles descent through the water column towards the seafloor. This "fall-out" of particulate organic carbon also fuels benthic life. Ca. 1 - 5 % of the surface net primary production of the open ocean reaches the deep sea sediments³. In coastal regions about 25 - 50 % of the organic matter is deposited in the sediment bed⁴, where the major part is remineralised under oxygen consumption to carbon dioxide and other inorganic compounds (e.g., NO_3^- , PO_4^{3-} etc.)⁵. Coastal sediments are the most important source of inorganic nutrients to the overlying water column. The seawater - sediment interface in such areas is characterised by steep gradients of various physical and chemical parameters within a narrow zone of < 0.5 mm to a few millimetres^{6,7} reflecting the multiple biogeochemical reactions and fluxes of reactants or products between the overlying water and the sediment. Oxygen, carbon dioxide and pH are key parameters involved in these biogeochemical processes. Respiration, benthic photosynthesis (in shallow regions), chemoautotrophic activity, nitrification or oxidation of reduced species diffusing from anaerobic sediment areas to the oxygenated sediment surface are all coupled to one or more of these parameters.

Ca. 0.17 - 0.26 % of the annual marine net primary production is permanently buried. Thus, on a geological time-scale CO_2 is removed from the atmosphere via the biological pump and stored in permanent deposits in marine sediments^{8,9}. For the last 200 years, however, the fraction of anthropogenic carbon dioxide in the atmosphere has increased rapidly (from ca. 280 ppm in preindustrial times to ca. 370 ppm today) due to burning of fossil fuels and deforestation and signs for a global climate change become apparent¹⁰. About half of the anthropogenic carbon dioxide released to the atmosphere is estimated to be absorbed by the surface seawater of the oceans. The oceans are a huge reservoir of CO_2 . Dissolved inorganic carbon (DIC) present in the water column includes carbon dioxide as

well as bicarbonate and carbonate ions. In marine sediments large deposits of calcium carbonate are found. The oceans can therefore act both as source and sink of the greenhouse gas CO₂.

A thorough understanding of the biogeochemical processes in marine ecosystems has become increasingly important to refine models of the global budget of various elements such as oxygen, nitrogen and especially carbon but also to investigate alterations within these ecosystems in response to changes in environmental conditions. Against this background, the investigation of benthic distributions, fluxes and exchange rates of CO₂, O₂ and pH has achieved a high significance in marine biogeochemistry in the last decades¹¹⁻¹³. Microelectrodes and fibre optic microoptodes have been applied to record profiles of these parameters¹⁴⁻¹⁶. However, due to the distinct spatial heterogeneity exhibited by surface sediments, a calculation of fluxes based on the extrapolation from a few microprofiles to larger sediment areas is often problematic or even impossible^{17,18}. A promising technique for two-dimensional measurements combines luminescent planar optodes with CCD technology. In recent years, planar optical oxygen sensors have been successfully applied to quantify oxygen distributions at heterogeneous benthic interfaces such as sediments, microbial mats or biofilms with high spatial and temporal resolution¹⁹⁻²¹. The transfer of this technique to other relevant biogeochemical variables is therefore highly desirable.

The aim of this thesis was to synthesise and characterise luminescent sensor materials suitable for the two-dimensional determination of pH and pCO₂ in marine systems. Emphasis was put on the adaptation of the dynamic range of the resulting sensor membranes to meet the conditions in marine environment and on the optimisation of the materials for the use in time-resolved luminescence imaging applications. In addition to the development and characterisation of single parameter optodes, this thesis presents the development of planar optical dual sensors for the mapping of pH/pO₂ as well as pCO₂/pO₂ and of a practical measurement strategy for the time-resolved and intrinsically referenced detection of the respective parameter couples with a fast-gated CCD camera.

1.2. The role of pH, Carbon Dioxide and Oxygen in Marine Systems

pO₂ and pCO₂ in the upper surface seawater are mainly determined by the rapid gas exchange with the atmosphere, the water temperature and the biota in this area. In the euphotic zone of the water column (depth of ca. 20 - 150 m) oxygen is formed and CO₂ is consumed upon

photosynthesis activity of phytoplankton, while below this zone heterotrophic respiration starts to become the dominant form of energy generation (Fig. 1.1, eq. 1.1). A further source of CO_2 are calcifying organisms (e.g. coccolithophorids, foraminifera, shellfish, corals), which precipitate CaCO_3 in skeletal or protective tissues (eq. 1.2). The water of the deep oceans (ca. 80 % of the total seawater) is supplied with oxygen and carbon dioxide from the influx of down-welling cold surface seawater in polar regions which is saturated with atmospheric gases. Less oxygen is consumed in the deep sea since food supply and population of organisms are depleted. Therefore, the oxygen level of deep ocean waters is comparatively high and the water is enriched with carbon dioxide and nutrients.

In aqueous solution carbon dioxide adds water to form carbonic acid, which is in equilibrium with hydrogen carbonate and carbonate according to eqs. 1.3a - 1.3c²². The pH of seawater is kept constant within a relatively narrow range between ca. pH 8.2 (surface seawater) and pH 7.8 (deep-sea water) mainly by the carbonate buffer system ($\text{HCO}_3^-/\text{CO}_3^{2-}$) of the oceans (borate also plays a minor role as buffer substance). Thus, seawater pH and the marine carbon cycle are strongly interrelated. At pH 8.2 and pH 7.8 the molar percentages of the three dissolved inorganic carbon species $\text{CO}_{2(\text{aq})} : \text{HCO}_3^- : \text{CO}_3^{2-}$ in seawater are 0.4 : 84.6 : 15.0 and 1.1 : 92.4 : 6.5, respectively (the concentration of free carbonic acid is only ca. 0.1 % of the $\text{CO}_{2(\text{aq})}$ concentration).

The pH, carbon dioxide and oxygen levels within the sediment bed depend on a variety of factors such as flow conditions, organic carbon input and usability and macro- and micro-biota activity. In most sediments, transport processes of dissolved substances (e.g., oxygen) between overlying water and sediment pore water are driven by concentration gradients (\rightarrow diffusion). Large coastal areas are covered by coarse grain (sandy) sediments, where advection is the dominant transport mode. Here oxygenated seawater penetrates deeper into the surface sediment layer and increases the degradation efficiency of buried organic matter. In shallow, photic regions, photosynthesis activity of patches of benthic autotrophic microorganisms can additionally increase the oxygen partial pressure in the respective surface sediment areas, while CO_2 is depleted. Within the first few millimetres of the sediment the pO_2 decreases to zero due to respiration and fermentation reactions in the course of organic matter remineralisation. At the same time CO_2 is formed and therefore the pH slightly decreases. Below that region other chemical species such as sulfate, nitrate, iron(III) oxides or manganese(IV) oxide replace oxygen as oxidants during the anaerobic degradation of organic matter. The majority of these processes is mediated by different populations of specialised microorganisms present in the respective regions. The reduced chemical species slowly

diffuse back upwards into the aerated zone where they are reoxidised under oxygen consumption (e.g., eqs. 1.4 - 1.6)²³⁻²⁵. This oxic-anoxic interface (= redox boundary layer) is characterised by a steep pH decline. Burrowing animals play a major role in the process and rate of organic matter degradation in their ecosystems^{26,27}. They rework the sediment during the building of burrows (= bioturbation) and actively pump oxygenated bottom water through their burrow system (= bioirrigation), thus, stimulating bacterial activity and reoxidation of reduced species in deeper sediment regions. pH and pCO₂ are also master variables involved in the dissolution or precipitation of CaCO₃ deposits in the sediment²⁸.

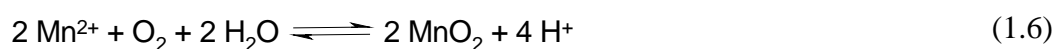
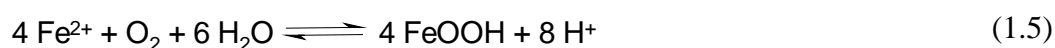
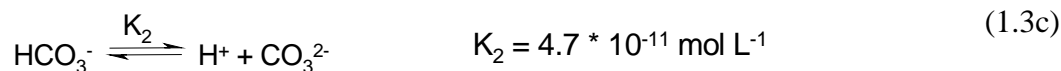
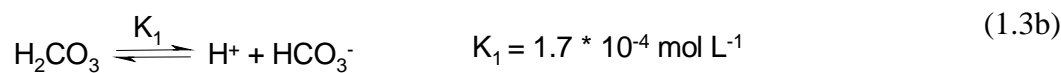
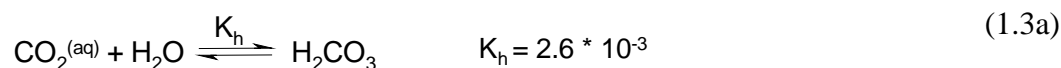
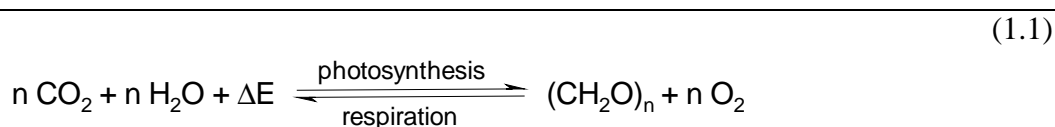


Fig. 1.1. Examples of chemical equilibria in marine systems.

pH values occurring in marine sediments are predominantly in the range between pH 7.2 and pH 9.2. High pH values are found mainly in photosynthetically active areas where the pCO₂ can decline to < 0.03 hPa while pO₂ levels of > 600 hPa are reached. Upon high respiration or degradation rates, the pCO₂ within the sediment can increase to > 12 hPa.

1.3. pH, pCO₂ and pO₂ Sensors – State of the Art

Besides the importance of pH, pO₂ and pCO₂ in environmental monitoring²⁹⁻³⁴, the determination of these parameters is of vital interest in many other application fields. In clinical diagnostics the monitoring of respiration gases or of pH, pO₂ and pCO₂ levels in tissue or body fluids constitutes an essential means for assessing the status of critically ill and surgical patients³⁵⁻⁴². The food industry uses pH, pO₂ and/or pCO₂ as quality parameters indicating the sterility of food and beverages⁴³⁻⁴⁷. In biotechnology the monitoring of one or more of the parameters is applied for process control in bioreactors⁴⁸⁻⁵¹. Additionally, pH is an important control factor in industrial waste water treatment^{52,53}. pCO₂ and pO₂ determination is used to control exhaust emission in the automobile industry⁵⁴⁻⁵⁷. Numerous sensing methods for these parameters have been developed to meet the requirements of the various application areas.

1.3.1. pH Sensors

The most widely used tool for pH detection is the glass electrode first described by Cremer (1906), MacInnes and Dole (1929)^{58,59}. This potentiometric electrode usually consists of an Ag⁺/AgCl working electrode immersed in an internal KCl buffer solution with defined pH and an Ag⁺/AgCl reference electrode. It exploits the potential difference establishing in the proton-selective glass membrane separating the internal buffer solution and the external test solution as a measure for the proton activity in the sample. Ion-selective field effect transistors (ISFETs) on the basis of metal oxide screen field effect transistor (MOSFET) technology⁶⁰ offer an alternative in fields where the risk of breakage limits the use of glass electrodes (e. g. quality control in food industry, in-vivo pH detection). Lately an iridium oxide-based electrode has been reported with good stability even in strongly alkaline solutions or samples containing hydrofluoric acid, which normally cause errors or irreversibly damage the ion-selective membranes of glass electrodes, ISFETs or other metal oxide electrodes⁶¹. pH electrodes show a linear (Nernstian) response towards pH allowing a fast two-point calibration and they usually feature a wide working range (ca. pH 2 - pH 12).

However, there are also several drawbacks, which make the use of pH electrodes difficult or even impossible for certain applications. Measurements with electrodes can generally be biased by electromagnetic fields, changing flow velocity of the test solution or

solutes such as heavy metals, proteins or hydrogen sulfide. ISFET and metal/metal oxide electrodes are cross-sensitive towards redox changes in the sample. During long-term measurements small variations of pH are difficult to observe, since the electrode signal drifts with time. The dependence of the liquid junction potential on the composition and concentration of the sample can be a further source of error. pH detection in small sample volumes or high resolution pH detection in heterogeneous systems requires miniaturisation of the working electrode and sometimes also the reference electrode, which involves complex fabrication procedures. Optical chemical pH sensors overcome many of these problems and can therefore provide an alternative to electrochemical pH sensors.

Optical sensors generally comprise a light source (e.g., xenon lamp, light emitting diode (LED), laser diode, laser), a detector (e.g., photodiode, photomultiplier tube (PMT), CCD-chip) and the sensing element (= optode) responsible for the selective analyte recognition and signal transduction. In case of optical pH sensors this optode is usually composed of an indicator dye immobilised in a proton-permeable polymer matrix by covalent coupling, adsorption or entrapment. pH indicators are weak acids or bases, which reversibly alter their optical properties (e.g., absorbance, fluorescence intensity) upon protonation/deprotonation. Non-bleeding pH test stripes can be considered as a first type of simple pH optodes for the rough determination of pH using the eye as detector. In 1980 Peterson et al. published a fibre-optical pH sensor applying the absorbance dye phenol red covalently bound to polyacrylamide microspheres as pH indicator⁶². The first fluorescence-based pH sensors were as well fibre-optical sensors reported by Saari and Seitz (1982)⁶³. Fluoresceinamine covalently immobilised on controlled-pore glass and on cellulose were used as sensing materials, respectively. Many absorbance-based pH sensors employing indicators such as phenol red, bromothymol blue and other have been reported⁶⁴⁻⁶⁸. However, the majority of pH optodes found in literature are fluorescence-based due to the higher sensitivity of the resulting sensors, the low indicator concentrations required and a less complex measurement set-up (no light transmission through the analyte necessary, excitation and signal read-out from one side of the sensor membrane). To date the most frequently used fluorescent pH indicators in pH optodes are 8-hydroxypyrene-1,3,6-trisulfonic acid sodium salt (HPTS), fluorescein derivatives, seminaphthorhodafluor (SNARF) dyes and hydroxycoumarines⁶⁹⁻⁷³, whereat the criteria for the choice of the indicator are such as the pKa value, quantum yields, photostability, Stokes shift, lifetime, excitation and emission wavelengths.

Since optical pH sensors measure the proton concentration and not the activity they are cross-sensitive towards the ionic strength of the sample, which has to be corrected. This influence, however, can be minimised by the selection of suitable indicator and sensor polymer combinations⁷⁴. The polymer matrix has a strong impact on the characteristics of the pH optode. The microenvironment in the polymer can induce a shift of the apparent pKa (pKa') of the indicator by stabilising its protonated or deprotonated form. Optical pH sensors composed of an pH indicator, which is electrostatically immobilised on commercial ion-exchangers⁷⁵⁻⁷⁷ or entrapped in hydrophobic plasticised PVC⁷⁸ have been reported. Sol-gel glasses are a further intensively investigated pH sensor matrix⁷⁹⁻⁸¹. However, one of the disadvantages of these approaches are slow response and/or recovery times. Additionally, plasticised PVC membranes are not stable since the plasticiser leaches from the membrane with time thereby changing the characteristics of the pH sensor. The preparation of intact sol-gel membranes is time-consuming and difficult and sol-gel-based optodes show a poor reproducibility. The most widely employed pH sensor polymers are cellulose derivatives⁸²⁻⁸⁵ and hydrogels such as polyurethane^{86,87} or PHEMA⁸⁸, which possess an excellent permeability for water and ions.

In contrast to electrochemical sensors pH optodes show a sigmoidal response towards pH and the dynamic range is usually limited to ca. $\text{pKa}' \pm 1.5$. Yet, the small dynamic range results in a high signal change with pH and therefore in a high sensor resolution. Furthermore, a sensor working range of ca. 3 pH units is sufficient for many analytical problems. Within the pH range of ca. $\text{pKa}' \pm 0.5$ the optode response is quasi-linear, which can be exploited for a fast two-point calibration provided that only small pH changes are to be detected. A signal drift like in the case of pH electrodes can be avoided by applying referenced measurement schemes instead of measuring the absorbance or fluorescence intensity (see chapter 1.5).

1.3.2. pCO₂ Sensors

One of the standard methods for the determination of gaseous carbon dioxide (e.g., atmospheric CO₂, respiratory gases) is infrared spectroscopy (CO₂ absorbance maxima: 2600 nm, 4300 nm)^{89,90}, where carbon dioxide is directly detected. Most sensors for the measurement of dissolved carbon dioxide are modified pH sensors exploiting the fact that carbon dioxide lowers the pH of an aqueous solution. Severinghaus and Bradley introduced an electrochemical pCO₂ sensor in 1958⁹¹. The Severinghaus-type electrode comprises a pH

glass electrode immersed into a small volume of a weak bicarbonate buffer solution, which is then enclosed in a gas-permeable but ion-impermeable membrane, such as teflon, silicone or polytetrafluoroethylene (PTFE). The membrane prevents a cross-sensitivity towards the pH of the test solution. A different concept is followed with the potentiometric carbonate-selective electrode reported by Choi et al. (2002) for the indirect determination of carbon dioxide in seawater⁹². This electrode features a low cross-sensitivity towards other anions, fast response times and a precision comparable to that of conventional Severinghaus-type electrodes. Yet, important drawbacks are that the electrode is limited to measurements in slightly basic samples where the equilibrium concentration of carbonate is within the detection limit and that the calculation of pCO₂ from the measurement is only possible when the pH of the sample is known, which makes an in situ application in inhomogeneous samples difficult.

In 1975 Lübbers and Opitz reported an optical pCO₂ sensor on the basis of the pCO₂ dependent fluorescence intensity change of 4-methylumbelliferone in a bicarbonate buffer solution covered with an PTFE membrane⁹³. pCO₂ optodes can essentially be classified in Severinghaus-type optodes (where the pH electrode is replaced by a pH-sensitive dye dissolved in an aqueous bicarbonate buffer solution⁹⁴ or immobilised in a solid support (e.g. Hydrogel, Sephadex) soaked with a bicarbonate buffer⁹⁵⁻⁹⁷) and solid state optodes. Severinghaus-type optical pCO₂ sensors (like the electrodes) usually suffer from long response times and a dependence on the osmotic pressure between the internal buffer and the sample solution. Some authors reported optical sensing devices with the possibility to continuously renew the intrinsic indicator - buffer solution^{98,99}. This technique allows for calibration-free pCO₂ detection over a long period of time even in samples with high salinity like seawater but it does not overcome the slow response times of the sensor.

The first solid state pCO₂ optode was reported by Raemer et al. in 1991¹⁰⁰. This sensor type is composed of a pH indicator dye and a lipophilic organic buffer (e.g. tetraoctylammonium hydroxide) incorporated in a hydrophobic polymer, such as ethyl cellulose, silicone, polystyrene or sol-gel¹⁰¹⁻¹⁰⁴. The polymer acts as ion barrier and therefore reduces a cross-sensitivity towards the pH of the sample. Sometimes a plasticiser (e.g. tributyl phosphate) is added to facilitate the diffusion of CO₂ into the sensor membrane and to enhance the response times of the sensor¹⁰⁵. Thus, response times (t₉₀) less than 1 s were reported. This approach also minimises the problem of different sample osmolarities because the sensor contains no "wet" buffer.

The dynamic range of optical pCO₂ sensors is determined by the apparent pK_a of the employed pH indicator (which especially in case of the solid state membranes sometimes

differs substantially from the real pK_a) and the concentration of the HCO_3^- ions of the bicarbonate buffer (Severinghaus-type optodes) or the amount and nature of the lipophilic buffer substance (solid state optodes), respectively. $p\text{CO}_2$ optodes as well as Severinghaus electrodes are cross-sensitive towards neutral weak acids or bases such as H_2S or NH_3 which can also permeate into the sensor. In general this signal change is reversible. Only H_2S irreversibly changes the reference potential of the Severinghaus electrode (formation of Ag_2S in the Ag^+/AgCl reference electrode). Gaseous anhydrides of strong acids such as NO_x or SO_2 , however, irreversibly poison the $p\text{CO}_2$ sensors.

1.3.3. $p\text{O}_2$ Sensors

A wide variety of oxygen detection methods have been established in answer to the specific analytical problems. Paramagnetic analysers are often employed for the determination of gaseous oxygen (e.g., atmospheric gas samples)¹⁰⁶. Potentiometric high temperature electrodes using oxygen ion conducting solid electrolytes find extensive use for oxygen detection in automobile exhaust gases. A standard method for the determination of dissolved oxygen (e.g., in natural waters) is the Winkler titration¹⁰⁷. The most frequently applied oxygen sensors for dissolved oxygen are amperometric electrodes such as the Clark electrode introduced in 1956¹⁰⁸. It comprises a platinum (or gold) electrode and a silver reference electrode both immersed in an internal KCl solution and separated by an oxygen permeable membrane from the test solution. The electric current flow between the two electrodes (cathode reaction: $\frac{1}{4} \text{O}_2 + \text{e}^- + \frac{1}{2} \text{H}_2\text{O} \rightarrow \text{OH}^-$, anode reaction: $\text{Ag} + \text{Cl}^- \rightarrow \text{AgCl} + \text{e}^-$) when polarised with a potential between -0.6 and -0.8 V (vs. Ag/AgCl) is proportional to the oxygen partial pressure in the sample. The major drawbacks of amperometric $p\text{O}_2$ sensors are the oxygen consumption in the cathode reaction, which causes severe errors at the detection of low $p\text{O}_2$ levels and their limited operational lifetime since the anode reaction slowly passivates the reference electrode.

The sensing reaction of most optical $p\text{O}_2$ sensors is based on the dynamic (collisional) quenching of the excited state of a luminescent indicator dye by oxygen and does therefore not consume the analyte. The first $p\text{O}_2$ optode was described by Bergman in 1968 and was composed of fluoranthene adsorbed on a porous glass support¹⁰⁹. More recent optical oxygen sensors utilise indicator dyes immobilised in oxygen-permeable, non-polar polymers which ideally provide a mechanically and chemically stable optode matrix and increase the sensor

selectivity in being impermeable to other quenchers such as heavy metals or iodide. Frequently applied matrix polymers fulfilling these requirements are silicone rubbers, polystyrene, PMMA, PVC or cellulose derivatives¹¹⁰⁻¹¹⁴. Silicon rubber features an oxygen-permeability about 2 orders of magnitudes higher than of other organic polymers, which leads to high quenching efficiencies¹¹⁵. Sol-gel-based pO₂ optodes have proved to be suitable for gas phase measurements¹¹⁶. When used for the detection of dissolved oxygen organically modified sol-gel matrices are superior, since they reduce otherwise long response times and indicator leaching¹¹⁷.

Although oxygen is long known to be a notorious quencher reducing the quantum yields and lifetimes of many luminophores¹¹⁸, only for a limited number of dyes the quenching efficiency and rate is large enough to make them useful indicators for optical pO₂ sensing. Photostability, high quantum yield, long lifetime, high molar absorbance, compatibility with low-priced excitation light sources (e.g., LEDs, diode lasers) and adequate solubility in the sensor polymer are important aspects in the choice of the indicator. Among the first employed indicators in pO₂ optodes were fluorescent polycyclic aromatic hydrocarbons (PAH) (e.g., pyrene, pyrene derivatives, fluoranthene, decacyclene or anthracene derivatives)¹¹⁹⁻¹²¹. Most of these dyes have a relatively long fluorescence lifetime around 200 ns but usually also display unfavourable excitation wavelengths in the UV region. The most widely used group of pO₂ indicators are ruthenium(II)diimine complexes (with ligands such as 2,2'-bipyridyl, 1,10-phenanthroline or 4,7-diphenyl-1,10-phenanthroline), which feature high quantum yields, lifetimes in the range of 0.2 - 6 μs, large Stokes shifts (ca. 150 nm) and excitation wavelengths around 450 nm (matching the emission of blue LEDs)^{119,122-124}. These charged indicators are usually incorporated into non-polar sensor polymers in form of lipophilic ion pairs (with anions such as 3-(trimethylsilyl)-1-propanesulfonate or tetraphenylborate) or adsorbed on polar materials such as silica gel¹²⁵⁻¹²⁷. Phosphorescent platinum(II)- and palladium(II)-porphyrin derivatives are a third important group of pO₂ indicators displaying high quantum yields and a high sensitivity towards oxygen due to their extremely long lifetimes in the range of ca. 50 - 100 μs and ca. 0.5 - 1 ms, respectively. Lipophilic Pt(II) and Pd(II) complexes with fluorinated ligands such as tetrakis(pentafluorophenyl)-porphyrin possess excellent photostability, are soluble in the prevalent sensor polymers and have excitation bands in the near UV and the visible range and an emission band around 650 nm.

Since the lifetime of the excited state of the luminescent indicator and the oxygen permeability of the sensor polymer both determine the probability of the excited state

deactivation by collisional quenching, the sensitivity of pO_2 optodes can be tuned by the choice of the indicator and the polymer used as matrix. The fact that the oxygen partial pressure affects not only the quantum yield but also the decay time of the indicator enables intrinsically referenced, lifetime-based measurements resulting in a high sensor signal stability and reproducibility¹²⁸.

1.4. Methods for biogeochemical studies in marine sediments

Conventional techniques to study flux rates between sediment and overlying seawater (e.g., DIC, oxygen), to quantify benthic primary production or remineralisation rates include measurements in laboratory-incubated intact sediment cores or in-situ measurements using benthic flux chamber landers. However, these methods do not probe into the sediment and hence give only a limited understanding of the processes taking place at the sediment-water-interface or within the sediment. Moreover, the sampling and recovery of sediment cores often causes artefacts due to decompression, temporary temperature increase, inhibition or exclusion of marine benthos etc.¹²⁹.

1.4.1 Electrochemical and optical chemical microsensors

In the last decades microsensors have been developed for the in situ determination of a variety of parameters in marine sediments with a high spatial resolution¹³⁰. Microelectrodes for pH detection are usually glass electrodes. LIX-based pH microelectrodes (a liquid ion-exchanger incorporated in PVC acts as the proton selective membrane) have also been reported^{131,132}. They are easier to miniaturise and show faster response times (< 5 s, glass microelectrode: ca. 100 s) but also have very short lifetimes (a few days). Severinghaus-type and Clark-type microelectrodes are the most common formats for electrochemical pCO_2 and pO_2 sensing, respectively. Clark-type pO_2 microelectrodes are the most widely used microsensors for marine applications and have excellent measurement properties such as short response times (< 1 s) and small stirring cross-sensitivity (1 - 2 %)¹³³. pH, pCO_2 and pO_2 microelectrodes can be fabricated with tip diameters < 20 μm ¹³⁴. A major limitation for their more frequent use is, however, that the construction of well-working microelectrodes is time consuming and requires a significant amount of training. Commercially available products are expensive and

do not always feature optimal measurement properties. Besides the drawbacks mentioned in chapter 1.3., microelectrodes are extremely fragile, which often leads to breakage in field application and a high hydrostatic pressure in deep-sea measurements may cause damage.

Klimant et al. (1995) introduced the first microoptodes for the detection of oxygen in marine systems¹³⁵. This sensor type has found increasing application in aquatic microbiology since. Fibre optical microsensors benefit from low production costs and simple miniaturisation procedures. The sensor chemistry is deposited onto the tip of the tapered optical fibre. Typically microoptodes with tip diameters of 30 - 40 μm are used since smaller optodes display insufficient signal intensities. Solid state and Severinghaus-type microoptodes for pCO_2 measurements in marine environment have also been described^{12,136}. The development of suitable pH microoptodes is difficult. Considering that the total pH range of interest in marine systems is between 6.5 and 10 and that the dynamic range of pH optodes in general covers only ca. 3 pH units, the optimum pKa' of the pH optode is near the pH of seawater (ca. 8.2). Most fluorescent pH indicators available have dynamic ranges in the acidic or neutral pH region, while indicators with a pKa in the near basic region are rare. Therefore mainly pH microoptodes incorporating colorimetric indicators have been reported for the application in marine systems^{137,138}. Compared to microelectrodes microoptodes can show a higher signal stability, are not cross-sensitive towards the stirring velocity and can be operated under high hydrostatic pressures.

Microsensors allow the recording of profiles with a spatial resolution $< 50 \mu\text{m}$ and have strongly increased the understanding of microenvironmental controls within microbial communities. However, these sensors are limited to single point measurements and are, therefore, not suitable to resolve the strong spatial heterogeneities within marine sediments (e.g. due to patchy distribution of photosynthetically active phytobenthos, activity of burrowing benthic fauna etc.).

1.4.2 Planar luminescent optical chemical sensor

Planar luminescent optodes where the sensing chemistry is spread onto a transparent, inert foil in combination with a CCD camera as detector overcome these problems to some extent. Glud et al. first applied this technique to record images of the two-dimensional oxygen distribution in marine sediments with a high temporal and spatial (ca. 26 μm per pixel) resolution¹³⁹. Since then planar oxygen optodes proved to be a useful tool in a variety of studies in marine

systems¹⁴⁰⁻¹⁴³. Planar optical pH sensors for the two-dimensional detection of pH marine sediments have been reported by Hulth et al.¹⁴⁴ and Zhu et al.¹⁴⁵. However, in both cases HPTS served as pH indicator resulting in sensors with a dynamic range between ca. pH 6.2 and 8.2, which covers only a small part of the most relevant pH range in marine systems. Benthic landers have been developed for the in situ measurements in marine sediments with both, microsensors and planar optodes¹⁴⁶⁻¹⁴⁸.

1.5. Referencing Methods for Measurements with Luminescent Optical pH, pCO₂ and pO₂ Sensors

The sensing mechanism of a luminescent optical sensor is based on an interaction between indicator and target analyte, which leads to a measurable change of the optical properties of the indicator dye. Depending on the sensing reaction various properties of the emitted luminescence can be related to the analyte concentration (e.g., intensity, lifetime, spectral distribution or polarisation). In contrast to the luminescence intensity, the luminescence lifetime as an intrinsic parameter is virtually independent of the indicator concentration, membrane thickness, light scattering or reflection or variations in the opto-electronic system. Lifetime-based sensing techniques are therefore the method of choice for optical oxygen sensing. Furthermore, the decay times of most pO₂ indicators are rather long (μs -range), which enables the use of less sophisticated, cost-efficient measurement devices.

1.5.1 Time domain and frequency domain lifetime measurements

The luminescence lifetime τ is defined as the average time a luminescent molecule remains in the excited state before it returns to the ground state. Considering a sample of many luminescent molecules with their statistical distribution of individual lifetimes and provided that a single exponential decay can be assumed, τ is the time after which 1/e of the initially excited luminophores still exist in the excited state. The luminescence intensity $I(t)$ at a time t after a δ -shaped excitation pulse is then related to the decay time τ by eq. 1.7

$$I(t) = I_0 \cdot \exp\left(\frac{-t}{\tau}\right) \quad (1.7)$$

where I_0 is the luminescence intensity at $t = 0$.

The lifetime can either be measured in the time-domain or the frequency domain¹⁴⁹. In the time-domain or pulse method the sample is excited by short light pulses and the time-dependent decay of the luminescence intensity is recorded. In the frequency domain or phase modulation method the luminophore is excited by sinusoidally modulated light. The modulation frequency is adapted to the excited state lifetime in a way that the lifetime causes a time delay between the excitation light intensity and the luminescence emission intensity. This leads to a phase shift between the modulated excitation light and the likewise modulated luminophore emission and to a decreased emission amplitude (intensity) relative to the incident light, called demodulation m (Fig. 1.2).

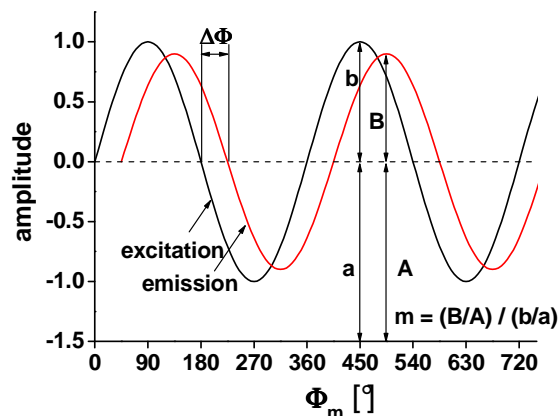


Fig. 1.2. Schematic of the phase modulation method; the emission of the luminophore is demodulated (m) and phase shifted (Φ) relative to the excitation light.

The correlation between the phase shift Φ and the lifetime τ for a single-exponential luminescence decay is given by eq. 1.8

$$\tau = \frac{\tan \Phi}{2 \cdot \pi \cdot f_{\text{mod}}} \quad (1.8)$$

where f_{mod} is the modulation frequency of the excitation light. The resolution of a multi-exponential decay behaviour is rather complex both with time domain and frequency domain

methods. Thus, the application of a "real" decay time as measurement parameter in optical chemical sensing is not convenient. There are several factors that cause the observed luminescence decay of indicator molecules embedded in a polymer matrix to be multi-exponential (e.g., matrix effects, light scattering, trace contamination). As a consequence, the weighted average lifetime over all luminophores calculated from the phase shift measured at a single frequency by means of eq. 1.8 is normally used as intrinsically referenced, analyte-dependent parameter.

The luminescence decay time is influenced by dynamic quenching, energy transfer from the excited state or excited state reactions. Since the protonation or deprotonation of a pH indicator is mostly a ground state reaction only a limited number of lifetime-based optical pH (or pCO₂) sensors exist. Very few indicators such as acridine¹⁵⁰ and some SNARF and SNAFL derivatives¹⁵¹ display sufficiently different lifetimes in the protonated and the deprotonated form to utilise the lifetime change for pH detection. Other pH optodes have been reported, which exploit the resonance energy transfer from an inert, μ s-lifetime Ru(phen)₃ complex (donor) to a colorimetric pH indicator (acceptor)¹⁵². Yet, these sensors display a high cross-sensitivity towards temperature and have a limited photostability. Therefore, ratiometric measurements are commonly applied as referencing technique in optical pH and pCO₂ sensing.

1.5.2 Referencing via Ratiometric Measurements

Provided that acidic and basic form of the pH indicator are fluorescent (e.g., HPTS, SNAFL and SNARF dyes), the ratio of the emission intensities of the two forms can be used as measurement signal. Depending on the spectral characteristics of the indicator single excitation/dual emission, dual excitation/single emission or dual excitation/dual emission wavelength measurements are possible. This dual-wavelength method references alterations in the indicator concentration and fluctuations in the light-source intensity or the detector sensitivity. However, light scatter and reflection contribute to effects which are not compensated. In case that only the protonated or the deprotonated form of the pH indicator is fluorescent a second pH-independent dye can be used as reference for ratiometric measurements. Here an indicator/reference couple is required with either overlapping excitation and different emission bands or vice versa to enable the efficient separation of the emission or excitation intensities.

1.5.3 Frequency domain dual lifetime referencing

The frequency domain dual lifetime referencing (fd-DLR) scheme is a further ratiometric measurement method^{153,154}, which exploits the difference in the lifetime of the fluorescent pH indicator (ns lifetime) and a pH-independent reference dye with a μs to ms lifetime (Fig. 1.3).

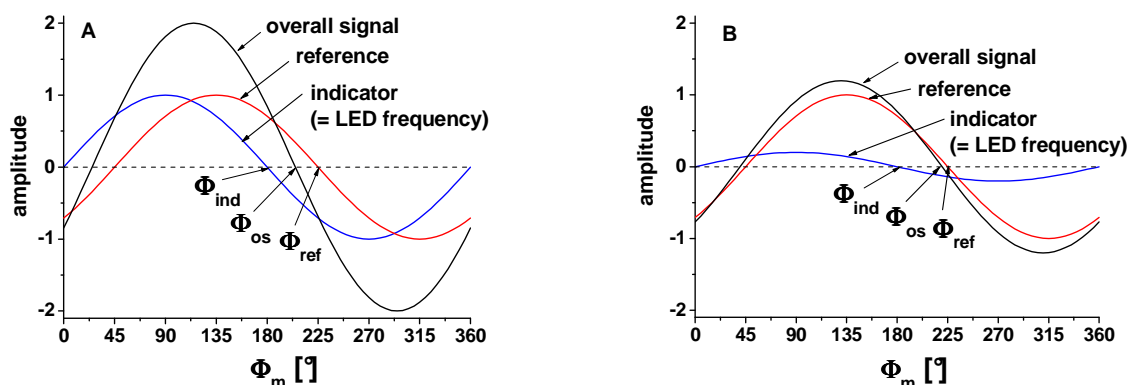


Fig. 1.3. Phase shift of the indicator (Φ_{ind}), the reference (Φ_{ref}) and the overall luminescence (Φ_{os}) in absence (A) and presence (B) of the analyte.

Two luminophores with overlapping (ideally identical) excitation and emission spectra are required to allow simultaneous excitation and signal detection with a single light source and detector system. The excitation light is modulated with a frequency adapted to the lifetime of the long-lived reference dye and the phase shift Φ_{os} of the overall sensor signal is measured. Provided that an inert reference standard (no quenching from any potential interferent such as oxygen) is utilised, the overall phase shift reflects the ratio of the pH-dependent indicator fluorescence intensity A_{ind} and the constant reference luminescence intensity A_{ref} (both expressed as their amplitudes) (eq. 1.9). There is a linear relation between the cotangent of the phase shift and the fluorescence intensity of the pH indicator.

$$\cot \Phi_{os} = \cot \Phi_{ref} + \frac{1}{\sin \Phi_{ref}} \cdot \frac{A_{ind}}{A_{ref}} \quad (1.9)$$

The presented referencing techniques employing a second dye as reference standard depend strongly on a constant ratio of the indicator/reference concentrations. Therefore photodecomposition and leaching of the indicator or the reference dye are not compensated by these methods.

1.6. Time-Resolved Luminescence Imaging Methods Using Planar Optodes

Luminescence imaging has become a well-established tool in chemo- and bioanalytics. Newly developed methods in combination with the continually increasing number of commercially available fluorescent labels and probes enable to visualise the tracing of biomolecules or detection of various parameters (e.g. pH, pO_2 , Ca^{2+}) in cells or tissues¹⁵⁵⁻¹⁵⁷. Within the last ten years imaging techniques have been extended to optical chemical sensing using luminescent planar optodes¹⁵⁸⁻¹⁶⁰. This allows the two-dimensional detection of analyte distributions and gradients in heterogeneous samples. Imaging devices usually comprise a CCD camera as detector, whereat the single photosensitive picture elements (=pixels) of the CCD chip act like independent single point detectors recording the emission light of the corresponding optode segment. As with single point luminescence measurement methods several referencing schemes have been developed for luminescence imaging exploiting the luminescence intensity, lifetime or spectral distribution of the indicator. Single intensity imaging is extremely error-prone. Besides the temporal variations in the concentration of the indicator or the opto-electronic devices also spatial variations influence the resulting image. Fig. 1.4 (left) shows the surface plots of luminescence intensity images of an optical oxygen sensor at 0 hPa pO_2 (nitrogen) and at 212 hPa pO_2 (air).

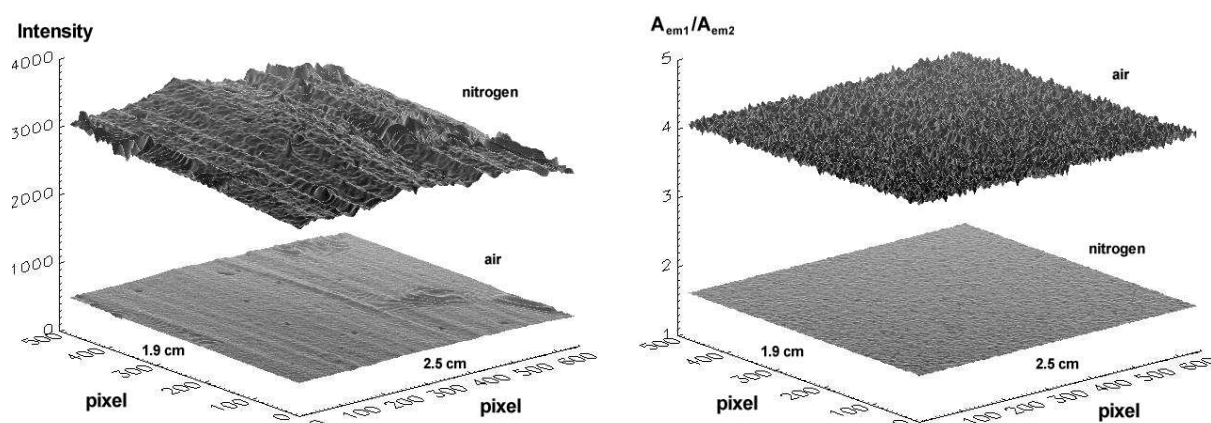


Fig. 1.4. Surface plots of intensity images (**left**) and image ratios (**right**) of an optical oxygen sensor at 0 hPa pO_2 (nitrogen) and at 212 hPa pO_2 (air).

The image not only reflects any inhomogeneous distribution of the indicator dye but also the inhomogeneous intensity of the excitation light field. Intensity imaging can be accomplished with very simple and inexpensive instrumentation. Yet, a rather complicated pixel to pixel calibration is inevitable and errors due to displacement of camera and sensor foil during the measurement are difficult to correct. Internally referenced measurements are therefore again

preferable. The methods described in section 1.5 can in principle be transferred to imaging applications. However, frequency-domain imaging methods like phase shift or fd-DLR measurements require the use of expensive image intensifiers which (in contrast to camera shutters) can be sinusoidally modulated^{161,162}. An alternative provide time-domain (or time-gated) imaging techniques.

1.6.1 Rapid lifetime determination

The rapid lifetime determination (RLD) is a widely used time-domain method for lifetime-based imaging which circumvents the measurement and analysis of complete decay curves^{163,164}. The optode is excited with a square wave-pulsed light source and a CCD camera is used to record the integrated intensity of the emission light in two consecutive time intervals in the period after the excitation pulse (Fig. 1.5).

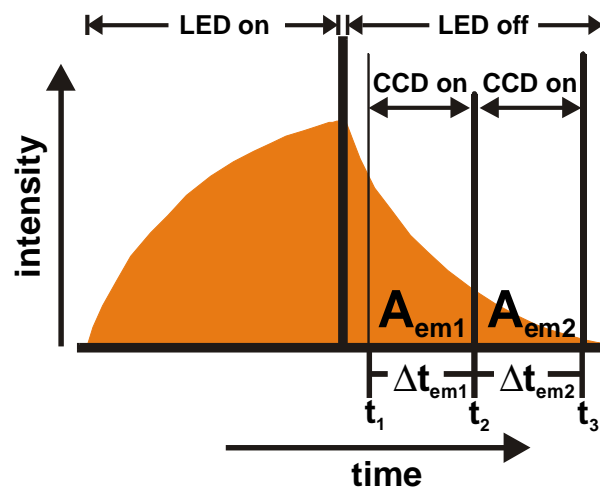


Fig. 1.5. Schematic of the rapid lifetime determination method applied for time-resolved imaging of pO_2 .

Provided that identical gate-widths were chosen and a single-exponential luminescence decay can be assumed the lifetime τ can be determined by means of the two intensity integrals (= images) A_{em1} and A_{em2} according to eq. 1.10

$$\tau = \frac{t_2 - t_1}{Ln \frac{A_{em1}}{A_{em2}}} \quad (1.10)$$

where t_2 and t_1 are the times at which the second and first integration interval start, respectively. For multi-exponential decays, the "apparent" lifetime determined by the RLD method is again a weighted average of all lifetime components. The measurement is corrected for spatial inhomogeneities of the excitation light field or indicator distribution (Fig. 1.4, right). In case that the lifetime of the indicator is in the μs - to ms -range inexpensive devices such as LEDs and fast gateable CCD cameras without intensifier can be applied. Furthermore, interfering short-lived background fluorescence of the sample or optical components of the measurement system such as filters can be excluded by starting the recording of the first image after the background fluorescence has already decayed (ca. 100 ns). In this work, the RLD method was generally applied for imaging of pO_2 .

1.6.2 Time domain dual lifetime referencing

The time domain DLR (td-DLR) method was employed for referenced two-dimensional pH (and pCO_2) measurements (Fig. 1.6).

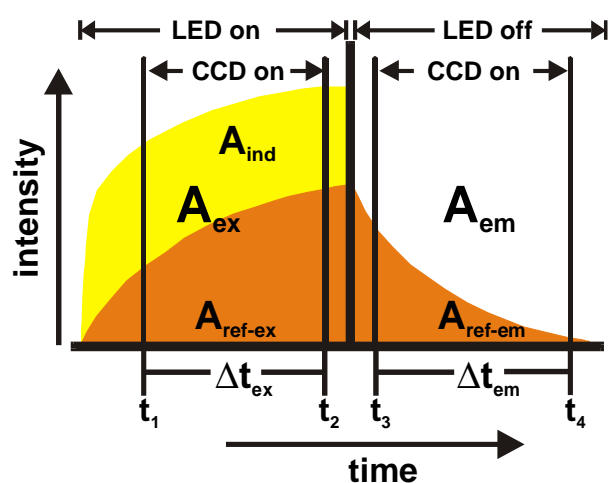


Fig. 1.6. Schematic of the dual lifetime referencing method.

The td-DLR scheme was described in detail by Liebsch et al.¹⁶⁵. Like the fd-DLR method, it makes use of the different lifetimes of an indicator/reference dye couple with spectral characteristics allowing the application of the same excitation light source, detector and optical filter combination. In case of using a square wave-gated LED light source coupled with a gateable CCD detector, two individual luminescence images (during and after excitation) are recorded. The first image A_{ex} which is recorded during the excitation, contains the integrated intensities of the reference $A_{\text{ref-ex}}$ and the pH indicator A_{ind} together. The second

image A_{em} is recorded with a time delay of at least 200 ns to the end of the excitation pulse when the fluorescence of the pH indicator and any afterglow of the LED is already decayed. It contains only the integrated intensity of the long-lived reference A_{ref-em} . The ratio of both images results in a referenced image which is independent from the overall intensity of a single pixel. The correlation between pH (or pCO_2) and image ratio R is given in eq. 1.11.

$$R = \frac{A_{ex}}{A_{em}} = \frac{A_{ind} + A_{ref-ex}}{A_{ref-em}} \quad (1.11)$$

Thus, the td-DLR scheme like the RLD scheme overcomes the problem of a complicated single pixel correction. Negative effects like leaching of the indicator from the sensor membrane, a heterogeneous distribution of indicator and reference standard which leads to a varying ratio of the intensities of both dyes or photobleaching of one of the luminophores, however, are not referenced by this method and have to be minimised.

1.7. Luminescent dual sensors

The development of optical dual sensors is an area of active research. Several dual optodes have been reported to date mainly for the parameter combinations pO_2 /temperature (temperature-compensated pressure sensitive paints) and pCO_2/pO_2 . Whereat two different concepts for the sensor membrane composition have been used so far. Firstly, double-layer membranes^{166,167}, where the sensor chemistry for each of the two analytes is immobilised in a separate, suitable matrix polymer and the first sensing layer is coated with the second. Secondly, hybrid membranes¹⁶⁸⁻¹⁷⁰ (which are an integrated form of the dual sensor) where the sensor chemistry for both analytes is immobilised in the same single-layer polymer matrix (see chapter 4.3.1). One advantage of this latter membrane type is the straightforward sensor fabrication procedure. It was used for the dual sensors in this work and its beneficial and limiting effects on the sensor performance were investigated.

Optical dual sensors are of special interest for the detection and correlation of analytes in inhomogeneous samples with a high spatial resolution. A drawback of this method is the necessity to separate the signals for the two analytes from the overall measurement signal of the dual sensor, which complicates the instrumentation and/or evaluation of the measurement. For some applications, where only a one-dimensional information on different parameters is required, adequately miniaturised fibre-optic multi-analyte sensors (e.g., bundles of separately

addressable fibre optodes) might therefore provide a simpler alternative. Planar luminescent dual optodes in combination with CCD technology, however, represent a most powerful tool for the mapping of gradients and distributions of two parameters in heterogeneous systems (e.g., metabolism studies in biofilms, plants or tissues such as skin, tumours or engineered tissues, wind-tunnel research, studies of biogeochemical processes in marine sediments).

1.8. References

- [1] Field C. B., Behrenfeld M. J., Randerson J. T., Falkowski P., *Primary production of the Biosphere: Integrating Terrestrial and Oceanic Components*. Science (1998), 281, 237 - 240.
- [2] Butcher S. S., Charlson R. J., Orians G. H., Wolfe G. V., *Global Biogeochemical Cycles*. Academic Press, London (1992).
- [3] Martin J. H., Knauer G. A., Karl D. M., Broenkow W. W., *VERTEX: carbon cycling in the northeast Pacific*. Deep-Sea Res. (1987), 34, 267 - 285.
- [4] Wollast R., *The coastal organic carbon cycle: fluxes, sources and sinks*. In: Ocean margin processes in global change. (Eds. Mantoura M. J. M., Wollast R.), John Wiley & Sons, London (1991), 364 - 382.
- [5] Bender M., Jahnke R., Weiss R., Martin W., Heggie D., Orchardo J., Sowers T., *Organic carbon oxidation and benthic nitrogen and silica dynamics in San Clemente Basin, a continental borderland site*. Geochim. Cosmochim. Acta (1989), 53, 685 - 697.
- [6] Revsbech N. P., Jørgensen B. B., *Microelectrodes: their use in microbial ecology*. Adv. Microb. Ecol. (1986), 9, 293 - 352.
- [7] Kühl M., Lassen C., Jørgensen B. B., *Optical properties of microbial mats: light measurements with fiber-optic microprobes*. In: Microbial Mats: Structure, Development and Environmental Significance. (Eds. Stal L. J., Caumette P.), Springer, Berlin (1994), 149 - 167.
- [8] Berner R. A., *Burial of organic carbon and pyrite sulfur in the modern ocean: Its geochemical and environmental significance*. Amer. J. Sc. (1982), 282, 451 - 473.
- [9] Archer D., Maier-Reimer E., *Effect of deep-sea sedimentary calcite preservation on atmospheric CO₂ concentration*. Nature (1994), 367, 260 - 263.

- [10] Gitay H., Suárez A., Watson R. T., Dokken D. J., *Climate Change and Biodiversity*. Intergovernmental Panel on Climate Change, Technical Paper V, (2002).
- [11] Smith K. L., *Benthic community respiration in the N.W. Atlantic Ocean: in situ measurements from 40 to 5200 m*. Mar. Biol. (1978), 47, 337 - 347.
- [12] Wenzhöfer F., Adler M., Kohls O., Hensen C., Strotmann B., Boehme S., Schulz H. D., *Calcite dissolution driven by benthic mineralization in the deep-sea: In situ measurements of Ca²⁺, pH, pCO₂ and O₂*. Geochim. Cosmochim. Acta (2001), 65, 2677 - 2690.
- [13] Reimers C. E., Ruttenger K. C., Canfield D. E., Christiansen M. B., Martin J. B., *Porewater pH and authigenic phases formed in the uppermost sediments of the Santa Barbara Basin*. Geochim. Cosmochim. Acta (1996), 60, 4037 - 4057.
- [14] Holst G., Glud R. N., Kühl M., Klimant I., *A microoptrode array for fine-scale measurements of oxygen distribution*. Sens. Actuators, B (1997), 38, 122 - 129.
- [15] Köhler-Rink S., Kühl M., *Microsensor analysis of photosynthesis and respiration in larger symbiotic foraminifera: 1. The physico-chemical microenvironment of Amphistegina lobifera, Amphisorus hemprichii and Marginopora vertebralis*. Mar. Biol. (2000), 137, 473 - 486.
- [16] Komada T., Reimers C. E., Boehme S. E., *Dissolved Inorganic Carbon Profiles and Fluxes Determined using pH and pCO₂ microelectrodes*. Limnol. Oceanogr. (1998), 43, 769 - 781.
- [17] Jørgensen B. B., Glud R. N., Holby O., *Oxygen distribution and bioirrigation in Arctic fjord sediments (Svalbard, Barents Sea)*. Mar. Ecol. Prog. Ser. (2005), 292, 85 - 95.
- [18] Glud R. N., Santegoeds C. M., De Beer D., Kohls O., Ramsing N. B., *Oxygen dynamics at the base of a biofilm studied with planar optodes*. Aquat. Microb. Ecol. (1998), 14, 223 - 233.
- [19] Glud R. N., Kuehl M., Kohls O., Ramsing N. B., *Heterogeneity of oxygen production and consumption in a photosynthetic microbial mat as studied by planar optodes*. J. Phycol. (1999), 35, 270 - 279.
- [20] König B., Kohls O., Holst G., Glud R. N., Kühl M., *Fabrication and test of sol-gel based planar oxygen optodes for use in aquatic sediments*. Mar. Chem. (2005), 97, 262 - 276.
- [21] Glud R. N., Wenzhöfer F., Tengberg A., Middelboe M., Oguri K., Kitazato H., *Distribution of oxygen in surface sediments from central Sagami Bay, Japan: In*

- situ measurements by microelectrodes and planar optodes*. Deep-Sea Res. (2005), 52, 1974 - 1987.
- [22] Butler J. N., *Carbon Dioxide Equilibria and Their Applications*. CRC Press, Boca Raton (1991).
- [23] Van Capellen P., Wang Y., *Cycling of iron and manganese in surface sediments: a general theory for the coupled transport and reaction of carbon, oxygen, nitrogen, sulfur, iron and manganese*. Am. J. Sci. (1996), 296, 197 - 243.
- [24] Schlesinger W. H., *Biogeochemistry: An analysis of global change*. Academic Press, San Diego (1991).
- [25] Cai W. J., Reimers C. E., *The Development of pH and pCO₂ microelectrodes for studying the carbonate chemistry of pore waters near the sediment-water interface*. Limnol. Oceanogr. (1993), 38, 1762 - 1773.
- [26] Wenzhöfer F., Glud R. N., *Small-scale spatial and temporal variability in coastal benthic O₂ dynamics: Effects of faunal activity*. Limnol. Oceanogr. (2004), 49, 1471 - 1481.
- [27] Kristensen, E., *Organic matter diagenesis at the oxic/anoxic interface in coastal marine sediments, with emphasis on the role of burrowing animals*. Hydrobiologia (2000), 426, 1 - 24.
- [28] Boudreau B. P., *A steady-state diagenetic model for dissolved carbonate species and pH in the porewaters of oxic and suboxic sediments*. Geochim. Cosmochim. Acta (1987), 51, 1985 - 1996.
- [29] Motellier S., Noiré M. H., Pitsch H., Duréault B., *pH determination of clay interstitial water using a fiber-optic sensor*. Sens. Actuators B (1995), 29, 345 - 352.
- [30] French C. R., Carr J. J., Dougherty E. M., Eidson L. A. K., Reynolds J. C., DeGrandpre M. D., *Spectrophotometric pH measurements of freshwater*. Anal. Chim. Acta (2002), 453, 13 - 20.
- [31] Bellerby R. G. J., Olsen A., Johannessen T., Croot P., *A high precision spectrophotometric method for on-line shipboard seawater pH measurements: the automated marine pH sensor (AMpS)*. Talanta (2002), 56, 61 - 69.
- [32] Keeling R. F., *Measuring correlations between atmospheric oxygen and carbon dioxide mole fractions: A preliminary study in urban air*. J. Atm. Chem. (1997), 7, 153 - 176.
- [33] DeGrandpre M. D., Hammar T. R., Smith S. P., Sayles F. L., *In situ measurements of seawater pCO₂*. Limnology and Oceanography (1995), 40, 969 - 975.

- [34] Tankere S. P. C., Bourne D. G., Muller F. L. L., Torsvik V., *Microenvironments and microbial community structure in sediments*. Environ. Microbiol. (2002), 4, 97 - 105.
- [35] Mills A., Lepre A., Wild L., *Breath-by-breath measurement of carbon dioxide using a plastic film optical sensor*. Sens. Actuators B (1997), 39, 419 - 425.
- [36] Wolfbeis O. S., Klimant I., Werner T., Huber C., Kosch U., Krause C., Neurauter G., Durkop A., *Set of luminescence decay time based chemical sensors for clinical applications*. Sens. Actuators B (1998), 51, 17 - 24.
- [37] Cooney C. G., Towe B. C., Eyster C. R., *Optical pH, oxygen and carbon dioxide monitoring using a microdialysis approach*. Sens. Actuators B (2000), 69, 183 - 188.
- [38] Soller B. R., Hsi C., Favreau J., Cingo N., Lancey R. A., Okike O. N., Vander Salm T. J., *Multiparameter fiber optic sensor for the assessment of intramyocardial perfusion*. J. Card. Surg. (2004), 19, 167 - 174.
- [39] Moreno-Bondi M. C., Wolfbeis O. S., Leiner M. J. P., Schaffar B. P., *Oxygen optrode for use in a fiber-optic glucose biosensor*. Anal. Chem. (1990), 62, 2377 - 2380.
- [40] Kolle C., Gruber W., Trettnak W., Biebernik K., Dolezal C., Reiningner F., O'Leary P., *Fast Optochemical Sensor for Continuous Monitoring of Oxygen in Breath-gas Analysis*. Sens. Actuators B (1997), 38, 141 - 149.
- [41] Durham R. M., Weigelt J. A., *Monitoring gastric pH levels*. Surgery, Gynecology & Obstetrics (1989), 169, 14 - 16.
- [42] Mordon S., Devoisselle J. M., Soulie S., *Fluorescence spectroscopy of pH in vivo using a dual-emission fluorophore (C-SNAFL-1)*. J. Photochem. Photobiol. B (1995), 28, 19 - 23.
- [43] John G. T., Goelling D., Klimant I., Schneider H., Heinzle E., *pH-Sensing 96-well microtitre plates for the characterization of acid production by dairy starter cultures*. J. Dairy Res. (2003), 70, 327 - 333.
- [44] Dybko A., Wroblewski W., Rozniecka E., Pozniakb K., Maciejewski J., Romaniuk R., Brzozka Z., *Assessment of water quality based on multiparameter fiber optic probe*. Sens. Actuators B (1998), 51, 208 - 213.
- [45] Young O. A., Thomson R. D., Merhtens V. G., Loeffen M. P. F., *Industrial application to cattle of a method for the early determination of meat ultimate pH*. Meat Sci. (2004), 67, 107 - 112.
- [46] von Bueltingsloewen C., McEvoy A. K., McDonagh C., MacCraith B. D., Klimant I., Krause C., Wolfbeis O. S., *Sol-gel based optical carbon dioxide sensor employing*

- dual luminophore referencing for application in food packaging technology*. Analyst (UK) (2002), 127, 1478 - 1483.
- [47] Mills A., *Oxygen indicators and intelligent inks for packaging food*. Chem. Soc. Rev. (2005), 34, 1003 - 1011.
- [48] Ge X., Kostov Y., Rao G., *High-stability non-invasive autoclavable naked optical CO₂ sensor*. Biosens. Bioelectron. (2003), 18, 857 - 865.
- [49] Jeevarajan A. S., Vani S., Taylor T. D., Anderson M. M., *Continuous pH monitoring in a perfused bioreactor system using an optical pH sensor*. Biotechnol. Bioeng. (2002), 78, 467 - 472.
- [50] Ferguson J. A., Healey B. G., Bronk K. S., Barnard S. M., Walt D. R., *Simultaneous monitoring of pH, CO₂ and O₂ using an optical imaging fiber*. Anal. Chim. Acta (1997), 340, 123 - 131.
- [51] Ulber R., Frerichs J.-G., Beutel S., *Optical sensor systems for bioprocess monitoring*. Anal. Bioanal. Chem. (2003), 376, 342 - 348.
- [52] Tang T. B. et al., *Toward a miniature wireless integrated multisensor microsystem for industrial and biomedical applications*. IEEE Sensors Journal (2002), 2, 628 - 635.
- [53] Bourilkov J., Belz M., Boyle W., Grattan K., *Electrical pH control in aqueous solutions*. Proc. SPIE (1999), 3538, 268 - 277.
- [54] Popp P. J., Bishop G. A., Stedman D. H. J., *Development of a High-Speed Ultraviolet Spectrometer for Remote Sensing of Mobile Source Nitric Oxide Emissions*. Air Waste Manage. Assoc. (1999), 49, 1463 - 1468.
- [55] Barrass S., Gerard Y., Holdsworth R. J., Martin P. A., *Near-infrared tunable diode laser spectrometer for the remote sensing of vehicle emissions*. Spectrochim. Acta A (2004), 60, 3353 - 3360.
- [56] Riegel J., Neumann H., Wiedenmann H. M., *Exhaust Gas Sensors for Automotive Emission Control*. Solid State Ionics (2002), 152 - 153, 783 - 800.
- [57] Maskell W. C., Steele H. B. C., *Solid state potentiometric oxygen sensors*. J. Appl. Electrochem. (1986), 16, 475 - 485.
- [58] Cremer M., *Über die Ursache der elektromotorischen Eigenschaften der Gewebe, zugleich ein Beitrag zur Lehre von den polyphasischen Elektrolytketten*. Z. Biol. (1906), 47, 562 - 608.
- [59] MacInnes D. A., Dole M., *Tests of a new type glass electrode*. Ind. Eng. Chem. Anal. (1929), 1, 57 - 59.

- [60] van den Berg A., Bergveld P., Reinhoudt D. N., Sudholter E. J. R., *Sensitivity control of ISFETs by chemical surface modification*. Sens. Actuators (1985), 8, 129 - 135.
- [61] Wang M., Yao S., *Carbonate-Melt Oxidized Iridium Wire for pH Sensing*. Electroanalysis (2003), 15, 1606 - 1615.
- [62] Peterson J. I., Goldstein S. R., Fitzgerald R. V., Buckhold D. K., *Fiber optic pH probe for physiological use*. Anal. Chem. (1980), 52, 864 - 869.
- [63] Saari L. A., Seitz W. R., *pH sensor based on immobilized fluoresceinamine*. Anal. Chem. (1982), 54, 821 - 823.
- [64] Jordan D. M., Walt D. R., Milanovich F. P., *Physiological pH Fiber Optic Chemical Sensor Based on Energy Transfer*. Anal. Chem. (1987), 59, 437 - 439.
- [65] Liu Z., Liu J., Chen T., *Phenol red immobilized PVA membrane for an optical pH sensor with two determination ranges and long-term stability*. Sens. Actuators B (2005), 107, 311 – 316.
- [66] Sotomayor P. T., Raimundo I. M., de Oliveira Neto G., de Oliveira W. A., *Evaluation of fibre optical chemical sensors for flow analysis systems*. Sens. Actuators B (1998), 51, 382 - 390.
- [67] Lobnik A., Majcen N., Niederreiter K., Uray G., *Optical pH sensor based on the absorption of antenna generated europium luminescence by bromothymol blue in a sol-gel membrane*. Sens. Actuators B (2001), 74, 200 - 206.
- [68] Allain L. R., Sorasaene K., Xue Z., *Doped Thin-Film Sensors via a Sol-Gel Process for High-Acidity Determination*. Anal. Chem. (1997), 69, 3076 - 3080.
- [69] Wolfbeis O. S., Fuerlinger E., Kroneis H., Marsoner H., *Fluorimetric analysis. I. A study on fluorescent indicators for measuring near neutral ("physiological") pH values*. Fresenius' Z. Anal. Chem. (1983), 314, 119 - 124.
- [70] Whitaker J. E., Haugland R. P., Prendergast F. G., *Spectral and photophysical studies of benzo[c]xanthene dyes: dual emission pH sensors*. Anal. Biochem. (1991), 194, 330 - 344.
- [71] Offenbacher H., Wolfbeis O. S., Fuerlinger E., *Fluorescence optical sensors for continuous determination of near-neutral pH values*. Sens. Actuators B (1986), 9, 73 - 84.
- [72] Zhujun Z., Seitz W. R., *A fluorescence sensor for quantifying pH in the range from 6.5 to 8.5*. Anal. Chim. Acta (1984), 160, 47 - 55.

- [73] Xu Z., Rollins A., Alcalá R., Marchant R. E., *A novel fiber-optic pH sensor incorporating carboxy SNAFL-2 and fluorescent wavelength-ratiometric detection*. J. Biomed. Mater. Res. (1998), 39, 9 - 15.
- [74] Weidgans B. M., Krause C., Klimant I., Wolfbeis O. S., *Fluorescent pH sensors with negligible sensitivity to ionic strength*. Analyst (UK) (2004), 129, 645 - 650.
- [75] Dybko A., Maciejewski J., Romaniuk R. S., Wroblewski W., *Colorimetric sensor based on two optical fiber couplers*. Proc. SPIE (1993), 2085, 131 - 136.
- [76] Vishnoi G., Goel T. C., Pillai P. K. C., *pH optrode for the complete working range*. Proc. SPIE (1999), 3538, 319 - 325.
- [77] Moreno-Bondi M. C., Jiménez M., Pérez-Conde C., Cámara C., *Analytical performance of an optical pH sensor for acid-base titrations*. Anal. Chim. Acta. (1990), 230, 35 - 40.
- [78] Papkovsky D. B., Ponomarev G. V., Wolfbeis O. S., *Protonation of porphyrins in liquid PVC membranes: Effects of anionic additives and application to pH-sensing*. J. Photochem. Photobiol. A (1997), 104, 151 - 158.
- [79] Cajlakovic M., Lobnik A., Werner T., *Stability of new optical pH sensing material based on cross-linked poly(vinyl alcohol) copolymer*. Anal. Chim. Acta (2002), 455, 207 - 213.
- [80] Rottman C., Turniansky A., Avnir D., *Sol-Gel Physical and Covalent Entrapment of Three Methyl Red Indicators: A Comparative Study*. J. Sol-Gel Sci. (1998), 13, 17 - 25.
- [81] Butler T. M., MacCraith B. D., McDonagh C., *Leaching in sol-gel-derived silica films for optical pH sensing*. J. Non-Cryst. Solids, 224, 249 - 258.
- [82] Wolfbeis O. S., Rodríguez N. V., Werner T., *LED-compatible fluorosensor for measurement of near-neutral pH values*. Mikrochim. Acta (1992), 108, 133 - 141.
- [83] Mohr G. J., Wolfbeis O. S., *Optical sensors for a wide pH range based on azo dyes immobilized on a novel support*. Anal. Chim. Acta. (1994), 292, 41 - 48.
- [84] Kostov Y. V., *Immobilized Bromophenol Blue as sensing element in optical pH sensor*. Sens. Actuators B (1992), 8, 99 - 101.
- [85] Dybko A., Wroblewski W., Maciejewski J., Romaniuk R. S., Brzózka Z., *Efficient reagent immobilization procedure for ion-sensitive optomembranes*. Sens. Actuators B (1997), 39, 207 - 211.

- [86] Werner T., Huber C., Heinel S., Kollmannsberger M., Daub J., Wolfbeis O.S., *Novel Optical pH Sensor Based on a Boradiaza-indacene Derivative*. Fresenius' J. Anal. Chem. (1997), 359, 150 - 154.
- [87] Draxler S., Lippitsch M. E., *Effect of Polymer Matrices in Lifetime Based Sensing*. Proc. SPIE (1995), 2388, 363 - 368.
- [88] Parker J. W., Laksin O., Yu C., Lau M. L., Klima S., Fisher R., Scott I., Atwater B. W., *Fiber-optic sensors for pH and carbon dioxide using a self-referencing dye*. Anal. Chem. (1993), 65, 2329 - 2334.
- [89] Schulz K., Jensen M. L., Balsley B. B., Davis K., Birks J. W., *Tedlar Bag Sampling Technique for Vertical Profiling of Carbon Dioxide through the Atmospheric Boundary Layer with High Precision and Accuracy*. Environ. Sci. Technol. (2004), 38, 3683 - 3688.
- [90] Thrall K. D., Toth J. J., Sharpe S. W., *Analysis of exhaled breath by laser detection*. Proc. SPIE (1996), 2676, 136 - 146.
- [91] Severinghaus J. W., Bradley A. F., *Electrodes for blood pO₂ and pCO₂ determination*. J. Appl. Physiol. (1958), 13, 515 - 520.
- [92] Choi Y. S., Lvova L., Shin J. H., Oh S. H., Lee C. S., Kim B. H., Cha G. S., Nam H., *Determination of Oceanic Carbon Dioxide Using a Carbonate-Selective Electrode*. Anal. Chem. (2002), 74, 2435 - 2440.
- [93] Lübbers D. W., Opitz N., *The pCO₂ /pO₂ optrode: A new probe for measuring pCO₂ and pO₂ of gases and liquids*. Z. Naturforschung (1975), 30C, 532 - 533.
- [94] He X., Rechnitz G. A., *Linear Response Function for Fluorescence-Based Fiber-Optic CO₂ Sensors*. Anal. Chem. (1995), 67, 2264 - 2268.
- [95] Orellana G., Moreno-Bondi M. C., Segovia E., Marazuela M.D., *Fiber-optic sensing of carbon dioxide based on excited-state proton transfer to a luminescent ruthenium(II) complex*. Anal. Chem. (1992), 64, 2210 - 2015.
- [96] Munkholm C., Walt D. R., Milanovich F. P., *A fiber-optic sensor for carbon dioxide measurement*. Talanta (1988), 35, 109 - 112.
- [97] Nivens D. A., Schiza M. V., Angel S. M., *Multilayer sol-gel membranes for optical sensing applications: single layer pH and dual layer CO₂ and NH₃ sensors*. Talanta (2002), 58, 543 - 550.
- [98] DeGrandpre M. D., Baehr M. M., Hammar T. R., *Calibration-Free Optical Chemical Sensors*. Anal. Chem. (1999), 71, 1152 - 1159.

- [99] Ertekin K., Klimant I., Neurauder G., Wolfbeis O. S., *Characterization of a reservoir-type capillary optical microsensor for pCO₂ measurements*. *Talanta* (2003), 59, 261 - 267.
- [100] Raemer D. B., Walt D. R., Munkholm C., *CO₂ Indicator and the Use Thereof to Evaluate Placement of Tracheal Tubes*. US Pat. 5 005 572 (1991).
- [101] Mills A., Chang Q., McMurray N., *Equilibrium studies on colorimetric plastic film sensors for carbon dioxide*. *Anal. Chem.* (1992), 64, 1383 - 1389.
- [102] Mills A., Lepre A., Wild L., *Effect of plasticizer-polymer compatibility on the response characteristics of optical thin film CO₂ and O₂ sensing films*. *Anal. Chim. Acta* (1998), 362, 193 - 202.
- [103] von Bultzingslowen C., McEvoy A. K., McDonagh C., MacCraith B. D., *Lifetime-based optical sensor for high-level pCO₂ detection employing fluorescence resonance energy transfer*. *Anal. Chim. Acta* (2003), 480, 275 - 283.
- [104] Weigl B. H., Wolfbeis O. S., *New hydrophobic materials for optical carbon dioxide sensors based on ion pairing*. *Anal. Chim. Acta* (1995), 302, 249 - 254.
- [105] Mills A., Monaf L., *Thin plastic film colorimetric sensors for carbon dioxide: effect of plasticizer on response*. *Analyst* (UK) (1996), 121, 535 - 540.
- [106] Kocache R., *Gas sensors*. *Sensor Rev.* (1994), 14, 8 - 12.
- [107] Carpenter J. H., *The Accuracy of the Winkler Method for Dissolved Oxygen Analysis. & The Chesapeake Bay Institute Technique for the Winkler Dissolved Oxygen Method*. *Limnol. Oceanogr.* (1965), 10, 135 - 143.
- [108] Clark L. C., *Monitor and control of blood and tissue oxygenation*. *Tr. Am. Soc. Artif. Intern. Org.* (1956), 2, 41 - 45.
- [109] Bergman I., *Rapid-response Atmospheric Oxygen Monitor based on Fluorescence Quenching*. *Nature* (1968), 218, 396.
- [110] Mills A., *Controlling the sensitivity of optical oxygen sensors*. *Sens. Actuators B* (1998), 51, 60 - 68.
- [111] Mills A., Lepre A., *Controlling the Response Characteristics of Luminescent Porphyrin Plastic Film Sensors for Oxygen*. *Anal. Chem.* (1997), 69, 4653 - 4659.
- [112] Hartmann P., Trettnak W., *Effects of Polymer Matrices on Calibration Functions of Luminescent Oxygen Sensors Based on Porphyrin Ketone Complexes*. *Anal. Chem.* (1996), 68, 2615 - 2620.
- [113] He H., Fraatz R. J., Leiner M. J. P., Rehn M. M., Tusa J. K., *Selection of silicone polymer matrix for optical gas sensing*. *Sens. Actuators B* (1995), 29, 246 - 250.

- [114] Xu W., Schmidt R., Whaley M., Demas J. N., DeGraff B. A., *Oxygen sensors based on luminescence quenching: interactions of metal complexes with the polymer supports*. Anal. Chem. (1994), 66, 4133 - 4141.
- [115] Yasuda H., Stannett V., *Permeability coefficients*. Polymer Handbook 4th ed., Wiley, New York (1999).
- [116] O'Keeffe G., MacCraith B. D., McEvoy A. K., McDonagh C. M., McGilp J. F., *Development of a LED-based phase fluorometric oxygen sensor using evanescent-wave excitation of a sol-gel immobilised dye*. Sens. Actuators B (1995), 29, 226 - 230.
- [117] McDonagh C., MacCraith B. D., McEvoy A. K., *Tailoring of sol-gel films for optical sensing of oxygen in gas and aqueous phase*. Anal. Chem. (1998), 70, 45 - 50.
- [118] Kautsky H., *Quenching of luminescence by oxygen*. Trans. Faraday Soc. (1939), 35, 216 - 219.
- [119] Wolfbeis O. S., *Fiber Optic Chemical Sensors and Biosensors*. CRC Press, Boca Raton (1991).
- [120] Peterson J. I., Fitzgerald R. V., Buckhold D. K., *Fiber-optic probe for in vivo measurement of oxygen partial pressure*. Anal. Chem. (1984), 56, 62 - 67.
- [121] Bacon J. R., Demas J. N., *Determination of Oxygen Concentrations by Luminescence Quenching of a Polymer Immobilized Transition Metal Complex*. Anal. Chem. (1987), 59, 2780 - 2785.
- [122] Mingoarranz F. J., Moreno-Bondi M. C., García-Fresnadillo D., de Dios C., Orellana G., *Oxygen-sensitive layers for optical fibre devices*. Microchim. Acta (1995), 121, 107 - 118.
- [123] Hartmann P., Leiner M. J. P., Lippitsch M. E., *Response Characteristics of Luminescent Oxygen Sensors*. Sens. Actuators B (1995), 29, 251 - 257.
- [124] Klimant I., Wolfbeis O. S., *Oxygen-sensitive luminescent materials based on silicone-soluble ruthenium diimine complexes*. Anal. Chem. (1995), 67, 3160 - 3166.
- [125] Papkovsky D.B., *New oxygen sensors and their application to biosensing*. Sens. Actuators B (1995), 29, 226 - 230.
- [126] Papkovsky D.B., Ponomarev G.V., Trettnak W., O'Leary P., *Phosphorescent complexes of porphyrin-ketones: optical properties and application to oxygen sensing*. Anal. Chem. (1995), 67, 4112 - 4117.
- [127] Lee S.-K., Okura I., *Photostable Optical Oxygen Sensing Material: Platinum Tetrakis(pentafluorophenyl)porphyrin Immobilised in Polystyrene*. Anal. Commun. (1997), 34, 185 - 188.

- [128] Lippitsch M. E., Pusterhofer I., Leiner M. J. P., Wolfbeis O. S., *Fibre-Optic Oxygen Sensor with the Fluorescence Decay Time as the Information Carrier*. Anal. Chem. Acta. (1998), 205, 1 - 6.
- [129] Glud R. N., Gundersen J. K., Jørgensen B. B., Revsbech N. P., Schulz H. D., *Diffusive and total oxygen uptake of deep-sea sediments in the eastern South Atlantic Ocean: in situ and laboratory measurements*. Deep-Sea Res. (1987), 41, 1767 - 1788.
- [130] Kühl M., Revsbech N. P., *Biogeochemical Microsensors for Boundary Layer Studies*. In: The Benthic Boundary Layer. (Eds. Boudreau B. P., Jørgensen B. B.), Oxford University Press, New York (2001), 180 - 210.
- [131] Ammann D., Lanter F., Steiner R. A., Schulthess P., Shijo Y., Simon W., *Neutral carrier based hydrogen ion selective microelectrode for extra- and intracellular studies*. Anal. Chem. (1981), 53, 2267 - 2269.
- [132] Lee W., de Beer D., *Oxygen and pH microprofiles above corroding mild steel covered with a biofilm*. Biofouling (1995), 8, 273 - 280.
- [133] Revsbech, N. P., *An oxygen microelectrode with a guard cathode*. Limnol. Oceanogr. (1989), 55, 1907 - 1910.
- [134] Santegoeds C. M., Schramm A., de Beer D., *Microsensors as a tool to determine chemical microgradients and bacterial activity in wastewater biofilms and flocs*. Biodegradation (1998), 9, 159 – 167.
- [135] Klimant I., Meyer V., Kühl, M., *Fiber-optic oxygen microsensors, a new tool in aquatic biology*. Limnol. Oceanogr. (1995), 40, 1159 - 1165.
- [136] Neurauter G., Klimant I., Wolfbeis O. S., *Fiber-optic microsensor for high resolution pCO₂ sensing in marine environment*. Fresenius J. Anal. Chem. (2000), 366, 481 - 487.
- [137] Kohls O., Klimant I., Holst G., Kühl, M., *Development and comparison of pH microoptodes for use in marine systems*. Proc. SPIE (1997), 2978, 82 - 94.
- [138] Kosch U., Klimant I., Wolfbeis O. S., *Long-lifetime based pH micro-optodes without oxygen interference*. Fresenius J. Anal. Chem. (1999), 364, 48 - 53.
- [139] Glud R. N., Ramsing N. B., Gundersen J. K., Klimant I., *Planar optodes, a new tool for fine scale measurements of two-dimensional O₂ distribution in benthic communities*. Mar. Ecol. Prog. Ser. (1996), 140, 217 - 226.
- [140] Precht E., Franke U., Polerecky L., Huettel M., *Oxygen dynamics in permeable sediments with wave-driven pore water exchange*. Limnol. Oceanogr. (2004), 49, 693 - 705.

- [141] Polerecky L., Franke U., Werner U., Grunwald B., de Beer D., *High spatial resolution measurement of oxygen consumption rates in permeable sediments*. Limnol. Oceanogr.: Methods (2005), 3, 75 - 85.
- [142] Frederiksen M. S., Glud R. N., *Oxygen dynamics in the rhizosphere of Zostera marina: A two-dimensional planar optode study*. Limnol. Oceanogr. (2006), 51, 1072 - 1083.
- [143] Franke U., Polerecky L., Precht E., Huettel M., *Wave tank study of particulate organic matter degradation in permeable sediments*. Limnol. Oceanogr. (2006), 51, 1084 - 1096.
- [144] Hulth S., Aller R. C., Engstrom P., Selander E., *A pH plate fluorosensor (optode) for early diagenetic studies of marine sediments*. Limnol. Oceanogr. (2002), 47, 212 - 220.
- [145] Zhu Q., Aller R. C., Fan Y., *High-Performance Planar pH Fluorosensor for Two-Dimensional pH Measurements in Marine Sediment and Water*. Environ. Sci. and Technol. (2005), 39, 8906 - 8911.
- [146] Glud R. N., Tengberg A., Kühl M., Hall P. O. J., Klimant I., Holst G., *An in situ instrument for planar O₂ optode measurements at benthic interfaces*. Limnol. Oceanogr. (2001), 46, 2073 - 2080.
- [147] Tengberg A. et al., *Benthic chamber and profile landers in oceanography - a review of design, technical solutions and functioning*. Progr. Oceanogr. (1995), 35, 253 - 293.
- [148] Reimers C. E., *An in situ microprofiling instrument for measuring interfacial pore water gradients: methods and oxygen profiles from the North Pacific Ocean*. Deep-Sea Res. (1987), 34, 2019 - 2035.
- [149] Lakowicz J. R., *Principles of Fluorescence Spectroscopy*. 2nd ed., Kluwer Academic/Plenum Publishers, New York (1999).
- [150] Ryder A. G., Power S., Glynn T. J., *Evaluation of acridine in Nafion as a fluorescence-lifetime-based pH sensor*. Appl. Spectrosc. (2003), 57, 73 - 79.
- [151] Szmacinski H., Lakowicz J. R., *Optical measurements of pH using fluorescence lifetimes and phase-modulation fluorometry*. Anal. Chem. (1993), 65, 1668 - 1674.
- [152] Kosch U., Klimant I., Werner T., Wolfbeis O. S., *Strategies To Design pH Optodes with Luminescence Decay Times in the Microsecond Time Regime*. Anal. Chem. (1998), 70, 3892 - 3897.

- [153] Klimant I., *Verfahren und Vorrichtung zur Referenzierung von Fluoreszenzintensitätssignalen*. Ger. Pat. Appl. DE 198.29.657 (1997).
- [154] Lakowicz J. R., Castellano F. N., Dattelbaum J. D., Tolosa L., Rao G., Gryczynski I., *Low-frequency modulation sensors using nanosecond fluorophores*. Anal Chem. (1998), *70*, 5115 - 5121.
- [155] Nomura S., Nakao M., Nakanishi T., Takamatsu S., Tomita K., *Real-time imaging of microscopic pH distribution with a two-dimensional pH-imaging apparatus*. Anal Chem. (1997), *69*, 977 - 981.
- [156] Rumsey W. L., Vanderkooi J. M., Wilson D. F., *Imaging of phosphorescence: a novel method for measuring oxygen distribution in perfused tissue*. Science (1988), *241*, 1649 - 1651.
- [157] Lakowicz J. R., Szmecinski H., Nowaczyk K., Lederer W. J., Kirby M. S., Johnson M. L., *Fluorescence lifetime imaging of intracellular calcium in COS cells using QUIN-2*. Cell Calcium (1994), *15*, 7 - 27.
- [158] Liebsch G., Klimant I., Frank B., Holst G., Wolfbeis O. S., *Luminescence lifetime imaging of oxygen, pH, and carbon dioxide distribution using optical sensors*. Appl. Spectrosc. (2000), *54*, 548 - 559.
- [159] Holst G., Kohls O., Klimant I., König B., Kühl M., Richter T., *A modular luminescence lifetime imaging system for mapping oxygen distribution in biological samples*. Sensors and Actuators, B: Chemical (1998), *B51*, 163 - 170.
- [160] Hartmann P., Ziegler W., *Lifetime Imaging of Luminescent Oxygen Sensors Based on All-Solid-State Technology*. Anal Chem. (1996), *68*, 4512 - 4514.
- [161] Morgan C. G., Murray J. G., Mitchell A. C., *Frequency-domain imaging using array detectors: present status and prospects for picosecond resolution*. Proc SPIE (1991), *1525*, 83 - 90.
- [162] Lakowicz J. R., Szmecinski H., Nowaczyk K., Berndt K. W., Johnson M., *Fluorescence lifetime imaging*. Anal. Biochem. (1992), *202*, 316 - 330.
- [163] Woods R. J., Scypinski S., Cline Love L. J., Asworth H. A., *Transient Digitizer for the Determination of Microsecond Luminescence Lifetimes*. Anal. Chem. (1984), *56*, 1395 - 1400.
- [164] Ballew R. M., Demas J. N., *An error analysis of the rapid lifetime determination method for the evaluation of single exponential decays*. Anal. Chem. (1989), *61*, 30 - 33.

- [165] Liebsch G., Klimant I., Krause C., Wolfbeis O. S., *Fluorescent Imaging of pH with Optical Sensors Using Time Domain Dual Lifetime Referencing*. Anal. Chem. (2001), 73, 4354 - 4363.
- [166] Wolfbeis O. S., Weis L. J., Leiner M. J. P., Ziegler W. E., *Fiber-optic fluorosensor for oxygen and carbon dioxide*. Anal. Chem. (1988), 60, 2028 - 2030.
- [167] Borisov S. M., Krause C., Arain S., Wolfbeis O. S., *Composite Material for Simultaneous and Contactless Luminescent Sensing and Imaging of Oxygen and Carbon Dioxide*. Adv Mater (2006), 18, 1511 - 1516.
- [168] Zelelow B., Khalil G. E., Phelan G., Carlson B., Gouterman M., Callis J. B., Dalton L. R., *Dual luminophor pressure sensitive paint II. Lifetime based measurement of pressure and temperature*. Sens. Actuators, B (2003), B96, 304 - 314.
- [169] Hradil J., Davis C., Mongey K., McDonagh C., MacCraith B. D., *Temperature-corrected pressure-sensitive paint measurements using a single camera and a dual-lifetime approach*. Meas. Sci. Technol. (2002), 13, 1552 - 1557.
- [170] Stehning C., Holst G. A., *DSP-based measuring system for temperature-compensated fiber optical oxygen sensors*. Proc. SPIE (2002), 4578, 259 - 270.

2. Instruments and Methods

2.1. pH Meter

The pH value of solutions was determined using a digital pH538 multical[®] pH meter with internal temperature compensation from WTW. The pH meter was calibrated with standard buffer solutions of pH 7.00 and pH 4.00 from Carl Roth at $T = 20 \pm 2$ °C.

2.2. Knife-coating device

Planar optodes were fabricated by spreading the sensor solution (A) onto a dust-free polyester (Mylar[®]) foil (B) using a knife-coating device from Coesfeld and a custom-made coating knife (Fig. 2.1). The coating-knife comprises a stainless steel knife (C) fixed to a frame (D), which allows the adjustment of a defined wet thickness of the sensor membrane layer. By manipulating the micrometer screw the tilt angle of the frame is changed and the distance between knife edge and polyester foil can be adjusted (E).

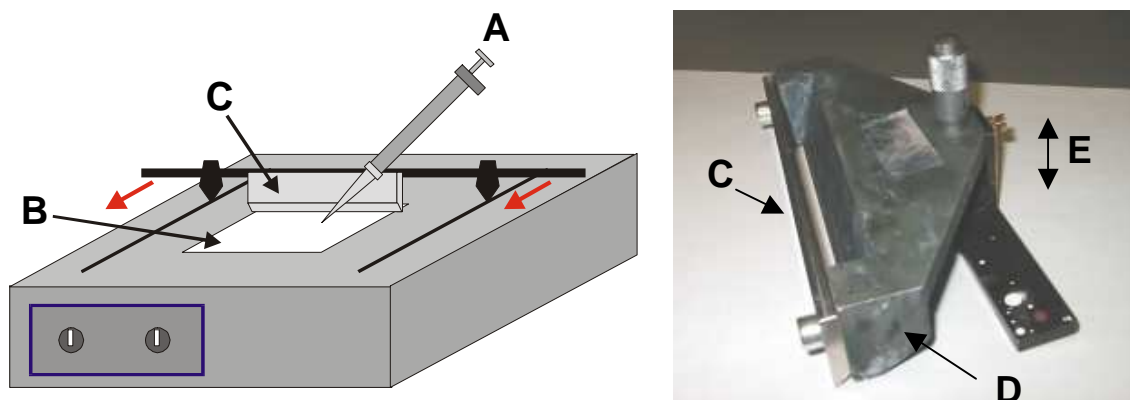


Fig. 2.1. Knife-coating device (**left**) and custom-made coating-knife (**right**).

2.3. Absorbance measurements

Absorbance spectra were recorded with a two-channel UV/VIS scanning spectrophotometer U-3000 equipped with a deuterium and a tungsten iodide lamp as light sources from Hitachi as shown in Fig. 2.2. Polystyrene or quartz cuvettes with a cell length of 1 cm were used to measure the spectra of solutions. The baseline was determined against the applied solvent, which was also used as reference. A thermostated custom-made flow cell was employed for spectroscopic absorbance studies of sensor membranes using blank polyester foils for baseline determination and in the reference optical path.



Fig. 2.2. U-3000 Hitachi UV/VIS scanning spectrophotometer.

2.4. Luminescence measurements

Luminescence excitation and emission spectra were acquired on an Aminco Bowman Series 2 luminescence spectrophotometer from SLM-Aminco using a continuous wave 150-W xenon lamp as light source (Fig. 2.3, left). For luminescence measurements with sensor membranes, the excitation light was filtered by a monochromator and was focused on one branch of a bifurcated fibre bundle (\varnothing 6 mm) of randomised glass fibres. The fibre bundle was positioned at the back of the sensor membrane mounted in a custom-made flow cell as shown in Fig. 2.3 (right). The emitted light of the sensor film was guided back by the other branch of the fibre bundle through a monochromator to the photomultiplier tube (PMT) of the spectrophotometer.

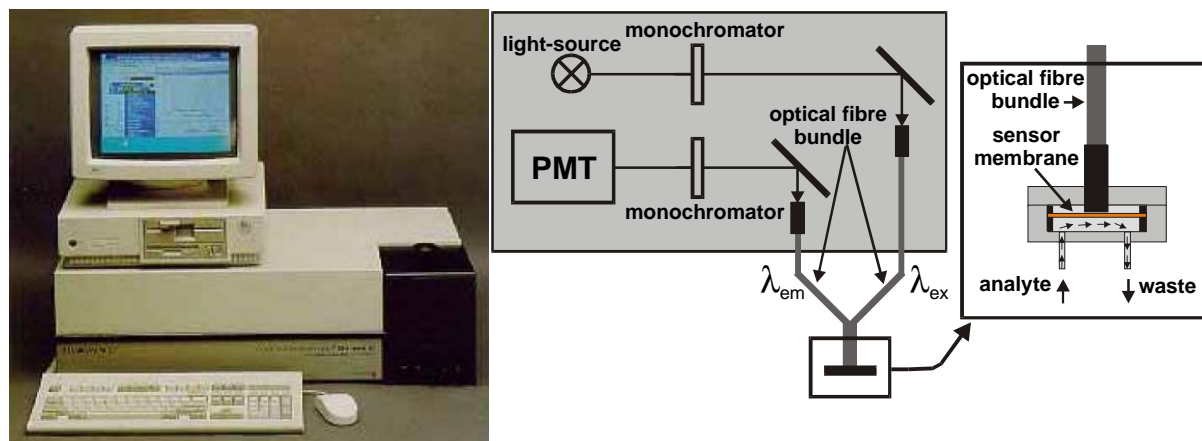


Fig. 2.3. Aminco Bowman Series 2 luminescence spectrophotometer (**left**); schematic of the instrumental set-up applied for luminescence measurements with sensor membranes (**right**).

2.5. Frequency-domain lifetime measurements

Frequency domain lifetime measurements were performed with a dual-phase lock-in amplifier from Stanford Research Systems (Fig. 2.4). Sensor membranes were fixed with silicone grease on the distal end of a bifurcated glass fibre bundle ($\text{\O} 2 \text{ mm}$). One branch of the fibre bundle was directed to a lamp LED from Nichia. The excitation light was sinusoidally modulated by the lock-in amplifier. The second branch of the fibre bundle was connected to a red-sensitive PMT from Hamamatsu Photonics Deutschland to convert the modulated optical emission signal into an electronic input signal. During the measurement the fibre bundle with the sensor spot was immersed into test solutions.

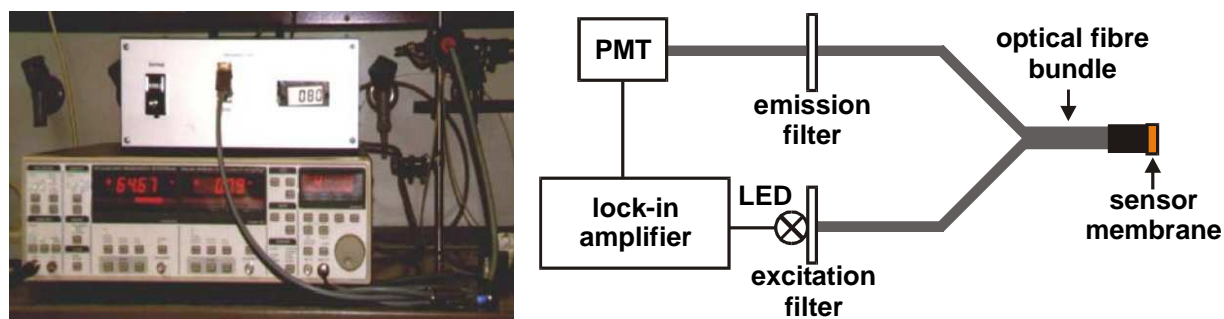


Fig. 2.4. Dual-phase lock-in amplifier and red-sensitive photomultiplier tube (**left**); schematic of the optical arrangement for frequency domain lifetime measurements (**right**).

2.6. Chemical analysis of synthesised ion pairs and indicators

Melting points. Melting points given are uncorrected and were determined in open capillary tubes with a SMP-20 melting point apparatus from Büchi.

Elemental analysis. A CHN-rapid analyser from Heraeus was used to for elemental analysis (C, H, N).

Mass spectra. Mass spectra were measured either with a Finnigan MAT 95 or a ThermoQuest Finnigan TSQ 7000 mass spectrometer from Thermo Electron.

Magnetic nuclear resonance spectra. ^1H -NMR spectra were recorded on an Avance 300 NMR spectrometer from Bruker BioSpin. Tetramethylsilane was used as internal standard.

2.7. Time-resolved lifetime imaging

The imaging set-up used for 2D luminescence measurements was described in detail by Liebsch (2000) and Holst et al. (2001)^{1,2}. In the following only a short overview is given and the modifications made for this work are presented.

2.7.1. System components and set-up

The imaging system comprises a fast gateable CCD camera (modified SensiCam) from PCO equipped with a 0.5 inch monochrome lens-on-chip CCD sensor with 640 x 480 pixels and 12-bit resolution (Fig. 2.5). Binning (= grouping of neighbouring pixels to "superpixels") is possible to increase the signal intensity of an image (for example binning factor 2 reduces the original 640 x 480 pixels to 320 x 240 pixels). The camera is computer controlled by means of a PCI board which corresponds with the camera via a fibre optic link (FOL). An additional coax input at the backside of the camera allows an external activation/deactivation of the CCD chip to define time gates of interest relative to the excitation pulse. The camera can be gated with a minimum step width of 100 ns.

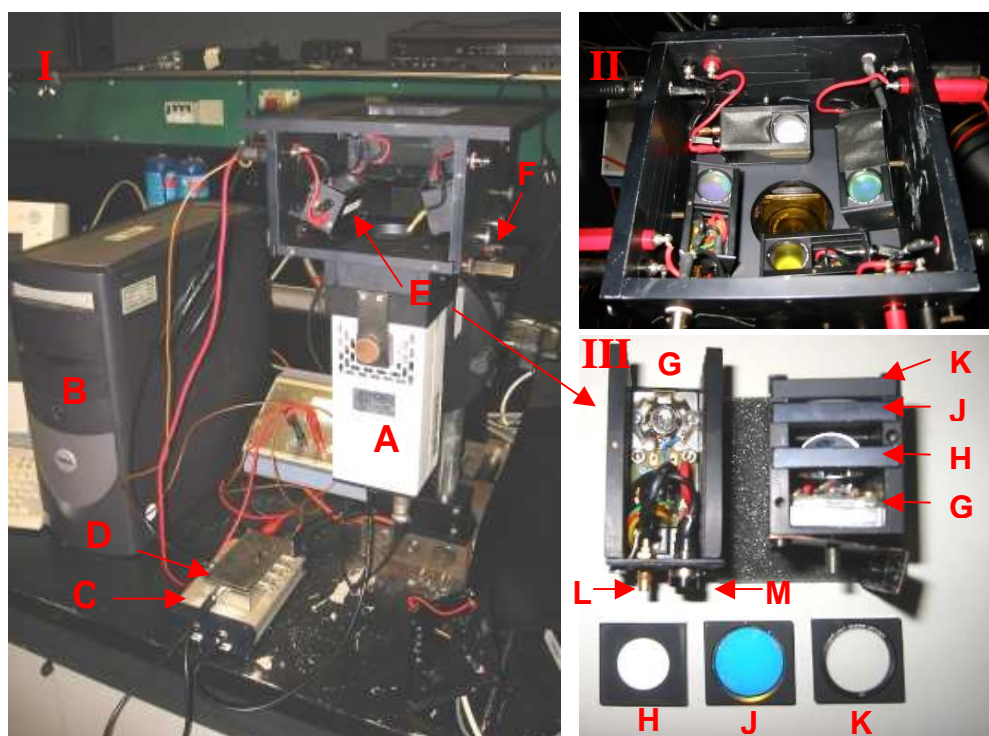


Fig. 2.5. I: Imaging set-up comprising a fast gateable CCD camera (A), a personal computer (B), a custom-made trigger device (C), a TTL signal amplifier (D) and excitation light source modules (E); **F:** emission filter slide; **II:** integrated light source modules; **III:** light source module composed of a fast pulsable chip LED (G), a convex lens (H), an optical filter (J) and a holographic diffuser (K); **L:** coax connector for TTL signal transmission, **M:** power supply connectors.

A custom-made trigger device (B. Grunwald, MPI Bremen, Germany) triggers the CCD camera and the fast pulsable excitation light source. The lamp LED array which was formerly used was replaced by integrated light source modules comprising a LuxeonTM V Star chip LED, lambertian type from Lumileds equipped with a convex lens, a holographic diffuser both from Edmund Industrie Optik and optical filters. The LED was driven at 7 V and 1 A. A coax connector enables the transmission of trigger pulses from the trigger device controlling the light source activation/deactivation. Rise and decay delay of the square shaped light pulses is below 200 ns. A signal amplifier connected between trigger device and light source modules allows the simultaneous gating of up to 4 light sources. The newly built camera support system is fixed to a rotating disk (adjustable in 90° steps) and a xyz-manipulator which enables the exact positioning of the camera.

2.7.2. Characterisation of the chip LED excitation light sources

Various types of light sources emitting in the visible and near UV range are available. Lasers are of high brightness, can be pulsed in the ns-range but are still relatively expensive and restricted to certain wavelengths. Low-priced alternatives are xenon lamps or LEDs. However, the commonly available xenon lamps have a pulse duration in the μs to ms range and can suffer from a significant afterglow, while LEDs can be pulsed in the ns-range with a low decay delay after a square shaped light pulse. Meanwhile LEDs are fabricated with high output power levels in the visible wavelength range. Thus, Luxeon V Star lambertian type chip LEDs (460 nm (blue), 505 nm (cyan) and 530 nm (green)) were chosen as excitation light sources in the imaging set-up due to their high brightness. The LEDs were additionally equipped with a plano-convex lens of 18 mm in diameter and a back focal length of 11.2 mm to collimate the diverging LED emission (Fig. 2.6). At least 90 % of the total luminous flux of the LED are captured at a total included angle of 150° (2β). A 5 mm distance between LED chip and plano-convex lens was chosen as a compromise. Thus, the luminous flux emitted in a total angle of 120° (2α) is collected, which is ca. 80 % of the total luminous flux, according to the radiation pattern given by the manufacturer.

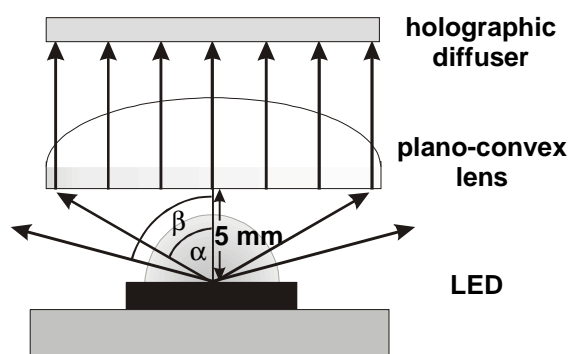


Fig. 2.6. Schematic of a lambertian type LED equipped with a plano-convex lens and a holographic diffuser; the radial emitted light is collimated by the lens; at least 90 % of the total luminous flux are emitted within a total included angle of 150° ($= 2\beta$). ca. 80 % of the total luminous flux are captured when a distance of 5 mm between lens and LED chip is chosen ($2\alpha = 120^\circ$).

Fig. 2.7 depicts the intensity contour plots of 8-bit greyscale images of the 505 nm LED light field without (A) and with the plano-convex lens (B). The intensity of the light field in plot B is significantly increased due to the collimation of the excitation light but the light field is very inhomogeneous. Although the lens does not reproduce an image of the LED chip due to the displacement from the focal point, capillary linear structures of steep intensity gradients

are visible. Therefore, a holographic diffuser with an diffusing angle of 10° was additionally inserted in the excitation path. Compared to other diffusing materials, intensity losses due to back scattering are kept low with this component (transition efficiency $> 85\%$) and a homogeneous intensity of the light field is obtained (Fig. 2.7, C).

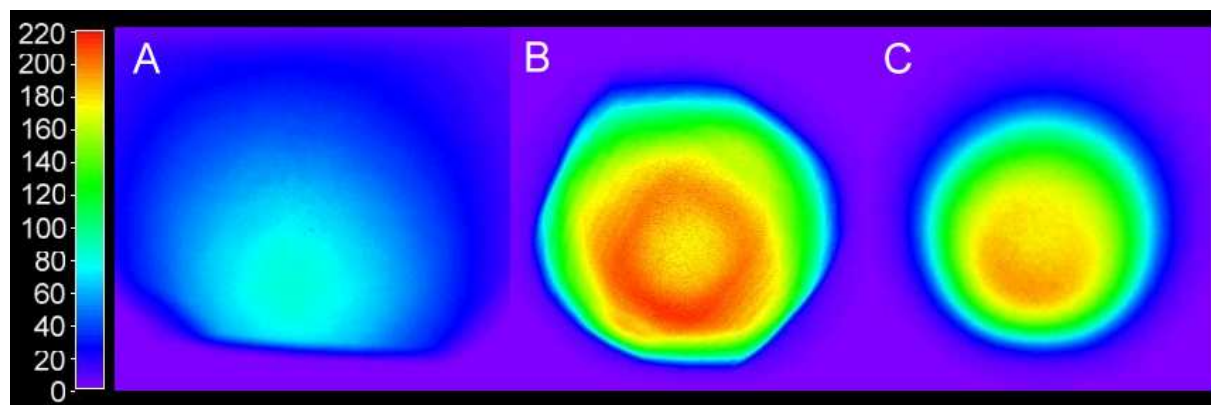


Fig. 2.7. Intensity contour plots of 8-bit greyscale images of the 505 nm LED light field without any optical components (A), with the plano-convex lens (B) and with the plano-convex lens and the holographic diffuser (C).

The use of the plano-convex lens and the holographic diffuser affects also the homogeneity of the light field as to the dominant wavelengths. The wavelength of the emission maximum ($\lambda_{em.}$) at different positions of the light field was determined for the 460 nm LED and the 505 nm LED by recording the emission spectra at thirteen positions distributed over the whole light field with a multi-channel analyser (photonic multi-channel analyser PMA-11 C5966 (CCD version) from Hamamatsu Photonics Deutschland). The mean $\lambda_{em.}$ values and maximum errors recorded with the 505 nm LED without the optical components, with the plano-convex lens and with lens and holographic diffuser were 504.8 ± 1.3 nm, 504.6 ± 1 nm, 504.4 ± 0.7 nm, respectively. Measurements with the completely equipped 460 nm LED gave 459.2 ± 1 nm. A homogeneous wavelength distribution is especially important in ratiometric measurement schemes where a second dye serves as reference for the indicator (td-DLR and td-DLR/RLD measurements), since the excitation spectra of the two dyes are usually not identical. Thus, a shift in the excitation wavelengths within the imaged area results in varying emission intensity ratios of the two luminophores causing errors in the measured analyte concentration.

The size of the light field at the distance where the sensor membranes were placed during the measurements was ca. 80 cm^2 . The average irradiance on this area was calculated from the total radiometric power given by the manufacturer (772 mW for the 460 nm LED,

567 mW for the 505 nm LED and 271 mW for the 530 nm LED). Considering the intensity losses due to the reduced light source emission angle utilised and the back-scattering and reflection from the lens, the optical filters and the diffuser, an average irradiance of 5.6 mW/cm^2 (460 nm LED), 3.4 mW/cm^2 (505 nm LED) and 2 mW/cm^2 (530 nm LED) was calculated, respectively. However, the characterisation of the planar optodes with the imaging set-up was accomplished with $5 \times 5 \text{ cm}$ sensor foils mounted into a flow cell which was positioned in the centre of the light field during the measurements. Here the excitation light intensity is ca. 50 % higher than the average intensity. Thus, the irradiance in this centre area (= average irradiance on the optode surface) was estimated to be ca. 8.4 mW/cm^2 (460 nm LED), 5.1 mW/cm^2 (505 nm LED) and 3 mW/cm^2 (530 nm LED), respectively.

2.7.3. Data acquisition and processing

The data acquisition in the CCD-based system for time-resolved imaging was controlled by the software module Look@MOLLI². The trigger data and camera settings such as the position of the image time gates relative to the excitation pulse, the length of the excitation pulse and the recording time gates as well as the binning factors and the total exposure time can be set in the dialog window of the data acquisition software. Fig. 2.8 shows a schematic of the data acquisition process when using the RLD method. This measurement scheme requires the recording of images within two different time gates after the square-shaped excitation pulse. A multi-exposure of the CCD-chip with on-chip-integration of the charges is possible. The overall images of the two time-gates and their corresponding dark images are recorded successively in the following order: *dark* a_{em1} , a_{em1} , *dark* a_{em2} , a_{em2} . Initially, the trigger data for the first overall image (*dark* a_{em1}) are transferred to the trigger device which is responsible for the synchronisation of the light source and the CCD chip of the camera within nanoseconds. The emission intensity detected within a single time gate is integrated over a number of recording cycles (depending on the total exposure time) into the same frame on the CCD chip and is afterwards read out into one image file. The time span between the start of the excitation pulse and the end of the last image time gate set (= total gate width) defines together with the total exposure time the number of these image acquisition cycles. Thus, a total exposure time of 100 ms and a total gate width of 10 μs results in the integration of 10000 single images to one overall image. Afterwards the data are transferred from the camera to the PC (typically 25 ms) and the new trigger data for the following image (a_{em1}) are

passed from the PC to the trigger device (typically 75 ms). With a total exposure time of 100 ms the recording of all images requires therefore 800 ms. The signal-to-noise ratio (SNR) can be increased by a function that allows the repeating of the acquisition circuit and the subsequent averaging of the respective overall images. The number of repetitions can be preset. In case of a low emission intensity of the optode, an increase of the total exposure time (up to 500 ms) or the binning factor is possible. However, all measures are either at the cost of speed or spatial resolution.

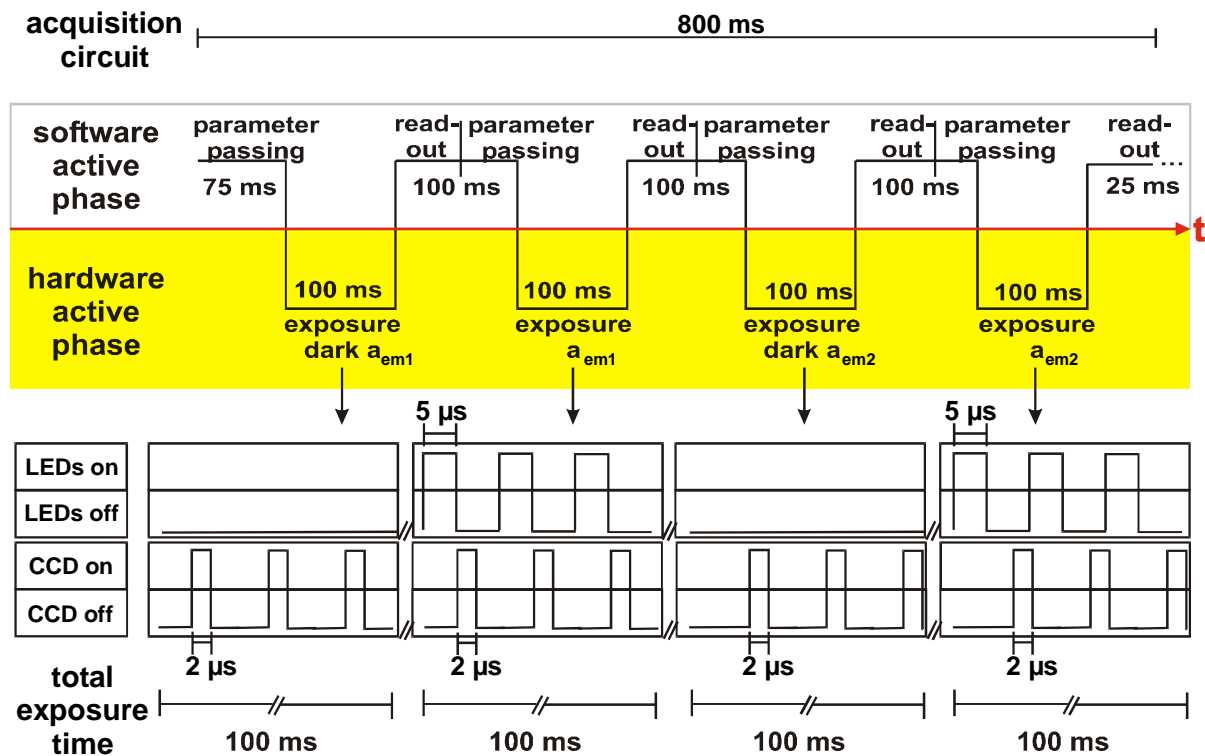


Fig. 2.8. Schematic of the data acquisition process considering time-resolved luminescence lifetime imaging as example.

The dark images are taken in the respective time gate without an excitation pulse and contain therefore the measured noise due to permanent ambient light and the thermal noise of the CCD chip. These dark images are subtracted from their corresponding images to improve the SNR which results in the background-corrected overall images (or intensity integrals) A_{em1} and A_{em2} .

These background-corrected overall images are the basis data obtained from one measurement. An application developed in IDL 5.3 from Research Systems was used to process and visualise these images. This software module includes features like 3D-plotting, contour-plotting, some mathematical calculation routines for image manipulation or the

selection of user defined regions of interest¹. Data matrices can be saved as image files or as DAT-files containing the numerical values of the matrix pixels. For the evaluation of dual sensor measurements the numerical values of image ratios were used in an iteration procedure. The data handling and the calculations were performed with visual basic applications in excel (see chapter 12).

2.8. References

- [1] Liebsch G., *Time-Resolved Luminescence Lifetime Imaging with Optical Chemical Sensors: Set-up, Controlling, Concepts and Applications*. Ph.D. Thesis, University of Regensburg (2000).
- [2] Holst G., Grunwald B., *Luminescence lifetime imaging with transparent oxygen optodes*. Sens. Actuators, B (2001), 74, 78 - 90.

3. pH Fluorosensors for Use in Marine Systems

In this chapter, fluorescence-based optical pH sensors especially designed for pH measurements in marine environment are presented. Embedded in an uncharged, highly proton-permeable hydrogel matrix, the two novel lipophilic carboxyfluorescein derivatives 2',7'-dihexyl-5(6)-N-octadecyl-carboxamidofluorescein (DHFA) and 2',7'-dihexyl-5(6)-N-octadecyl-carboxamidofluorescein ethyl ester (DHFAE) have apparent pKa values of approximately 8.4. The pH transition range of the sensors therefore perfectly matches the pH range predominantly found in seawater and marine sediment (pH 7.2 - pH 9.2). The cross-sensitivity towards ionic strength (IS) was found to be low for DHFA-containing membranes and was even negligible when using DHFAE as indicator. The optical properties of the indicators allow internal referencing of the measurements. Dual-wavelength measurements are possible with the DHFAE chromophore since the emission maxima of the basic and acidic form of DHFAE differ by 30 nm. Dual lifetime referencing (DLR) measurements were made with pH sensors incorporating ruthenium(II) tris(4,7-diphenyl-1,10-phenanthroline) (Ru(dpp)₃)-containing reference particles in addition to the indicator. This type of sensor can be applied for imaging or for phase modulation measurements of pH. Examples of imaging of pH in heterogeneous natural marine sediments are shown and discussed.

3.1. Introduction

Many important biogeochemical processes like photosynthesis, metabolic processes, diagenesis, calcium carbonate sedimentation or dissolution cause strong changes of chemical and physical parameters in seawater, marine sediments and/or their interface layer. The pH is besides oxygen and CO₂ one of the key parameters describing these processes and gives valuable information about their progress¹⁻⁴. The well-established tool for pH measurement is the glass electrode. However, electrodes are limited to single-point measurements and are not comfortable to obtain distribution information on pH. An alternative are optical pH sensors, which can be easily produced in various shapes. Combined with optical fibre technology

microoptodes for non-invasive pH measurements can be fabricated^{5,6}. Planar solid supports coated with a sensor layer enable the mapping of two-dimensional pH profiles^{7,8}. Another advantage of using pH optodes is the possibility of their combination with oxygen optodes in marine applications, which are the preferred choice with respect to such important parameters as accuracy, reproducibility and long-term stability⁹.

A well-known problem of pH optodes limiting their practical use is their signal dependency on the IS and therefore on the ionic composition of the sample¹⁰. This effect is not critical for pH sensing in the open sea, since here the salinity is fairly constant and differs only in the range between 33 ‰ and 37 ‰. In contrast to that, optical pH measurements often fail in coastal regions where a mixing of freshwater and seawater results in large fluctuations of salinity down to 2.5 ‰. Here pH optodes are requested with a negligible cross-sensitivity towards IS fluctuations. An alternative is the parallel determination of salinity with either a conductivity sensor or an optical chloride sensor¹¹ and the consequent correction of the pH signal.

Whereas numerous examples for optical pH sensing in physiological samples were described^{12,13} only a few promising examples for seawater monitoring are known. A promising approach is the use of spectrophotometric pH sensors in flow systems reported recently^{14,15}. The samples are mixed with a sulfonephthalein pH indicator solution and the pH is determined by absorbance measurements in a miniaturised flow-through cell. In 1990 Serra et al. published a fibre-optic pH sensor for seawater monitoring employing phenol red immobilised on amberlite XAD-2 resin¹⁶. Hulth et al. described a planar pH sensor incorporating the fluorescent indicator HPTS with cellulose acetate as matrix for two-dimensional pH mapping in early diagenetic studies of marine sediments¹⁷. This system has two drawbacks. The given dynamic range of pH 5.4 - pH 7.4 does not match the average pH range in marine systems (pH 7.2 - pH 9.2). Furthermore this sensor based on HPTS is highly cross-sensitive towards IS changes¹⁸.

Besides the problems related to IS, the general problem of applying fluorescence based pH optodes is that only few fluorophores have pH transition intervals in the region around pH 8. Some SNAFL and SNARF indicators fulfil this requirement¹⁹. They are suitable for internally referenced dual-wavelength pH measurements since the excitation and emission maxima of the deprotonated/protonated form differ at least by 20 nm in wavelength²⁰. Drawbacks, however, are the low quantum yields (QYs) of these fluorophores and the extraordinarily high price of commercially available derivatives.

An approach to design pH optodes with minimised IS effects was published recently²¹. It is based on lipophilic fluorescein derivatives physically entrapped in a neutral polyurethane hydrogel with mixed hydrophobic and hydrophilic domains. This matrix also increases the apparent pK_a values by approximately 2 units. Substitution of fluorescein in 2',7'-position results in a series of sensors responding from pH 4.5 - pH 6.5 (dichloro derivative) up to pH 7.5 - pH 9.5 (dihexyl derivative). On the basis of these results two new lipophilic 2',7'-dihexylcarboxyfluorescein derivatives were synthesised. Main focus was set on achieving a suitable pH transition range which matches the important pH range in marine systems and on the possibility of referenced pH measurements. The sensors were characterised with respect to their spectral properties, IS and temperature cross-sensitivities. A DLR-based sensor was applied for two-dimensional measurements of pH distributions patterns in natural marine sediment.

3.2. Experimental

3.2.1. Materials

1,2,4-Benzenetricarboxylic anhydride (97 %), 4-hexylresorcinol (99 %), octadecylamine (97 %) and titanium(IV) oxide (powder, < 5 µm) were obtained from Aldrich. N-Hydroxysuccinimide, N,N'-dicyclohexylcarbodiimide (99 %), ethyl bromide (99 %), methanesulfonic acid and N,N-dimethylformamide (puriss. abs. ca. 99.8 %) were purchased from Fluka. The other solvents used were of analytical grade and obtained from Merck except for absolute ethanol which was purchased from Mallinckrodt Backer and diethyl ether which was obtained from Carl Roth. The polyurethane hydrogel HydroMed D4 (D4) from Cardiotech was used as sensor matrix. A polyethylene terephthalate foil (Mylar[®]) of 125 µm thickness from Goodfellow served as solid support for the sensor membranes. The luminescent reference particles were a gift from PreSens. The standard buffer solutions (pH 4 and pH 7) applied for the calibration of the pH meter were purchased from Carl Roth. All salts used for buffer preparation were obtained from Merck except for CaCl₂ which was purchased from Carl Roth. All other substances used were obtained from Merck. Doubly distilled water was applied throughout.

3.2.2. Buffer preparation

Phosphate buffer stock solutions with defined IS were made up with the appropriate sodium salt of dihydrogen phosphate, hydrogen phosphate or phosphate and with sodium chloride as background electrolyte. If not otherwise stated, the buffer concentration and IS of the buffer stock solutions were 50 mM and 500mM, respectively, except for the IS cross-sensitivity measurements where 15 mM phosphate buffer stock solutions were used. Buffer stock solutions for IS cross-sensitivity measurements with artificial seawater as background electrolyte were prepared with tris-(hydroxymethyl)aminomethane (TRIS) and tris-(hydroxymethyl)aminomethane hydrochloride (buffer concentration: 15 mM), respectively. The artificial seawater was made up according to Kester et al.²². The amount of background electrolyte added to the buffer stock solutions was calculated by means of eq. 3.1

$$IS = 0.5 \cdot \sum_i z_i^2 \cdot c_i \quad (3.1)$$

where z_i is the valency of each ion species i and c_i is its concentration. The buffer solutions with defined pH used for sensor calibration were obtained by mixing the respective acidic and basic stock solutions (dihydrogen phosphate/hydrogen phosphate buffer: pH range 5 - 9 and hydrogen phosphate/phosphate buffer: pH range 9 - 10). The adjusted pH was controlled by means of a pH meter.

3.2.3. Apparatus

UV/VIS absorbance spectra and single wavelength absorbance time scans were recorded with a U-3000 UV/VIS double-beam spectrophotometer from Hitachi. Fluorescence spectra as well as the single and dual wavelength fluorescence time scans were acquired with an Aminco Bowman Series 2 luminescence spectrophotometer from SLM-Aminco. Time domain DLR measurements were accomplished with the imaging set-up described in chapter 2.7. A light source module comprising a LuxeonTM V Star LED ($\lambda_{em.} = 505$ nm) from Lumileds was used for excitation of the sensor foils. Sensor calibration was accomplished with 5 x 5 cm sensor membranes mounted into a thermostated custom-made flow cell. To ensure constant flow rates a Miniplus-3 peristaltic pump from Gilson was used in all experiments to pump the buffer solutions through flow cells at a rate of 1 ml min⁻¹. Frequency domain DLR

measurements were performed with a dual-phase lock-in amplifier from Stanford Research Systems using a cyan lamp LED ($\lambda_{em.} = 505 \text{ nm}$) from Nichia as excitation light source. The sensor spot fixed with silicone grease to the distal end of the applied bifurcated fibre bundle was immersed into thermostated buffer solutions with defined pH values during the measurement. The same optical filters were used for fd-DLR and td-DLR measurements. The LED light was filtered with the combination of a GG 495 glass filter and a C54 cyan dichroic filter, and an OG 570 glass filter was used for the emission path. All optical filters were obtained either from Schott (GG 495, OG 570) or from Linos Photonics (Dichrolight™ C54 cyan). All measurements were performed at 20°C, if not stated otherwise.

3.2.4. Sensor fabrication

A 10 % (w/w) D4 stock solution was prepared by dissolving 1 g D4 in 9 g of a 9 : 1 (v/v) ethanol/water mixture. 10 mg indicator were dissolved in 1 ml ethanol to obtain the dye stock solutions. The final sensor cocktails were made up by adding aliquots of the respective indicator stock solution to 1 g of the polymer solution. The luminescent reference particles and titanium dioxide enhancing light scattering were added in case of the DLR sensor cocktails (Table 3.1).

Table 3.1. Composition of the pH sensor membranes.

membrane	indicator	indicator/polymer fraction [mmol kg ⁻¹ polymer]	D4 : reference particles: TiO ₂ /weight fraction
M1_DHFAE	DHFAE	3	– ^(a)
M2_DHFAE	DHFAE	3	10 : 1 : 9
M1_DHFA	DHFA	3	– ^(a)
M2_DHFA	DHFA	3	10 : 4 : 9

(a) no addition of reference particles and TiO₂

The DLR sensor cocktails were stirred for at least 24 h to achieve a homogeneous dispersion of the particles. The other cocktails were stirred about 12 h before use. The sensor films were fabricated by spreading the cocktails onto dust-free Mylar® foil with a knife-coating device from Coesfeld. The wet thickness of the sensor films was 60 µm for the DLR sensors (M2) and 120 µm for the M1 sensors which resulted in a thickness of approx. 12 µm after solvent

evaporation. The membranes were left to dry overnight before characterisation. Table 3.1 indicates the composition of the sensor films.

3.2.5. Preparation of sediment measurements

Measurements in natural sediments were performed at the Marine Biological Laboratory in Helsingør, Denmark. Only a brief overview is given in the following. For a more detailed description see ref. 23. Sediment was collected in squared frames at a shallow water site (ca. 1 m depth) in the Helsingør Marina (Denmark)²⁴. The sediment hosted a high density ($> 500 \text{ ind m}^{-2}$) of burrowing polychaetes (*Hediste diversicolor*). Patches of photosynthetically active benthic diatoms covered the sediment surface. The back of a M2_DHF AE sensor membrane (5.5 x 5.5 cm) was attached to an inside wall of a small aquarium constructed of transparent Plexiglas. The sediment was carefully transferred to the aquarium and after addition of water from the sampling site the set-up was allowed to settle for 1 day prior to any measurements. To mimic natural conditions, an artificial 12 h day/night cycle was imposed to the set-up (Schott halogen lamp, 150 Watt). To avoid any interference from ambient light when taking images during the day cycle, the light was turned off prior to taking the images with the CCD camera. Parallel to the imaging measurements, a pH glass microelectrode²⁵ continuously monitored the pH of the water phase. A pH microelectrode was also used to measure pH profiles next to the planar optode for comparison. The electrode had a tip diameter of 30 - 50 μm . It was equipped with an external calomel reference electrode from Radiometer Danmark and both were connected to a high impedance voltmeter.

3.3. Synthesis

The carboxyfluorescein derivatives were synthesised according to the methods reported by Matray et al.²⁶ and Wang et al.²⁷.

3.3.1. Synthesis of 5(6)-carboxy-2',7'-dihexylfluorescein (DHCF)

15 ml methanesulfonic acid was added to 1,2,4-benzenetricarboxylic anhydride (990 mg, 5.2 mmol) and 4-hexylresorcinol (2 g, 10.3 mmol) in a 100 ml round bottom flask. The resulting suspension was refluxed for 30 min. at 130°C using an oil bath. Afterwards the deep red solution was cooled to room temperature and then added drop wise to ca. 150 ml of rapidly stirred water. The orange solid precipitate was filtered, dried and recrystallised from acetonitrile to yield yellow crystals of 5(6)-carboxy-2',7'-dihexylfluorescein (0.59 g, 21 %).

Melting point: 244-247 °C; **Mass spectrum (esi) m/z (rel. intensity):** 544 (3; MH⁺), 500 (11), 455 (10), 430 (28), 415 (100).

3.3.2. Synthesis of 2',7'-dihexyl-5(6)-N-octadecyl-carboxamidofluorescein (DHFA)

5(6)-carboxy-2',7'-dihexylfluorescein (500 mg, 0.92 mmol) and N-hydroxysuccinimide (127 mg, 1.1 mmol) were put into a 50 ml round bottom flask. 10 ml dry DMF and 1 drop of triethylamine were added and the suspension is left to stir for 2 h at room. Afterwards N,N'-dicyclohexylcarbodiimide (227 mg, 1.1 mmol) and 1-octadecylamine (297 mg, 1.1 mmol) were added and the mixture was again stirred for 48 h. The white precipitate was removed by filtration and the remaining red solution was added drop wise into 50 ml of stirred water. The resulting fine orange precipitate was filtered, washed with water and dried. Purification was accomplished via column chromatography with silica gel 60 (0.063-0.200 mm) as stationary phase and an 1 : 9 ethanol/chloroform solution as mobile phase to afford an orange-red solid of 2',7'-dihexyl-5(6)-N-octadecyl-carboxamidofluorescein (66 mg, 9 %).

Melting point: 152-154 °C; **¹H-NMR (CDCl₃):** δ [ppm] = 0.6-0.95 (m, 9H, -CH₃), 0.95-1.85 (m, 48H, -CH₂-), 2.25-2.65 (t, 4H, aryl-CH₂-), 3.35-4.0 (m, 2H, -NH-CH₂-), 6.24-8.99 (m, 8H, aromatic and -NH-); **Mass spectrum (esi) m/z (rel. intensity):** 797 (100; MH⁺), 752 (7), 573 (21), 559 (7).

3.3.3. Synthesis of 2',7'-dihexyl-5(6)-N-octadecyl-carboxamidofluorescein ethyl ester (DHFAE)

A mixture of 2',7'-dihexyl-5(6)-N-octadecyl-carboxamidofluorescein (50 mg, 0.063 mmol), 1-bromoethane (5 μ l, 0.067 mmol) and K_2CO_3 solid (35 mg) in 5 ml DMSO was stirred in an oil bath at 65 °C for 20 h. The red precipitate that formed upon addition of 10 ml saturated NaCl was filtered, washed with water and redissolved in ethyl acetate with 1M HCl. The organic phase was separated, washed with phosphate buffer (pH 7.4) and water and was evaporated to dryness under reduced pressure. The product was purified by column chromatography with silica gel 60 (0.063-0.200 mm) as stationary phase and an 0.5 : 9.5 ethanol/chloroform solution as mobile phase to yield a red solid of 2',7'-dihexyl-5(6)-N-octadecyl-carboxamidofluorescein ethyl ester (13.4 mg, 26 %).

Melting point: 92-94 °C; **1H -NMR (CD_2Cl_2):** δ [ppm] = 0.68-0.92 (m, 12H, $-CH_3$), 1.09-1.8 (m, 48H, $-CH_2-$), 2.25-2.62 (t, 4H, aryl- CH_2-), 3.35-3.97 (m, 4H, $-O-CH_2-$ and $-NH-CH_2$), 6.54-8.71 (m, 8H, aromatic and $-NH-$); **Mass spectrum (esi) m/z (rel. intensity):** 825 (100; MH^+), 780 (4), 601 (8), 587 (5).

3.4. Results and discussion

3.4.1. Synthesis and characterisation of the lipophilic pH indicators

The two lipophilic pH indicators DHFA and DHFAE investigated in this work were synthesised starting from a carboxyfluorescein derivative with hexyl substituents at 2' and 7' position (DHCF). The hexyl residues fulfil two functions. Firstly, they have a positive inductive effect which diminishes the stability of the deprotonated form of the indicator especially in nonpolar media and therefore shifts the apparent pKa (pK_a') to higher values. Secondly, they increase the lipophilicity of the dye. Yet DHCF is still water-soluble to some extent. The pK_a' measured in a phosphate-buffered aqueous solution was 6.6 which is only slightly higher than that of 5(6)-carboxyfluorescein ($pK_a = 6.4$)²⁸ due to the polar solvent. To obtain pH indicators which can be immobilised in a lipophilic sensor matrix, the lipophilic character was further increased by amidation of the 5(6)-carboxyl group of DHCF with octadecylamine. The 2-carboxyl group of the resulting DHFA was converted into an ethyl ester group in a next step to obtain DHFAE. Like most fluoresceins the protonated form of

DHFA exists predominantly as lactone in a nonpolar surrounding. The esterification of the 2-carboxyl group in DHFAE prevents this lactonisation. Fig. 3.1 depicts the acid-base equilibria of the two lipophilic indicators.

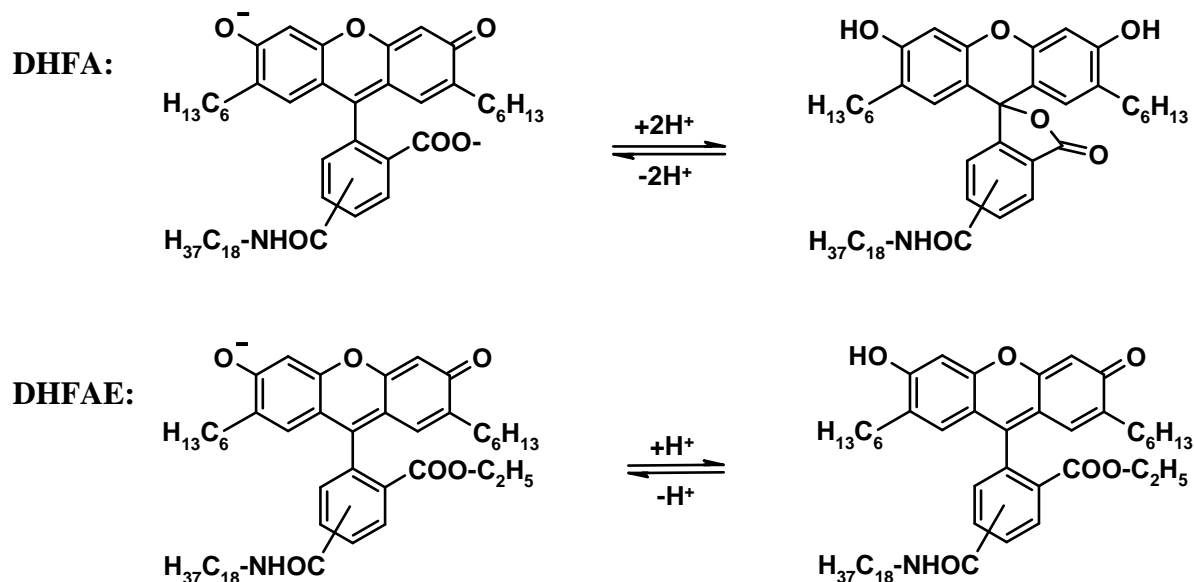


Fig. 3.1. Acid-base equilibria of the two lipophilic indicators DHFA and DHFAE.

The 2', 7' position of the hexyl groups was chosen since a substitution in 4' and 5' position decreases the QY of the fluorescein chromophore dramatically. The QY of DHCF was found to be 0.81_{basic} and is not significantly lower than that of fluorescein which is 0.97_{basic} in ethanolic solution²⁹. The basic form of DHFA has a QY of 0.94. The QYs of the deprotonated and the protonated form of DHFAE are 0.62 and 0.22, respectively. Table 3.2 summarises the optical properties of the fluorescein derivatives. Measurements were made with ethanolic solutions of the indicators.

Table 3.2. Summarised optical properties of the pH indicators in ethanolic solution.

indicator/sensor	$\lambda_{\max}(\text{exc.})$ [nm]	$\lambda_{\max}(\text{em.})$ [nm]	λ [$\text{L mol}^{-1} \text{cm}^{-1}$]	QY
DHCF	510 _{base}	535 _{base}	99000 _{base}	0.81 _{base}
DHFA	513 _{base}	539 _{base}	82000 _{base}	0.94 _{base}
DHFAE	463 _{acid} /523 _{base}	480 _{acid} /558 _{base}	64000 _{acid} / 94000 _{base}	0.22 _{acid} / 0.62 _{base}

The QYs of the dyes were calculated by means of eq. 3.2 using fluorescein in basic ethanolic solution as reference³⁰.

$$QY_X = QY_R \frac{A_R \cdot I_X \cdot n_X^2}{A_X \cdot I_R \cdot n_R^2} \quad (3.2)$$

The indices X and R refer to the dye and the reference, respectively, A is the absorbance at the excitation wavelength, I is the integrated area of the corrected emission spectrum and n is the refractive index of the solvent used.

3.4.2. Characterisation of the intensity-based pH sensors

The polyurethane type hydrogel D4 was used as sensor matrix throughout this work. D4 is a highly proton-permeable, uncharged polymer with a water uptake capacity of about 50 %. It contains hydrophilic regions and hydrophobic blocks in which the pH indicators DHFA and DHFAE were immobilised by adsorption with their alkyl side chains acting as lipophilic anchors.

Fig. 3.2 shows the absorbance and emission spectra of M1_DHFA and M1_DHF AE sensors at pH values varying from 10 to 6. The deviation from the isosbestic point at a pH lower than 8.5 in the absorbance spectra of M1_DHFA indicates the lactonisation of the dye (top, left). No clear absorbance maximum of the protonated form can be found. The deprotonated form of DHFA in the D4 matrix has an absorbance maximum at 516 nm. The membrane was excited at this wavelength to record the emission spectra. While the deprotonated form shows an emission maximum at 540 nm, the lactone form of DHFA is not fluorescent. The emission decreases to nearly zero at pH 6 which results in a high sensor dynamic (top, right). The absorbance spectra of M1_DHF AE at varying pH values reveal no deviation from the isosbestic point (bottom, left). The absorbance maxima of the protonated and deprotonated form are at 468 nm and 530 nm, respectively. The emission maxima at 524 nm (acidic form) and 554 nm (basic form) differ by 30 nm. Therefore measurements with this indicator can be internally referenced by ratiometric dual wavelength measurements. Fig. 3.2 (bottom, right) depicts the emission spectra of a M1_DHF AE membrane excited at 485 nm (wavelength of the isosbestic point). The sensor dynamic of the M1_DHF AE sensor is smaller than that of the M1_DHFA sensor since the emission of the protonated form of DHFAE is still comparatively high at the emission maximum of the deprotonated form.

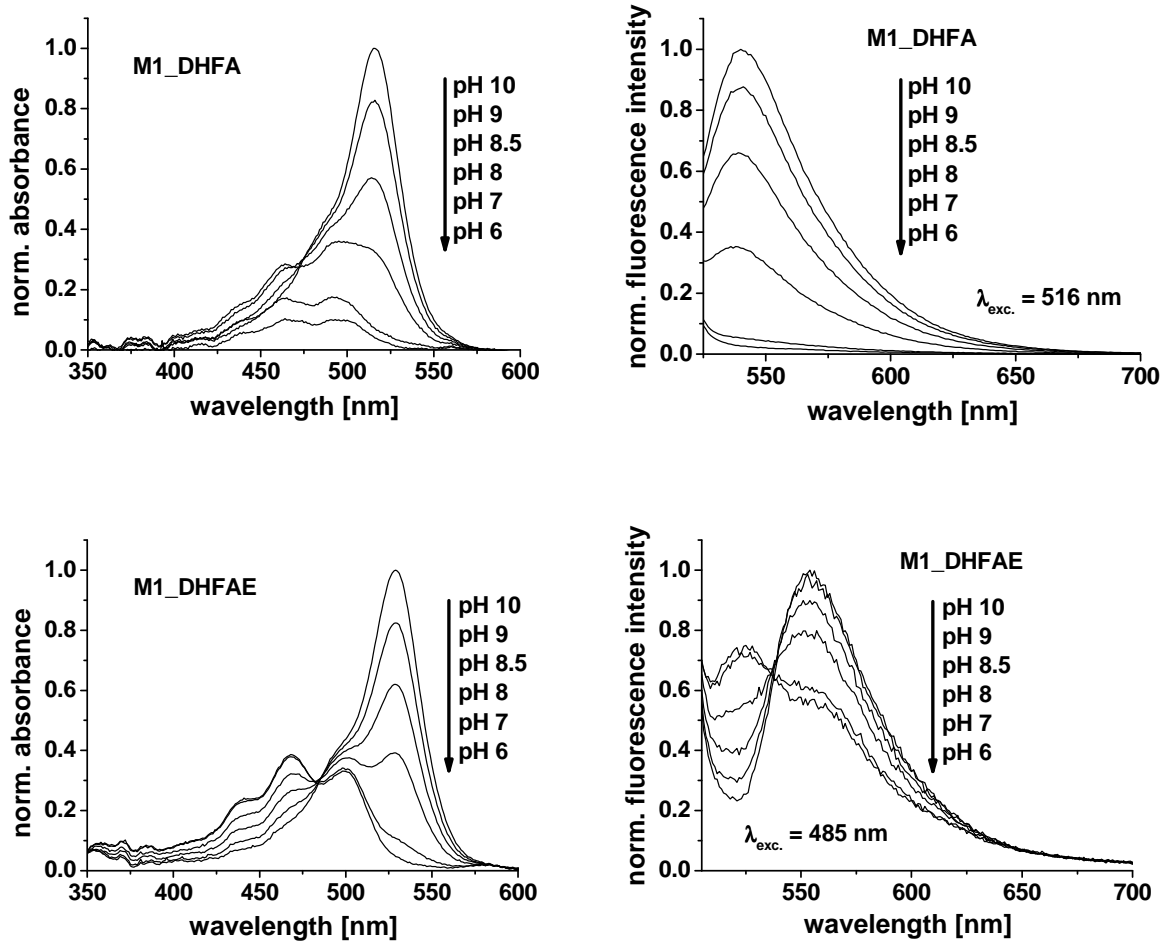


Fig. 3.2. top, left: Absorbance spectra of M1_DHFA at pH values varying from 10 to 6; a deviation from the isosbestic point occurs at pH values lower than 8.5 due to the lactonisation of the indicator. **top, right:** Fluorescence spectra of M1_DHFA excited at 516 nm; **bottom, left:** Absorbance spectra of M1_DHFAE; **bottom, right:** Fluorescence spectra of M1_DHFAE excited at the wavelength of the isosbestic point ($\lambda_{iso} = 485 \text{ nm}$).

For the calibration of the M1_DHFAE membranes a dual excitation scheme was applied. They were excited at the two excitation maxima 468 nm and 530 nm and the ratio of the two respective emission bands at 554 nm ($F_{(\lambda_{exc.} 530\text{nm})}/F_{(\lambda_{exc.} 468\text{nm})}$) was recorded as measurement signal. This ratio is independent of the pH of the indicator concentration and therefore of any intensity losses caused by photodecomposition or leaching of the indicator out of the sensor membrane. In the case of the M1_DHFA membranes no referenced measuring is possible. Thus, fluorescence intensity measurements were made ($\lambda_{exc.} = 516 \text{ nm}$ and $\lambda_{em.} = 540 \text{ nm}$). These measurement schemes were used throughout for the respective M1 sensors unless noted otherwise.

In Fig. 3.3 the normalised fluorescence signals of M1_DHFA (left) and M1_DHFAE (right) are plotted versus the pH to give the sigmoidal calibration curves of the sensors, which were fitted with the Boltzmann function (eq. 3.3).

$$\frac{F}{F^0} = \frac{m1 - m2}{1 + \exp\left(\frac{pH - pKa'}{p}\right)} + m2 \quad (3.3)$$

F and F^0 are the fluorescence signals measured at varying pH values and at the highest pH value used during the calibration (pH 10), respectively. The points of inflection corresponding to the pKa' values were at 8.35 for M1_DHFA and 8.36 for M1_DHFAE. The high pKa' values of the sensors result from the lipophilic surrounding of the indicators within the hydrogel which stabilises the protonated, uncharged form more than the deprotonated species.

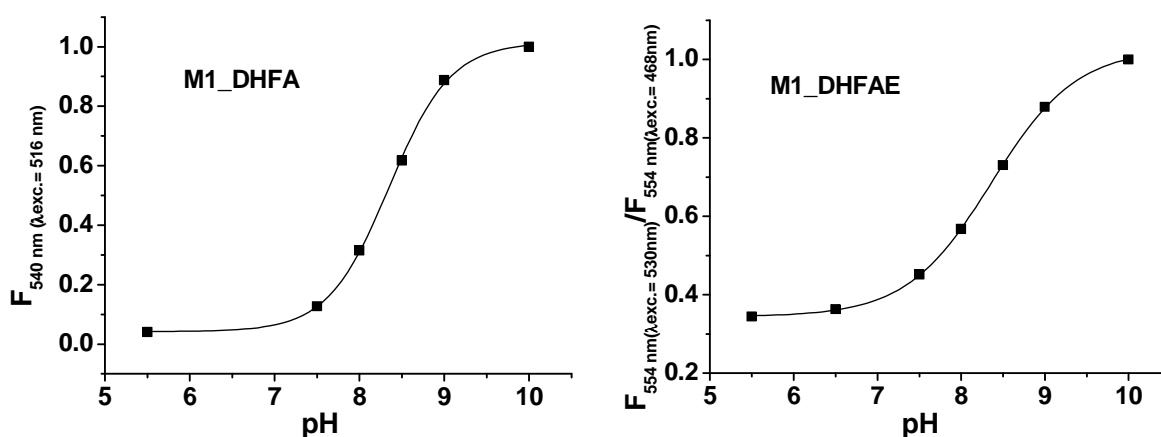


Fig. 3.3. Normalised calibration curves of M1_DHFA (left) and M1_DHFAE (right).

The pH in seawater normally varies between 7.8 and 8.2 due to dissolved atmospheric CO_2 and the carbonate and borate buffer systems. In upper marine sediment layers respiration activity (CO_2 evolution) can reduce the pH to 7.2, while photosynthesis (CO_2 consumption) is able to increase it to 9.2. This whole relevant pH range is covered excellently by the two sensors described here.

The sensor response time t_{90} of the M1 membranes was determined for pH transitions from 8.5 to 7.5 and back, since most of the pH changes occurring in marine systems are within this pH range. The sensor kinetic mainly depends on the membrane thickness which was approx. 12 μm and the flow-rate of the analyte solution (1 ml min^{-1}). The following mean t_{90} values were found for the M1 membranes: 120 s (pH 8.5 \rightarrow pH 7.5)/230 s (pH 7.5 \rightarrow

pH 8.5). Faster-responding sensors can be obtained by reducing the sensing layer thickness. However, a 6 μm thick membrane shows still a response time of 90 s (pH 8.5 \rightarrow pH 7.5) at the same measurement conditions.

The photostability of the M1 sensors was investigated at a pH of 8.2 which is a common pH value for surface seawater. Here the ratio of protonated to deprotonated form is about 1.6 for both indicators. The membranes were immersed in the appropriate phosphate buffer solution and were irradiated for 1 h with a continuous wave 150 W xenon lamp as light source (λ_{exc} : 516 nm (M1_DHFA) and 530 nm (M1_DHFAE)). The bandpass was adjusted to 4 nm for the excitation and the emission light which was the usual setting for all fluorescence measurements. The emission of the sensors was continuously recorded (λ_{em} : 540 nm (M1_DHFA) and 554 nm (M1_DHFAE)). After 1 h the fluorescence intensity of M1_DHFA and M1_DHFAE had dropped to 96.7 % and 93.9 % of the initial signal, respectively.

Leaching of the indicators from the membrane was tested in two experiments. Firstly, phosphate buffer solution (pH 8.2, IS = 720 mM) was pumped through a flow cell equipped with a M1 sensor for 48 h at a constant flow rate of 1 ml min⁻¹. The fluorescence intensity at the emission maximum of the deprotonated species was recorded in 1 min intervals after 2 h, 4 h, 6 h, 24 h and 48 h. After 6 h the leaching of indicator was almost linear with time for both sensor types. A leaching rate was determined from the fluorescence intensity decrease in percent in the time interval between 24 h and 48 h. It was -0.24 %/h for the M1_DHFA membrane and -0.18 %/h for M1_DHFAE. Within the first 24 h a stronger leaching of both indicators was observed which results in a signal decrease to 96.2 % (M1_DHFA) and 96.5 % (M1_DHFAE) after 6 h and 91.7 % (M1_DHFA) and 93.8 % (M1_DHFAE) after 24 h, respectively. The pronounced loss of indicator in that time is due to DHCF impurities still present in the indicator which are less lipophilic and to indicator molecules which are only adsorbed to the membrane surface. An improvement should therefore be reached by further purification of the indicator dyes and a preconditioning of the membranes in buffer solution before the measurement. Secondly, M1 membranes were stirred in 80 ml of phosphate buffer solution (pH 8.2, IS = 720 mM) for one week. The absorbance A at the maximum of the deprotonated indicator was measured initially and after this week at pH 10 and pH 8.2. The relation $[1 - \{(A(\text{pH } 10) - A(\text{pH } 8.2))_{7 \text{ days}} / (A(\text{pH } 10) - A(\text{pH } 8.2))_{0 \text{ days}}\}] * 100$ gives the leaching rate over this time in percent. It was 18.1 % for M1_DHFA and 11.2 % for M1_DHFAE, respectively. Both experiments show that the leaching of the indicators from the sensor membrane is relatively high. In case of the M1_DHFAE sensor this indicator loss

is referenced by the ratiometric measurement scheme. The M1_DHFA sensor, however, is limited to short-time pH measurements.

3.4.3. Cross-sensitivity towards ionic strength

The cross-sensitivity of optical pH sensors towards IS originates in the fact that during pH measurements the proton activity of the solution is correlated to the concentration of the respective pH indicator species $c(I^-)$ and $c(HI)$ and not to their activities. Eq. 3.4 can be derived from the mass action law of the indicator reaction. In optical sensing the two terms of eq. 3.4 containing the activity coefficients f_{HI} and f_I of the protonated and deprotonated indicator and the solvent activity a_{H_2O} are not detected. The point of inflection of the sigmoidal calibration curve in optical pH measurement is therefore only an apparent pK_a value (pK_a') which includes these two terms.

$$pH = pKa + \lg \frac{c(I^-)}{c(HI)} + \lg \frac{f_I}{f_{HI}} - \lg a_{H_2O} = pKa' + \lg \frac{c(I^-)}{c(HI)} \quad (3.4)$$

While the logarithm of the solvent activity is negligible in aqueous solutions with an IS up to 4 M, the activity coefficients f_{HI} and f_I of the protonated and deprotonated indicator species tend to unity only in very diluted solutions which is not given in seawater samples. The Debye-Hueckel theory relates the activity coefficients to the IS of the solution³¹. The IS in the microenvironment of the indicator is determined by the concentration and charge of the dissolved ions and the indicator molecule itself. Fixed charges in the immediate vicinity of the indicator like charges immobilised in the polymer matrix of the sensor also contribute to the IS and therefore cause a change of the pH within the membrane compared to that of the bulk solution³². This change is quantified by the surface potential of the matrix. To reduce these disturbing effects an uncharged hydrogel with a high water uptake capacity was employed as sensor matrix in this work. Hence, the bulk and inner-membrane pH was considered to be the same and any IS effects were contributed to the IS of the analyte solutions.

The average IS of open sea water is 720 mM which corresponds to a salinity of 35 ‰. The salinity is the amount of inorganic substance in solution expressed in g per kg seawater or in parts per thousands (‰). Since the relative composition of the seawater salt is constant, the salinity of seawater is only influenced by the water content. Thus, it can increase to > 40 ‰ due to water evaporation (e.g. Mediterranean sea) or decrease to < 2.5 ‰ because of fresh

water influx in brackish water regions. The correlation between salinity S and IS of seawater is given by $IS = 19.92 * S / (1000 - 1.005 * S)^{33}$ (Fig. 3.4).

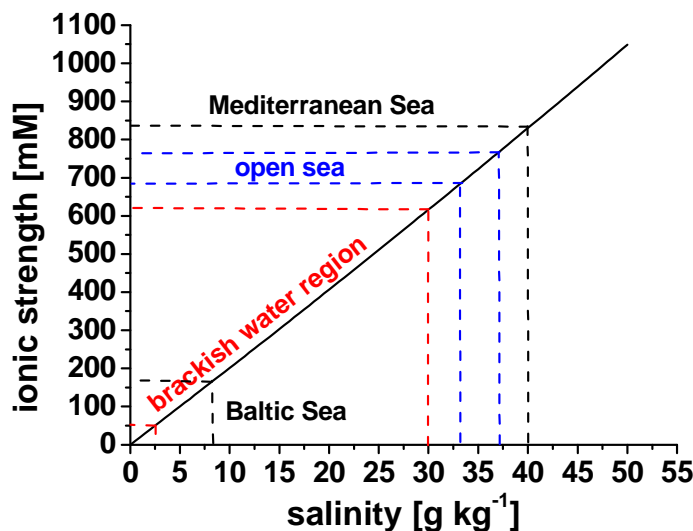


Fig. 3.4. Ionic strength-salinity correlation plot; given ionic strength and salinity values are average values for the respective area.

The cross-sensitivity of the sensor response of M1_DHFA and M1_DHFAE towards IS was investigated in an IS range from 50 mM to 720 mM with two different buffer systems. Phosphate buffers with a buffer concentration of 15 mM and an IS of 100 mM, 200 mM, 300 mM and 500 mM with sodium chloride as background electrolyte were used for a first sensor calibration. A second sensor calibration was made with 15 mM TRIS buffers and artificial seawater (ASW) as background electrolyte. Here the IS was adjusted to 50 mM, 200 mM, 500 mM and 720 mM. Fig. 3.5 depicts the calibration curves of M1_DHFA (left) and M1_DHFAE (right) measured with the TRIS/ASW buffers. The IS effect is almost negligible for M1_DHFAE. The reason for the difference in IS cross-sensitivity of the two sensors is the additional negative charge at the 2-carboxyl group in the basic form of DHFA. For measurements in marine environment a sensor accuracy of 0.02 pH units is desirable.

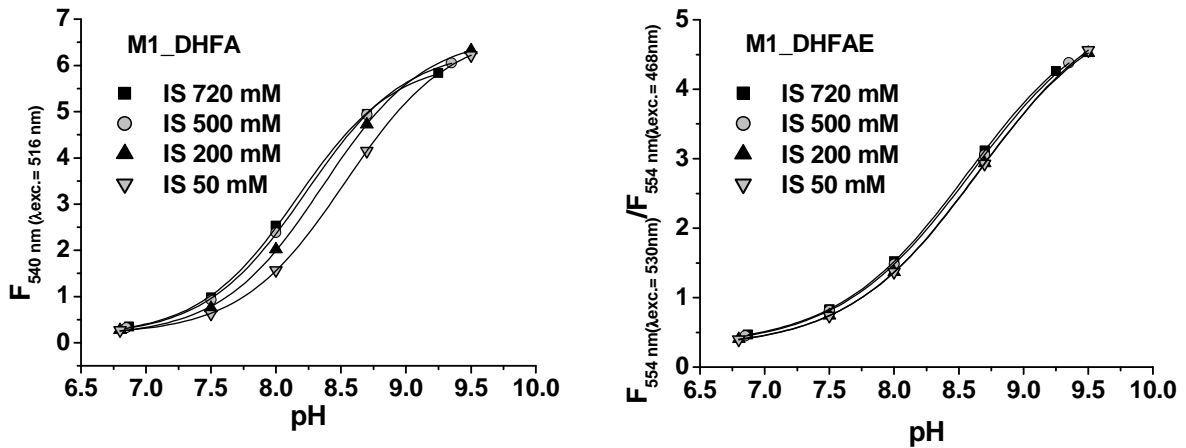


Fig. 3.5. Calibration curves of M1_DHFA (**left**) and M1_DHFAE (**right**) measured with 15 mM TRIS buffer solutions with artificial seawater as background electrolyte and IS values varying from 50 mM to 720 mM.

Fig. 3.5 shows that the IS effect on the calibration curves of both sensors is minimal at IS values higher than 500 mM. $\Delta\text{pH}/\Delta\text{IS}$ gradients determined from the maximum error in the measured pH ($\Delta_{\text{max}}\text{pH}$) due to an IS change from 720 mM to 200 mM at pH 8 allow for the calculation of $\Delta_{\text{max}}\text{pH}$ at pH 8 in open sea measurements. Here the IS ranges between 765 mM and 680 mM. A shift between those boundaries results in a $\Delta_{\text{max}}\text{pH}$ of 0.02 for M1_DHFA and 0.01 for M1_DHFAE which is within the limits of the measurements precision. Thus, in open sea water both sensors can be used without signal correction for the IS effect. The IS of brackish water can strongly fluctuate in a range from 720 mM to 50 mM. The $\Delta_{\text{max}}\text{pH}$ caused by this IS change at pH values from 7.5 to 8.5 were as follows: $\Delta_{\text{max}}\text{pH}$ (pH 7.5) = 0.26 / 0.1, $\Delta_{\text{max}}\text{pH}$ (pH 8) = 0.29 / 0.09 and $\Delta_{\text{max}}\text{pH}$ (pH 8.5) = 0.26 / 0.08 for M1_DHFA and M1_DHFAE, respectively. Calibration measurements with the phosphate/NaCl buffer solutions (data not shown) gave comparable results. Whereas an error of almost 0.3 pH units found for M1_DHFA is not acceptable, M1_DHFAE can be used in brackish water without further signal correction for measurements where a sensor accuracy of 0.1 pH units is sufficient. In case that a more precise pH detection is required, a parallel determination of the IS by conductivity measurement or by an optical salinity sensor¹¹ is necessary. However, there is no need for high precision in this IS determination since an IS error of 100 mM only causes a $\Delta_{\text{max}}\text{pH}$ of 0.015 pH units within the pH range from 7.5 to 9. In comparison with pH electrodes the investigated optical sensors show a similar measurement precision in open sea application. Due to the necessity of signal correction in brackish water for the optical sensors, the performance of pH electrodes might be here slightly better. However, conventional glass

electrodes show a cross-sensitivity towards sodium at pH values higher than 9. The pH at which a significant sodium error occurs can be shifted to higher values (> 10 pH) by the choice of appropriate glass materials for the electrode. The pKa' values found for M1_DHFA and M1_DHFAE at varying IS with the two buffer systems are summarised in Table 3.3. With decreasing IS the pKa' tends to increase for both sensors. It can also be seen that the pKa' values differ between the two buffer systems with an average of 0.17 units. In the case of M1_DHFA the pKa' values were lower in TRIS/ASW buffer solutions than in phosphate/NaCl buffer solutions. For M1_DHFAE the tendency was vice versa. This can be due to a quenching effect by the TRIS buffer salt which is in its deprotonated form a tertiary amine.

Table 3.3. pKa' values of M1_DHFA and M1_DHFAE at varying IS (or salinity S).

IS [mM] pKa'	720 (35 ‰ S)	500 (24.5 ‰ S)	300 (15 ‰ S)	200 (10 ‰ S)	100 (5 ‰ S)	50 (2.5 ‰ S)
(M1_DHFA) ^(a)	n.d.	8.42	8.45	8.51	8.57	n.d.
(M1_DHFA) ^(b)	8.16	8.23	n.d.	8.36	n.d.	8.53
(M1_DHFAE) ^(a)	n.d.	8.42	8.44	8.48	8.47	n.d.
(M1_DHFAE) ^(b)	8.57	8.60	n.d.	8.64	n.d.	8.66

(a) 15 mM phosphate buffer solutions with NaCl as background electrolyte

(b) 15 mM TRIS buffer solutions with artificial seawater as background electrolyte

3.4.4. Temperature effect

The temperature of the oceans' surface seawater is exclusively determined by the daily amount of sun light and the angle in which the sun rays hit the water. Thus, the average surface water temperature in regions near the equator can be as high as +30 °C while it declines towards the poles where water temperatures down to -2 °C are possible. The water of the deep sea has a considerably constant temperature. Here temperature zones between +5 °C and -2 °C are found since the density of seawater is not only dependent on the temperature but also on the salinity. Hence, strong temperature changes within the water column can occur with varying depth especially at mid-latitudes.

The temperature cross-sensitivity of M1_DHFA and M1_DHFAE was quantified from +4 °C to +35 °C and is shown in Fig. 3.6. Temperature affects the sensor signal in two different ways. Firstly, the luminescence quantum yield of the protonated and deprotonated

form of the indicator drops with increasing temperature due to enhanced internal and external conversion. Secondly, the pKa' values of the indicators increase with increasing temperature.

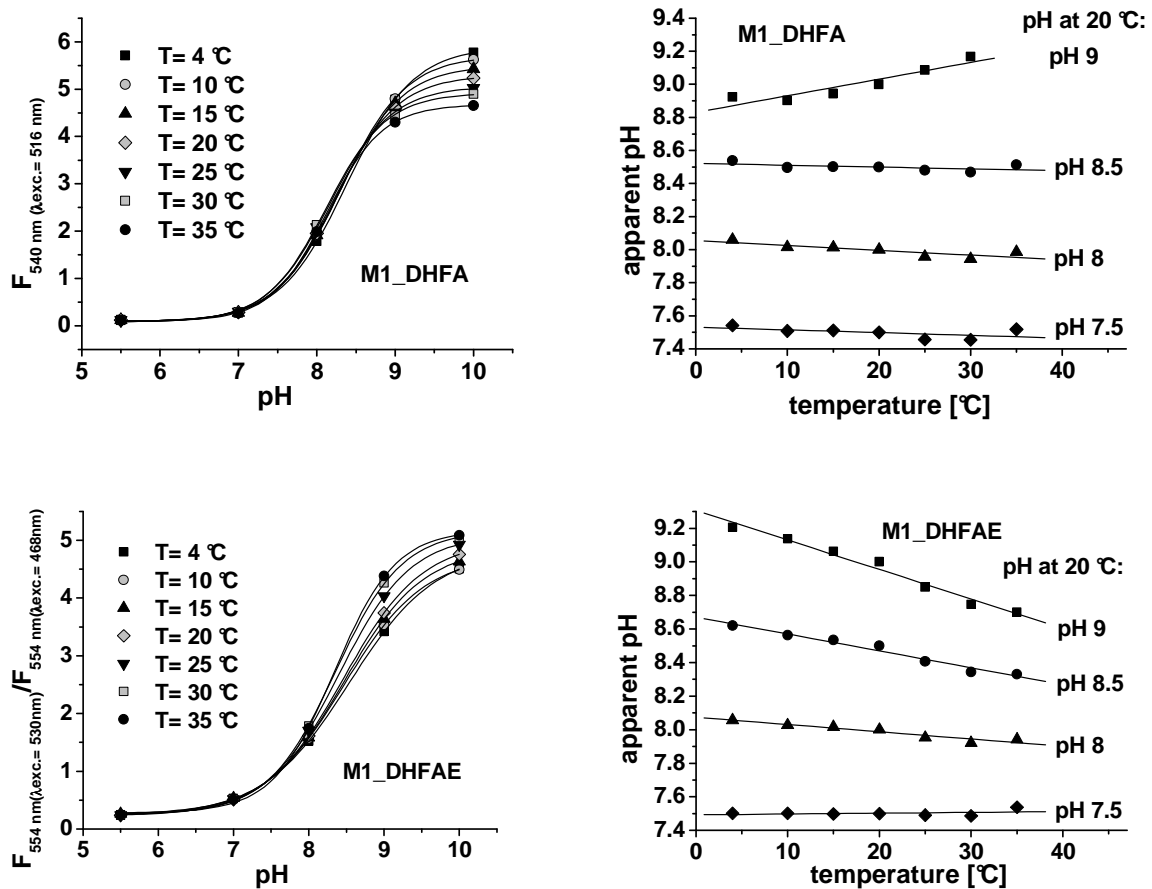


Fig. 3.6. left: Temperature dependent calibration curves of M1_DHFA (**top**) and M1_DHFAE (**bottom**); **right:** Measured sensor signals in the pH range from 7.5 to 9 at 20 °C were used to calculate the apparent pH values at the other temperatures. Linear regressions gave the following $\Delta\text{pH}/\Delta\text{T}$ gradients: -0.0017 (pH 7.5), -0.003 (pH 8), -0.0011 (pH 8.5) and 0.0101 (pH 9) for M1_DHFA (**top**) and 0.0005 (pH 7.5), -0.0043 (pH 8), -0.01 (pH 8.5) and -0.0176 (pH 9) for M1_DHFAE (**bottom**).

The temperature-dependent calibration curves of M1_DHFA show that here both effects compensate up to pH 8.5. At higher pH values internal and external conversion become predominant (Fig. 3.6, top). For M1_DHFAE sensors the temperature effect is only negligible up to pH 8 since here internal and external conversion influence also the fluorescence intensity of the protonated form of the indicator (Fig. 3.6, bottom). The gradients $\Delta\text{pH}/\Delta\text{T}$ determined at pH 8 (Fig. 3.6, right) are -0.003 for M1_DHFA and -0.0043 for M1_DHFAE. Here a temperature correction is not necessary up to a temperature variation of 5 °C. This is normally given for measurements in the same water layer. In applications at different

positions of the water column strong temperature changes can occur which make a signal correction inevitable. However, even at higher pH values the cross-sensitivity of the two optical sensors towards temperature is definitely lower than that of conventional pH electrodes. The main influence due to temperature variation can be calculated from the Nernst equation. The pH error is in the order of 0.03 pH units per °C.

3.4.5. pH sensors for DLR-based referencing schemes

Luminescence intensity-based optical sensing techniques are often disturbed by fluctuations in the opto-electronic system (e.g. light source, detection system), degradation of the sensor element (e.g. caused by indicator loss due to leaching or photodecomposition) or variable optical properties of the sample (e.g. scattering). Thus, a careful referencing of the sensor signal is essential to obtain reliable results. Sensors based on DHFAE described here allow the use of ratiometric referencing methods (either with dual excitation or emission) as shown before. Unfortunately, sensors based on DHFA are not suitable for these methods since the protonated form is non-luminescent due to lactonisation. For such sensors the fd-DLR scheme³⁴ is the solution of choice (see chapter 1.5.3). The ruthenium(II) tris(4,7-diphenyl-1,10-phenanthroline) complex was used as reference standard. Incorporated into polyacrylonitrile-derived nanospheres (average particle diameter: 70 nm), it is efficiently shielded from external quenching by oxygen and other compounds. The reference standard is excitable in the range from 400 nm to 510 nm and shows a broad emission with a maximum around 600 nm. Since its decay time is approx. 6 μ s a modulation frequency of 45 kHz was selected. Spectral properties of the reference-DHFA couple in the M2 membrane are shown in Fig. 3.7 (left).

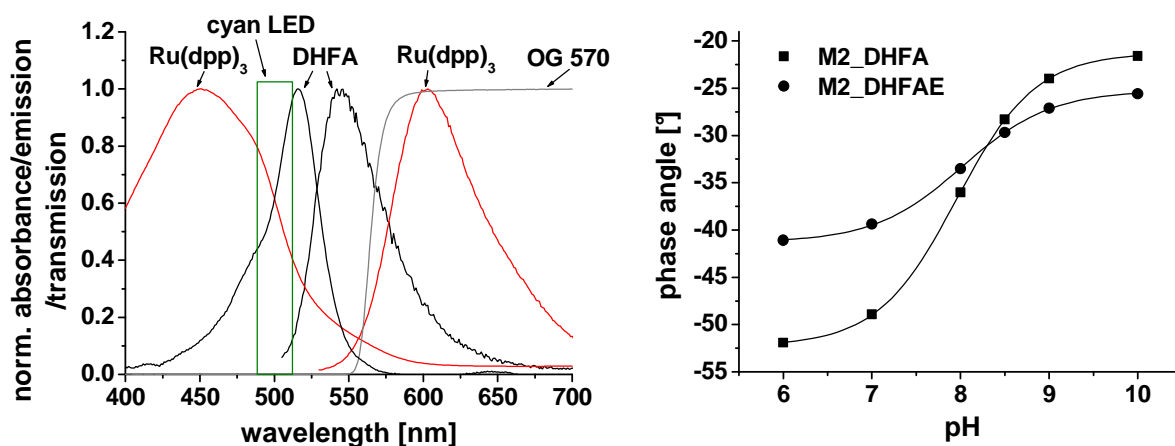


Fig. 3.7. Spectral properties of the dyes and optical components in the DLR measurement schemes with DHFA as pH indicator; the absorbance and emission spectra of Ru(dpp)₃ and DHFA and the transmission spectrum of the long pass filter OG 570 for the emission path are shown. All spectra are normalised. The excitation wavelength range emitted by the cyan LED equipped with the filter combination of the excitation path is plotted schematically (**left**); calibration curves of M2_DHFA and M2_DHFAE measured with the phase-modulation method; the sensor dynamic of M2_DHFAE is by a factor of approx. 2 lower than that of M2_DHFA (**right**).

One can see that the cyan LED ($\lambda_{em.} = 505 \text{ nm}$) is the best compromise for the simultaneous excitation of both luminophores. The 570 nm long-pass filter on the emission side allows the simultaneous detection of the two signal components. The same optical set-up is suitable for M2 sensors based on DHFAE as indicator. Fig. 3.7 (right) depicts the pH-dependent phase shifts of the two DLR sensors M2_DHFA and M2_DHFAE. Phase resolution in the most relevant pH interval between pH 7.5 and pH 8.5 was $13.6^\circ/\text{pH}$ and $6.4^\circ/\text{pH}$ for M2_DHFA and M2_DHFAE, respectively. The about twice higher resolution of M2_DHFA is caused by the higher dynamic in the fluorescence intensity signal as shown in Fig. 3.2. Whereas DHFA is non-fluorescent in the protonated form, DHFAE shows still a significant emission. A higher resolution for this sensor could be obtained by using the green emitting 530 nm LED. However, this results in a rather poor excitation of the reference.

DLR can not only be performed in the frequency domain but also in the time domain as shown by Liebsch et al.⁸. td-DLR is the method of choice for using the sensors described here for imaging of pH (see chapter 1.6.2). Fig. 3.8 (top, left) depicts the 2D greyscale plots of the ratiometric images of M2_DHFA taken at pH 5.5 and pH 10. They give a good impression of the spatial homogeneity of the referenced sensor signal. The calibration curve of M2_DHFA is shown in Fig. 3.8 (top, right). The plotted R values were obtained by averaging the mean values of six randomly chosen 10 x 10 pixel areas of the ratiometric image. The

error bars represent the standard deviation of the mean values ($< \pm 1.3\%$). The pK_a' value of the td-DLR membrane was found to be 8.27 ± 0.03 .

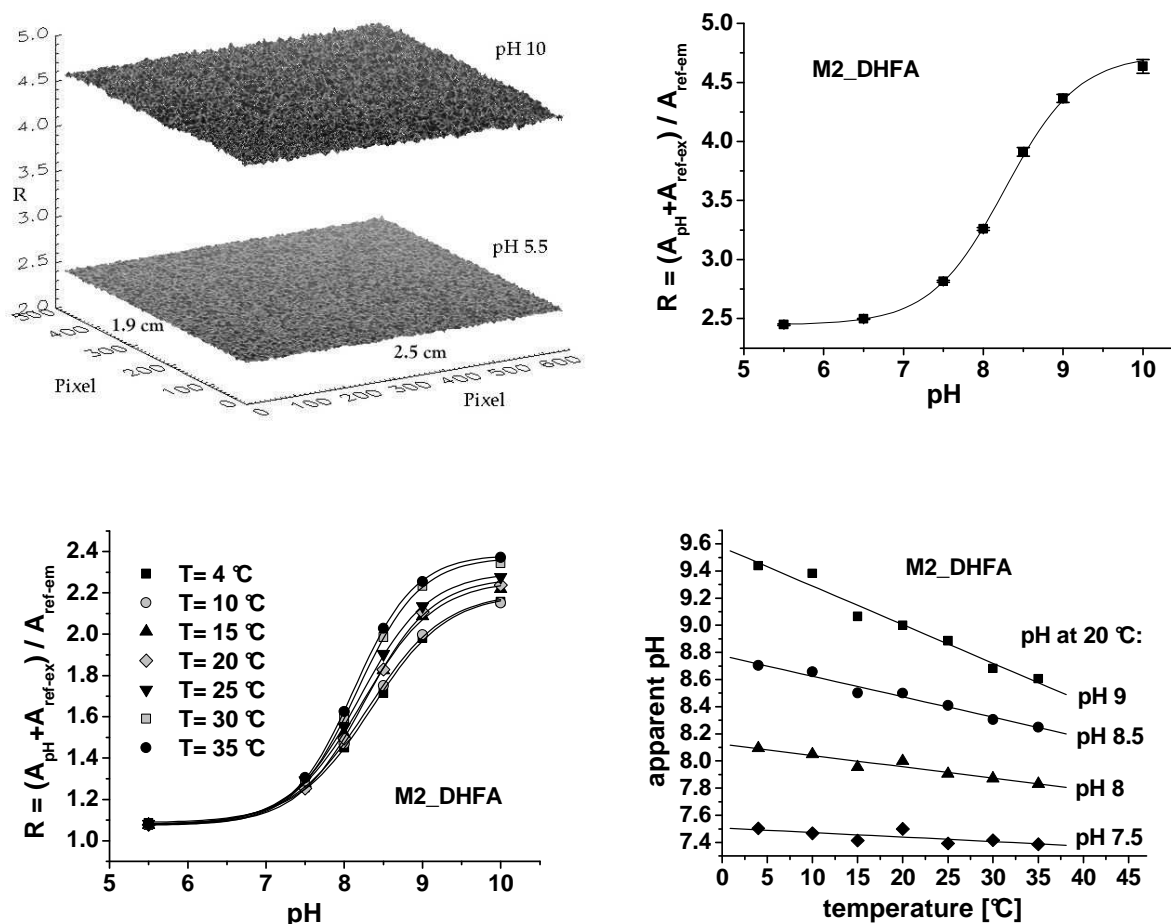


Fig. 3.8. top, left: Images of the M2_DHFA membrane at pH 5.5 and pH 10 referenced with the td-DLR scheme; top, right: Calibration curve of M2_DHFA recorded in a td-DLR pH imaging scheme; bottom, left: Calibration curves of M2_DHFA at varying temperatures; the increased cross-sensitivity of the DHFA based DLR sensor towards temperature is due to the high temperature effect on the signal of the reference dye; bottom, right: plots of the apparent pH (calculated from R values in the pH range from 7.5 to 9 at 20 °C) versus temperature; the $\Delta pH/\Delta T$ gradients determined from linear regression were -0.0033 (pH 7.5), -0.0084 (pH 8), -0.0151 (pH 8.5) and -0.0285 (pH 9).

Temperature cross-sensitivity of M2_DHFA was tested from +4 °C to +35 °C. The calibration curves depicted in Fig. 3.8 (bottom, left) show that the overall signal R increases with increasing temperature over the whole measured pH range. The temperature-caused pH error here becomes already significant at pH values higher than 7.5 (bottom, right). The reason is the strong effect of temperature on the quantum yield of the reference dye. The lifetime decrease of the reference standard with increasing temperature was determined and the

gradient $\Delta\tau/\Delta T$ was found to be $-0.022 \mu\text{s K}^{-1}$ within the considered temperature range. Thus, the decrease of the denominator in eq. 1.11 is the dominant effect on the measured signal R.

3.4.6. pH measurements in natural marine sediment using the M2_DHFAE sensor³⁵

Time series of calibrated pH images were recorded in a natural sediment sample using a M2_DHFAE sensor membrane. The obtained images expressed a marked spatio-temporal variability in the pH distribution across the sediment-water interface (Fig. 3.9). The first image (Fig. 3.9 A) was taken after 10 min of light exposure (after the dark phase of the artificial 12 h day/night cycle) and displayed a significant variation in pH. Overall the surface sediment expressed a strong pH gradient declining from 8.1 to 7.5 - 7.2 at a subsurface minimum at 3 - 5 mm sediment depth, indicative of an intense reoxidation of anaerobic metabolites close to the oxic-anoxic interface³⁶. In the deeper sediment layers the pH increased to around 7.8 which is typical for sediments with an intense anaerobic heterotrophic activity. One inhabited burrow of the polychaete *Hediste diversicolor* is visible and active ventilation of the burrow from the right hand side induce a pH from ca. 8.1 to ca. 7.8 at the ejection, left hand side. As a consequence a plume of water presumably suboxic and with a lower pH emerge to the overlying water above the left hand side burrow. However, it must be noted that rapid fluctuations in the pH, caused by e.g. bioirrigation events, might be underestimated by our measurements due to the relatively slow sensor response. The pH minimum zone along the primary interface extends along the burrow wall reflecting how bioirrigation activity stimulates oxidation of reduced solutes and solids along the burrow lining. The deeper pH minimum zone (pH ca. 7.2) observed in the left hand side of the images indicates a local hotspot of intensified activity. Furthermore, clearly well-defined microniches with relative low pH were visible in different sections of the sediment (Fig. 3.9 D). After the light exposure prolonged benthic photosynthesis gradually increased the pH to > 8.6 along the interface (Fig. 3.9 B - D). The heterogeneous pH distribution reflected an uneven distribution of the microphytobenthic biomass.

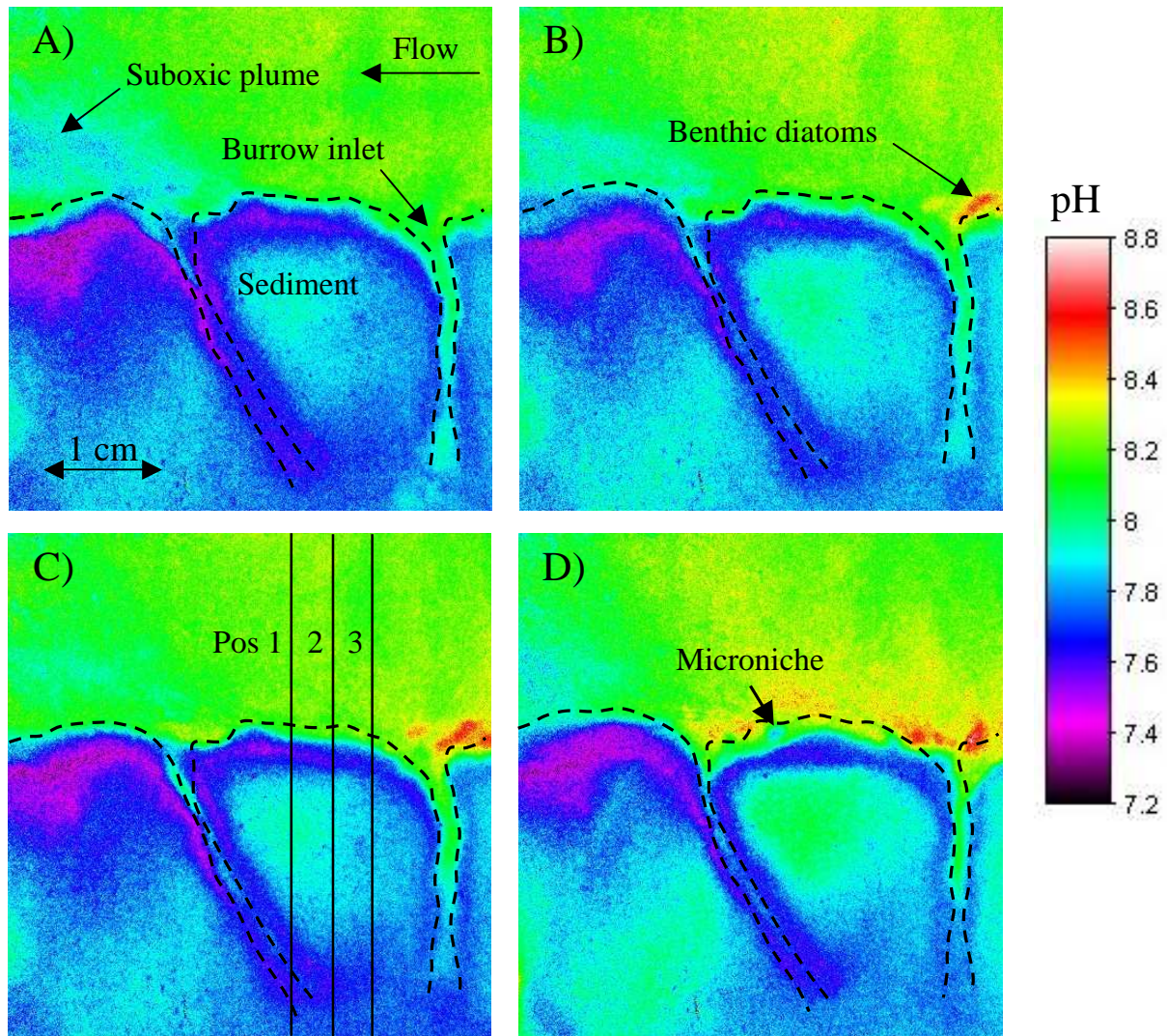


Fig. 3.9. Time series of pH images (A=8:32, B=9:02, C=9:22, D=12:35 h) taken after the light was turned on. They show the temporal dynamics in the two-dimensional distribution patterns of pH. The surface area of each image is 21 cm². Dotted lines indicate the relative position of the visually determined sediment surface and burrow linings. Vertical solid lines in image C, indicate the positions (1, 2, 3) where image profiles (i.e. single row of pixels) and microelectrode profiles were extracted (depicted in Fig. 3.10 and 3.11).

Over time the photosynthesis enhanced the pH in the water close to the interface and shifted the redox boundary layer (i.e. the pH minimum zone) downward. This temporal pH dynamic is also illustrated by 3 single pH profiles, extracted from the same position at the same time, in the planar optode images during the day (Fig. 3.10).

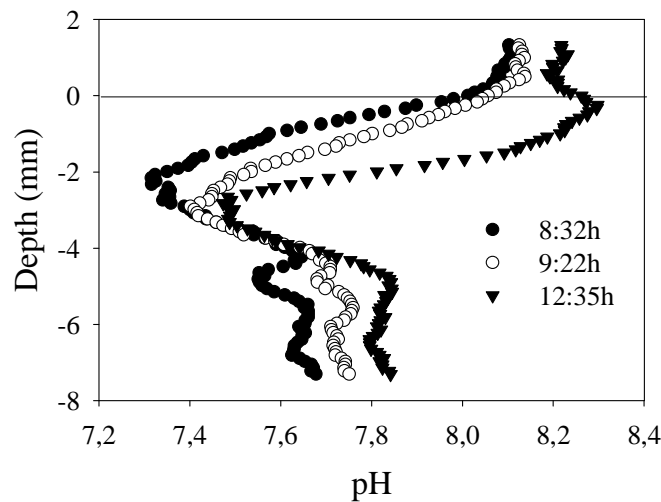


Fig. 3.10. Time series of extracted vertical profiles across the sediment water-interface, from the same position (pos 2) in the planar optode image (8:32 h: after 12 h in darkness, 9:22 h: after ca. 1 h in light; 12:35 h: after ca. 4 h in light). Profiles were smoothed by running average ($n=10$).

These profiles clearly show a temporal response in the pH distribution induced by the gradual CO_2 consumption. For comparison, single vertical pH profiles, extracted from the pH images were aligned with pH microelectrode profiles measured at 2 mm distance in front of the planar optode at position 1 and 3 (Fig. 3.11). Given the microscale heterogeneity, the electrode profile closely resembles the profiles extracted from the planar optode images.

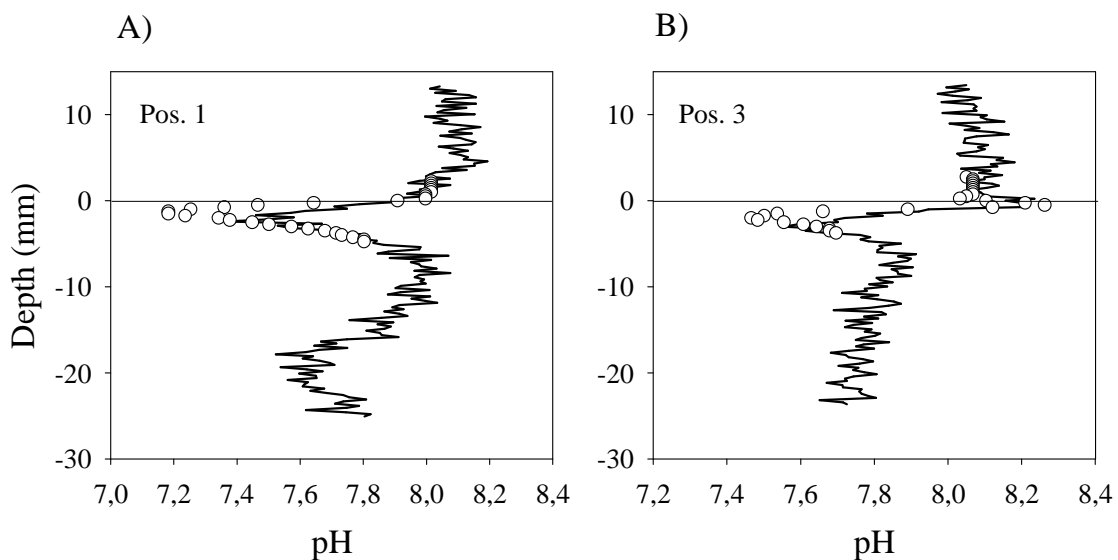


Fig. 3.11. Extracted vertical pH profiles from the planar optode images (solid line, no smoothing) vs. pH profiles obtained with microelectrodes (open circles) 2 mm in front of the planar sensor. Graph A corresponds to position 1 in the first image (Fig. 3.9 A) and graph B to position 3 in the last image (Fig. 3.9 D), respectively.

During a 24 h cycle the pH varied from ca. 7.3 (during night time) to > 8.8 along the sediment water interface (Fig. 3.12. A and B). The strong diurnal variation in the benthic pH shifted the overall pH value in the overlying water from ca. pH 7.8 during the night time to a maximum of ca. 8.3 during the day. This diurnal pH variation in the overlying water also was reflected deep down in the sediment as the polychaete continuously ventilated the burrow.

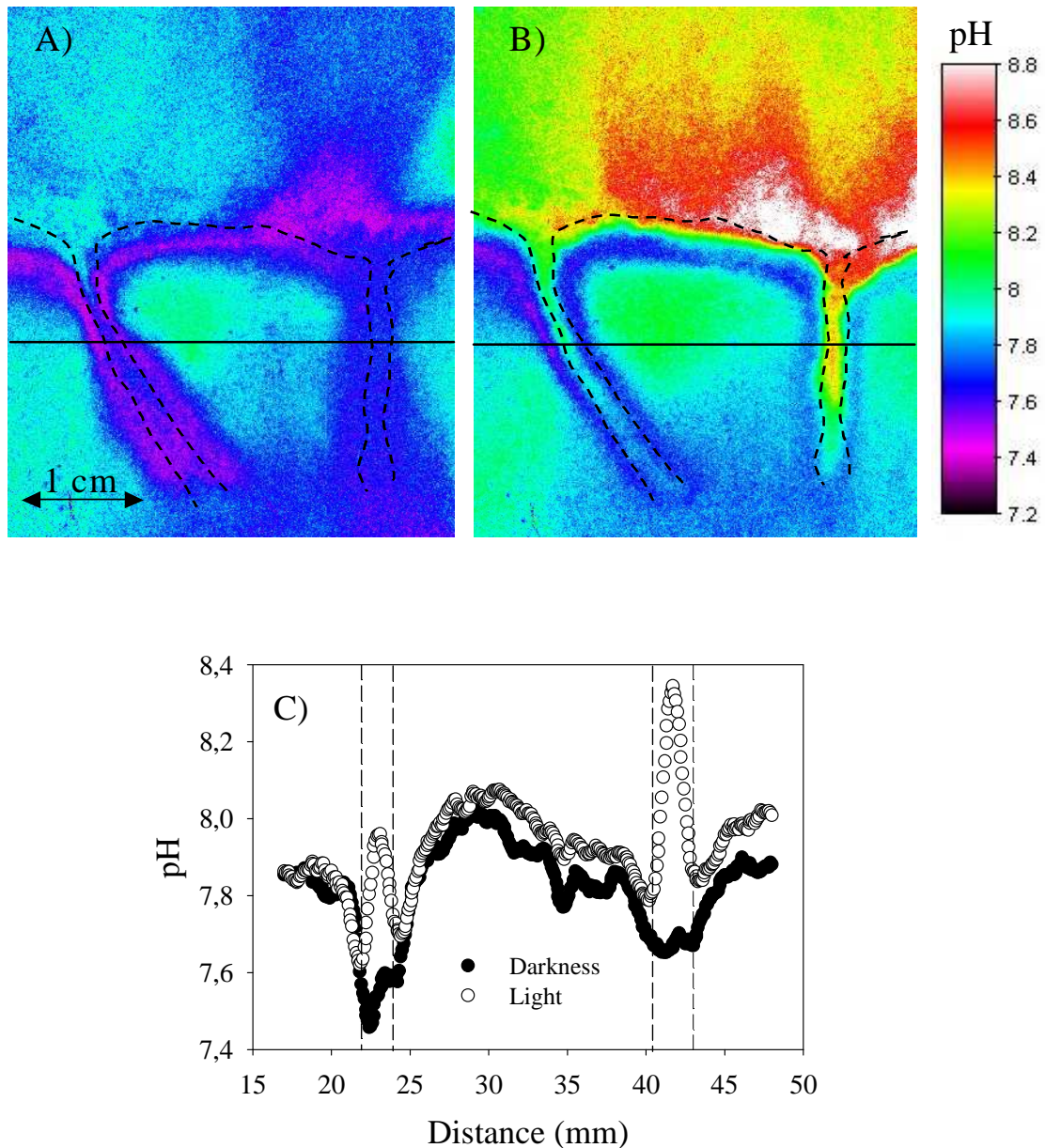


Fig. 3.12. A and B: Corresponding pH images showing the two-dimensional pH distribution across the sediment water interface after 12 h in darkness and at maximum photosynthetic activity in the afternoon. Horizontal solid lines show the position of the extracted profiles (ca. 1.5 cm depth) displayed in graph C. **C:** Horizontally extracted day/night profiles (open/black circles) across the burrow lumens and in the sediment. Dotted lines indicate the walls of the burrow lumens. Profiles were smoothed by running average ($n=10$).

Extracted horizontal profiles across the lumen of the two burrows showed a significant variation (> 0.6 pH units) between day and night at the same depth (ca. 1.5 cm) in the sediment (Fig. 3.12. C). In both instances the pH along the borrow wall clearly indicated a local minimum reflecting intensified reoxidation activity along the burrow.

3.5 Conclusion

Novel pH sensors specially designed for use in marine environment and based on lipophilic 2',7'-dihexylcarboxyfluorescein derivatives were presented. The lipophilic indicator dyes can be prepared in a straightforward synthesis with adequate yields. Physically entrapped in a polyurethane hydrogel, they have a dynamic range which perfectly matches the requirements for optical pH sensing in marine systems. The cross-sensitivity towards IS is almost negligible for M1_DHFAE membranes. Thus, the utilisation of these sensors in brackish water regions with an IS down to 50 mM is possible. The DHFA-containing sensors show a stronger IS effect due to the additional anionic charge of the dye and are therefore more useful for open sea measurements where the IS is high and nearly constant. The temperature cross-sensitivity was found to be small for both M1 sensors. Especially for M1_DHFA it is almost negligible between pH 7.5 and pH 8.5. Compared to conventional pH electrodes both sensors show a similar accuracy and performance. The influence of temperature on the optodes is even lower. Especially in deep sea measurements the monolithic optical sensors might be superior to electrodes because of the high hydrostatic pressure. However, the optodes were not yet characterised under these conditions which requires access to appropriate pressure tanks. Due to the photo-physical properties of DHFA and DHFAE different referenced measurement schemes are accessible. Ratiometric dual wavelength measurements (dual excitation as well as dual emission) is possible with DHFAE-containing sensors. Furthermore, both sensors are suitable for DLR measurements with $\text{Ru}(\text{dpp})_3$ particles as reference standard. Here DHFA-containing DLR sensors show a higher sensor dynamic than those incorporating DHFAE. However, summarising all characteristics, DHFAE-based sensors are superior for marine application due to their optimal dynamic range combined with the smallest IS effect and the lowest indicator loss caused by leaching. Therefore, the DHFAE-incorporating DLR sensor was chosen for time-resolved imaging of pH in a natural marine sediment sample. pH maps were obtained, which visualise the two-dimensional heterogeneities within the observed sediment intersection with a high spatial resolution (ca. $83 \times 83 \mu\text{m}^2/\text{pixel}$). Nevertheless, the

response time of the pH optode (2 - 4 min.) has to be taken into account when correlating the measured pH values with the investigated processes. Whereas slower processes such as the shift of the redox boundary layer due to the diurnal variation of benthic photosynthesis activity can be correctly monitored, fast dynamic changes within the sediment e.g., due to animal activities give only average pH values over the sensor response time. However, the recorded pH maps allow to localise regions of interest and to interrelate the single events (e.g., bioirrigation by a burrowing animal → anoxic plume at the seawater-sediment interface). They give therefore a valuable insight into the complex biogeochemical processes within marine sediments. The pH values acquired with the optical sensor were in good agreement with the pH values measured in parallel with the pH glass microelectrode.

3.6 References

- [1] Koehler-Rink S., Kuehl M., *Microsensor studies of photosynthesis and respiration in larger symbiotic foraminifera. I The physico-chemical microenvironment of Marginopora vertebralis, Amphistegina lobifera and Amphisorus hemprichii.* Marine Biology (2000), 137, 473 - 486.
- [2] Reimers C. E., Ruttenger K. C., Canfield D. E., Christiansen M. B., Martin J. B., *Porewater pH and authigenic phases formed in the uppermost sediments of the Santa Barbara Basin.* Geochim. Cosmochim. Acta (1996), 60, 4037 - 4057.
- [3] Joergensen B. B., Revsbech N. P., *Colorless Sulfur Bacteria, Beggiatoa spp. and Thiouvulum spp., in O₂ and H₂S Microgradients.* Appl. Environ. Microbiol. (1983), 45, 1261 - 1270.
- [4] Wenzhoefer F., Adler M., Kohls O., Hensen C., Strotmann B., Boehme S., Schulz H. D., *Calcite dissolution driven by benthic mineralization in the deep-sea: In situ measurements of Ca²⁺, pH, pCO₂ and O₂.* Geochim. Cosmochim. Acta (2001), 65, 2677 - 2690.
- [5] McCulloch S., Uttamchandani D., *Development of a fibre optic micro-optode for intracellular pH measurements.* IEEE Proc. Optoelectronics (1997), 144, 162 - 167.
- [6] Song A., Parus S., Kopelman R., *High-Performance Fiber-Optic pH Microsensors for Practical Physiological Measurements Using a Dual-Emission Sensitive Dye.* Anal. Chem. (1997), 69, 863 - 867.
- [7] Walt D. R., *Fiber Optic Imaging Sensors.* Acc. Chem. Res. (1998), 31, 267 - 278.

- [8] Liebsch G., Klimant I., Krause C., Wolfbeis O. S., *Fluorescent Imaging of pH with Optical Sensors Using Time Domain Dual Lifetime Referencing*. Anal. Chem. (2001), 73, 4354 - 4363.
- [9] Klimant I., Kuehl M., Glud R. N., Holst G., *Optical measurement of oxygen and temperature in microscale: Strategies and biological applications*. Sens. Actuators, B (1997), 38, 29 - 37.
- [10] Wolfbeis O. S., *Fiber Optic Chemical Sensors and Biosensors*. CRC Press, Boca Raton, FL, vol.1 (1991).
- [11] Huber C., Klimant I., Krause C., Werner T., Mayr T., Wolfbeis O. S., *Optical sensor for seawater salinity*. Fresenius' J. Anal. Chem. (2000), 368, 196 - 202.
- [12] Mordon S., Devoisselle J. M., Soulie S., *Fluorescence spectroscopy of pH in vivo using a dual-emission fluorophore (C-SNAFL-1)*. J. Photochem. Photobiol. B: Biol. (1995), 28, 19 - 23.
- [13] Leiner M. J. P., *Optical sensors for in vitro blood gas analysis*. Sens. Actuators, B (1995), 29, 169 - 173.
- [14] Bellerby R. G. J., Olsen A., Johannessen T., Croot P., *A high precision spectrophotometric method for on-line shipboard seawater pH measurements: the automated marine pH sensor (AMpS)*. Talanta (2002), 56, 61 - 69.
- [15] Martz T. R., Carr J. J., French C. R., DeGrandpre M. D., *A Submersible Autonomous Sensor for Spectrophotometric pH Measurements of Natural Waters*. Anal. Chem. (2003), 75, 1844 - 1850.
- [16] Serra G., Schirone A., Boniforti R., *Fiber-optic pH sensor for seawater monitoring using a single dye*. Anal. Chim. Acta (1990), 232, 337 - 344.
- [17] Hulth S., Aller R. C., Engstrom P., Selander E., *A pH plate fluorosensor (optode) for early diagenetic studies of marine sediments*. Limnol. Oceanogr. (2002), 47, 212 - 220.
- [18] Opitz N., Luebbers D. W., *New fluorescence photometrical techniques for simultaneous and continuous measurements of ionic strength and hydrogen ion activities*. Sens. Actuators, B (1983), 4, 473 - 479.
- [19] Whitaker J. E., Haugland R. P., Prendergast F. G., *Spectral and photophysical studies of benzo[c]xanthene dyes: dual emission pH sensors*. Anal. Biochem. (1991), 194, 330 - 344.

- [20] Parker J. W., Laksin O., Yu C., Lau M. L., Klima S., Fisher R., Scott I., Atwater B. W., *Fiber-optic sensors for pH and carbon dioxide using a self-referencing dye*. Anal. Chem. (1993), 65, 2329 - 2334.
- [21] Weidgans B. M., Krause C., Klimant I., Wolfbeis O. S., *Fluorescent pH sensors with negligible sensitivity to ionic strength*. Analyst (UK) (2004), 129, 645 - 650.
- [22] Kester D. R., Duedall I. W., Connors D. N., Pytkowicz R. M., *Preparation of Artificial Seawater*. Limnol. Oceanogr. (1967), 12, 176 - 179.
- [23] Stahl H., Glud A., Schroeder C. R., Klimant I., Tengberg A., Glud R. N., *Time-resolved pH imaging in marine sediments with a luminescent planar optode*. Limnol. Oceanogr.: Methods, in press.
- [24] Wenzhöfer F., Glud R. N., *Small-scale spatial and temporal variability in coastal benthic O₂ dynamics: Effects of fauna activity*. Limnol. Oceanogr. (2004), 49, 1471 - 1481.
- [25] Revsbech N. P., Jorgensen B. B., *Microelectrodes - Their use in microbial ecology*. Adv. Micr. Ecol. (1986), 9, 293 - 352.
- [26] Matray T., Hernandez V., Singh S., *Electrophoretic tag reagents comprising fluorescent compounds*. U.S. Pat. Appl. Publ. 20020146726 (2002).
- [27] Wang E., Wang G., Ma L., Stivanello C. M., Lam S., Patel H., *Optical films for protamine detection with lipophilic dichlorofluorescein derivatives*. Anal. Chim. Acta (1996), 334, 139 - 147.
- [28] Data Table – 20.2 Probes useful at near neutral pH, <http://www.probes.com/servlets/datatable?item=194&id=28859>, Nov. 30, 2004
- [29] Seybold P. G., Gouterman M., Callis J., *Calorimetric, photometric, and lifetime determinations of fluorescence yields of fluorescein dyes*. Photochem. Photobiol. (1969), 9, 229 - 242.
- [30] Crosby G. A., Demas J. N., *Measurement of photoluminescence quantum yields. Review*. J. Phys. Chem. (1971), 75, 991 - 1024.
- [31] Janata J., *Do optical sensors really measure pH?* Anal. Chem. (1987), 59, 1351 - 1356.
- [32] Agi Y., Walt D. R., *Fluorescence monitoring of the microenvironmental pH of highly charged polymers*. J. Polym. Sci., A (1997), 35, 2105 - 2110.
- [33] Millero F. J., *Thermodynamics of the carbon dioxide system in the oceans*. Geochim. Cosmochim. Acta (1995), 59, 661 - 677.

- [34] Huber C., Klimant I., Krause C., Wolfbeis O. S., *Dual Lifetime Referencing as Applied to a Chloride Optical Sensor*. Anal. Chem. (2001), 73, 2097 - 2103.
- [35] Citation from Ref. 23
- [36] Boudreau B. P., Canfield D. E., *A Provisional Diagenetic Model for pH in Anoxic Porewaters - Application to the Foam Site*. J. Mar. Res. (1988), 46, 429 - 455.

4. Time-resolved Mapping of pH and pO₂ with Luminescent Dual Sensors

A method for combined and intrinsically referenced 2D mapping of pH and pO₂ is described. The experimental set-up comprises a fast gateable CCD camera as detector, a single LED as excitation light source and a hybrid dual sensor membrane as optical transducer. The planar optode incorporates a lipophilic fluorescein derivative (lifetime $\tau \sim 5$ ns) and platinum(II) meso-tetrakis(pentafluorophenyl)-porphyrin (Pt(PFPP)) ($\tau \sim 70$ μ s in the absence of a quencher) immobilised in a hydrogel matrix. Depending on the fluorescent pH indicator, a pH transition in the physiological range (pH 6 - pH 8) or in the near basic region (pH 7 - pH 9) can be achieved. The measurement scheme involves the time-resolved acquisition of images in three windows during a series of square-shaped excitation pulses: one during the light-on intervals, containing the luminescence of both indicators and two during the light-off intervals, containing only the long-lived Pt(PFPP) phosphorescence. A method allowing the calculation of both parameters from these three images is presented. The pH/pO₂ dual sensor incorporating the pH indicator 2',7'-dihexyl-5(6)-N-octadecyl-carboxamidofluorescein (DHFA) is characterised in detail as to its stability and its cross-sensitivity towards ionic strength (IS) and temperature. The sensor was tested for imaging of pH and pO₂ in a natural marine sediment sample.

4.1. Introduction

Simultaneous detection of two or more parameters is a field of growing interest in chemical optical sensor development. Multi-analyte optical sensors have been used for the investigation of samples with homogeneous analyte distribution, e.g., in the clinical field for combined measurements of pH, pO₂ and pCO₂ in blood or tissue¹⁻⁴. These sensors incorporate absorbent or luminescent dyes as indicators and can be regarded as an assembly of single optodes where every optode is addressed separately. Since sensing occurs at different positions, a correlation

of the analyte signals in inhomogeneous samples is feasible only if the sensors are sufficiently miniaturised⁵.

The combination of planar optodes and CCD technology led to a significant improvement in high spatial resolution two-dimensional mapping of single analytes in inhomogeneous samples. This single optode sensor type has been successfully used for gaining insight into 2D distributions and dynamics of pO₂ and pH in marine systems⁶⁻¹³, for non-invasive quantification of oxygen supply in engineered tissues¹⁴ or to visualise airflow patterns in wind tunnel research^{15,16}. Since most geochemical, biological and technical processes involve changes in two or more parameters (e.g., pH, pO₂, pCO₂, Ca²⁺, glucose, temperature), the information provided by a planar single optode may be insufficient to understand these processes and their close spatio-temporal coupling. The combination of planar optodes incorporating luminescent indicators for more than one analyte and the CCD-based imaging technology is therefore a logical step in the development of tools suitable for monitoring of multiple analytes in inhomogeneous systems.

Resolving the signal corresponding to the single analyte from the overall signal of such a sensor becomes increasingly complex with a growing number of target analytes. To date, only optodes for two parameters (= dual optodes) have been reported. Whereat signal resolution is accomplished either spectrally (e.g., by using different emission/excitation filters or excitation light sources) or temporally (taking advantage of different decay times of the applied indicators).

Wolfbeis et al. reported a luminescent pCO₂/pO₂ dual sensor based on a double layer design where the signal of each indicator was detected at different wavelengths¹⁷. Zelelow et. al. described a pO₂/temperature dual optode where a long wave emitting platinum porphyrin and an europium complex were employed as pO₂ and temperature indicators, respectively, and ratiometric intensity measurements with different emission filters were used for quantification of each parameter¹⁸.

Neurauter reported a pCO₂/pO₂ dual sensor where both individual sensors contribute to a single optical signal¹⁹. Frequency domain luminescence phase detection with different modulation frequencies allowed the separation of the oxygen (lifetime) and the carbon dioxide (DLR) signals. The advantage of this concept is a very simple and inexpensive optical set-up (single light source and detector). Using a slightly modified concept Stehning and Holst reported a pO₂/temperature fibre-optic dual sensor incorporating two phosphorescent indicators. With a multifrequency measurement they were able to extract the temperature and the pO₂ information from a rather complex decay behaviour of the overall signal^{20,21}.

The frequency domain detection schemes are optimally suited for the signal readout from single sensor spots. However, their transfer towards imaging applications requires set-ups with expensive image intensifiers^{22,23}. CMOS based chips could offer an alternative in the future but are still too insensitive for luminescence-based applications. A feasible alternative is offered by CCD cameras whose image acquisition can be controlled by a rapidly modulated (~100 ns) digital signal. This type of instrumentation enabled the development of intrinsically referenced imaging methods such as the RLD²⁴⁻²⁶ and td-DLR²⁷ measurement concepts. Hradil et al. reported a imaging application using a rapidly modulated CCD camera, where a temperature and pressure sensitive paint was employed for temperature-corrected imaging of pO₂²⁸. The optode incorporated two phosphorescent indicators with lifetimes in the μ s (pO₂) and ms (temperature) range. Assuming mono-exponential decay of both indicators and a constant signal contribution of the long-lived temperature indicator to the fast decaying pO₂ indicator signal, the lifetimes of the dyes were calculated from two sequences of intensity images with increasing time delay from the excitation pulse.

In this chapter a novel time-resolved imaging method is presented which combines the RLD and td-DLR techniques into a three window measurement scheme and allows the combined mapping of pH and pO₂. The efficiency of the new evaluation method which enables the signal separation is investigated. The dual sensors applied were optimised with respect to the compatibility of the photophysical properties of the incorporated indicators with available LED technology. In addition, the sensing properties were optimised for the use in marine systems or under physiological conditions. A dual sensor incorporating 2',7'-dihexyl-5(6)-N-octadecylcarboxamido-fluorescein (DHFA) with a pH transition range in the near basic region and Pt(PFPP) as oxygen-sensitive component is characterised in detail and its stability and cross-sensitivity towards ionic strength and temperature is investigated. As an application example this dual sensor is used for the detection of two-dimensional pH/pO₂ distributions in marine sediment.

4.2. Experimental

4.2.1. Materials

Platinum(II) meso-tetrakis(pentafluorophenyl)porphyrin (Pt(PFPP)) was purchased from Frontier Scientific. 2'-chloro-7'-hexylfluorescein octadecyl ester (CHFOE) and 2',7'-

Dihexyl-5(6)-N-octadecyl-carboxamidofluorescein (DHFA) were synthesised according to procedures described previously²⁹ (see chapter 3.3). Titanium(IV) oxide (powder, $\text{\O} < 5 \mu\text{m}$) was obtained from Aldrich. The polyurethane type hydrogel HydroMed D4 (D4) was purchased from Cardiotech. The polyethylene terephthalate foil (Mylar[®], thickness: 125 μm) was obtained from Goodfellow. All buffer salts and organic solvents applied were of analytical grade and were purchased from Merck except for ethanol which was obtained from Mallinckrodt Baker. Doubly distilled water was used throughout. The standard buffer solutions (pH 4 and pH 7) applied for the calibration of the pH meter were purchased from Carl Roth. Phosphate buffer stock solutions with a defined ionic strength (IS) and buffer concentration (15 mM for IS cross-sensitivity measurements, otherwise 50 mM) were prepared with the appropriate sodium salt of dihydrogen phosphate, hydrogen phosphate or phosphate and with sodium chloride as background electrolyte. These buffer stock solutions were used for the preparation of buffer solutions with defined pH according to the procedure described in chapter 3.2.2. If not otherwise stated, the IS of the buffer solutions was adjusted to 500 mM and 150 mM for measurements with DHFA- and CHFOE-incorporating sensors, respectively. Nitrogen and oxygen (purity > 99.9 %) as well as synthetic air (20 % v/v oxygen in nitrogen) were obtained from Linde and were applied to adjust defined oxygen partial pressures during sensor calibration. The sediment and seawater used in the demonstration measurements were from the sand flat Janssand near the island of Spiekeroog, Wadden Sea (North Germany). During the measurements, the seawater was equilibrated with compressed air, which was purchased from Linde.

4.2.2. Sensor preparation

1 g D4 hydrogel was dissolved in 9 g of a 9 : 1 (v/v) ethanol/water mixture to give a 10 % (w/w) stock solution of the sensor matrix polymer. Indicator stock solutions were prepared by dissolving 10 mg pH indicator in 1 g ethanol and 15 mg Pt(PFPP) in 0.5 g acetone. Aliquots of the dye stock solutions were pipetted to 1 g of the hydrogel solution to make up the final sensor cocktails. Titanium (IV) oxide (TiO₂) powder was added to the sensor solutions of the dual sensors and the single oxygen sensor to enhance light scattering within the sensing layer. The composition of the sensor membranes of the single and dual sensors are listed in Table 4.1. The sensor solutions were stirred for at least 12 h and were afterwards spread onto dust-free Mylar[®] foils using a knife-coating device from Coesfeld to obtain sensor films with a wet

thickness of 60 μm . The membranes were left to dry over night before measurements and were kept in the dark throughout storage.

Table 4.1. Composition of the sensor membranes

membrane	DHFA/ polymer fraction [mmol kg ⁻¹]	CHFOE/ polymer fraction [mmol kg ⁻¹]	Pt(PFPP)/ polymer fraction [mmol kg ⁻¹]	TiO ₂ /polymer fraction [kg kg ⁻¹]
M _{DHFA}	3	0	0	0
M _{CHFOE}	0	3	0	0
M _{Pt(PFPP)_1}	0	0	6	0
M _{Pt(PFPP)_2}	0	0	6	9/10
M _{DHFA-Pt(PFPP)}	3	0	6	9/10
M _{CHFOE-Pt(PFPP)}	0	3	3	9/10

4.2.3. Instruments

Absorbance and transmission spectra were recorded using a U-3000 UV/VIS double-beam spectrophotometer from Hitachi. Luminescence spectra were acquired with an Aminco Bowman Series 2 luminescence spectrophotometer from SLM-Aminco. The set-up used for time-resolved imaging (Fig. 4.1 A) was described in chapter 2.7. A light source module equipped with a LuxeonTM V Star LED ($\lambda_{\text{em.}} = 505 \text{ nm}$) from Lumileds was used for excitation of the sensor foils. All optical filters used were obtained from Schott (GG 495, OG 570, OG590, FITCE) or from Linos Photonics (DichrolightTM C54 cyan). Time-resolved image acquisition was controlled by a computer using a custom-made software module^{31,32}. The system settings applied for the imaging measurements in the following are listed in Table 4.2. An application developed in IDL 5.3 from Research Systems was used for image processing.

Table 4.2. System settings applied for the imaging measurements

chapter	membrane	excitation pulse	Δt_{ex} [μs]	Δt_{em1} [μs]	Δt_{em2} [μs]	exposure time [ms]
4.3.3	M _{Pt(PFPP)₂}	50	-	50.5 - 85.5	85.5 - 120.5	140
4.3.4.2	M _{DHFA-Pt(PFPP)}	50	0 - 50	50.5 - 85.5	85.5 - 120.5	350
4.3.4.3	M _{CHFOE-Pt(PFPP)}	50	0.5 - 35.5	50.5 - 85.5	85.5 - 120.5	400
4.3.4.6 - 8	M _{DHFA-Pt(PFPP)}	50	0.5 - 35.5	50.5 - 85.5	85.5 - 120.5	300

For calibration measurements, the CCD camera and the light source were positioned at the back side of a 5 x 5 cm sensor membrane mounted into a custom-made flow cell (Fig. 4.1 B). Buffer solutions with varying pH were equilibrated with nitrogen/oxygen or nitrogen/synthetic air mixtures, respectively, to adjust varying oxygen partial pressures. The pH of the buffer solutions was monitored using a digital pH meter (pH538 multical[®]) with internal temperature compensation from WTW. Binary gas mixtures were made up using two 1259CC mass flow controllers in combination with a two-channel PR4000 Digital Power Supply and Readout from MKS Instruments Deutschland. The analyte solutions with defined pH and oxygen partial pressure were pumped through a stainless steel tubing into the flow cell by a Miniplus-3 peristaltic pump from Gilson connected to the flow cell outlet. The flow rate was kept constant at 1 ml min⁻¹. All measurements were done at 20 °C, if not otherwise stated.

Measurements in a natural marine sediment sample were conducted in accordance to procedures described previously⁸. Pieces of the sensor membrane (1.5 x 5cm) were fixed to the inner wall of an aquarium made of polycarbonate by a tape (Fig. 4.1 C). A thin water-film provided the optical contact between the membrane and the aquarium wall. Afterwards, natural surface sediment was added and natural, aerated seawater was let flow slowly above its surface. After several hours in the dark, steady-state oxygen gradient between the anoxic sediment and aerated water developed and several sets of pH/pO₂ images were acquired. pH and pO₂ profiles were additionally measured using microelectrodes^{33,34}.

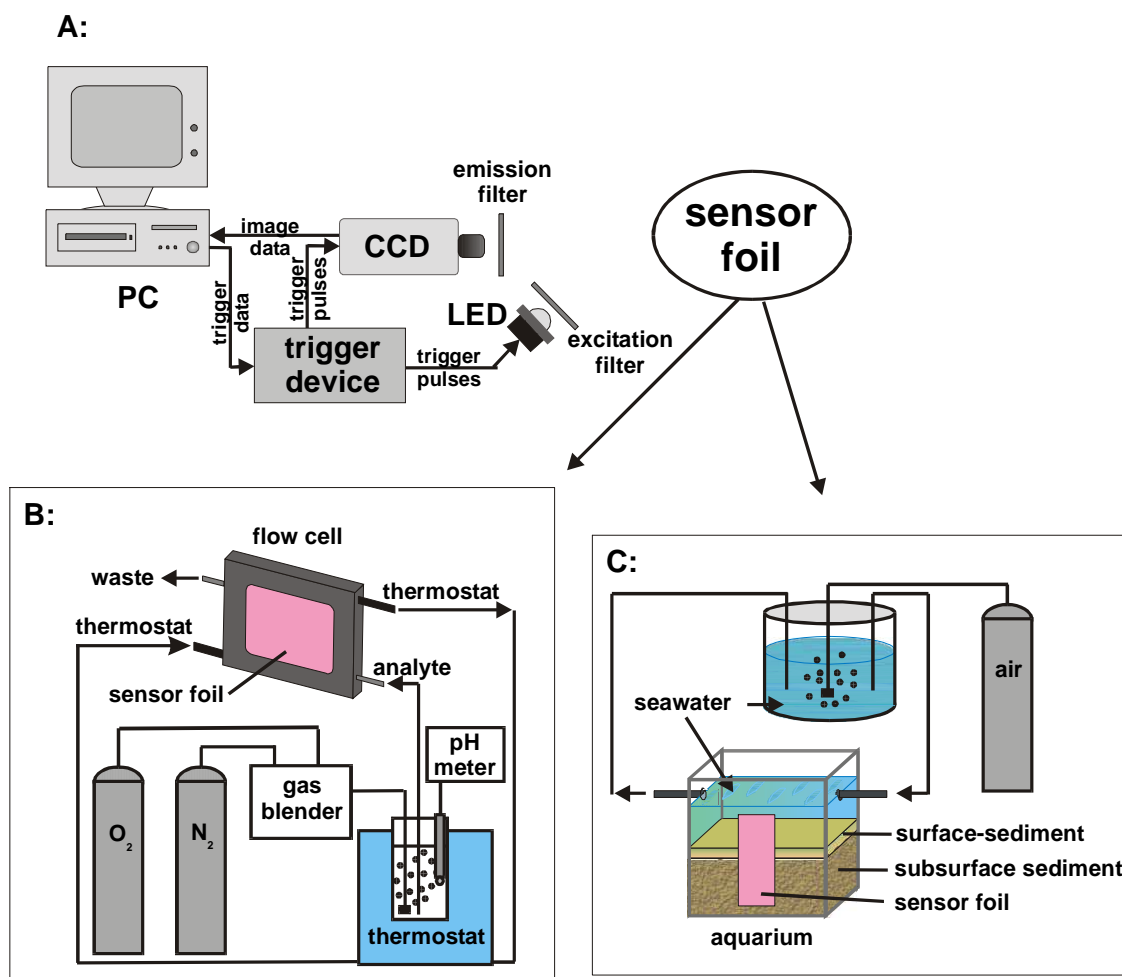


Fig. 4.1. Schematic of the imaging set-up (A) and the experimental set-up used for the sensor characterisation (B) and for the measurement in marine sediment (C).

4.3. Results and discussion

4.3.1. Membrane design

The composition of a dual sensor should ideally ensure that the signals for the single target analytes are not influenced by the other analyte or by an interaction between the two indicators. The two-layer design applied by Wolfbeis et al.¹⁷ for a fibre-optical pCO₂/pO₂ dual sensor prevents a possible resonance energy transfer (RET) between the luminophores due to their spatial separation. Each indicator is embedded in a polymer matrix optimal for the detection of the respective target analyte. Furthermore, the highly reactive singlet oxygen formed during the collisional quenching process between the ground-state oxygen and the

excited-state oxygen indicator is efficiently separated from the second indicator, which increases the long-term stability of the dual sensor. However, a satisfactory control of the sensing layer thickness during the membrane preparation by knife-coating is difficult. Variations in the thickness of the two layers result in different intensity ratios of the two luminophores within the sensing area. Yet, a constant indicator ratio is important in the presented 2D dual sensing scheme, since otherwise a varying pH is simulated. Alternative membrane designs are described in literature where the oxygen indicator is encapsulated in oxygen-permeable polymer particles dispersed in the sensor polymer together with the second indicator^{21,22,35}. Particles with diameters in the nm range allow for the fabrication of highly homogeneous single layer sensors. However, an increased photobleaching due to singlet oxygen is not prevented since the distance between the indicators is still too small. μm -sized particles overcome this problem but have the drawback that they often tend to sediment during the membrane preparation process. This results in spatial variations of the calibration curves. A compromise has to be made either as to the sensor homogeneity and therefore its precision or as to the long-term stability of the sensor. In this work it was decided to use single layer hybrid membranes with the two indicator dyes dissolved in the polyurethane based matrix polymer. The beneficial aspects of this concept are the straightforwardness of the sensor preparation and the homogeneity of the sensor films with a uniform molecular distribution of both dyes, as demonstrated by the raw sensor images R_{pH} and R_{pO_2} (Fig. 4.2). However, possible effects like RET, inner filter effects or increased photobleaching were not evaded by this approach and were therefore characterised in detail below.

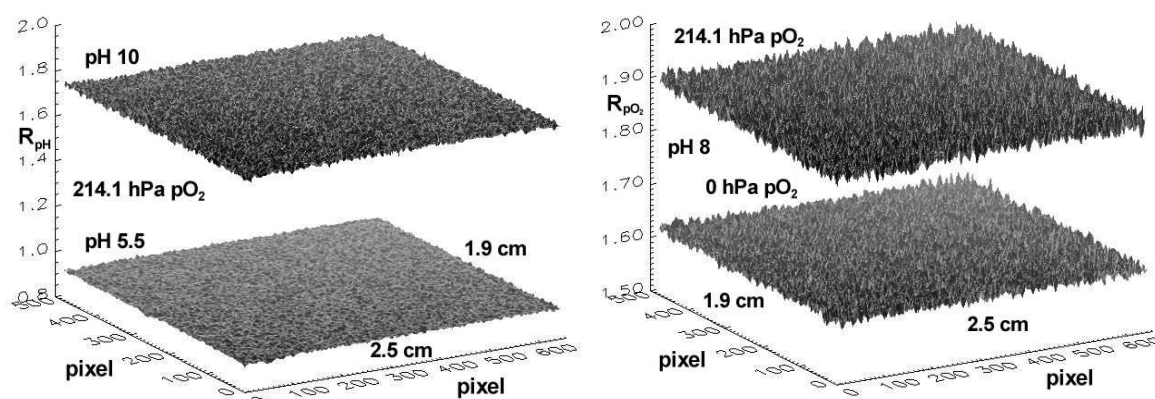


Fig. 4.2. Uncorrected images (2.5 x 1.9 cm areas) of the $M_{\text{DHFA-Pi(PFPP)}}$ sensing membrane; **left:** td-DLR-pH measurement (R_{pH}) taken at pH 5.5 and 10 ($p\text{O}_2 = 214.1$ hPa); **right:** RLD-oxygen measurement (R_{pO_2}) taken at 0 and 214.1 hPa $p\text{O}_2$ (pH = 8).

4.3.2. Choice of indicators and optical components

An important criterion for the choice of a pH and pO₂ indicator combination was the possibility to apply one single excitation light source and the same optical filters for both dyes. The fluorescent pH indicators considered for the use in dual sensors were the two lipophilic fluorescein derivatives DHFA and CHFOE^{29,30}. They were combined with the phosphorescent oxygen-sensitive indicator Pt(PFPP). The uncharged, highly proton-permeable hydrogel Hydromed D4 served as the sensor matrix. The protonated DHFA exists predominantly as non-fluorescent lactone due to the lipophilic character of the polymer matrix. The absorbance and emission maxima of the deprotonated DHFA are at 516 nm and 540 nm, respectively. An esterification of the 2-carboxyl group in the fluorescein chromophore like in CHFOE prevents the lactonisation of the dye at low pH values. Hence, the protonated form of the ester is also fluorescent. The absorbance/emission maxima of the protonated and deprotonated form of CHFOE are at 470 nm/523 nm and 526 nm/545 nm, respectively. Pt(PFPP) embedded in D4 shows absorbance maxima at 391 nm (Soret-band), 507 nm and 539 nm. The latter two are in the same wavelength region as the absorbance maxima of the deprotonated fluoresceins, which allows the usage of low-cost excitation light sources such as LEDs or xenon lamps.

The 505 nm emitting LED equipped with the filter combination GG495/C54 cyan is ideally suited for simultaneous excitation of both indicators in the DHFA/Pt(PFPP) dual sensor (Fig. 4.3, top, left). The OG570 long pass emission filter is needed to remove any LED stray light. Thus, only a small part of the emission of the deprotonated DHFA is recorded, while the emission of Pt(PFPP) with a maximum at 648 nm is recorded completely due to the strong Stokes shift of the dye (Fig. 4.3, top, right). This is acceptable because of the high QY of DHFA (see Table 3.2). The sensor dynamics towards pH is still high since the protonated form of DHFA is not fluorescent, so that the emission decreases to nearly zero at pH 5.5.

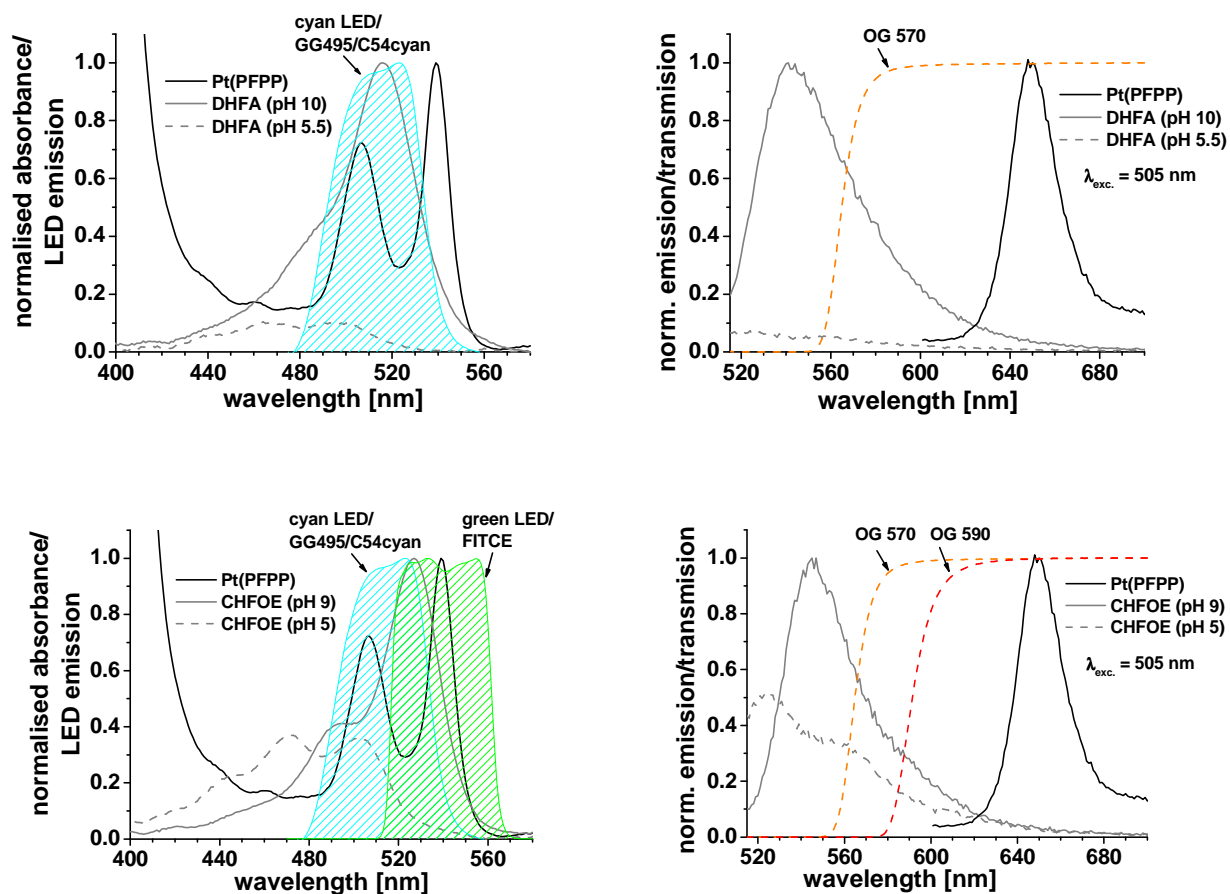


Fig. 4.3. Normalised absorbance (**left**) and luminescence (**right**) spectra of the indicators applied in the dual sensors $M_{DHFA-Pt(PFPP)}$ (recorded with M_{DHFA} and $M_{Pt(PFPP)_1}$ (**top**)) and $M_{CHFOE-Pt(PFPP)}$ (recorded with M_{CHFOE} and $M_{Pt(PFPP)_1}$ (**bottom**)); emission spectra of suitable light sources combined with the transmission spectra of applicable filter sets (**left**) as well as the transmission spectra of the emission filters (**right**) are also shown.

The same LED and filter combination were used for the CHFOE/Pt(PFPP) dual sensor although it was not optimal, as the protonated form of CHFOE is also excited by the 505 nm LED (Fig. 4.3, bottom, left). Therefore, the sensor dynamics of the pH sensor is reduced, since the fluorescence emission of the protonated CHFOE is relatively high within the detected wavelength region. An alternative approach, comprising the 530 nm LED and the FITCE filter for excitation, was not pursued, because it would require the usage of the OG590 emission filter, which leads to a strong decrease of the detected fluorescence from the pH indicator (Fig. 4.3, bottom, right).

4.3.3. Characteristics of the single parameter sensors

Calibration curves of the pH membranes M_{CHFOE} and M_{DHFA} were recorded using a fluorescence spectrometer. M_{DHFA} was excited at 516 nm and the fluorescence intensity at 540 nm was recorded. An internally referenced dual excitation scheme was used for M_{CHFOE} . The sensor was excited at 470 nm and 526 nm and the fluorescence ratio $F_{\lambda_{\text{exc.526}}}/F_{\lambda_{\text{exc.470}}}$ at 545 nm was detected. The normalised fluorescence and the normalised fluorescence ratio were plotted against pH, respectively (Fig. 4.4, left), and fitted by the Boltzmann function (eq. 3.3).

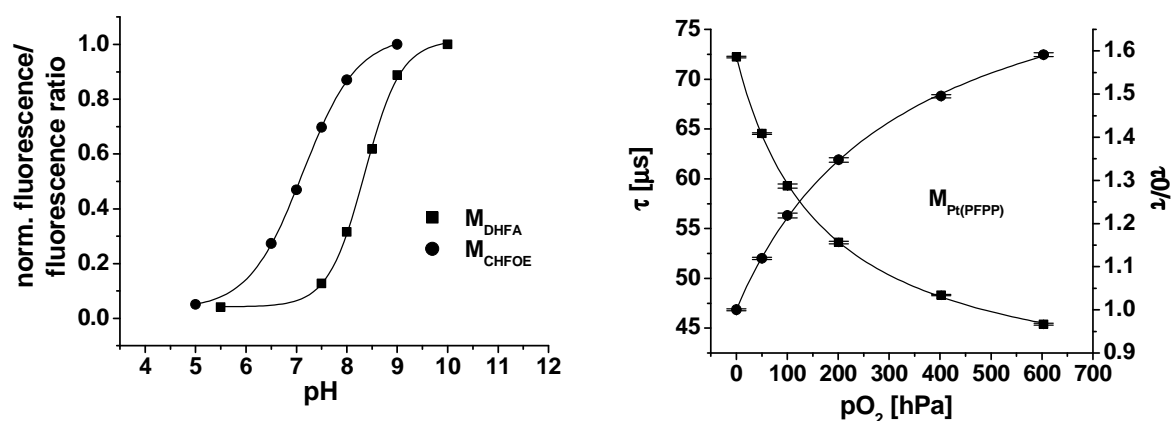


Fig. 4.4. Calibration curves of the pure pH sensors M_{DHFA} and M_{CHFOE} (left) and the pure oxygen sensor $M_{\text{Pt(PFPP)}}$ (right).

The points of inflection corresponding to the apparent pKa values (pKa') were at 7.13 and 8.35 for M_{CHFOE} and M_{DHFA} , respectively. Thus, pH sensors incorporating CHFOE cover the important pH range for physiological applications (e.g., in medicine and biotechnology), while hexyl substituents in 2'- and 7'-position of DHFA shift the dynamic range of the sensor to the near basic region, which is ideal for pH measurements in marine environment.

Phosphorescence lifetimes of the pure oxygen sensor $M_{\text{Pt(PFPP)2}}$ were recorded using the CCD camera and applying the RLD scheme^{36,37} (see chapter 1.6.1). During the calibration, $M_{\text{Pt(PFPP)2}}$ was equilibrated with phosphate buffer solutions at pH 7 and oxygen partial pressures varying from 0 hPa to 603 hPa. Average values of six randomly chosen areas (10 x 10 pixel) in the image ratio $A_{\text{em1}}/A_{\text{em2}}$ were used to calculate the mean value R_{pO_2} and its standard deviation for each oxygen partial pressure. The corresponding lifetimes τ were calculated as

$$\tau = \frac{t_2 - t_1}{\ln(R_{pO_2})} \quad \text{with} \quad R_{pO_2} = \frac{A_{em1}}{A_{em2}} \quad (4.1)$$

where A_{em1} and A_{em2} are the first and second intensity images taken after the excitation pulse, respectively, and t_2 and t_1 are the time delays between the end of the excitation pulse and the start of the recording of the corresponding image. The lifetimes τ and the ratio τ_0/τ were plotted against pO_2 (Fig. 4.4, right) and fitted by the modified Stern-Volmer-equation based on two-site quenching model^{38,39}

$$\frac{\tau_0}{\tau} = \left[\frac{f}{1 + K_{sv} \cdot pO_2} + (1-f) \right]^{-1} \quad (4.2)$$

where τ_0 and τ are the lifetime of Pt(PFPP) in the absence and presence of oxygen, respectively. K_{sv} is the Stern-Volmer constant, which contains the bimolecular quenching constant of the dynamic quenching reaction, f and $(1-f)$ represent the quenchable and non-quenchable fraction of the luminescence, respectively. The following fitting parameters were found: $\tau_0 = 72.26 \pm 0.18 \mu s$, $f = 0.474 \pm 0.005$, $K_{sv} = (5.95 \pm 0.21) * 10^{-3} \text{ hPa}^{-1}$. The sensitivity of Pt(PFPP) in D4 towards oxygen is quite low, which makes the sensor applicable over a wide pO_2 range. Although this is at the cost of the sensor resolution at small pO_2 values, a better resolution is obtained for oxygen partial pressures between 200 and 600 hPa.

4.3.4. Characterisation of the DHFA/Pt(PFPP) dual sensor

4.3.4.1. Spectral interactions between the two indicator dyes

The $M_{DHFA-Pt(PFPP)}$ sensor membrane was immersed in phosphate buffer solutions at pH 10 and pH 5.5 and equilibrated either with nitrogen (0 hPa pO_2) or air (216.8 hPa pO_2). The recorded luminescence intensity spectra (Fig. 4.5) show that the phosphorescence intensity of Pt(PFPP) is influenced by pH. The intensity of the band at 648 nm significantly decreases at the transition from the N_2 /pH 10 buffer to the N_2 /pH 5.5 buffer, where it is even slightly lower than that detected with the air/pH 10 buffer. Both emission bands of DHFA at pH 10 (N_2 and air) show an intensity decrease in the wavelength range between 534 nm and 547 nm. This intensity loss at selective wavelengths indicates an inner filter effect, which is promoted by the TiO_2 particles dispersed in the membrane. This is due to an overlap of the absorbance

band of Pt(PFPP) at 539 nm and the emission band of DHFA in this range of the spectrum, which also enables RET from DHFA to Pt(PFPP).

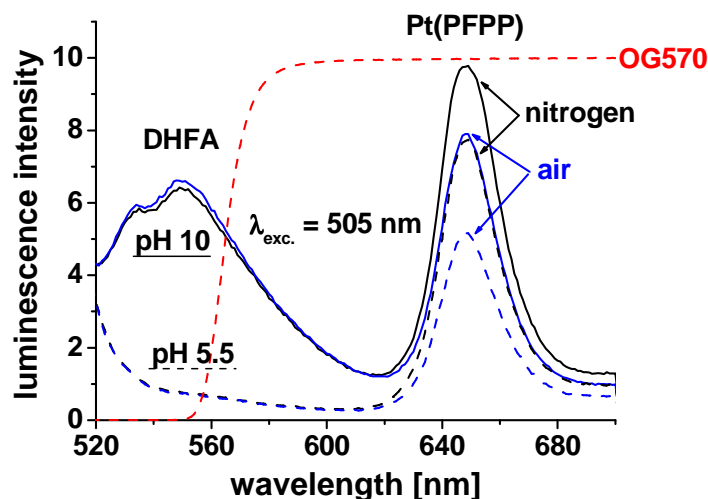


Fig. 4.5. Luminescence spectra of $M_{\text{DHFA-Pt(PFPP)}}$ measured with buffer solutions at pH 10 (solid lines) and pH 5.5 (dashed lines) equilibrated with nitrogen (black lines) and air (blue lines).

4.3.4.2. td-DLR/RLD measurement scheme

The measurement scheme applied for time-resolved imaging with the pH/pO₂ dual sensors combines the two-window based RLD and td-DLR measurement schemes into a single, three-window scheme (Fig. 4.6). It enables the recording of the signals for both parameters during one measurement sequence. The first image A_{ex} ($\Delta t_{\text{ex}} = 35$ or $50 \mu\text{s}$) is recorded during the excitation pulse and contains the luminescence emission of both indicators A_{pH} and A_{pO_2} . The second and third intensity images A_{em1} and A_{em2} ($\Delta t_{\text{em1}} = \Delta t_{\text{em2}} = 35 \mu\text{s}$) are recorded after the excitation pulse. Recording starts a short time delay (500 ns) after the end of the excitation pulse, during which any short-lived fluorescence is decayed. Consequently, the images A_{em1} and A_{em2} contain only the phosphorescence emission of the oxygen indicator.

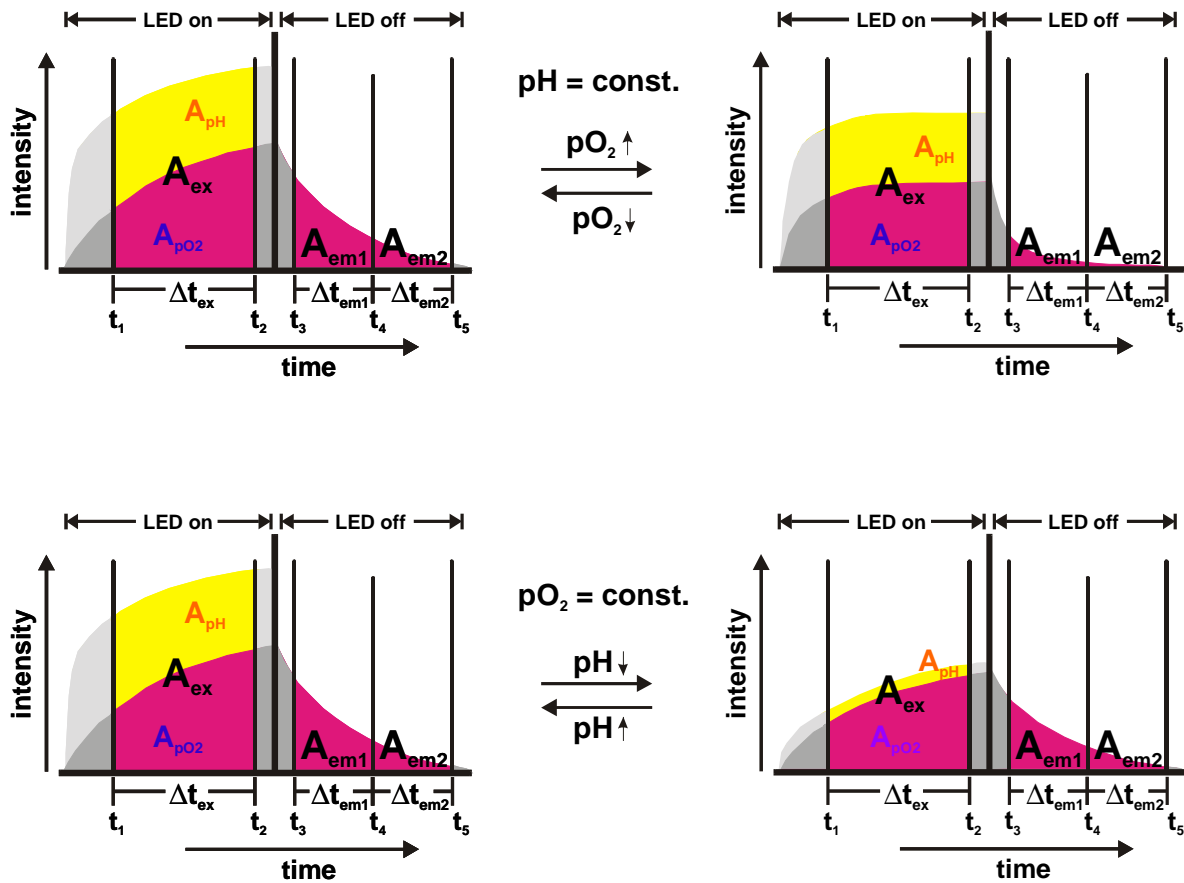


Fig. 4.6. Schematics of the three-window td-DLR/RLD scheme used for the simultaneous mapping of pH and pO₂.

The oxygen signal R_{pO_2} is then given by the image ratio A_{em1}/A_{em2} accordingly to the RLD method. This ratio is independent of variations in the excitation light field intensity, the distribution of the indicator within the sensing membrane and does not change if the indicator leaches or undergoes photodecomposition. Information about pH is carried by the image ratio $R_{pH} = A_{ex}/(A_{em1}+A_{em2})$ and is independent of the absolute intensity from a single pixel. However, a homogeneous distribution of the two indicators is important, since a change in the proportion of the dyes simulates variations in pH. Furthermore, intensity losses due to leaching or photo-bleaching of one or both luminophores are not referenced out in this scheme.

Since the signal of the pH indicator A_{pH} is not referenced with the constant signal of an inert, long-lived reference dye (as it is done in the original td-DLR scheme) but with the oxygen-dependent signal of the second indicator, R_{pH} is a function of both pH and pO₂ (eq. 4.3).

$$R_{pH}(pH, pO_2) = \frac{A_{pH}}{(A_{em1} + A_{em2})} + \frac{A_{pO_2}}{(A_{em1} + A_{em2})} \quad (4.3)$$

Thus, a two-dimensional calibration function describing the behaviour of R_{pH} over the relevant range of pH and pO_2 is required to enable the recovery of pH and pO_2 of an unknown sample from the measured R_{pH} and R_{pO_2} values. The pO_2 of the sample is determined by means of the R_{pO_2} versus pO_2 calibration function and the pH is afterwards calculated with this pO_2 from the $R_{pH}(pH, pO_2)$ function.

Eq. 4.3 can be separated into a pH-dependent and an oxygen-dependent part. The fluorescence intensity of the pH indicator reaches saturation within a few ns after the onset of the excitation pulse (50 μ s duration). It can, therefore, be assumed to be time-independent and A_{pH} can be expressed in the form of a Boltzmann equation (cp. eq. 3.3). The pO_2 influence on R_{pH} is due to the oxygen dependence of A_{pO_2} and $(A_{em1}+A_{em2})$ (Fig. 4.6). Introducing the Boltzmann equation and two oxygen-dependent functions $C_1(pO_2) = A_{pO_2}/(A_{em1}+A_{em2})$ and $C_2(pO_2) = (A_{em1}+A_{em2})^{-1}$ into eq. 4.3, R_{pH} can be written as

$$R_{pH}(pH, pO_2) = C_2(pO_2) \cdot \left(\frac{M_1 - M_2}{1 + \exp\left(\frac{pH - pKa'}{P}\right)} + M_2 \right) + C_1(pO_2) \quad (4.4)$$

Eq. 4.4 was used to fit the calibration plots of R_{pH} versus pH measured for the $M_{DHFA-Pi(PFPP)}$ sensor (Fig. 4.7, top, left). In the first step, the calibration plot measured at $pO_2 = 0$ hPa was fitted with the parameters M_2 , pKa' , P and C_1 being variable and the parameters C_2 and M_1 being fixed to 1 and 0, respectively. Fixing C_2 at $pO_2 = 0$ hPa to 1 corresponds to an arbitrary normalisation, which at the same time implies that A_{pH} is referenced by this constant factor. In the subsequent steps, M_1 and the values for M_2 , pKa' and P found in the first step were fixed and only C_1 and C_2 were varied to fit the R_{pH} versus pH calibration plots at the other oxygen partial pressures. The correlation coefficients R^2 of the R_{pH} versus pH fits were always higher than 0.9984. The values of C_1 and C_2 found by this fitting procedure were plotted against pO_2 and fitted with second order polynomials (see below). Introduction of $C_1(pO_2)$, $C_2(pO_2)$ and the Boltzmann fit parameters into eq. 4.4 leads to the required two-dimensional $R_{pH}(pH, pO_2)$ function. The corrected R_{pH} versus pH calibration plots show that all calibration points lie on the Boltzmann function found in the fitting procedure (Fig. 4.7, top, right).

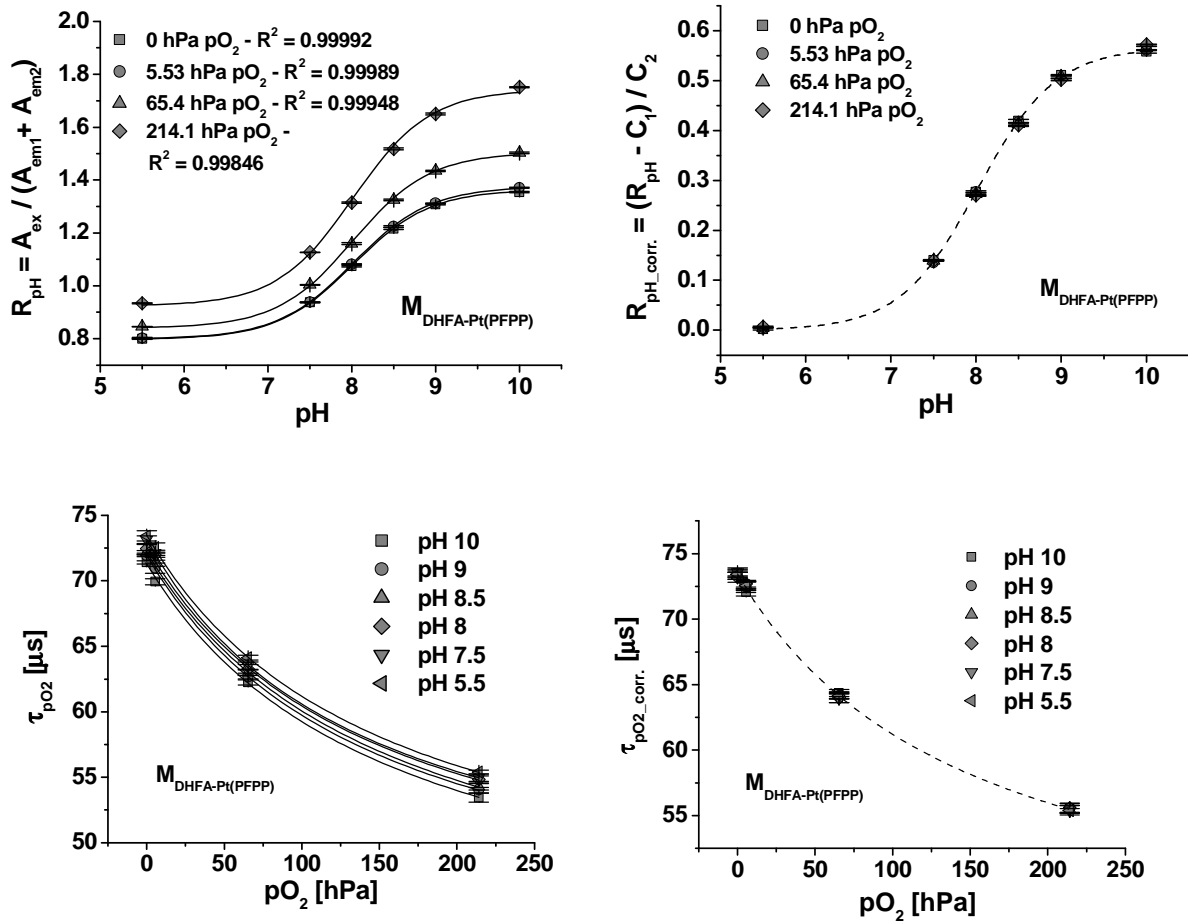


Fig. 4.7. Uncorrected and corrected R_{pH} versus pH (**top**) and τ_{pO_2} versus pO₂ (**bottom**) calibration curves of $M_{DHFA-Pi(PFPP)}$.

As shown in the td-DLR/RLD scheme, the detection of the oxygen signal R_{pO_2} is not influenced by the fluorescence of the pH indicator (Fig. 4.6). However, the calibration plots of the uncorrected values of τ_{pO_2} calculated from eq. 4.1 clearly display a cross-sensitivity towards pH of the buffer solution (Fig. 4.7, bottom, left). This is due to the pH-dependent water uptake capacity of the hydrogel D4 used as the sensor matrix. Examination of the Stern-Volmer calibration functions (eq. 4.2) revealed that only τ_0 depends on pH, while the other two parameters f and K_{sv} were not significantly influenced. This shows that the changing pH alters the polarity within the polymer matrix but not its permeability for oxygen. Therefore, a relatively simple correction of the τ_{pO_2} calibration curves for the pH dependence is possible. Average offsets from the calibration curve at pH 5.5 were calculated as $\Delta\tau_{pO_2,mean}(pH) = \tau_{pO_2}(pH) - \tau_{pO_2}(pH=5.5)$ and fitted with a Boltzmann function (data not shown). Hence, the pH-independent pO₂ calibration function $\tau_{pO_2,corr.}$ can be determined as

$$\tau_{pO_2_corr.}(pO_2) = \frac{t_4 - t_3}{Ln(R_{pO_2}(pH, pO_2))} + \Delta\tau_{pO_2_mean}(pH) \quad (4.5)$$

The mean $\tau_{pO_2_corr.}$ values of the corrected τ_{pO_2} calibration plots were fitted by a Stern-Volmer function (Fig. 4.7, bottom, right). Substitution of $\tau_{pO_2_corr.}(pO_2)$ in eq. 4.5 by this mean Stern-Volmer function gives the two-dimensional equation, which describes R_{pO_2} as a function of pH and pO₂ (eq. 4.6).

$$R_{pO_2}(pH, pO_2) = \exp \left(\frac{t_4 - t_3}{\tau_0 \cdot \left[\frac{f}{1 + K_{sv} \cdot pO_2} + (1 - f) \right] - \Delta\tau_{pO_2_mean}(pH)} \right) \quad (4.6)$$

4.3.4.3. Considerations on the correction functions C₁ and C₂

The predefinition of the parameters M₁ and C₂(0 hPa pO₂) has several consequences for the properties of the correction functions found by the fitting of the calibration functions. They do not necessarily match the theoretical correction functions C₁(pO₂) = A_{pO₂}/(A_{em1}+A_{em2}) and C₂(pO₂) = (A_{em1}+A_{em2})⁻¹ and are therefore addressed to as C₁'(pO₂) and C₂'(pO₂) in the following. Arbitrarily fixing M₁ in eq. 4.4 to 0 implies that at low pH values the Boltzmann equation representing A_{pH} approaches 0 and, hence, R_{pH} equals C₁'. However, C₁'(pO₂) is only identical with C₁(pO₂) = A_{pO₂}/(A_{em1}+A_{em2}) when the protonated form of the pH indicator is not fluorescent in the detected wavelength region. Otherwise, C₁'(pO₂) includes the detected fluorescence emission of the protonated pH indicator.

The C₂ values originally represent the reciprocal of the phosphorescence emission of the oxygen indicator recorded in the two images after the excitation phase (A_{em1}+A_{em2})⁻¹. C₂(pO₂) is therefore no ratiometric but a purely intensity based function. Considering the 12 bit resolution of the camera, the C₂ values should be in the region between 5*10⁻⁴ and 10⁻³. As mentioned above, the setting of C₂'(0 hPa pO₂) to 1 implies a normalisation of the C₂'(pO₂) function. The predefinition of M₁ and C₂'(0 hPa pO₂) leads, therefore, to a modification of eq. 4.4 (eq. 4.7)

$$R_{pH} = C_2'(pO_2) \cdot A_{pH}'(pH) + C_1'(pO_2) \quad \text{with} \quad (4.7)$$

$$C_1'(pO_2) = \frac{A_{pO_2} + A_{pH}(pH_{\min})}{(A_{em1} + A_{em2})} \quad \text{and} \quad (4.7a)$$

$$C_2'(pO_2) \cdot A_{pH}'(pH) = C_2norm.(pO_2) \cdot C_2(0hPa - pO_2) \cdot [A_{pH}(pH) - A_{pH}(pH_{\min})] \quad \text{and} \quad (4.7b)$$

$$C_2norm(pO_2) = \frac{C_2(pO_2)}{C_2(0hPa - pO_2)} \quad (4.7c)$$

where pH_{\min} is a pH value at which only the protonated form of the pH indicator is present. Provided that $A_{pH}(pH_{\min})$ equals zero, eqs. 4.4 and 4.7 are identical. This applies to the R_{pH} versus pH calibration curves of the $M_{DHFA-Pt(PFPP)}$ sensor since the fluorescence spectra of DHFA in Fig. 4.3 show that the fluorescence emission of the indicator is almost zero at pH 5.5. However, in that case suitable correction functions can also be obtained directly from the measurement without the necessity of the fitting procedure. $C_1(pO_2)$ equals the R_{pH} versus pO_2 plot at the lowest pH where no more emission of the pH indicator is detected. While $C_2(pO_2)$ at any rate equals the measured $(A_{em1}+A_{em2})^{-1}$ values plotted versus pO_2 . These measured functions and the correction functions found in the fitting procedure then obviously should be identical.

Fig. 4.8 (left) depicts the functions $R_{pH}(pH5.5, pO_2)$, $C_1'(pO_2)$ and in addition the $C_1(pO_2)$ function acquired by a separate measurement with the single oxygen sensor $M_{Pt(PFPP)_2}$ (using the same camera settings and optical components as for the dual sensor calibration). $R_{pH}(pH5.5, pO_2)$ and $C_1'(pO_2)$ are as expected nearly identical. The small deviation (especially pronounced at higher pO_2 values) is due to the different origin of the $R_{pH}(pH5.5)$ and C_1' values. While the $R_{pH}(pH5.5)$ values are measurement points derived from the calibration measurement, the C_1' values originate from the fitting procedure where all measurement points of the calibration are considered. The $C_1(pO_2)$ function obtained with the $M_{Pt(PFPP)_2}$ sensor clearly differs from $R_{pH}(pH5.5, pO_2)$ and $C_1'(pO_2)$. This indicates that the addition of the pH indicator causes a change in the matrix properties, which alters the ratio $A_{pO_2}/(A_{em1}+A_{em2})$ of Pt(PFPP) in dependence of pO_2 in the dual sensor. The correct $C_1(pO_2)$ function of the dual sensor is therefore not accessible from measurements with the single oxygen sensor. The $C_2'(pO_2)$ function obtained in the fitting procedure and the measured and normalised $C_2norm.(pO_2) = (A_{em1}+A_{em2})^{-1}$ function are again nearly identical (Fig. 4.8, right).

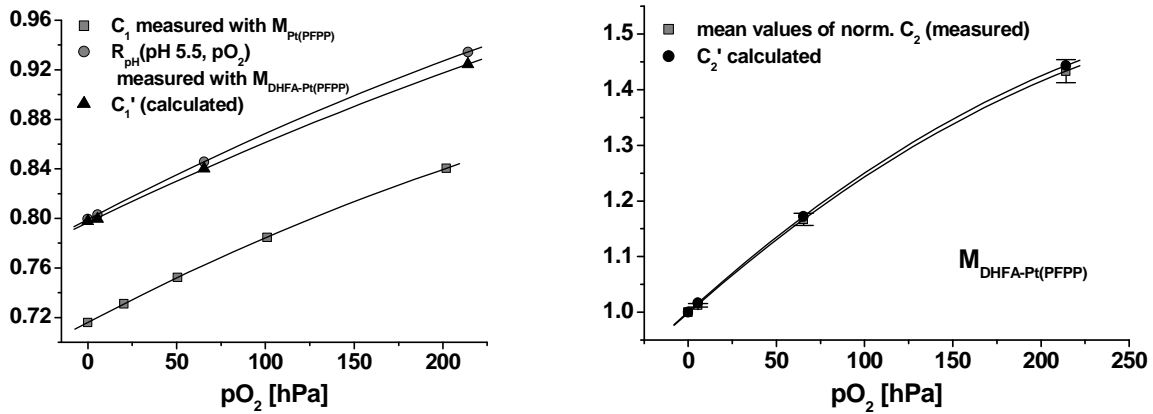


Fig. 4.8. Comparison of the $C_1'(pO_2)$ correction function found in the fitting procedure with the $R_{pH}(pH5.5, pO_2)$ function of the $M_{DHFA-Pt(PFPP)}$ dual sensor and the $C_1(pO_2)$ function of the pure oxygen sensor $M_{Pt(PFPP)_2}$ (**left**); comparison of the $C_2'(pO_2)$ function acquired in the fitting procedure and the $C_{2norm.}(pO_2)$ function gathered from the calibration measurement (**right**).

However, if the protonated form of the pH indicator applied in the pH/pO₂ dual sensor is luminescent in the detected wavelength region, a function equal to the theoretical $C_1(pO_2)$ function of the dual sensor is not accessible and, hence, the measured $C_{2norm.}(pO_2)$ should not be suitable to sufficiently correct the R_{pH} signal. This was tested with the R_{pH} calibration plots of the second dual sensor $M_{CHFOE-Pt(PFPP)}$. When using the 505 nm LED as excitation light source together with the filter combination GG495/C54 cyan and OG570, the detected fluorescence emission of the protonated CHFOE at pH 5 is quite high (see Fig. 4.3).

Fig. 4.9 (top, left) depicts the calculated $C_1'(pO_2)$, the measured $R_{pH}(pH 5, pO_2)$ and as well the $C_1(pO_2)$ function obtained with the single oxygen sensor $M_{Pt(PFPP)_2}$. Here, the difference between $C_1(pO_2)$ and $C_1'(pO_2)$ is even more pronounced, due to the contribution of $A_{pH}(pH_{min})$ to $C_1'(pO_2)$. As expected from their definition, $R_{pH}(pH5, pO_2)$ and $C_1'(pO_2)$ are again nearly identical. $C_{2norm.}(pO_2)$ and the $C_2'(pO_2)$, however, differ significantly (Fig. 4.9 top, right). The C_2' values found in the fitting procedure are lower than the measured and normalised C_2 values and the difference increases with pO₂. The reason for this is that the additional factor $A_{pH}(pH_{min})/(A_{em1}+A_{em2})$ in C_1' also increases with pO₂ causing an increased deviation from the theoretical correction function $C_1(pO_2)$. Subtraction of $C_1'(pO_2)$ from R_{pH} during the signal correction, therefore, leads to values which are too low. This deviation is compensated in the fitting procedure by the reduction of the correction function $C_2'(pO_2)$.

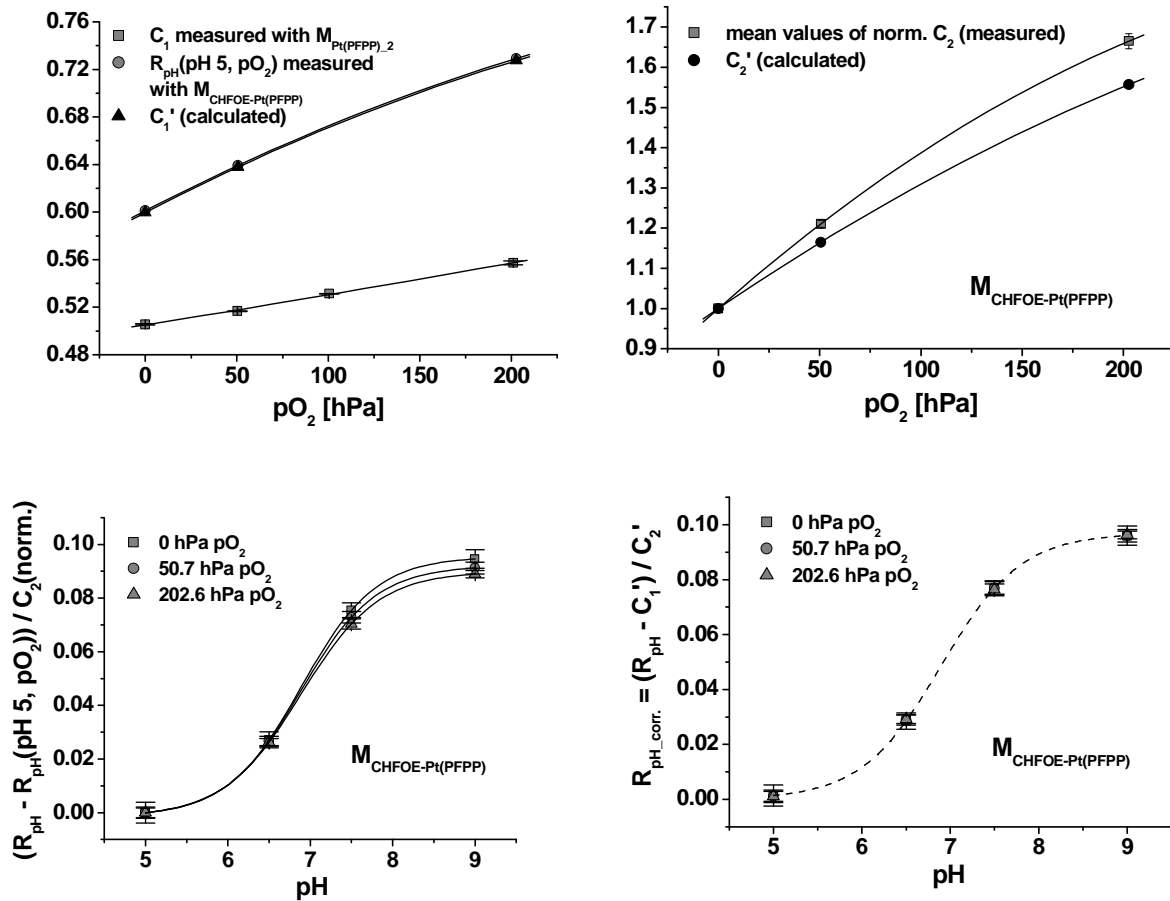


Fig. 4.9. Comparison of the correction functions $R_{pH}(pH5, pO_2)$ and $C_1'(pO_2)$ of the $M_{CHFOE-Pt(PFPP)}$ dual sensor and the $C_1(pO_2)$ function acquired with the oxygen sensor $M_{Pt(PFPP)_2}$ (**top, left**); the C_2' values found in the iteration procedure are lower than the measured and normalised C_2 values and the difference increases with pO_2 (**top, right**); results obtained when using the measured functions $R_{pH}(pH5, pO_2)$ and $C_2(\text{norm.})$ (**bottom, left**) or the calculated functions $C_1'(pO_2)$ and $C_2'(pO_2)$ (**bottom, right**) for the correction of the R_{pH} calibration plots.

Fig. 4.9 (bottom) depicts the different results obtained when using the measured functions $R_{pH}(pH5, pO_2)$ and $C_2(\text{norm.})$ (left) or the calculated functions $C_1'(pO_2)$ and $C_2'(pO_2)$ (right) for the correction of the R_{pH} calibration plots. While the measured correction functions are insufficient to correct the pH calibration curves, good results are obtained with the calculated functions. Hence, the fitting procedure represents a method, which is generally applicable in combination with the td-DLR/RLD measurement scheme to correct of the td-DLR signal of the dual sensor for the spectral influence of the second, long-lived indicator.

4.3.4.4. Influence of RET and inner filter effect

The pK_a' values of the pH part of both dual sensors are shifted to lower values compared to those of the single parameter sensors. The pK_a' values found for M_{DHFA-Pi(PFPP)} and M_{CHFOE-Pi(PFPP)} are 8.02 and 6.89, respectively, in contrast to the pK_a' values 8.35 and 7.13 of M_{DHFA} and M_{CHFOE}. This is caused by the fact that, during the evaluation of the dual sensor signal, the pH signal A_{pH} is multiplied with the oxygen-independent normalisation factor C₂(0 hPa pO₂) (cp. eq. 4.7 b). For both dual sensors M_{DHFA-Pi(PFPP)} and M_{CHFOE-Pi(PFPP)}, however, C₂(0 hPa pO₂) = (A_{em1}+A_{em2})⁻¹_{0 hPa pO₂} increases with decreasing pH due to the inner filter effect and RET between pH and oxygen indicator (data not shown). This results in a decreased slope and a shift of the point of inflection of the pH calibration curves of the dual sensors.

4.3.4.5. Iteration procedure

Since R_{pH} and R_{pO₂} depend both on pH and pO₂, an iterative evaluation is necessary to determine pH and pO₂ of an unknown sample from the set of calibration curves characterising the dual sensor. In the first step, the two-dimensional calibration functions R_{pH}(pH, pO₂) (eq. 4.4) and R_{pO₂}(pH, pO₂) (eq. 4.6) were resolved for the pH and the pO₂, respectively. Subsequently, pH 8 was selected as the pH starting value and was inserted into R_{pO₂}(pH, pO₂) together with the measured R_{pO₂} to calculate an initial pO₂ value. This pO₂ value was used together with the measured R_{pH} and R_{pH}(pH, pO₂) to determine a new pH value. Generally the iteration procedure was repeated until the difference of the pO₂ values of the actual and the previous iteration step was less than 0.05 hPa. Then the pO₂ value was used to calculate the final pH. This iteration procedure was tested with five buffer solutions (S1 - S5) and with a M_{DHFA-Pi(PFPP)} sensor calibrated according to the procedures described above. Table 4.3 lists the pH and pO₂ values adjusted in the test buffer solutions and those calculated by the iteration procedure without a convergence criterion in 3 iteration steps. The results show that already after the first iteration step the pO₂ values can be assumed to be constant within the precision of measurement, due to the small pH dependence of the oxygen signal (Fig. 4.7, bottom, left). As a consequence, final pH values are obtained in the second iteration step. The deviation between the calculated and the adjusted pH values increases at the upper and lower boundary of the dynamic range of the dual sensor, inducing also a stronger deviation of the determined pO₂ values (see S1).

Table 4.3. pH and pO₂ values calculated iteratively from the R_{pH} and R_{pO₂} values measured by the M_{DHFA-Pt(PFPP)} sensor in 5 test buffer solutions.

iteration step	calculated pH/pO ₂ values									
	S1 (pH 9.2/ 91.2 hPa pO ₂)		S2 (pH 8.7/ 121.6 hPa pO ₂)		S3 (pH 8.2/ 60.8 hPa pO ₂)		S4 (pH 7.6/ 20.3 hPa pO ₂)		S5 (pH 6.5/ 202.6 hPa pO ₂)	
	pH	pO ₂ [hPa]	pH	pO ₂ [hPa]	pH	pO ₂ [hPa]	pH	pO ₂ [hPa]	pH	pO ₂ [hPa]
0	8.0	103.7	8.0	128.1	8.0	64.4	8.0	20.9	8.0	193.0
1	8.91	98.2	8.67	123.4	8.22	63.3	7.6	22.3	6.72	200.2
2	9.00	97.7	8.72	123.1	8.23	63.2	7.59	22.3	6.62	200.4
3	9.01	97.6	8.72	123.1	8.23	63.2	7.59	22.3	6.61	200.4

4.3.4.6. Sensor stability - leaching and photodecomposition of the indicators

The leaching of the indicators from the membrane was tested with a phosphate buffer solution adjusted to pH 8.2 (IS = 500 mM) and saturated with ambient air. A M_{DHFA-Pt(PFPP)} sensor was mounted into the flow cell and calibrated. Subsequently, the pH 8.2 buffer solution was pumped through the cell at a constant flow-rate of 1 ml min⁻¹ and images were taken after 2, 4, 6 and 24 hours. Between the measurements the cell was kept in the dark. The measured R_{pH} values were converted into apparent pH values using the calibration function and the detected deviations from the set pH 8.2 were plotted against time. After a strong decrease of the apparent pH of -0.14 within the first two hours, the apparent pH decreased at a constant rate of $\Delta\text{pH}/\Delta t = -0.0031 \text{ h}^{-1}$ (data not shown). The leaching of the oxygen indicator was less pronounced. Within the investigated time of 24 h A_{em1}+A_{em2} decreased to 98.6 % of the initial value. The strong signal change at the beginning of the measurement due to an increased leaching of the pH indicator suggests a preconditioning of the sensor membrane. After this period, however, the pH error caused by indicator leaching is comparatively small.

A more serious problem is the indicator loss due to photodecomposition. While the oxygen indicator has an increased photostability because of the fluoro-substituents of the porphyrin ligand⁴⁰, fluoresceins and especially the dihexyl-derivative DHFA are less stable (see chapter 3.4.2). To investigate the photodecomposition of the indicators, the dual sensor

was first calibrated in the flow cell with buffer solutions of the same composition as used in the leaching experiment. After calibration of the sensor membrane, the measurement cell was filled with the pH 8.2 buffer solution and a series of 100 measurements were made. During each measurement, the membrane was exposed to 6250 excitation pulses (50 μ s duration) with an irradiance of ca. 5.1 mW/cm² (see chapter 2.7.2), which corresponds to the total exposure of ca. 1.6 mJ/cm². The decrease of the apparent pH was approximately linear and amounted to $\Delta\text{pH} = -0.002$ per measurement, while $A_{\text{em1}} + A_{\text{em2}}$ decreased by 0.015 % per measurement.

4.3.4.7. Cross-sensitivity towards ionic strength

The effect of the IS on the sensor signal is a well-known problem in optical pH sensing⁴¹. This cross-sensitivity originates from the fact that the proton activity of the sample is detected via the change in an optical property (e.g., absorbance, fluorescence intensity) and, therefore, a concentration change of the protonated and/or deprotonated pH indicator. Thus, the activity coefficients of the two indicator species and the solvent activity are not taken into account. Changes in these factors, however, shift the measured signal and simulate a different pH. The IS cross-sensitivity of the pure pH sensors with the indicators DHFA and CHFOE in D4 was described previously²⁹ (see chapter 3.4.3). While the IS effect on the CHFOE sensor was negligible, the DHFA-containing sensor displayed a stronger cross-sensitivity due to the additional negative charge of the 2-carboxyl group at high pH values. The effect of IS on the corrected pH calibration curves of the $M_{\text{DHFA-Pi(PFPP)}}$ membrane is small at IS values higher than 300 mM (Fig. 4.10, left). The maximum deviation in the measured pH ($\Delta_{\text{max}}\text{pH}$) in the pH range from 7.5 to 9 at a transition from 500 mM to 300 mM is 0.05, which is within the measurement precision. At a transition to lower IS values, however, the cross-sensitivity becomes more pronounced.

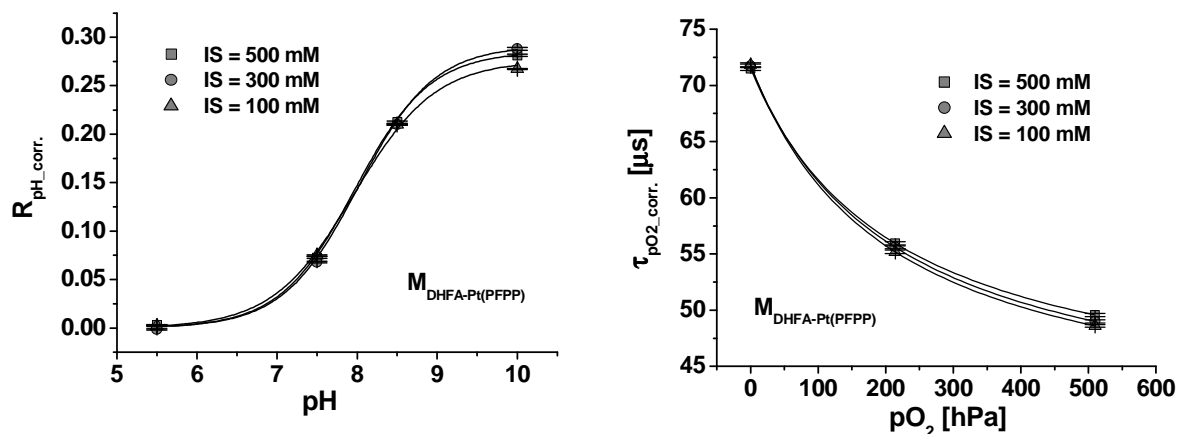


Fig. 4.10. Corrected pH (**left**) and pO₂ (**right**) calibration curves of $M_{\text{DHFA-Pt(PFPP)}}$ measured with phosphate buffer solutions adjusted to IS values varying from 100 mM to 500 mM.

The corrected pO₂ calibration curves also depend on IS (Fig. 4.10, right). The sensitivity of the sensor towards pO₂ increases with decreasing IS, while τ_0 is nearly unaffected. This suggests that the permeability of the hydrogel D4 for oxygen slightly decreases with increasing IS of the aqueous sample. The influence of the IS was quantified by using the $\tau_{\text{pO}_2\text{_corr.}}$ values at varying IS and at 0, 100, 210, 300 and 400 hPa pO₂ to calculate apparent pO₂ values from the calibration curve at 500 mM IS. The obtained apparent pO₂ values were plotted against the IS and linear regression gave the $\Delta\text{pO}_2/\Delta\text{IS}$ gradients, which are summarised in Table 4.4.

4.3.4.8. Temperature effect

Variations in temperature have an impact on the signal of both indicators in $M_{\text{DHFA-Pt(PFPP)}}$. The deactivation of the excited state is enhanced at increasing temperatures due to internal and external conversion. In the case of DHFA, there is also an influence on the equilibrium constant of the acid-base reaction. Previous measurements with the pure pH sensor in the temperature range from 277 to 308 K showed that these two effects compensate over a wide pH range for DHFA in D4, so that the temperature cross-sensitivity is negligible up to pH 8.5 (see chapter 3.4.4). The corrected pH and pO₂ calibration curves of $M_{\text{DHFA-Pt(PFPP)}}$ both depend strongly on temperature (Fig. 4.11).

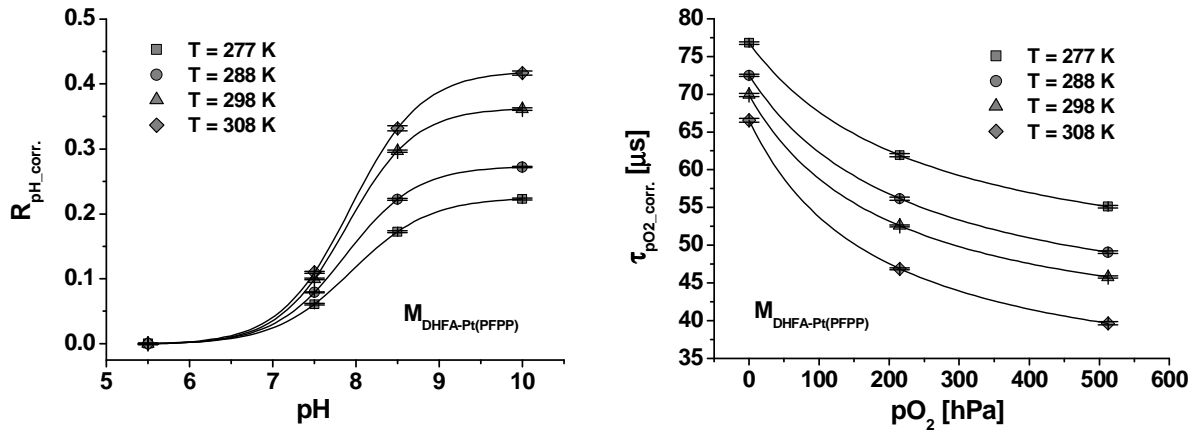


Fig. 4.11. The corrected pH (**left**) and pO₂ calibration curves (**right**) of $M_{\text{DHFA-Pt(PFPP)}}$ recorded at temperatures from 277 to 308 K both display a strong temperature cross-sensitivity.

The contrast between the large temperature dependence of the pH part of the dual sensor and that of the pure pH sensor is due to the fact that the dual sensor pH signal A_{pH} is referenced with the constant factor $C_2(\text{pO}_2 = 0 \text{ hPa})$ originating from the highly temperature-dependent pO₂ indicator luminescence. This is the predominant effect on the corrected pH signal and leads to increasing $R_{\text{pH,corr}}$ values at increasing temperature. The influence of the temperature on the measured pH and pO₂ was quantified applying the calibration curves at 298 K to calculate apparent pH and pO₂ values from the measured values at other temperatures. Table 4.4 shows the $\Delta\text{pO}_2/\Delta T$ and $\Delta\text{pH}/\Delta T$ gradients found by linear regression. $\Delta\text{pH}/\Delta T$ gradients were calculated for two different oxygen partial pressures exemplarily, due to the strong temperature influence on the $C_1(\text{pO}_2)$ and $C_2(\text{pO}_2)$ functions.

Table 4.4. Influence of IS and temperature on the apparent pH and pO₂ measured with the $M_{\text{DHFA-Pt(PFPP)}}$ dual sensor.

pH	$\Delta\text{pH}_{\text{max}}$ (IS: from 500 to 100 mM)	pH	$\Delta\text{pH}/\Delta T$ [K ⁻¹] at pO ₂ = 0 hPa	$\Delta\text{pH}/\Delta T$ [K ⁻¹] at pO ₂ = 210 hPa	pO ₂ [hPa]	$\Delta\text{pO}_2/\Delta\text{IS}$ [hPa mM ⁻¹]	$\Delta\text{pO}_2/\Delta T$ [hPa K ⁻¹]
7.5	0.02	7.2	0.008	0.024	0	0.0057	1.85
8	0.03	7.6	0.011	0.028	100	-0.017	4.11
8.5	0.09	7.8	0.014	0.029	210	-0.053	7.17
9	0.19	8	0.017	0.034	300	-0.09	9.89
		8.2	0.022	0.037	400	-0.142	13.12

4.3.5. Imaging of pH and pO₂ in natural marine sediment

As a proof of principle, the M_{DHFA-Pt(PFPP)} dual sensor was applied for the mapping of pH and pO₂ in marine sandy sediment. The raw data of the images of the sediment measurements were used to calculate the pH and pO₂ distribution over the entire area of the sensor membrane according to the iteration procedure described above. Fig. 4.12 depicts examples of pseudo-colour images of the pH and pO₂ distributions (left). Vertical profiles extracted from these images (white lines in the maps) as well as the profiles obtained using microelectrodes are displayed in the graph on the right.

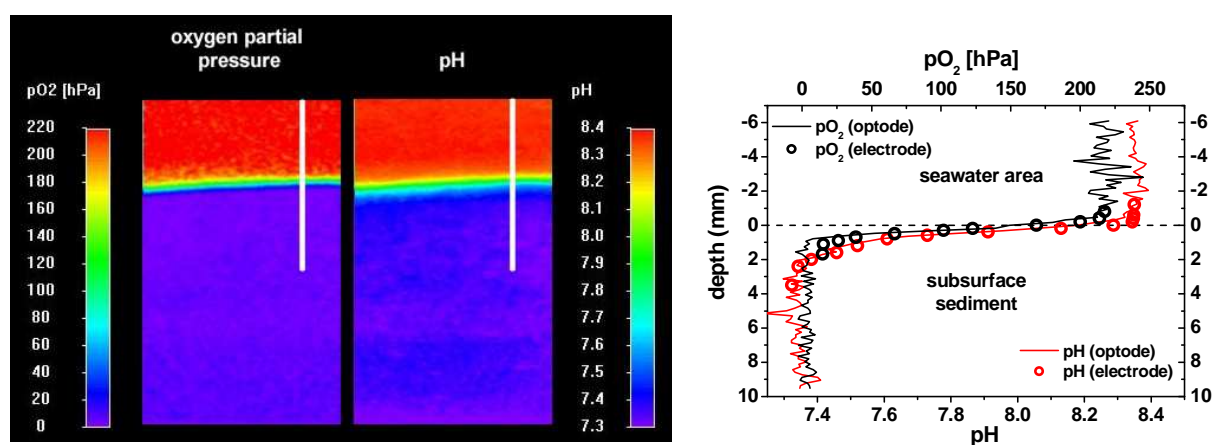


Fig. 4.12. Pseudo-colour maps of the pH and pO₂ (left) distributions in natural marine sediment; profiles extracted from the maps as well as profiles measured with microelectrodes (right).

4.4. Conclusion

A novel measurement scheme was successfully applied for the combined, internally referenced imaging of pH and pO₂ with planar, optical dual sensors. In principle, this scheme allows the detection of the pH signal as a dual signal dependent on pH and pO₂ and the pO₂ signal as a pure signal only dependent on pO₂. A generally applicable procedure to generate a two-dimensional function describing the pH signal in dependence of pH and pO₂ is introduced. The planar optical dual sensors were fabricated by dissolving the two indicators in a single-layer polymer matrix. The benefits are the straightforwardness of the procedure and the homogeneity of the resulting hybrid sensor membranes but consequences are also a reduced long-term stability and an influence of pH on the measured pO₂ signal, due to pH-

dependent polarity of the sensor polymer. Therefore an iteration procedure is necessary to calculate the pH and pO₂ values from the measured raw data of the dual sensors presented in this work. Test measurements with four DHFA- and Pt(PFPP)-containing dual membranes showed that the pH and pO₂ can be detected with a maximum deviation of 0.12 pH units (0.08 pH units near the point of inflection) and 9.1 hPa pO₂ within the range of pH 7.6 - pH 8.7 and 0 - 200 hPa pO₂. Thus, the benefit of the simultaneous detection of pH and pO₂ is at the cost of a decreased precision compared to the respective single sensors, where usually a pH sensor precision of ± 0.03 pH units and a pO₂ sensor precision of ± 2 hPa can be achieved. A high leaching rate of the pH indicator was detected within the first 2 hours, which is not referenced by the measurement scheme and causes a shift of the apparent pH by ca. 0.14 pH units. After this time errors due to leaching are negligible. Therefore the sensor foils should be preconditioned before measurements. Long-term use of the sensors suffers from problems related to photo-bleaching, affecting the pH signal. The IS cross-sensitivity of the pH part of the dual sensor is comparable to that of the pure pH sensor. A slight IS cross-sensitivity of the pO₂ signal is due to an increasing oxygen permeability of the sensor matrix at decreasing IS. The temperature influence on the signals of both parameters, however, is comparably high. Thus, a parallel temperature control and signal correction is inevitable. The application of the DHFA/Pt(PFPP) dual sensor in natural marine sediment gave the expected trends in the pH and pO₂ distribution. However, these experiments were performed under light exclusion. Minimisation of the photo-decomposition effects on the membrane long-term performance is vital to make the dual sensor useful for practical studies, especially if they involve illumination over extended time periods. That can be achieved by using an optically isolated sensor layer, which in addition also excludes possibly interfering background fluorescence of the sample. This, however, requires further development of the sensor composition. Due to the possibility to replace DHFA by a pH indicator with a dynamic range in the physiological region (CHFOE), this sensing system can be extended to further application fields, such as non-invasive monitoring of transcutaneous pO₂ and pH, or measuring of pO₂ and pH in biofilm research.

4.5. References

- [1] Soller B. R., Hsi C., Favreau J., Cingo N., Lancey R. A., Okike O. N., Vander Salm T. J., *Multiparameter fiber optic sensor for the assessment of intramyocardial perfusion*. J. Card. Surg. (2004), 19, 167 - 174.
- [2] Venkatesh B., Clutton-Brock T. H., Hendry S. P., *Evaluation of the Paratrend 7 intravascular blood gas monitor during cardiac surgery: comparison with the C4000 in-line blood gas monitor during cardiopulmonary bypass*. J. Cardiothorac. Vasc. Anesth. (1994), 9, 412 - 419.
- [3] Soller B. R., Heard S. O., Cingo N. A., Hsi C., Favreau J., Khan T., Ross R. R., Puyana J. C., *Application of fiberoptic sensors for the study of hepatic dysoxia in swine hemorrhagic shock*. Crit. Care Med. (2001), 29, 1438 - 1444.
- [4] Cooney C. G., Towe B. C., Eyster C. R., *Optical pH, oxygen and carbon dioxide monitoring using a microdialysis approach*. Sens. Actuators, B (2000), B69, 183-188.
- [5] Ferguson J. A., Healey B. G., Bronk K. S., Barnard S. M., Walt D. R., *Simultaneous monitoring of pH, CO₂ and O₂ using an optical imaging fiber*. Anal. Chim. Acta (1997), 340, 123 - 131.
- [6] Hulth S., Aller R. C., Engstrom P., Selander E., *A pH plate fluorosensor (optode) for early diagenetic studies of marine sediments*. Limnol. Oceanogr. (2002), 47, 212 - 220.
- [7] Zhu Q., Aller R. C., Fan Y., *High-Performance Planar pH Fluorosensor for Two-Dimensional pH Measurements in Marine Sediment and Water*. Environ. Sci. and Technol. (2005), 39, 8906 - 8911.
- [8] Stahl H., Glud A., Schroeder C. R., Klimant I., Tengberg A., Glud R. N., *Time-resolved pH imaging in marine sediments with a luminescent planar optode*. Limnol. Oceanogr.: Methods (2006), in press.
- [9] Glud R. N., Ramsing N. B., Gundersen J. K., Klimant I., *Planar optodes: A new tool for fine scale measurements of two-dimensional O₂ distribution in benthic communities*. Mar. Ecol. Prog. Ser. (1996), 140, 217 - 226.
- [10] Glud R. N., Kuehl M., Kohls O., Ramsing N. B., *Heterogeneity of oxygen production and consumption in a photosynthetic microbial mat as studied by planar optodes*. J. Phycol. (1999), 35, 270 - 279.

- [11] Precht E., Franke U., Polerecky L., Huettel M., *Oxygen dynamics in permeable sediments with wave-driven pore water exchange*. Limnol. Oceanogr. (2004), 49, 693 - 705.
- [12] Polerecky L., Franke U., Werner U., Grunwald B., de Beer D., *High spatial resolution measurement of oxygen consumption rates in permeable sediments*. Limnol. Oceanogr.: Methods (2005), 3, 75 - 85.
- [13] Franke U., Polerecky L., Precht E., Huettel M., *Wave tank study of particulate organic matter degradation in permeable sediments*. Limnol. Oceanogr. (2006), 51, 1084 - 1096.
- [14] Kellner K., Liebsch G., Klimant I., Wolfbeis O. S., Blunk T., Schulz M. B., Gopferich A., *Determination of oxygen gradients in engineered tissue using a fluorescent sensor*. Biotechnol. and Bioeng. (2002), 80, 73 - 83.
- [15] Bell J. H., Schairer E. T., Hand L. A., Mehta R. D., *Surface pressure measurements using luminescent coatings*. Ann. Rev. Fluid Mech. (2001), 33, 155 - 206.
- [16] Engler R. H., Klein C., Trinks O., *Pressure sensitive paint systems for pressure distribution measurements in wind tunnels and turbomachines*. Meas. Sci. Technol. (2000), 11, 1077 - 1085.
- [17] Wolfbeis O. S., Weis L. J., Leiner M. J. P., Ziegler W. E., *Fiber-optic fluorosensor for oxygen and carbon dioxide*. Anal. Chem. (1988), 60, 2028 - 2030.
- [18] Zelelow B., Khalil G. E., Phelan G., Carlson B., Gouterman M., Callis J. B., Dalton L. R., *Dual luminophor pressure sensitive paint II. Lifetime based measurement of pressure and temperature*. Sens. Actuators, B (2003), B96, 304 - 314.
- [19] Neurauther G., *Frequency domain pCO₂ sensing*. Ph. D. Thesis, University of Regensburg (2000).
- [20] Stehning C., Holst G. A., *DSP-based measuring system for temperature-compensated fiber optical oxygen sensors*. Proc. SPIE (2002), 4578, 259 - 270.
- [21] Stehning C., Holst G. A., *Addressing multiple indicators on a single optical fiber-digital signal processing approach for temperature compensated oxygen sensing*. IEEE Sensors Journal (2004), 4, 153 - 159.
- [22] Morgan C. G., Murray J. G., Mitchell A. C., *Frequency-domain imaging using array detectors: present status and prospects for picosecond resolution*. Proc SPIE (1991), 1525, 83 - 90.
- [23] Lakowicz J. R., Szmajcinski H., Nowaczyk K., Berndt K. W., Johnson M., *Fluorescence lifetime imaging*. Anal. Biochem. (1992), 202, 316 - 330.

- [24] Holst G., Kohls O., Klimant I., König B., Kühl M., Richter T., *A modular luminescence lifetime imaging system for mapping oxygen distribution in biological samples*. Sens. Actuators, B (1998), *B51*, 163 - 170.
- [25] Hartmann P., Ziegler W., *Lifetime Imaging of Luminescent Oxygen Sensors Based on All-Solid-State Technology*. Anal. Chem. (1996), *68*, 4512 - 4514.
- [26] Liebsch G., Klimant I., Frank B., Holst G., Wolfbeis O. S., *Luminescence lifetime imaging of oxygen, pH, and carbon dioxide distribution using optical sensors*. Appl. Spectrosc. (2000), *54*, 548 - 559.
- [27] Liebsch G., Klimant I., Krause C., Wolfbeis O. S., *Fluorescent Imaging of pH with Optical Sensors Using Time Domain Dual Lifetime Referencing*. Anal. Chem. (2001), *73*, 4354 - 4363.
- [28] Hradil J., Davis C., Mongey K., McDonagh C., MacCraith B. D., *Temperature-corrected pressure-sensitive paint measurements using a single camera and a dual-lifetime approach*. Meas. Sci. Technol. (2002), *13*, 1552 - 1557.
- [29] Weidgans B. M., Krause C., Klimant I., Wolfbeis O. S., *Fluorescent pH sensors with negligible sensitivity to ionic strength*. Analyst (UK) (2004), *129*, 645 - 650.
- [30] Schroeder C. R., Weidgans B. M., Klimant I., *pH Fluorosensors for use in marine systems*. Analyst (UK) (2005), *130*, 907 - 916.
- [31] Holst G., Grunwald B., *Luminescence lifetime imaging with transparent oxygen optodes*. Sens. Actuators, B (2001), *74*, 78 - 90.
- [32] Polerecky, L. unpublished report (2005).
- [33] Revsbech, N. P. *An oxygen microsensor with a guard cathode*. Limnol. Oceanogr. (1989), *34*, 474 - 478.
- [34] Revsbech N. P., Jorgensen B. B., *Microelectrodes - Their use in microbial ecology*. Adv. Micr. Ecol. (1986), *9*, 293 - 352.
- [35] Borisov S. M., Vasylevska G. S., Krause Ch., Wolfbeis O. S., *Composite Luminescent Material for Dual Sensing of Oxygen and Temperature*. Adv. Funct. Mater. (2006), in press.
- [36] Woods R. J., Scypinski S., Cline Love L. J., Asworth H. A., *Transient Digitizer for the Determination of Microsecond Luminescence Lifetimes*. Anal. Chem. (1984), *56*, 1395 - 1400.
- [37] Ballew R. M., Demas J. N., *An error analysis of the rapid lifetime determination method for the evaluation of single exponential decays*. Anal. Chem. (1989), *61*, 30 - 33.

- [38] Carraway E. R., Demas J. N., DeGraff B. A., *Luminescence quenching mechanism for microheterogeneous systems*. Anal. Chem. (1991), 63 , 332 - 336.
- [39] Carraway E. R., Demas J. N., DeGraff B. A., Bacon J. R., *Photophysics and photochemistry of oxygen sensors based on luminescent transition-metal complexes*. Anal. Chem. (1991), 63, 337 - 342.
- [40] Lee S.-K., Okura I., *Photostable Optical Oxygen Sensing Material: Platinum Tetrakis(pentafluorophenyl)porphyrin Immobilised in Polystyrene*. Anal. Commun. (1997), 34, 185 - 188.
- [41] Janata J., *Do optical sensors really measure pH?* Anal. Chem. (1987), 59 , 1351 - 1356.

5. Luminescent Dual Sensor for Time-Resolved Imaging of pCO₂ and pO₂ in Aquatic Systems

An optical dual sensor for the two-dimensional detection of pCO₂ and pO₂ is described. Tris(tetraoctylammonium)-8-hydroxypyrene-1,3,6-trisulfonate ((TOA)₃HPTS) acting together with the lipophilic buffer tetraoctylammonium hydrogen carbonate ((TOA)HCO₃) as pCO₂-sensing system and the oxygen indicator ruthenium(II) tris(4,7-diphenyl-1,10-phenanthroline) bis(3-(trimethylsilyl)-1-propanesulfonate) (Ru(dpp)₃TMS₂) are incorporated in a single layer ethyl cellulose matrix. A second layer of black silicone rubber served as optical isolation. The two indicators were simultaneously excited with a 460 nm LED and a fast-gateable CCD camera was used as the detector. The time-gated imaging scheme enables the mapping of pCO₂ and pO₂ within one measurement, where images in three different time windows during and after a series of square-shaped excitation pulses are recorded. A numerical evaluation method for the resolution of the single parameter maps from these three overall images is described. The response of the sensor has been optimised for use in aquatic systems.

5.1. Introduction

Carbon dioxide and oxygen are key parameters in a variety of essential reactions in biological, medical and biogeochemical overall processes. Since evolution and consumption of the two gases is often strongly interrelated (e.g. photosynthesis, respiration, decomposition of organic matter, fermentation), the simultaneous detection of both parameters is of significant analytical interest in biological research, clinical diagnosis or process control.

Well established detection methods based on electrochemical or optical chemical sensors exist for both gases¹⁻⁷. Assemblies of separately addressable microelectrodes or fibre optic sensors are suitable tools for the simultaneous determination of oxygen and carbon dioxide partial pressures in homogeneous samples (e. g., respiratory gases, blood etc.)^{8,9}. However, they are not comfortable to use for the detection of gradients in spatially

heterogeneous systems, since they are limited to single-point measurements. Detection also takes place at slightly different positions for each analyte, which makes a correlation difficult.

There are several reports on the combination of planar optical sensors incorporating luminescent indicators and CCD technology to acquire two-dimensional information about the distribution of a target analyte¹⁰⁻¹³. Planar optical oxygen sensors were used to investigate transport processes in surficial marine sediments, to image the pO₂ distribution in photosynthetic microbial mats and bacterial films, to study the oxygen supply in engineered tissues and to visualise airflow patterns in wind tunnel research with pressure sensitive paints (PSP)¹⁴⁻¹⁹.

The simultaneous determination of two parameters with this sensing strategy requires planar dual optodes where indicators for both analytes are present within the whole sensing area. Consequently, the overall signal of the dual optode has to be separated to give information about each single analyte. Signal resolution of optical dual sensors reported so far was accomplished by either taking advantage of different lifetimes or different spectral properties of the indicators²⁰⁻²³. Wolfbeis et al. reported a double layer pCO₂/pO₂ dual sensor in 1988²⁴. The inner pCO₂ sensing layer consisted of 8-hydroxypyrene-1,3,6-trisulfonate (HPTS) covalently immobilised onto cellulose granules and incorporated into a hydrogel matrix. This layer was soaked with a bicarbonate buffer and was afterwards covered by a highly gas permeable silicon rubber layer embedding the pO₂ indicator tris(2,2'-bipyridyl) ruthenium(II) dichloride. The emission bands of the indicators overlap only in a small wavelength range so that separate intensity signals for each analyte were acquired by using two different band pass filters for the emission light. This dual optode was designed for the application in fibre optical sensors. The two layer concept, however, can cause problems when used for spatially resolved measurements, since variations in the thickness of the layers result in significant errors in the measured emission intensities.

The double layer pCO₂/pO₂ dual sensor described by Borisov et al. circumvents this problem²⁵. The first (oxygen sensitive) layer consists of platinum(II)-5,10,15,20-tetrakis(2,3,4,5,6-pentafluorophenyl)porphyrin (Pt(PFPP)) dissolved in polystyrene. While the second (carbon dioxide sensitive) layer is composed of silicone rubber incorporating inert iridium(III) coumarin reference microparticles and pCO₂ sensing microparticles based on the sensor chemistry of a luminescent solid state pCO₂ sensor with HPTS as indicator and tetraoctylammonium hydrogen carbonate ((TOA)HCO₃) as lipophilic buffer²⁶. The signals of the two sensing layers are separately acquired by using appropriate light sources and filter combinations which exclude the luminescence of the respective other indicator. Intrinsically

referenced signals are obtained by measuring the oxygen-dependent lifetime of Pt(PFPP) and the carbon dioxide-dependent fluorescence intensity of HPTS relative to the constant phosphorescence intensity of the reference particles.

Neurauter reported a single layer pCO₂/pO₂ dual sensor²⁷. The sensor membrane was composed of an ethyl cellulose matrix incorporating the two indicators ruthenium(II) tris(4,7-diphenyl-1,10-phenanthroline) (Ru(dpp)₃) and HPTS as well as the lipophilic base tetraoctylammonium hydrogen carbonate ((TOA)HCO₃). Using the same light source and detector both luminescent indicators contribute to a single optical signal. Frequency domain luminescence phase detection with different modulation frequencies allowed the separation of the oxygen (lifetime) and the carbon dioxide (fd-DLR) signal. These frequency domain detection schemes are optimally suited for single point measurements, whereas their transfer to imaging applications requires set-ups with expensive image intensifiers^{28,29}. Alternatively, gateable CCD cameras were used for lifetime imaging in the microsecond range and intrinsically referenced intensity measurements based on the td-DLR concept with an acceptable instrumental effort³⁰.

In chapter 4 we have combined the RLD and the td-DLR scheme to a three window scheme for simultaneous mapping of pH and pO₂ with a fast-gateable CCD camera. This measurement concept was applied in this for the imaging of oxygen and carbon dioxide partial pressures with a single layer, planar dual optode. The sensing system was characterised and its precision was tested.

5.2. Experimental

5.2.1. Materials

Trisodium 8-hydroxypyrene-1,3,6-trisulfonate (HPTS, > 95 %), tetraoctylammonium bromide (> 98 %) and 20% (w/w) methanolic tetraoctylammonium hydroxide ((TOA)-OH) solution were obtained from Fluka. The synthesis of the ion pair ruthenium(II) tris(4,7-diphenyl-1,10-phenanthroline) bis(3-(trimethylsilyl)-1-propanesulfonate) (Ru(dpp)₃TMS₂) is described elsewhere³¹. Ethyl cellulose (ethoxyl content 49%) was purchased from Aldrich. The black silicone rubber Elastosil N189 is a product from Wacker-Chemie. A polyethylene terephthalate foil (Mylar®) of 125 μm thickness from Goodfellow was used as sensor support. All inorganic salts and organic solvents were of analytical grade and were purchased from

Merck except for ethanol, which was obtained from Mallinckrodt Baker. 0.1 N hydrogen chloride solution and 0.1 N sodium hydroxide solution were purchased from Carl Roth. Doubly distilled water was applied throughout. Nitrogen (> 99 %), oxygen (> 99 %), carbon dioxide (> 99 %) and 20 % CO₂ in nitrogen test gas were obtained from Linde.

5.2.2. Synthesis of the (TOA)₃HPTS ion pair

A solution of 104.9 mg (0.2 mmol) HPTS sodium salt and 0.5 g NaCl in 30 ml doubly distilled water was titrated with 0.1 N HCl until the indicator turned completely into its colourless, protonated form. 300.8 mg (0.55 mmol) of tetraoctylammonium bromide were dissolved in 50 ml toluene. The HPTS was extracted into the organic phase by shaking the two phases in a separating funnel. The organic phase was afterwards twice washed with water and dried over disodium sulfate. The solvent was evaporated and the ion pair was dried in a desiccator over silica gel, yielding 83.4 %. Elemental analysis: C₁₁₂H₂₁₁N₃O₁₀S₃ (1856.11 g/mol) (calc./found): C: 72.47/71.44, H: 11.46/11.89, N: 2.26/2.43.

5.2.3. Sensor preparation

1g of ethyl cellulose (EC49) was dissolved in 9 g of a 4 : 1 (v/v) toluene/ethanol mixture to give a 10 % (w/w) EC49 stock solution. Indicator stock solutions were prepared by dissolving 50 mg (TOA)₃HPTS ion pair in 1 ml ethanol and 10 mg Ru(dpp)₃TMS₂ ion pair in 1 ml of a 4 : 1 (v/v) toluene/ethanol mixture, respectively. Aliquots of, firstly, the 20 % (TOA)-OH solution in methanol and, secondly, the respective indicator stock solutions were pipetted to 1 g of the EC49 solution to make up the final sensor solutions.

After the addition of (TOA)-OH the sensor solutions were immediately exposed to a stream of carbon dioxide for some seconds to lower their strongly basic pH. This step is crucial especially with sensor solutions containing Ru(dpp)₃TMS₂, since otherwise the orange-red luminescent Ru(dpp)₃ complex turns to a dark brown, non-luminescent compound within 1 h. We think this is caused by a partial or complete substitution of 4,7-diphenyl-1,10-phenanthroline ligands by hydroxide ions in the ruthenium complex.

Table 5.1. Composition of the sensor membranes.

membrane	(TOA) ₃ HPTS /polymer fraction [mmol kg ⁻¹]	Ru(dpp) ₃ TMS ₂ /polymer fraction [mmol kg ⁻¹]	(TOA)-OH/polymer fraction [mol kg ⁻¹]
M _{HPTS}	19	-	0.32
M _{Ru(dpp)}	-	19	0.32
M _{HPTS-Ru(dpp)}	19	19	0.32

The compositions of the single and dual sensor membranes are listed in Table 5.1. The sensor solutions were stirred for at least 6 h before they were spread onto dust-free Mylar[®] foils with a knife-coating device from Coesfeld. The resulting sensor films had a wet thickness of 60 μm. The dual sensor M_{HPTS-Ru(dpp)} was coated with a second layer of black silicone rubber as optical isolation. In case that dissolved carbon dioxide is to be detected, this layer additionally acts as a proton barrier due to its impermeability for charged species and therefore minimises the cross-sensitivity of the sensor towards pH. 1 g silicone rubber was diluted in 1 g hexane and stirred for 2 h before use. The silicone rubber layer was spread over the sensing layer by knife-coating in a wet thickness of 60 μm.

The membranes were stored in a desiccator over 0.1 N sodium hydroxide solution overnight before calibration. This ensures that the organic solvent has evaporated completely from the sensing layer and that the polymerisation of the silicon rubber of the optically isolated sensors is completed. The sodium hydroxide solution acts as a sink for acidic gases and thus prevents irreversible protonation of the pCO₂ indicator. The optimal conditions for long-term storage are to keep the sensors in the dark and under a carbon dioxide atmosphere free of other acidic gases. By this means the decomposition of the sensor polymer or the indicators due to an increased pH within the sensor membrane or the photo-bleaching of the indicators is avoided.

5.2.4. Instrumentation

UV/VIS absorbance and transmission spectra were acquired with a U-3000 UV/VIS double-beam spectrophotometer from Hitachi. Luminescence measurements were recorded with an Aminco Bowman Series 2 luminescence spectrophotometer from SLM-Aminco. The set-up used for time-resolved imaging (Fig. 4.1 A) was described in chapter 2.7. A light source

module equipped with a blue LED (Luxeon™ V Star, lambertian type, $\lambda_{em.} = 460$ nm) from Lumileds was used as excitation light source. The excitation light was filtered using a FITCA band pass filter and an OG 530 glass filter placed in front of the camera lens excluded any excitation stray light. All optical filters were obtained from Schott.

The imaging data acquisition was controlled by a custom-made software module³². A measurement scheme involving the recording of images in three different time windows relative to a square-shaped excitation pulse was used for the dual sensors. With a total exposure time between 100 and 400 ms the recording of all images in the dual sensor measurement scheme required 1.2 - 3 s including the time for the data transfer (cp. chapter 2.7.3). The background-corrected overall images (or intensity integrals) were processed using an application developed in IDL 5.3 from Research Systems.

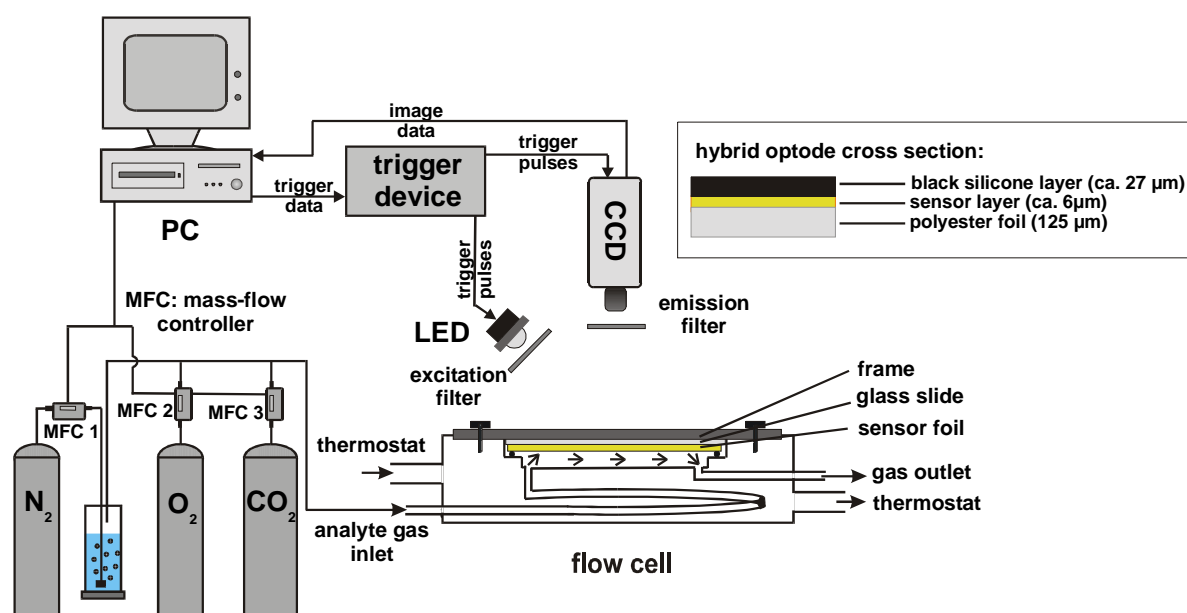


Fig. 5.1. Schematic of the dual optode cross section and of the experimental set-up used for the imaging measurements of pCO₂ and pO₂.

Fig. 5.1 depicts a schematic of the experimental set-up used for imaging measurements. The CCD camera and the excitation light source were directed to the back side of a 5 x 5 cm sensor membrane mounted into a thermostated home-made flow cell. All measurements were made at 20 °C. The calibration of the dual sensors was carried out with ternary gas mixtures of nitrogen, oxygen and 20 % carbon dioxide in nitrogen made up with a gas mixing device comprising three mass flow controllers (MFCs) (type 1179) from MKS Instruments Deutschland. The pure nitrogen acted as inert carrier gas for the two target gases oxygen and carbon dioxide. The carrier gas was humidified by bubbling the gas stream through a water-

filled fritted wash bottle and afterwards was blended with appropriate amounts of the target gases to achieve gas mixtures in the range between 0 and 21 % O₂ and 0 and 2.5 % CO₂. The total flow-rate was adjusted to 900 mL/min. The regulation of the gas flow rates of the MFCs was controlled by a custom-made software based on the National Instruments LabView[®] platform via application of rated voltages³³. Stainless steel tubings were used throughout for the gas transport from the gas cylinders to the measurement cell. The calibration of the pure oxygen sensor was accomplished accordingly but with a binary gas mixture of oxygen and nitrogen in the range between 0 and 42 % O₂.

5.3. Results and discussion

5.3.1. Choice of indicators and sensor polymer

The composition of the presented dual sensor is based on the sensor chemistry of optical, solid state pCO₂ sensors with ethyl cellulose used as sensor matrix. Ethyl cellulose is the matrix polymer most widely used for this sensor type, due to its good stability towards basic pH and the reproducibility, robustness and high sensitivity of the resulting sensors. In addition, ethyl cellulose shows a high permeability not only for carbon dioxide but also for oxygen^{33,34}, so that a high quenching efficiency of oxygen can be expected in the dual sensor.

HPTS was chosen as fluorescent indicator for the detection of pCO₂. pCO₂ sensors incorporating other fluorescent dyes such as seminaphthofluorescein (SNAFL) or seminaphthorhodafluor (SNARF) derivatives are also described in literature³⁵⁻³⁷. However, HPTS combines several advantageous properties compared to these fluorophores. It shows a high photostability and the QY of the analytically important deprotonated form of HPTS is near 100 %³⁸. Moreover, a high sensitivity towards pCO₂ can be reached especially when HPTS is applied in combination with the organic tetraoctylammonium cation (TOA⁺). Incorporated as (TOA)₃HPTS ion pair in an EC49 polymer matrix, the absorbance maximum of the deprotonated HPTS was determined to be at 465 nm. Thus, an inexpensive excitation light source like a 460 nm-LED can be used in the imaging application.

An important point for the choice of the oxygen indicator was that the same light source and optical filters can be applied as for the pCO₂ indicator to enable the simultaneous detection of both parameters in one measurement without the necessity of a change of optical components. Furthermore, the dual sensing scheme for simultaneous imaging of pCO₂ and

pO₂ with the applied set-up requires an indicator with a lifetime in the μs range. A substance class widely used as oxygen indicators fulfilling these criteria are ruthenium(II) diimine complexes. These compounds have a broad absorbance band around 450 nm. The indicator chosen for this work was the Ru(dpp)₃ complex with a comparatively long luminescence lifetime of ca. 5 μs in the absence of a quencher. Fig. 5.2 depicts the normalised absorbance and emission spectra of M_{HPTS} (at 0 and 1011 hPa pCO₂) and M_{Ru(dpp)} as well as the transmission spectra of the filters used for the imaging application.

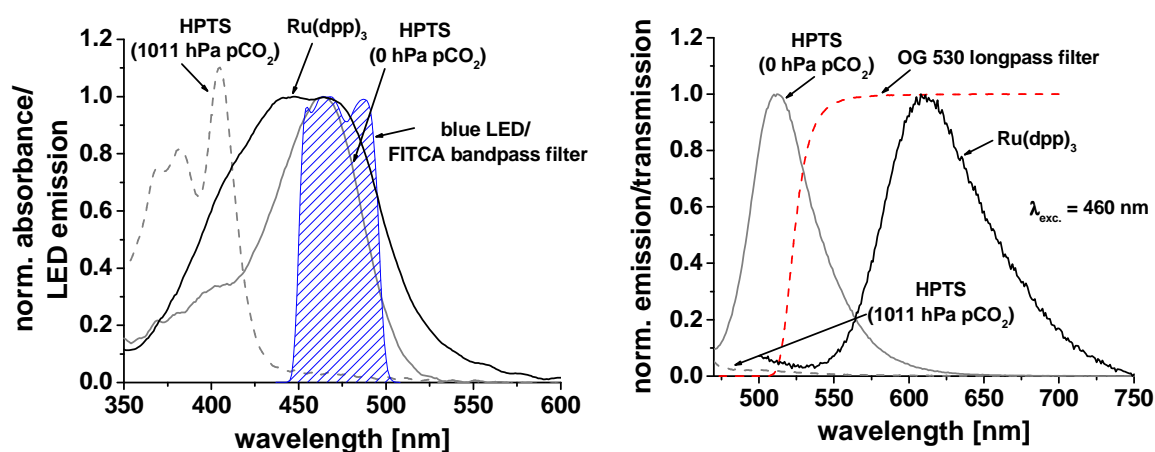


Fig. 5.2. Normalised absorbance (**left**) and emission (**right**) spectra of M_{Ru(dpp)} and M_{HPTS} (at 0 and 1011 hPa pCO₂; normalised to the maximum of the 0 hPa pCO₂ band), respectively, depicted together with the normalised transition spectra of the FITCA band pass excitation filter (**left**) and the OG 530 long pass emission filter (**right**).

The protonated form of HPTS has an absorbance maximum at 405 nm and is nearly not excited by the 460 nm LED equipped with a FITCA bandpass filter, whereas the deprotonated HPTS as well as the oxygen indicator Ru(dpp)₃ are both efficiently excited (Fig. 5.2, left). This is important since the first excited state of HPTS has a strongly decreased pK_a compared to that of the ground state depending on the polarity of the surrounding medium. In aqueous solution, the pK_a of the ground state and the excited state are at 7.3 and 1.4, respectively³⁹. Tests with the M_{HPTS} sensor gave that at 1011 hPa pCO₂ and an excitation wavelength at 405 nm, fluorescence emission still occurs to more than 50 % from the deprotonated species (spectrum not shown). An excitation in this wavelength range would therefore decrease the sensor dynamic for pCO₂.

The fluorescence emission maximum of the deprotonated HPTS is at 512 nm. The luminescence emission band of Ru(dpp)₃ shows a strong Stokes shift and has a maximum at 605 nm. An OG 530 long pass filter in front of the camera lens ensures that only the emission

light of the sensor is recorded, while the short-wave excitation light below 505 nm is blocked. Although a significant part of the HPTS emission is cut by these means, the sensor dynamics for pCO₂ is still quite high, since within this excitation wavelength range, the emission of HPTS decreases to nearly zero at a transition from 0 and 1011 hPa pCO₂ (Fig. 5.2, right). The emission ratio of the two indicators can be optimised by varying their amount in the dual sensor.

5.3.2. Characterisation of the sensor membranes for single parameter pCO₂ and pO₂ detection

The response of solid state, optical pCO₂ sensors like M_{HPTS} towards pCO₂ can be described by eq. 5.1⁶



where D⁻ and HD are the deprotonated and protonated form of HPTS, respectively, and α is the equilibrium constant of the reaction. Fig. 5.3 (left) shows the calibration curves of M_{HPTS}. The normalised fluorescence intensity recorded at 512 nm and the ratio F⁰/F are plotted against the carbon dioxide partial pressure. The linear relationship between F⁰/F and pCO₂ (eq. 5.2) can be derived from eq. 5.1⁴⁰

$$\frac{F^0}{F} = 1 + \alpha \cdot p\text{CO}_2 \quad (5.2)$$

where F⁰ and F are the fluorescence intensities at 0 hPa pCO₂ and at varying pCO₂, respectively. Least-square analysis of the line of best fit to the measurement points gave the following values: α = 0.3254 ± 0.0068 hPa⁻¹, correlation coefficient R² = 0.99935.

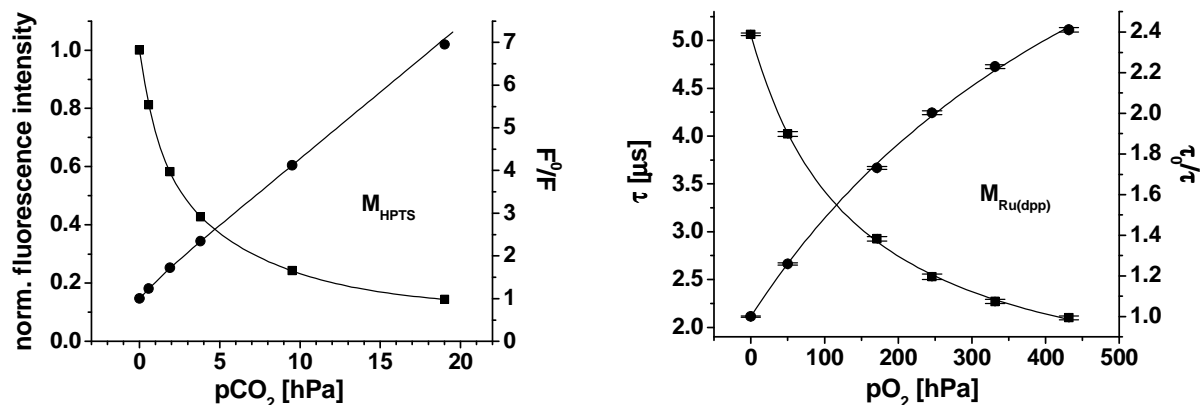


Fig. 5.3. Calibration curves of the single sensors M_{HPTS} (left) and $M_{\text{Ru(dpp)}}$ (right).

The sensor shows a high sensitivity towards carbon dioxide already in the low range between 0 and 5 hPa pCO₂. The reason for this significant increase of the pK_a of HPTS is, on one hand, a better stabilisation of the protonated indicator within the non-polar EC49 matrix, since the number of charges in HPTS is reduced by one upon protonation. On the other hand, the deprotonated HPTS is nearly spherically surrounded by the four TOA⁺ cations with their sterically demanding alkyl chains, due to its four negative charges. This prevents the formation of close ion pairs, which again facilitates the reprotonation of the hydroxyl group.

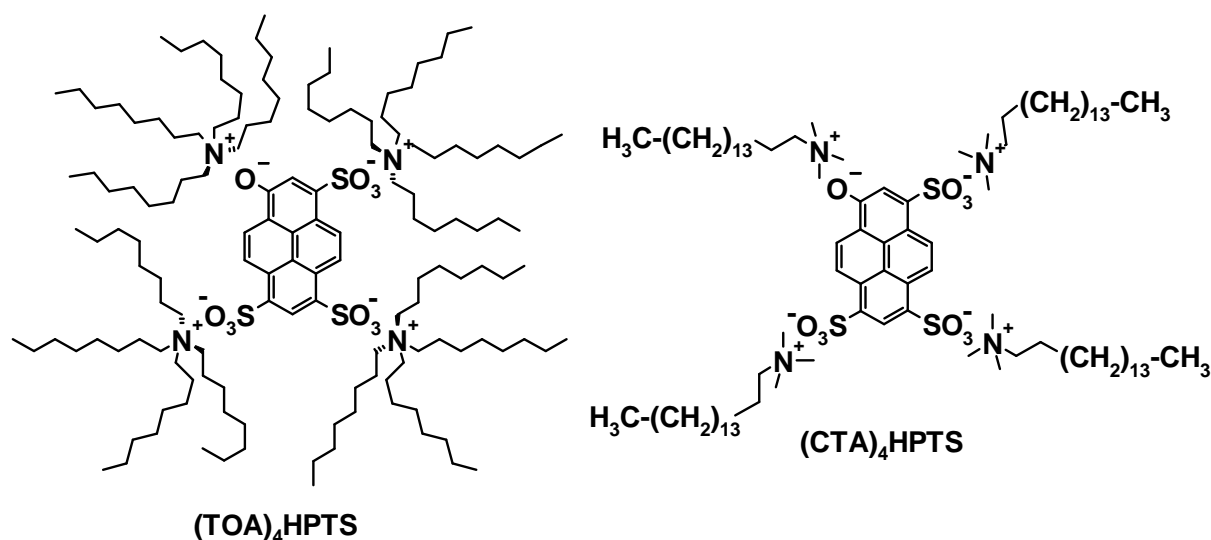


Fig. 5.4. Structure of the (TOA)₄HPTS ion pair (left) depicted together with that of a (CTA)₄HPTS ion pair (right).

In Fig. 5.4 the structure of the (TOA)₃HPTS ion pair (left) is depicted together with that of a (CTA)₃HPTS ion pair (right). CTA⁺ (hexadecyltrimethylammonium) is another lipophilic cation frequently applied as counter ion of the indicator and the buffer substance of solid state

pCO₂ sensors. Sensors incorporating CTA⁺ instead of TOA⁺ as HPTS counter ions are clearly less sensitive towards pCO₂, which is due to the formation of a closer ion pair with the sterically less demanding CTA⁺ cations. Thus, in principle a fine-tuning of the sensor sensitivity is possible by the choice of the lipophilic cation.

EC49 was also used as sensor polymer for the pure oxygen sensor M_{Ru(dpp)}. The same amount of (TOA)-OH as in the investigated dual sensor M_{HPTS-Ru(dpp)} was incorporated in this sensor besides the pO₂ indicator ion pair Ru(dpp)₃TMS₂. The calibration curve of M_{Ru(dpp)} was recorded with the imaging system according to the RLD scheme (see chapter 1.6.1). Oxygen partial pressures between 0 hPa and 430 hPa were adjusted. The following camera settings were applied: Δt_{exc. pulse}: 5 μs, Δt_{em1}: 5.5 - 8.5 μs, Δt_{em2}: 8.5 - 12.5 μs, total exposure time: 250 ms. The averaged values of six randomly chosen 10 x 10 pixel areas of the image ratio (A_{em1}/A_{em2}) were used to calculate the mean value R_{pO₂} and its standard deviation for each oxygen partial pressure. Provided that identical gate widths (Δt_{em1} = Δt_{em2}) are chosen and a mono-exponential decay can be assumed, the lifetime τ of the indicator can be calculated by means of eq. 5.3.

$$\tau = \frac{t_2 - t_1}{\ln R_{pO_2}} \quad \text{with} \quad R_{pO_2}(pO_2) = \frac{A_{em1}}{A_{em2}} \quad (5.3)$$

However, here the resulting lifetimes are mean lifetimes since the assumption of a mono-exponential decay cannot be made for the indicator embedded in a polymer matrix. In Fig. 5.3 (right) τ and the ratio τ₀/τ were plotted against the oxygen partial pressure. The fit functions for both curves are based on the modified Stern-Volmer-equation assuming a two-site quenching model (eq. 5.4)^{41,42}

$$\frac{\tau_0}{\tau} = \left[\frac{f}{1 + K_{sv} \cdot pO_2} + (1 - f) \right]^{-1} \quad (5.4)$$

where τ₀ and τ are the lifetime of the luminophor in the absence and presence of the quencher, respectively. K_{sv} is the Stern-Volmer constant implying the bimolecular quenching constant of the dynamic quenching reaction between the indicator and oxygen and f and (1-f) represent the quenchable and non-quenchable fraction of the indicator molecules, respectively. The following fit constants were found: τ₀ = 5.061 ± 0.025 μs, f = 0.782 ± 0.013, K_{sv} = (7.05 ± 0.37) * 10⁻³ hPa⁻¹, R² = 0.9997. The measurement shows that the highest

sensitivity of the sensor is between 0 and 210 hPa pO₂ but it is still applicable up to an oxygen partial pressure of 430 hPa.

5.3.3. Method

The dual measurement scheme used for the imaging of pCO₂ and pO₂ was described in detail in chapter 4.3.4.2. It combines the td-DLR and the RLD scheme into a three-window scheme, which enables the recording of intrinsically referenced signals of the two target parameters carbon dioxide and oxygen in a single measurement. Fig. 5.5 depicts a schematic of the method.

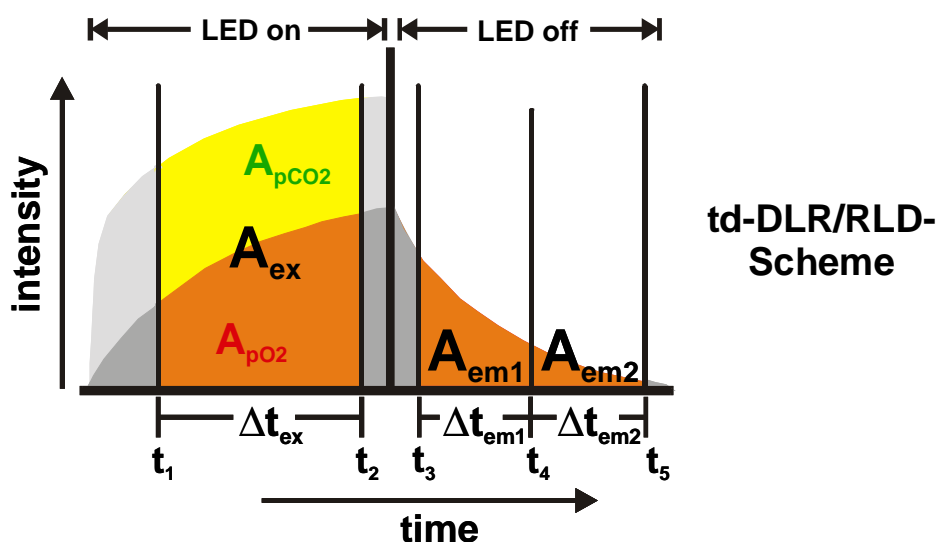


Fig. 5.5. Schematic of the three-window detection scheme.

One precondition for the dual imaging concept is that the luminescent indicators are both excitable with the same light source and that the same optical filters can be applied. Furthermore the concept is designed for a combination of an indicator with a decay time of 600 ns or higher (here for oxygen) and an indicator with a decay time at least 100 times lower (here for carbon dioxide). The CCD-chip of the camera is gateable with a minimal step width of 100 ns. Thus, it is possible to detect the lifetime of the long-lived dye applying the RLD scheme. The image A_{em1} is recorded with a time delay of 200 ns after the excitation pulse. Within these 200 ns the fluorescence of the pCO₂ indicator HPTS and any afterglow of the LED has completely decayed and only the luminescence of Ru(dpp)₃TMS₂ is recorded. A_{em2} is acquired immediately afterwards. The ratio of both images A_{em1}/A_{em2} is independent of the

absolute intensity of the oxygen indicator. Since the detection of the oxygen indicator signal is not influenced by the fluorescence of the pCO₂ indicator, the image ratio $R_{pO_2} = A_{em1}/A_{em2}$ should be only a function of pO₂.

The td-DLR scheme is based on the combination of the short-lived indicator with an inert, long-lived reference dye (see chapter 1.6.2). In the dual sensing scheme, however, the signal of the pCO₂ indicator is referenced with the oxygen dependent signal of the second indicator. Thus, the image ratio $R_{pCO_2} = A_{ex}/(A_{em1}+A_{em2})$ is a function of pCO₂ and pO₂ (eq. 5.5).

$$R_{pCO_2}(pCO_2, pO_2) = \frac{A_{pCO_2}}{(A_{em1} + A_{em2})} + \frac{A_{pO_2}}{(A_{em1} + A_{em2})} \quad (5.5)$$

To enable the recovery of the pCO₂ and the pO₂ from the R_{pCO_2} and R_{pO_2} values acquired in a measurement a function must be found describing the dependence of R_{pCO_2} on pCO₂ and pO₂ over the entire range of interest. Eq. 5.5 can be rewritten as follows

$$R_{pCO_2}(pCO_2, pO_2) = C_2 \cdot A_{pCO_2} + C_1 \quad (5.6)$$

with $C_1 = A_{pO_2}/(A_{em1}+A_{em2})$ and $C_2 = (A_{em1}+A_{em2})^{-1}$. C_1 and C_2 are both directly correlated to the decay of the Ru(dpp)₃ complex and are therefore only functions of pO₂. A_{pCO_2} is the intensity integral of the HPTS fluorescence recorded in the first window during excitation. Due to the ns-decay time of HPTS ($\tau \sim 5$ ns), the fluorophore reaches saturation within a few ns of excitation. Since the recording of the first window starts with a time delay of 1 μ s after the beginning of the excitation period (duration 4 μ s), A_{pCO_2} can be expressed in form of eq. 7 by means of eq. 5.2

$$A_{pCO_2} = \frac{A_{pCO_2}^0}{1 + \alpha \cdot pCO_2} \quad (5.7)$$

where $A_{pCO_2}^0$ is the intensity integral of HPTS at 0 hPa pCO₂. The introduction of eq. 5.7 into eq. 5.6 gives eq. 5.8.

$$R_{pCO_2} = C_2(pO_2) \cdot \left(\frac{A_{pCO_2}^0}{1 + \alpha \cdot pCO_2} \right) + C_1(pO_2) \quad (5.8)$$

After determining the functions $C_1(pO_2)$ and $C_2(pO_2)$, the pCO₂ and pO₂ of an investigated sample can be recovered from the corresponding R_{pCO_2} and R_{pO_2} values by means of the calibration functions eq. 5.3 and eq. 5.8.

5.3.4. Characterisation of the pCO₂-pO₂ dual sensor

The dual sensor $M_{HPTS-Ru(dpp)}$ was prepared as single layer hybrid sensor by dissolving the two indicator ion pairs and the organic buffer (TOA)-OH together in the ethyl cellulose matrix. Besides the straightforwardness of the sensor preparation procedure, this concept ensures a homogeneous distribution of the two indicators over the whole sensor membrane enhancing the precision of the pCO₂ detection. However, the pCO₂ indicator is not shielded from highly reactive singlet oxygen, which is formed during the collisional quenching reaction between the excited state $Ru(dpp)_3$ and triplet oxygen. Thus, the sensor was optically isolated with a second layer of black silicon rubber to increase the sensor stability.

Emission spectra of $M_{HPTS-Ru(dpp)}$ were recorded at an excitation wavelength of 460 nm and 0 hPa pCO₂ and 0 hPa pO₂ (black solid line), 0 hPa pCO₂ and 212.3 hPa pO₂ (blue solid line), 19.2 hPa pCO₂ and 0 hPa pO₂ (black dashed line) and 19.2 hPa pCO₂ and 212.3 hPa pO₂ (blue dashed line) to investigate possible interactions between the two dyes such as RET or inner filter effects (Fig. 5.6). The HPTS emission band and the $Ru(dpp)_3$ absorbance band overlap in the wavelength range between 470 and 580 nm. However, this overlap is not very efficient, since the excitation coefficient of $Ru(dpp)_3$ is already very low at wavelengths with a high fluorescence intensity of HPTS. Thus, no intensity increase of the $Ru(dpp)_3$ emission due to RET or inner filter effects has been observed.

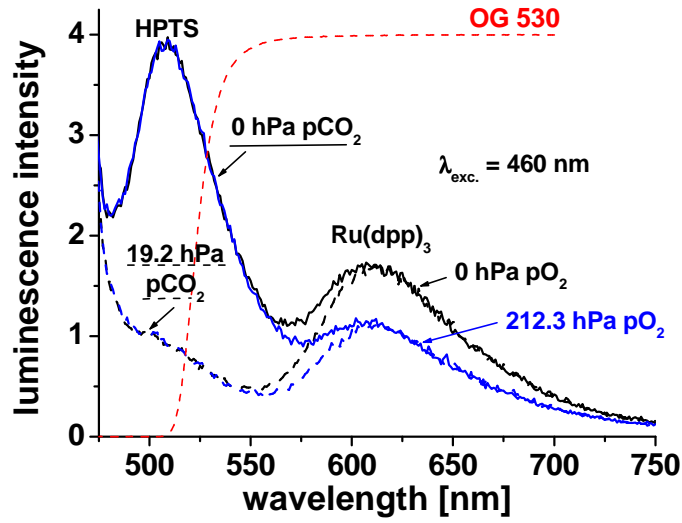


Fig. 5.6. Luminescence emission spectra of the dual sensor $M_{\text{HPTS-Ru(dpp)}}$ recorded at 0 hPa pCO₂ and 0 hPa pO₂ (black solid line), 0 hPa pCO₂ and 212.3 hPa pO₂ (blue solid line), 19.2 hPa pCO₂ and 0 hPa pO₂ (black dashed line) and 19.2 hPa pCO₂ and 212.3 hPa pO₂ (blue dashed line).

The calibration curves of the $M_{\text{HPTS-Ru(dpp)}}$ sensor were acquired with the imaging set-up using the following camera settings: $\Delta t_{\text{exc. pulse}}$: 4 μs , Δt_{ex} : 1 - 3 μs , Δt_{em1} : 4.2 - 5.7 μs , Δt_{em2} : 5.7 - 9.6 μs , total exposure time: 380 ms. Carbon dioxide and oxygen partial pressures were adjusted in the range from 0 - 25.1 hPa and 0 - 210.6 hPa, respectively. R_{pCO_2} and R_{pO_2} values were extracted from the measurement by calculating the mean values from six randomly chosen, averaged 10 x 10 pixel areas of the respective ratiometric images. Unless otherwise stated all errors given are standard deviations. Eq. 5.8 was used to fit the R_{pCO_2} versus pCO₂ plots at the varying pO₂ values (Fig. 5.7, top, left). For this fitting procedure, the two factors C_2 and $A_{\text{pCO}_2}^0$ were combined to a single fit parameter $C_2' = A_{\text{pCO}_2}^0 / (A_{\text{em1}} + A_{\text{em2}})$. This corresponds to a normalisation of the pure pCO₂ calibration curves and further leads to the referencing of the otherwise only intensity based C_2 values. The thus obtained fit function holds over the whole investigated pO₂ range, of course with an oxygen dependent shift of the fit parameters C_1 and C_2' (eqs. 5.9 and 5.9a).

$$R_{\text{pCO}_2} = C_2'(pO_2) \cdot \left(\frac{1}{1 + \alpha \cdot pCO_2} \right) + C_1(pO_2) \quad \text{with} \quad (5.9)$$

$$C_2'(pO_2) = \frac{A_{\text{pCO}_2}^0}{(A_{\text{em1}} + A_{\text{em2}})} \quad (5.9a)$$

The equilibrium constant α was fixed to the value found in the first fitting procedure with the R_{pCO_2} versus pCO_2 plot at 0 hPa pO₂ ($\alpha = 0.3236 \pm 0.0072 \text{ hPa}^{-1}$), in which α was varied also besides C_1 and C_2' . The correlation coefficients R^2 of the R_{pCO_2} versus pCO_2 fit functions at varying pO₂ were higher than 0.99939. The values found for the two fit parameters C_1 and C_2' were then plotted against the pO₂ and fitted with second order polynomials ($R^2 > 0.99936$). Both functions $C_1(pO_2)$ and $C_2'(pO_2)$ are depicted in fig. 7, top, right and bottom, left, respectively.

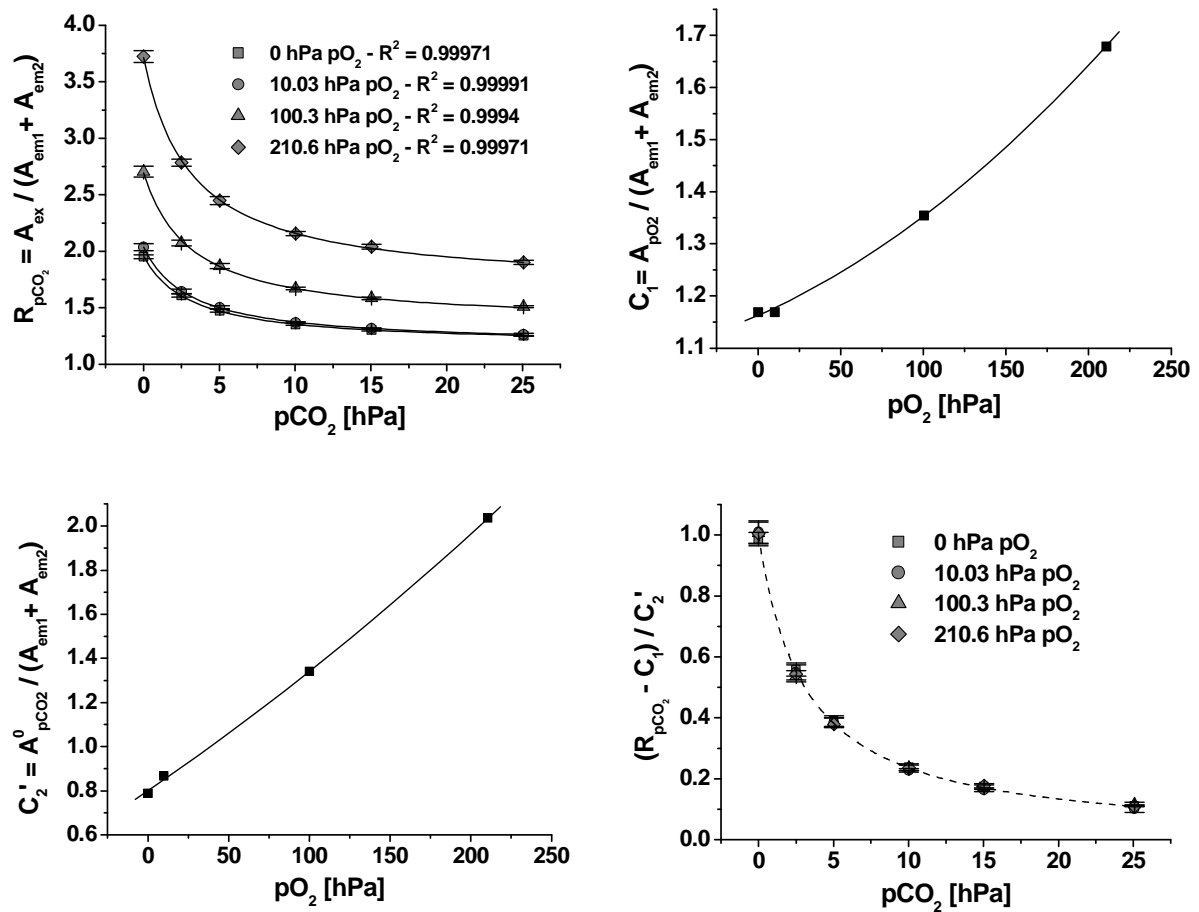


Fig. 5.7. pCO₂ calibration curves of the uncorrected R_{pCO_2} signal of M_{HPTS-Ru(dpp)} at varying oxygen partial pressures (**top, left**); pO₂ dependency of the two fit-parameters C_1 (**top, right**) and C_2 (**bottom, left**); pCO₂ calibration curves corrected for the influence of the pO₂-dependent part of the R_{pCO_2} signal (**bottom, right**).

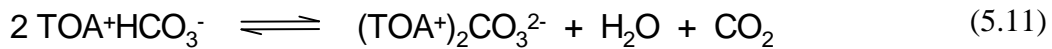
A substitution of $C_1(pO_2)$ and $C_2'(pO_2)$ in eq. 5.9 by the respective second order polynomial fit functions results in a two-dimensional equation describing the behaviour of R_{pCO_2} in dependence of pCO_2 and pO₂ in the investigated area. Least square analysis of the plane described by eq. 5.9 to the measured R_{pCO_2} values gave a correlation coefficient R^2 of 0.9998.

Furthermore eq. 5.9 can be separated in an oxygen-dependent and a carbon dioxide-dependent part (eq. 5.10).

$$\left(\frac{1}{1 + \alpha \cdot pCO_2} \right) = \frac{R_{pCO_2} - C_1(pO_2)}{C_2'(pO_2)} \quad (5.10)$$

Thus, a correction of the measured R_{pCO_2} for the pO_2 influence is possible (Fig. 5.7, bottom, right). This allows the direct comparison of the characteristics of the pCO_2 part of the dual sensor with other pCO_2 sensors.

The calibration plots of the R_{pO_2} values versus the pO_2 at varying carbon dioxide partial pressures are shown in Fig. 5.8 (top, left). In spite the fact that the measured R_{pO_2} is not influenced by the fluorescence signal of the pCO_2 indicator HPTS, a cross-sensitivity towards the pCO_2 can be observed. This influence is especially pronounced for the transition from 0 hPa pCO_2 to 2.51 hPa pCO_2 , while it becomes negligible at a further increase of the carbon dioxide partial pressure. In the presence of carbon dioxide, the counter ion of the lipophilic buffer cation TOA^+ is a hydrogen carbonate anion (in contact with ambient air during sensor preparation the initially present hydroxide immediately adds CO_2 to form hydrogen carbonate). However, exposing the sensor to a carbon dioxide-free atmosphere leads to a reaction according to eq. 5.11.



Considering that the fraction of the organic buffer in the sensor composition is relatively high (16.9 % (w/w) $(TOA)HCO_3^-$ or 15.9 % (w/w) $(TOA)_2CO_3^{2-}$ compared to the matrix polymer EC49) a substitution of the TOA^+ counter ion leads to a substantial change in the sensor chemistry and has therefore also an impact on the matrix properties. The clearly increased slope of the calibration plot at 0 hPa pCO_2 compared to the calibration curves at higher pCO_2 values indicates that the permeability of the sensor membrane for oxygen decreases with an increasing pCO_2 . Furthermore, the R_{pO_2} values at 0 hPa pO_2 show an offset that is especially pronounced for the 0 hPa pCO_2 calibration curve. This suggests a change of the polarity within the sensor membrane leading to an altered microenvironment of the oxygen indicator molecules and, hence, effecting the luminescence lifetime and the R_{pO_2} value.

The effect of the carbon dioxide partial pressure on the pO_2 measurement with the dual sensor complicates the recovery of the pCO_2 and pO_2 from the respective R_{pCO_2} and R_{pO_2} values acquired in a measurement. Again an equation must be found describing the behaviour of R_{pO_2} in dependence of pCO_2 and pO_2 . The two parameters pCO_2 and pO_2 have to be

determined then from the two functions $R_{pCO_2}(pCO_2, pO_2)$ and $R_{pO_2}(pCO_2, pO_2)$ in an iteration procedure. The R_{pO_2} versus pO_2 plots were fitted with second order polynomials of the form $R_{pO_2} = B_0 + B_1 * pO_2 + B_2 * (pO_2)^2$ ($R^2 > 0.99969$). The coefficients B_0 , B_1 and B_2 were set as fit parameters and their values were afterwards plotted against the pCO_2 . Fit functions of the form $B_x = a / (1 + b * pCO_2) + c$ were used to fit the B_0 and B_1 versus pCO_2 plots ($R^2 > 0.99936$) (Fig. 5.8, top, right and bottom, left). The B_2 versus pCO_2 plot revealed a scattering of the B_2 values in a narrow range between 3.29×10^{-6} and 3.55×10^{-6} . Thus, B_2 was assumed to be independent of pCO_2 and the mean value $3.44 \times 10^{-6} \pm 9.74 \times 10^{-8}$ was used for further calculations (Fig. 5.8, bottom, right).

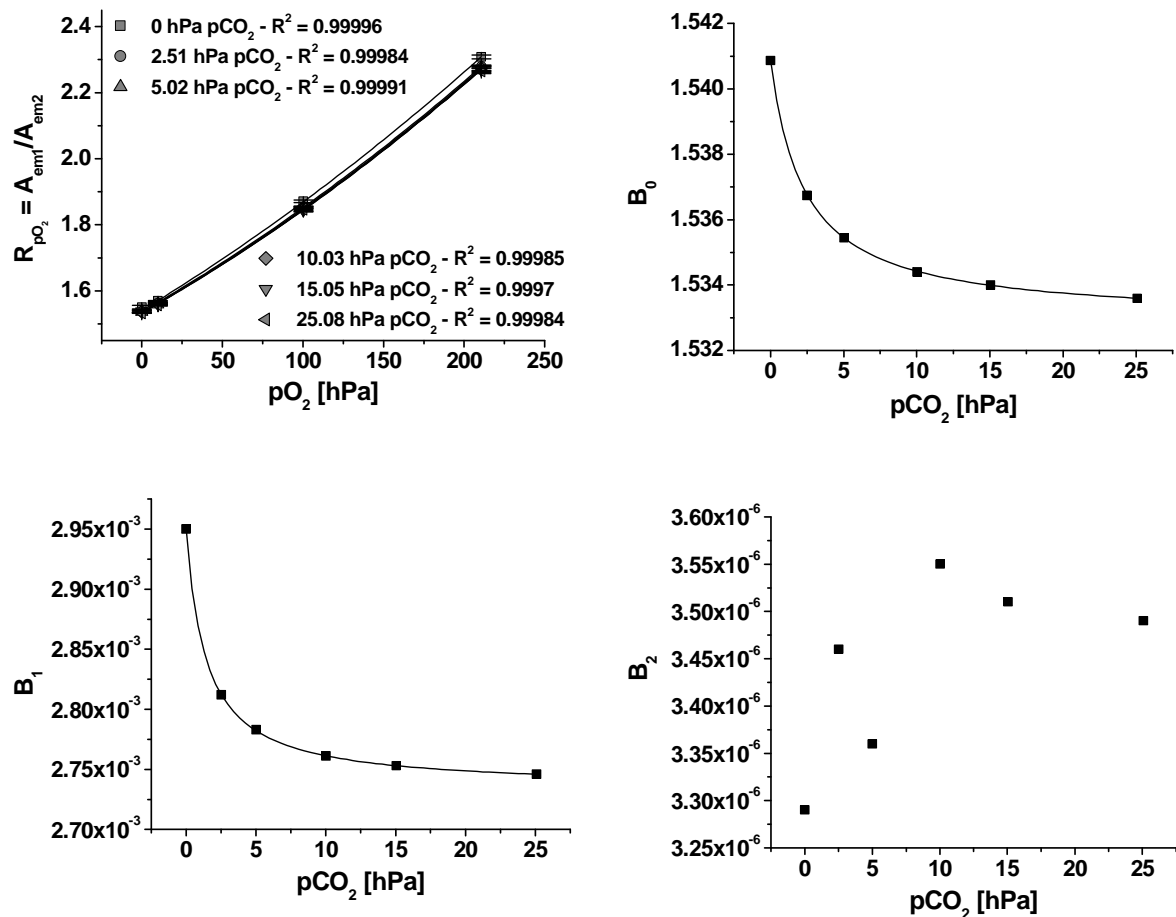


Fig. 5.8. Uncorrected R_{pO_2} versus pO_2 calibration plots of $M_{HPTS-Ru(dpp)}$ at varying carbon dioxide partial pressures (**top, left**); dependency of the fit parameters B_0 (**top, right**) and B_1 (**bottom, left**) on pCO_2 ; the B_2 versus pCO_2 plot revealed a scattering of the B_2 values in a narrow range between 3.29×10^{-6} and 3.55×10^{-6} (**bottom, right**). Thus, B_2 was assumed to be independent of pCO_2 and the mean value $3.44 \times 10^{-6} \pm 9.74 \times 10^{-8}$ was used for further calculations.

The functions $B_0(pCO_2)$ and $B_1(pCO_2)$ reflect the changes of the sensor matrix properties in dependence of pCO₂. $B_0(pCO_2)$ describes the shift of the intercepts of the R_{pO_2} versus pO₂ calibration curves in dependence of pCO₂ and is therefore related to the altered polarity within the sensor membrane. $B_1(pCO_2)$ is the only pCO₂ dependent factor affecting the slopes of the R_{pO_2} versus pO₂ curves and is, thus, related to the permeability of the sensor towards oxygen. The insertion of $B_0(pCO_2)$, $B_1(pCO_2)$ and B_2 as coefficients into the second order polynomial gives a two-dimensional equation describing the dependence of R_{pO_2} on pCO₂ and pO₂ over the entire calibration range (eq. 5.12). Least square analysis of eq. 5.12 to the R_{pO_2} measurement points gave a correlation coefficient of 0.99986.

$$R_{pO_2}(pCO_2, pO_2) = B_0(pCO_2) + B_1(pCO_2) \cdot pO_2 + B_2 \cdot pO_2^2 \quad (5.12)$$

The pCO₂ and pO₂ of a sample can be recovered from the measured R_{pCO_2} and R_{pO_2} values by means of an iteration procedure with eq. 5.9 and 5.12. For this purpose eq. 5.9 has to be solved for pCO₂ and eq. 5.12 for pO₂. Since eq. 5.12 is quadratic in pO₂ this leads to eq. 5.13 after case differentiation.

$$pO_2 = \frac{-B_1(pCO_2) + \sqrt{B_1(pCO_2)^2 - 4 \cdot B_2 \cdot B_0(pCO_2) + 4 \cdot B_2 \cdot R_{pO_2}}}{2 \cdot B_2} \quad (5.13)$$

The pCO₂ and pO₂ of three measurements chosen from the sensor calibration were recovered. For the iteration procedure, an initial pCO₂ value was used to calculate a pO₂ value from the measured R_{pO_2} by means of eq. 5.13. The pO₂ value found was introduced into eq. 5.9 together with the R_{pCO_2} to obtain a new pCO₂ value. With this pCO₂ value the iteration was repeated. In case that the initial pCO₂ value chosen is near the real pCO₂ of the investigated sample, the number of iteration steps can be minimised. One can see from Fig. 5.8 (top, left) that in the 2.51 to 25.1 hPa pCO₂ interval the R_{pO_2} versus pO₂ calibration curves are nearly independent from changes in pCO₂. Thus, a mean R_{pO_2} versus pO₂ calibration curve of this interval was used to recover a first set of pCO₂ and pO₂ values (iteration step 0) and the iteration was started with the pCO₂ found by these means. Table 5.2 shows the number of iteration steps and the pCO₂ and pO₂ values recovered therein for the three calibration measurements.

Table 5.2. Recovered carbon dioxide and oxygen partial pressures from three chosen calibration points.

iteration step	calculated pCO ₂ /pO ₂ values					
	at 0 hPa pCO ₂ and 210.6 hPa pO ₂ ⁽¹⁾ :		at 10.03 hPa pCO ₂ and 100.3 hPa pO ₂ ⁽¹⁾ :		at 2.51 hPa pCO ₂ and 0 hPa pO ₂ ⁽¹⁾ :	
	pCO ₂ [hPa]	pO ₂ [hPa]	pCO ₂ [hPa]	pO ₂ [hPa]	pCO ₂ [hPa]	pO ₂ [hPa]
0 ⁽²⁾	0.12	218.9	10.02	100.4	2.50	0.92
1	-0.03	208.8	10.12	101.1	2.45	0.07
2	-0.04	208.7	10.12	101.1	2.45	0.07
3	-0.04	208.7	10.12	101.1	2.45	0.07

(1) adjusted carbon dioxide and oxygen partial pressures during the recording of the images

(2) calculated with a mean calibration curve of the R_{pO₂} versus pO₂ plots in the 0.25 % to 2.5 % CO₂ interval

In the pCO₂ range between 2.51 hPa and 25.1 hPa the iteration procedure does not improve the precision of the recovered partial pressures and can therefore also be replaced by the use of a mean R_{pO₂} versus pO₂ calibration function. In case that the pCO₂ of the sample is near 0 hPa an iteration is necessary but the results can be considered to be constant within the precision of measurement after a single iteration step. The deviation of the recovered pCO₂ and pO₂ values from the corresponding adjusted partial pressures in the sample is relatively small confirming the accuracy of the two-dimensional fit functions R_{pCO₂}(pCO₂, pO₂) and R_{pO₂}(pCO₂, pO₂).

The iteration procedure was used for the recovery of two series of pCO₂ and pO₂ maps from the images taken during sensor calibration. The iteration was stopped when the absolute value of the difference between the pO₂ value of the current and the previous iteration step was smaller than 0.05 hPa. Each map reflects a 2.5 x 1.9 cm area of the sensor corresponding to a spatial resolution of 78 x 78 μm² per pixel. Fig. 5.9 (left) displays the maps recovered from the images taken at 210.6 hPa pO₂ (right column) and carbon dioxide partial pressures varying from 0 to 25.1 hPa (left column). Maps recovered from the images taken at 2.51 hPa pCO₂ (left column) and oxygen partial pressures varying from 0 to 210.6 hPa (right column) are depicted in Fig. 5.9 (right).

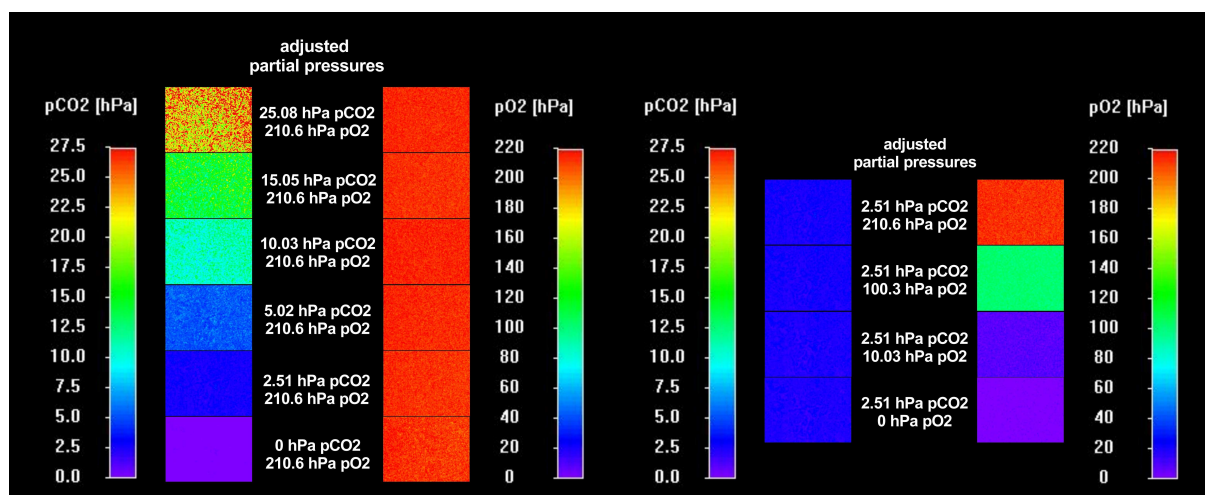


Fig. 5.9. Series of pCO₂ and pO₂ maps recovered from images taken during sensor calibration; each map reflects a 2.5 x 1.9 cm area of the sensor; **left:** maps recovered from images taken at 210.6 hPa pO₂ (right column) and carbon dioxide partial pressures varying from 0 to 25.1 hPa (left column); **right:** maps recovered from the images taken at 2.51 hPa pCO₂ (left column) and oxygen partial pressures varying from 0 to 210.6 hPa (right column).

All maps show a homogeneous distribution of the reflected parameter and the oxygen and carbon dioxide levels recalculated by means of the iteration procedure match those of the corresponding gas mixtures used during the sensor calibration. The strongly increased error in the pCO₂ measurements at 15.1 hPa pCO₂/210.6 hPa pO₂ and at 25.1 hPa pCO₂/210.6 hPa pO₂ shows that the useful working range of the pCO₂-sensing part of the dual sensor is between 0 and 10 hPa pCO₂ (cp. Fig. 5.7, bottom, right).

5.4. Conclusion

A luminescent optical dual sensor for the intrinsically referenced mapping of carbon dioxide and oxygen partial pressures was described. Imaging measurements and their evaluation were performed according to the method introduced in chapter 4. Maximum homogeneity of the sensor membrane was achieved by dissolving the sensor chemistry for both analytes in a single layer EC49 matrix. This also results in a certain cross-sensitivity of the pO₂ signal towards pCO₂. An iterative evaluation is necessary for the recovery of pCO₂ and pO₂ from a dual sensor measurement at CO₂ partial pressures near 0 hPa, however, in the important range between 2.5 and 25 hPa pCO₂ this interfering effect is negligible. Here the recovery of pCO₂ and pO₂ can be accomplished by means of a single pO₂ calibration curve. A further drawback of the hybrid membrane concept is the enhanced photodecomposition of the pCO₂ indicator

HPTS by singlet oxygen formed in the pO₂ sensor reaction. Although the dual sensor was optically isolated with a black silicone layer it was found to be suitable only for short term measurements (1-2 days). Due to the silicone layer which further acts as additional proton barrier, the described pCO₂/pO₂ dual sensor can also be used for the detection of dissolved gases. The working range of the sensor (0 - 10 hPa pCO₂ and 0 - 250 hPa pO₂) makes it an ideal tool for the mapping of pCO₂ and pO₂ gradients in heterogeneous aquatic systems such as freshwater or seawater sediments or microbial mats with high spatial resolution. The response and recovery times of the dual sensor towards dissolved gases was found to be 24 s/424 s at a transition from 0 to 20 hPa pCO₂ and 52 s/200 s at a transition from 0 to 210 hPa pO₂, respectively.

5.5. References

- [1] Amao Y., *Probes and polymers for optical sensing of oxygen*. Microchim. Acta (2003), 143, 1 - 12.
- [2] Ramamoorthy R., Dutta P. K., Akbar S. A., *Oxygen sensors: materials, methods, designs and applications*. J. Mater. Sci. (2003), 38, 4271 - 4282.
- [3] Severinghaus J. W., Bradley A. F., *Electrodes for blood pO₂ and pCO₂ determination*. J. Appl. Physiol. (1958), 13, 515 - 520.
- [4] Owen T. E., *Compensated infrared absorption sensor for carbon dioxide and other infrared absorbing gases*. US Pat. 6 969 857 (2005).
- [5] Leiner M. J. P., *Luminescence chemical sensors for biomedical applications: scope and limitations*. Anal. Chim. Acta (1991), 255, 209 - 222.
- [6] Mills A., Chang Q., McMurray N., *Equilibrium studies on colorimetric plastic film sensors for carbon dioxide*. Anal. Chem. (1992), 64, 1383 - 1389.
- [7] DeGrandpre M. D., *Measurement of seawater pCO₂ using a renewable-reagent fiber optic sensor with colorimetric detection*. Anal. Chem. (1993), 65, 331 - 337.
- [8] Meruva R. K., Meyerhoff M. E., *Catheter-type sensor for potentiometric monitoring of oxygen, pH and carbon dioxide*. Biosens. Bioelectron. (1998), 13, 201 - 212.
- [9] Soller B. R., Hsi C., Favreau J., Cingo N., Lancey R. A., Okike O. N., Vander Salm T. J., *Multiparameter fiber optic sensor for the assessment of intramyocardial perfusion*. J. Card. Surg. (2004), 19, 167 - 174.

- [10] Liebsch G., Klimant I., Frank B., Holst G., Wolfbeis O. S., *Luminescence lifetime imaging of oxygen, pH, and carbon dioxide distribution using optical sensors*. Appl. Spectrosc. (2000), 54, 548 - 559.
- [11] Holst G., Kohls O., Klimant I., König B., Kuhl M., Richter T., *A modular luminescence lifetime imaging system for mapping oxygen distribution in biological samples*. Sens. Actuators, B (1998), B51, 163 - 170.
- [12] Hartmann P., Ziegler W., *Lifetime Imaging of Luminescent Oxygen Sensors Based on All-Solid-State Technology*. Anal. Chem. (1996), 68, 4512 - 4514.
- [13] Hulth S., Aller R. C., Engstrom P., Selander E., *A pH plate fluorosensor (optode) for early diagenetic studies of marine sediments*. Limnol. Oceanogr. (2002), 47, 212 - 220.
- [14] Precht E., Franke U., Polerecky L., Huettel M., *Oxygen dynamics in permeable sediments with wave-driven pore water exchange*. Limnol. Oceanogr. (2004), 49, 693 - 705.
- [15] Glud R. N., Kuehl M., Kohls O., Ramsing N. B., *Heterogeneity of oxygen production and consumption in a photosynthetic microbial mat as studied by planar optodes*. J. Phycol. (1999), 35, 270 - 279.
- [16] Glud R. N., Santegoeds C. M., De Beer D., Kohls O., Ramsing N. B., *Oxygen dynamics at the base of a biofilm studied with planar optodes*. Aquat. Microb. Ecol. (1998), 14, 223 - 233.
- [17] Kellner K., Liebsch G., Klimant I., Wolfbeis O. S., Blunk T., Schulz M. B., Gopferich A., *Determination of oxygen gradients in engineered tissue using a fluorescent sensor*. Biotechnol. and Bioeng. (2002), 80, 73 - 83.
- [18] Nakakita K., Kurita M., Mitsuo K., Watanabe S., *Practical pressure-sensitive paint measurement system for industrial wind tunnels at JAXA*. Meas. Sci. Technol. (2006), 17, 359 - 366.
- [19] Engler R. H., Klein C., Trinks O., *Pressure sensitive paint systems for pressure distribution measurements in wind tunnels and turbomachines*. Meas. Sci. Technol. (2000), 11, 1077 - 1085.
- [20] Zelelow B., Khalil G. E., Phelan G., Carlson B., Gouterman M., Callis J. B., Dalton L. R., *Dual luminophor pressure sensitive paint II. Lifetime based measurement of pressure and temperature*. Sens. Actuators, B (2003), B96, 304 - 314.
- [21] Stehning C., Holst G. A., *DSP-based measuring system for temperature-compensated fiber optical oxygen sensors*. Proc SPIE (2002), 4578, 259 - 270.

- [22] Borisov S. M., Neurauther G., Schroeder C. R., Wolfbeis O. S., *Modified dual lifetime referencing method for simultaneous optical determination and sensing of two analytes*. Appl. Spectrosc. (2006), submitted.
- [23] Hradil J., Davis C., Mongey K., McDonagh C., MacCraith B. D., *Temperature-corrected pressure-sensitive paint measurements using a single camera and a dual-lifetime approach*. Meas. Sci. Technol. (2002), 13, 1552 - 1557.
- [24] Wolfbeis O. S., Weis L. J., Leiner M. J. P., Ziegler W. E., *Fiber-optic fluorosensor for oxygen and carbon dioxide*. Anal. Chem. (1988), 60, 2028 - 2030.
- [25] Borisov S. M., Krause C., Arain S., Wolfbeis O. S., *Composite Material for Simultaneous and Contactless Luminescent Sensing and Imaging of Oxygen and Carbon Dioxide*. Adv. Mater. (2006), 18, 1511 - 1516.
- [26] Mills A., Chang Q., *Fluorescence plastic thin-film sensors for carbon dioxide*. Analyst (UK) (1993), 118, 839 - 843.
- [27] Neurauther G., *Frequency domain pCO₂ sensing*. Ph. D. Thesis, University of Regensburg (2000).
- [28] Morgan C. G., Murray J. G., Mitchell A. C., *Frequency-domain imaging using array detectors: present status and prospects for picosecond resolution*. Proc SPIE (1991), 1525, 83 - 90.
- [29] Lakowicz J. R., Szmajcinski H., Nowaczyk K., Berndt K. W., Johnson M., *Fluorescence lifetime imaging*. Anal. Biochem. (1992), 202, 316 - 330.
- [30] Liebsch G., Klimant I., Krause C., Wolfbeis O. S., *Fluorescent Imaging of pH with Optical Sensors Using Time Domain Dual Lifetime Referencing*. Anal. Chem. (2001), 73, 4354 - 4363.
- [31] Kuerner J., *Nanospheres with shielded phosphorescent dyes as labels for bioassays*. Ph. D. Thesis, University of Regensburg (2002).
- [32] Holst G., Grunwald B., *Luminescence lifetime imaging with transparent oxygen optodes*. Sens. Actuators, B (2001), 74, 78 - 90.
- [33] Apostolidis A., Klimant I., Andrzejewski D., Wolfbeis O. S. *A Combinatorial Approach for Development of Materials for Optical Sensing of Gases*. J. Comb. Chem. (2004), 6, 325 - 331.
- [34] Yasuda H., Stannett V., *Permeability coefficients*. Polymer Handbook 4th ed., Wiley, New York (1999), p III-229.
- [35] Waldner A., Barnard S. M., *Optical carbon dioxide sensors*. US Pat. 6 969 857 (2002).

- [36] Tabacco M. B., Uttamlal M., McAllister M., Walt D. R., *An Autonomous Sensor and Telemetry System for Low-Level pCO₂ Measurements in Seawater*. Anal. Chem. (1999), 71, 154 - 161.
- [37] Parker J. W., Laksin O., Yu C., Lau M. L., Klima S., Fisher R., Scott I., Atwater B. W., *Fiber-optic sensors for pH and carbon dioxide using a self-referencing dye*. Anal. Chem. (1993), 65, 2329 - 2334.
- [38] Offenbacher H., Wolfbeis O. S., Fuerlinger E., *Fluorescence optical sensors for continuous determination of near-neutral pH values*. Sens. Actuators, B (1986), 9, 73 - 84.
- [39] Schulman S. G., Chen S., Bai F., Leiner M. J. P., Weis L., Wolfbeis O. S., *Dependence of the fluorescence of immobilized 1-hydroxypyrene-3,6,8-trisulfonate on solution pH: extension of the range of applicability of a pH fluorosensor*. Anal. Chim. Acta (1995), 304, 165 - 170.
- [40] He X., Rechnitz G. A., *Linear Response Function for fluorescence-based fiber-optic CO₂ sensors*. Anal. Chem. (1995), 67, 2264 - 2268.
- [41] Carraway E. R., Demas J. N., DeGraff B. A., *Luminescence quenching mechanism for microheterogeneous systems*. Anal. Chem. (1991), 63, 332 - 336.
- [42] Carraway E. R., Demas J. N., DeGraff B. A., Bacon J. R., *Photophysics and photochemistry of oxygen sensors based on luminescent transition-metal complexes*. Anal. Chem. (1991), 63, 337 - 342.

6. Effect of the Lipophilic Base in Solid State Optical pCO₂ Sensors

Solid-state optical pCO₂ sensors comprise mostly a pH indicator dye and a quaternary ammonium hydroxide incorporated in a hydrophobic polymer membrane. In this study we investigated a solid-state optical pCO₂ sensor in which the quaternary ammonium ion was replaced by the neutral phosphazene base P₁-t-Oct (PBO) and compared it with a conventional system containing tetraoctylammonium hydroxide (TOA-OH). The basic character of PBO is due to the unshared electron pair of the tertiary nitrogen atom linked to the phosphorus atom by a double bond. The phosphazene base forms together with water the buffer system of the sensor. Both sensor types have dynamic ranges between 0 and 50 hPa pCO₂. They show a completely reversible sensor response. A strong cross-sensitivity towards relative humidity (RH) of the analyte gas was found for the PBO-containing sensor. The ratio protonated form/deprotonated form (HD/D⁻) of the indicator dye increases continuously with decreasing RH. At the same time the sensitivity towards pCO₂ decreases. In the case of the TOA-OH- containing sensor the ratio HD/D⁻ stays nearly constant at RH values above 20%. At lower RH, however, it decreases significantly as well as the sensitivity towards pCO₂. The deviant behaviour of the two sensor types at the removal of water is due to the nature of the respective organic base and the resulting influence on the polarity within the sensor matrix.

6.1 Preliminary remarks

The optimal working range of the solid state pCO₂-sensor part (HPTS/TOA-OH/EC49) of the pCO₂/pO₂-dual sensor described in chapter 4 is between 0 and 10 hPa pCO₂. It is therefore suitable for the detection of respiration activity in marine systems but the sensitivity is too low to resolve pCO₂ changes during photosynthesis (0 - 0.6 hPa pCO₂). However, the HPTS/TOA-OH/EC49 sensor system belongs already to the most sensitive luminescent solid state pCO₂ sensors. The sensitivity of a solid state pCO₂ sensor generally depends on the pKa'

value of the indicator in the sensor polymer matrix, on the CO₂ permeability of the polymer and on the amount and nature of the lipophilic buffer substance added. TOA-OH-containing solid state pCO₂ sensors using HPTS (pK_a = 7.2) show a higher sensitivity towards pCO₂ than comparable sensors using pH indicators with a higher pK_a' such as 5'(6')-carboxy-seminaphthofluorescein. The reason for this are the sterical effects in the HPTS-TOA⁺ ion pair described in chapter 5.3.2. Starting from the HPTS/TOA-OH/EC49 system described in the previous chapter it was attempted to increase the sensor sensitivity by the following approaches: a) HPTS was replaced by 5'(6')-carboxy-11-methyl-seminaphthofluorescein; instead of TOA-OH b) (4',4'' (5'')-di-tert-butyl-dibenzo-18-crown-6)K-OH or c) phosphazene base P₁-t-Oct was used as lipophilic buffer substance. However, none of these approaches led to an increase of the sensor sensitivity towards pCO₂ compared to the HPTS/TOA-OH/EC49 system. Yet, the application of the neutral phosphazene base P₁-t-Oct resulted in fundamental changes in the pCO₂ sensor characteristics. These different properties were investigated in the following comparative study using colorimetric p-xylene blue/base/EC49 membranes as model system.

6.2 Introduction

Solid state pCO₂ optodes are typically composed of a pH indicator dye and a lipophilic organic base incorporated in a hydrophobic polymer, such as ethyl cellulose (see chapter 1.3.2). Compared to Severinghaus type pCO₂ optodes they show faster response times and a negligible cross-sensitivity towards differing sample osmolarities. The lipophilic base which is usually a quaternary ammonium hydroxide (e.g. tetraoctylammonium hydroxide) acts as the buffer system. Nevertheless, (like for the Severinghaus type pCO₂ sensors) only a limited shelf life of the solid state pCO₂ sensors is reported especially when stored in ambient air. This is due to the presence of other acidic gases besides CO₂ such as NO_x or SO₂ which can also permeate into the sensor and protonate the indicator. In contrast to CO₂ this process is not reversible because they form together with water strong acids. But even when stored under nitrogen atmosphere the properties of the sensor change slowly. Initially the sensitivity of the sensor towards CO₂ increases and after a while the indicator passes into its protonated form¹. Several authors suggested a slow decay of the quaternary ammonium via Hofmann degradation as the reason^{2,3}.

In this chapter the possibility of replacing the quaternary ammonium base by a neutral base with a tertiary nitrogen as basic position was tested. The use of phosphazene bases as neutral bases in optical pCO₂ sensors was first suggested by Brinz et al.⁴. The responding behaviour of sensors with the two different base types was compared as to their sensitivity towards pCO₂, their temperature and humidity cross-sensitivity. The deviant characteristics of the sensors due to the nature of the organic base were investigated.

6.3 Experimental

6.3.1 Materials

The organic bases tetraoctylammonium hydroxide (20% in methanol) and phosphazene base P₁-t-Oct (98 %) were purchased from Fluka. Ethyl cellulose (ethoxyl content 49 %) and p-xylene blue (XB) were obtained from Aldrich. Dodecyltrimethylammonium (DTMA) bromide was obtained from Serva. All other chemicals were purchased from Merck. Doubly distilled water was used throughout. The polyester foil (Mylar[®]) utilised as the solid support for the sensor films was purchased from Goodfellow. Nitrogen, carbon dioxide and compressed air (purity > 99 %) as well as the CO₂/N₂ test gas mixtures with CO₂ contents of 0.5 %, 1 %, 3 %, 5 % and 10 % were all obtained from Linde.

6.3.2 Synthesis of the XB-DTMA ion pair

134.0 mg (0.31 mmol) of p-xylene blue sodium salt and 0.5 g NaCl were dissolved in 50 ml water and the dye was titrated with 0.1N HCl until its colour turned from blue to completely yellow, the colour of the monoionic form. 92.5 mg (0.3 mmol) of dodecyltrimethylammonium bromide were dissolved in 50 ml CHCl₃. The dye was extracted into the organic phase by shaking the two phases in a separating funnel. The yellow organic phase was afterwards thrice washed with water and dried over disodium sulfate. The solvent was evaporated and the ion pair was dried in a desiccator over CaCl₂, yielding 71.2 %. Elemental analysis for the XB-DTMA ion pair (C₃₈ H₅₅ N S O₅ (637.9 g/mol)) gave (calc./found): C: 71.55/69.56, H: 8.69/8.14, N: 2.2/1.99.

6.3.3 Preparation of the sensor membranes

A stock solution of the ion pair was prepared by dissolving 52.1 mg XB-DTMA in 3 ml ethanol. 15 g ethyl cellulose (EC49) was dissolved in a mixture of 240 ml toluene and 60 ml ethanol. 518 µl of the dye stock solution were added to the polymer solution. The final sensor cocktails were made up by adding aliquots of the respective organic base to 1 g of the dye polymer solution. The sensor films were fabricated by spreading the cocktails onto dust-free polyester foils with a knife-coating device from Coesfeld. The wet thickness of the sensor films was 120 µm which resulted in a thickness of approximately 6 µm after solvent evaporation. Table 6.1 shows the composition of the resulting sensor membranes. The dry sensors were stored under nitrogen atmosphere in a desiccator over 0.1 N sodium hydroxide solution which acts as a sink for acidic gases.

Table 6.1. Composition of the TOA-OH-containing membranes M1_TOA - M5_TOA and the PBO-containing membranes M1_PBO - M5_PBO.

sensor	TOA-OH/EC [%(w/w)]	sensor	PBO/EC [%(w/w)]	base/polymer fraction [mol/kg dry EC]
M1_TOA	29.0	M1_PBO	17.4	0.6
M2_TOA	23.2	M2_PBO	13.9	0.48
M3_TOA	15.5	M3_PBO	9.3	0.32
M4_TOA	7.7	M4_PBO	4.7	0.16
M5_TOA	3.9	M5_PBO	2.3	0.08

6.3.4 Apparatus

All UV/VIS absorbance spectra as well as the single wavelength absorbance time scans were recorded with a U-3000 UV/VIS double-beam spectrophotometer from Hitachi. During the measurement the sensor film was fixed in a thermostated home-made flow cell. An identical flow cell equipped only with Mylar[®] foil served as reference. For all measurements the humidified analyte gases with varying CO₂ contents were delivered to the sensor film through stainless steel tubings at low flow rates, respectively. Small variations in the flow rate caused no change in the sensor signal which indicates that the pressure in the flow cell did not exceed

the air pressure within this low flow rate range. The humidification of the gases was accomplished by bubbling the gas stream successively through two thermostated fritted wash bottles filled with water. Analyte gases with varying relative humidities were made up by mixing the dry and the humidified gas with a gas blender from Scott Specialty Gases. Fig. 6.1 shows the schematic of the measurement set-up.

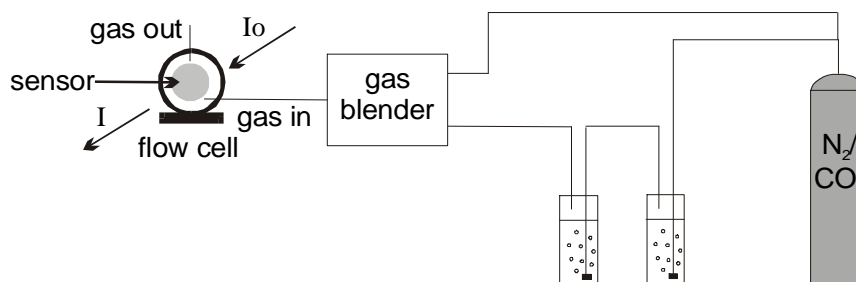


Fig. 6.1. Schematic of the set-up for absorbance measurements at varying humidity of the analyte gas.

6.4 Results and Discussion

6.4.1 Lipophilic organic bases

The solid state pCO₂ sensors investigated in this study had the general composition XB-DTMA/organic base/EC49. Fig. 6.2 depicts the two organic bases used. TOA⁺ is a quaternary ammonium ion with a fixed positive charge, while the phosphazene base PBO is neutral and needs water to form the buffer system of the sensor.

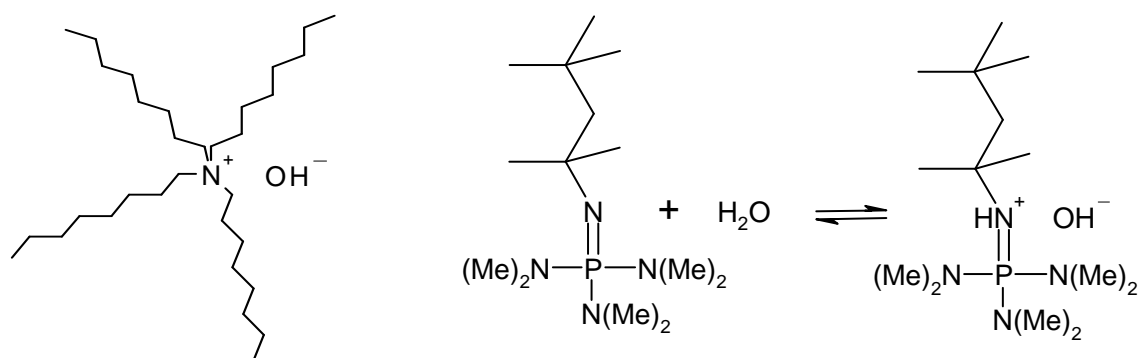
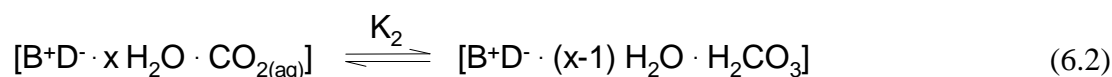
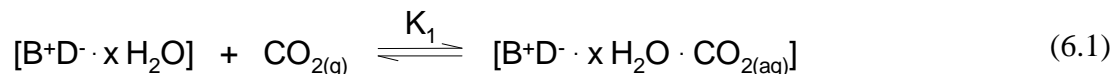
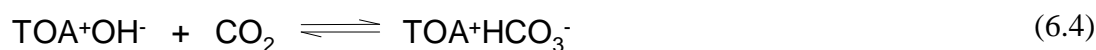


Fig. 6.2. Chemical structure of the investigated organic bases tetraoctylammonium hydroxide TOA-OH (**left**) and phosphazene base P₁-t-Oct PBO (**right**).

The organic base fulfils several functions within the sensor: The positively charged, sterically demanding cation of the base (B⁺) acts as a counterion for the indicator anion (D⁻). Thus the negative charge of the basic form of the dye is stabilised in the nonpolar EC49 matrix. At the same time the sterical hindrance ensures that the ion pairing is not too close so that the indicator can be protonated again at increasing pCO₂ which results in a high sensitivity of the sensor towards CO₂. The sensing reactions are as follows



One sees from these equations that the presence of some molecules of water of solvation within the membrane is essential for the formation of carbonic acid from CO₂. The addition of higher amounts of base prolongs the shelf life of the solid state pCO₂ sensor because the base acts also as a buffer for acidic gases other than CO₂ (e.g. NO_x, SO₂) and so keeps the indicator in its deprotonated form. The base as well binds some of the CO₂ diffusing into the sensor according to the following equations



As a result of these reactions the sensitivity of the sensor should decrease with increasing amount of base at low pCO₂. On the other hand the sensor membranes contain a considerable part of organic base. Compared to the EC49 content these are 3.9 % (w/w) and 2.3 % (w/w) in the sensors with the lowest and 29.0 % (w/w) and 17.4 % (w/w) in the sensors with the highest amount of base investigated for TOA-OH and PBO, respectively (see Table 6.1). Due to this fact the influence of the base on the polymer matrix properties can not be neglected. Although both bases have lipophilic residues to make them soluble in the EC49, TOA-OH has fixed charges while PBO forms together with water the charged buffer system of the sensor. In any case the polarity of the sensor matrix increases with increasing base content. Thus the dissociation of H₂CO₃ should be facilitated and therefore also the protonation of the indicator which increases the sensitivity of the pCO₂ sensor.

6.4.2 Sensitivity towards pCO₂ with different amounts of organic base

In aqueous solution the acidic form (HD) of the applied pH indicator XB (pK_a ~ 8.9) has an absorbance maximum at 438 nm and the basic form (D⁻) at 595 nm. Incorporated in the sensor membrane absorbance maxima of 436 nm (HD) and 612 nm (D⁻) have been found. Fig. 6.3 shows the absorbance spectra of sensor membranes with TOA-OH (left) and PBO (right), respectively. The measurements were made at a constant temperature of 298 K and 100% RH of the analyte gases. Except for the different organic bases the sensor composition was identical. In both cases the absorbance of the basic form at 612 nm decreases with increasing pCO₂.

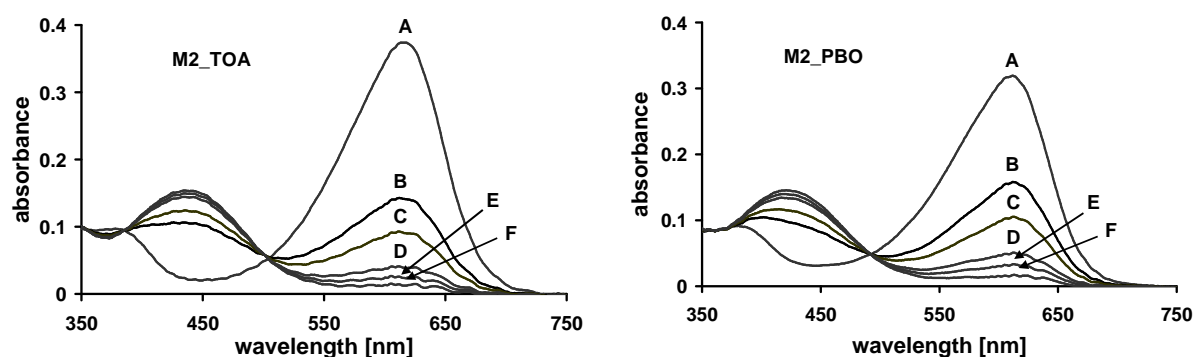


Fig. 6.3. Absorbance spectra of M2_TOA (left) and M2_PBO (right) at 0 % (A), 0.5 % (B), 1 % (C), 3 % (D), 5 % (E) and 10 % (F) CO₂ (T = 298 K; 100% RH). The absorbance of the deprotonated form of XB at 612 nm decreases with increasing pCO₂.

The indicator was added in form of an 1:1 ion pair with DTMA as counterion of the sulfonic acid group of the sulfonphthalein dye. Thus, the presence of sodium ions in the sensor solution was prevented which can cause an opacity of the final sensor film.

The following equation can be derived from the equilibria 6.1-3

$$\frac{A_0}{A} = 1 + K \cdot pCO_2 \quad (6.6)$$

where A_0 is the absorbance of the sensor film at 612 nm (D^-) in a stream of humidified nitrogen, A is the absorbance of D^- at varying pCO_2 and $K = K_1 \cdot K_2 \cdot K_3$. In Fig. 6.4 A_0/A is plotted versus pCO_2 for membranes containing different amounts of TOA-OH (left) and PBO (right) according to Table 6.1. The gradients of the calibration straight lines (eq. 6.6) reflect the sensitivity of the sensors towards pCO_2 .

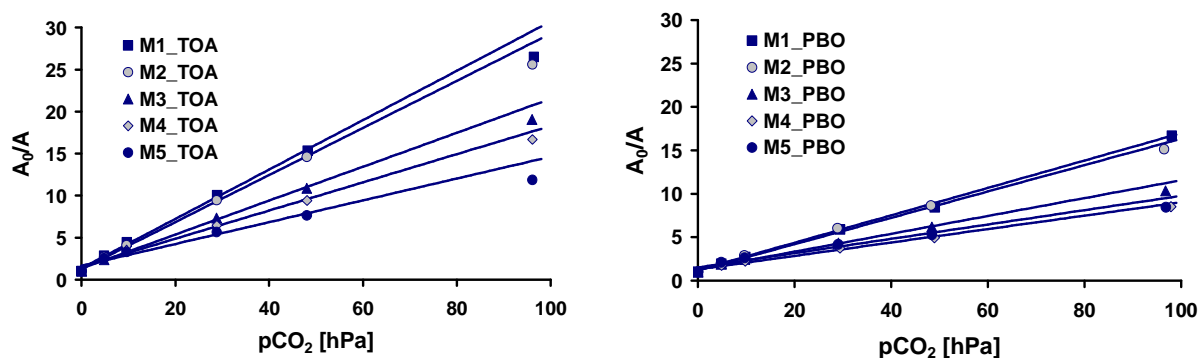


Fig. 6.4. A_0/A versus pCO_2 plots of membranes containing varying amounts of TOA-OH (**left**) and PBO (**right**) ($T = 298$ K; 100% RH). The smallest base amount applied was $8 \cdot 10^{-2}$ mmol base/g dry EC (M5). The highest base content was $6 \cdot 10^{-1}$ mmol base/g dry EC (M1).

The smallest base amount applied was $8 \cdot 10^{-2}$ mol base/kg dry EC49 (M5). This was the minimum base content necessary to initially deprotonate the indicator dye completely. Sensors with a higher base content than $6 \cdot 10^{-1}$ mol base/kg dry EC49 (M1) showed a slight opacity, especially those containing PBO. One can see that the PBO-comprising membranes are not as sensitive towards pCO_2 as those containing TOA-OH. At a transition from nitrogen to 4.8 hPa pCO_2 for instance the absorbance at 612 nm declines to 41 % (TOA-OH) and 52 % (PBO) of A_0 , respectively. Nevertheless, PBO is applicable as organic buffer in pCO_2 sensors due to its high basicity. All sensors were completely reversible. The deviation from linearity at higher A_0/A values possibly originates in the growing influence of variations in A caused by light scattering. In both cases the sensitivity towards pCO_2 increased with increasing base content due to the higher polarity of the sensor matrix as described above. Fig. 6.5 shows a

plot of K versus base content at 48.0 hPa pCO₂ for the PBO- and TOA-OH-containing membranes.

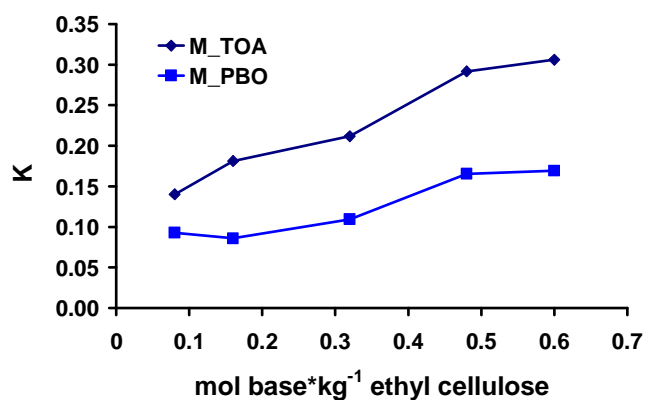


Fig. 6.5. Effect of the base content on the sensor sensitivity at a constant pCO₂ of 48.0 hPa.

The sensitivity of the membranes with base contents lower than $3.2 \cdot 10^{-1}$ mol/kg dry EC49 does not change significantly for both sensor types. Although the sensor matrix becomes more polar due to the increasing base amount this effect is partly compensated by the also increasing buffer capacity of the sensors. At a base content between $3.2 \cdot 10^{-1}$ and $4.8 \cdot 10^{-1}$ mol/kg dry EC49, however, K increases considerably which indicates a strong change of the polarity within the sensor matrix. For the M_PBO membranes the slope in K is less steep compared to the M_TOA sensors. Here the base has no fixed charge but forms the charged species in an equilibrium reaction (eq. 6.5) i.e. a certain fraction of PBO still is existent in its neutral form.

6.4.3 Temperature dependence

Solid state pCO₂ sensors are known to have a strong cross-sensitivity towards temperature. Therefore the temperature effect was investigated for the membranes M3_PBO and M3_TOA. Due to the lower solubility of CO₂ in the sensor matrix at higher temperatures the sensitivity decreases with increasing temperature. The cross-sensitivity towards temperature is less pronounced in the case of M3_PBO (Fig. 6.6). We think the reason for this fact is that the partial pressure of the water vapour in the humidified analyte gas and therefore also in the sensor membrane increases at higher temperature. This causes a shift towards the side of the

charged species in eq. 6.5. Due to the rising polarity of the membrane also the sensitivity towards pCO₂ is increased which partly compensates the effect of lower solubility of CO₂.

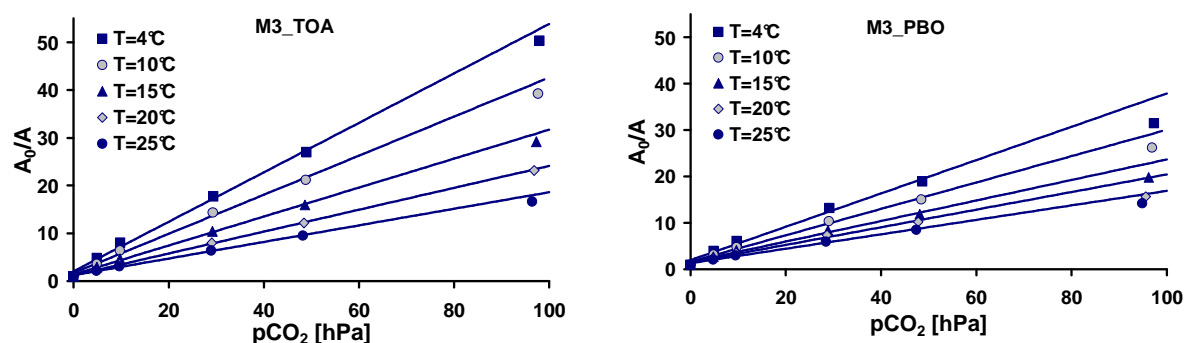


Fig. 6.6. Influence of the temperature on the sensor response of M3_TOA (left) and M3_PBO (right) (RH= 100%).

All calibration curves could be fitted with eq. 6.7. A plot of $\ln K$ versus $1/T$ showed a linear correlation for both sensors in the examined temperature range (data not shown). The standard enthalpy ΔH_R^0 and the standard entropy ΔS_R^0 of the protonation reaction of the indicator can be derived from the gradient and the intercept of the resulting straight lines according to the following equation given by Arrhenius

$$\ln(K) = -\frac{\Delta H_R^0}{R} \cdot \frac{1}{T} + \frac{\Delta S_R^0}{R} \quad (6.7)$$

where R is the molar gas constant 8.3145 J/(mol*K) (Table 6.2).

Table 6.2. Thermodynamic data derived from the Arrhenius plots for M3_TOA and M3_PBO.

sensor	gradient	intercept	ΔH_R^0 [kJ/mol]	ΔS_R^0 [J/(mol*K)]
M3_TOA	4.62 ± 0.19	-10.20 ± 0.65	-38.4 ± 1.6	-84.8 ± 5.4
M3_PBO	3.46 ± 0.07	-6.39 ± 0.24	-28.8 ± 0.6	-53.2 ± 2.0

6.4.4 Effect of relative humidity

For all previous measurements humidified gases were applied. Thereby no important difference in the characteristics of the two sensor types have been observed. Yet with analyte gases of varying RH completely different sensor responses were obtained. Fig. 6.7 shows the absorbance versus time scans at 612 nm for M3_TOA (left) and M3_PBO (right).

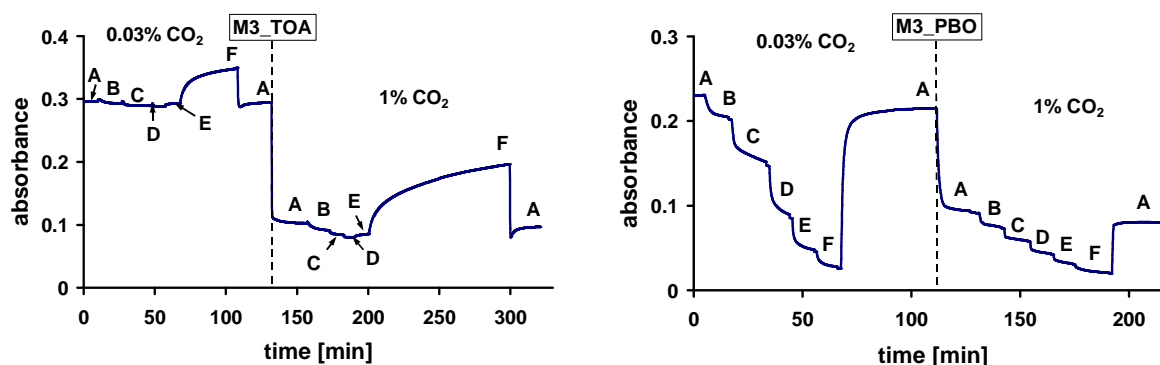


Fig. 6.7. Absorbance versus time scans at 612 nm of M3_TOA (left) and M3_PBO (right). The RH was adjusted to 100 % (A), 80 % (B), 60 % (C), 40 % (D), 20 % (E) and 0 % (F) at a constant pCO₂ of 0.03 % and 1 %.

The RH of the analyte gas was adjusted in 20 % steps from 100 % (A) to 0 % (F). Measurements were made with compressed air (0.03 % CO₂) and 1 % CO₂ in nitrogen test gas. The TOA-OH-containing sensor showed nearly no cross-sensitivity towards humidity in a range from 100 % to 20 % RH. Below this value, however, the absorbance at 612 nm increases significantly. In contrast to this the absorbance of the M3_PBO membrane declines continuously with decreasing RH. These tendencies were observed for both CO₂ partial pressures. The bar diagrams in Fig. 6.8 depict the normalised absorbance intensities at varying RH for M3_TOA (left) and M3_PBO (right).

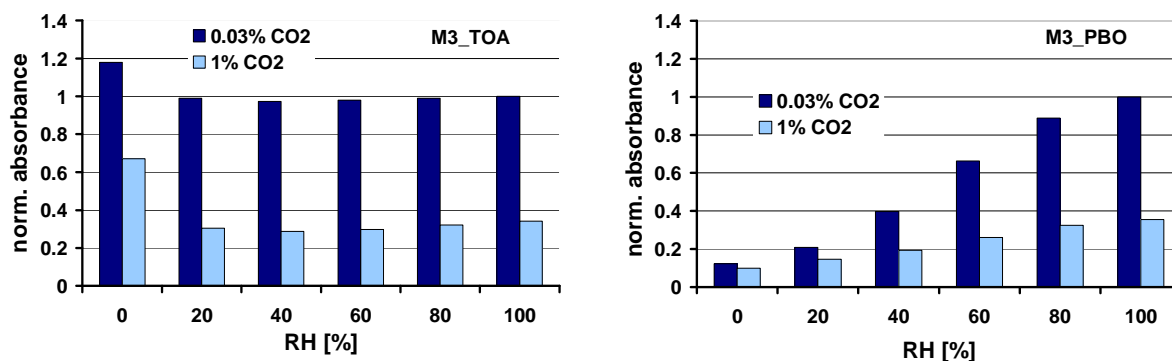


Fig. 6.8. Normalised absorbance intensities at varying RH for M3_TOA (left) and M3_PBO (right) at 0.03 % CO₂ and 1 % CO₂.

The deviant sensor response is due to the characteristics of the respective organic base. In the M3_TOA sensor water is only needed for the hydration of CO₂. Some molecules of water of solvation are sufficient to enable this pivotal reaction. In a dry gas stream these traces of water are partly removed from the sensor and the formation of H₂CO₃ is inhibited. As a consequence the equilibrium reactions of eqs. 6.1-3 are shifted towards the side of the deprotonated indicator even at the presence of CO₂.

In the M3_PBO sensor water is not only needed for the formation of H₂CO₃ from CO₂ but also to form the charged buffer HPBO⁺OH⁻. At the removal of water the already nonpolar character of the EC49 matrix even increases. TOA⁺ with its fixed charge which also requires a counterion for the reason of electroneutrality forces the existence of ions in this nonpolar matrix at any water content. HPBO⁺, on the other hand, is able to evade a decreasing polarity by shifting into its deprotonated, neutral form according to eq. 6.8.

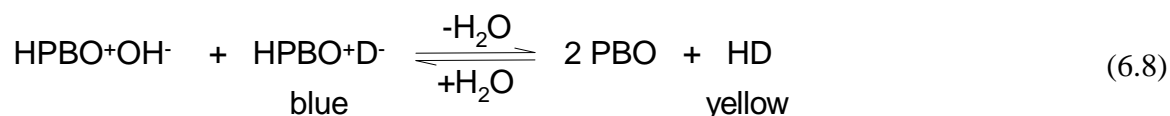


Fig. 6.9 shows the normalised absorbance spectra of M3_TOA (left) and M3_PBO (right) equilibrated with compressed air at varying RH.

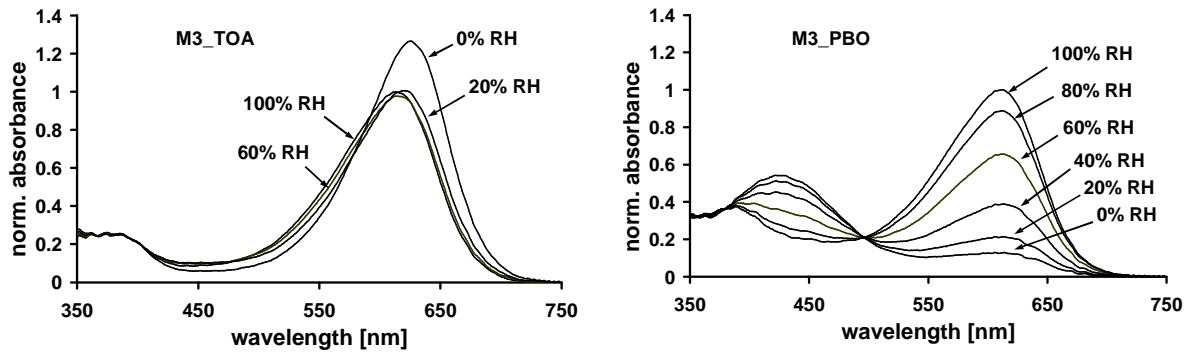


Fig. 6.9. Normalised absorbance spectra of M3_TOA (left) and M3_PBO (right) at 0.03 % CO₂. RH changes from 100 % to 0 %.

As can be expected from eqs. 6.1-3 and 6.8, also the sensitivity towards CO₂ is affected (Fig. 6.10). It decreases continuously with decreasing RH for M3_PBO (right). M3_TOA (left) shows a strong decrease at RH lower than 20 %. In both cases even at 0% RH the sensitivity towards CO₂ does not decline to zero. This proves that the water traces present in the sensor films are not completely removed.

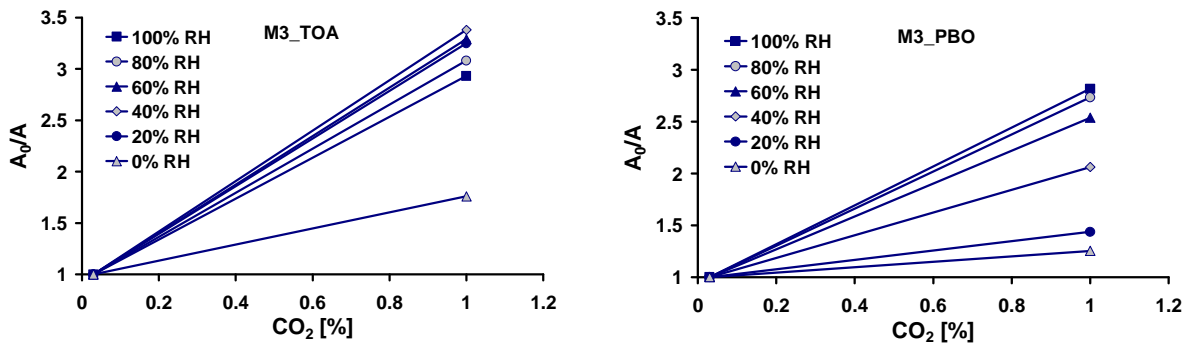
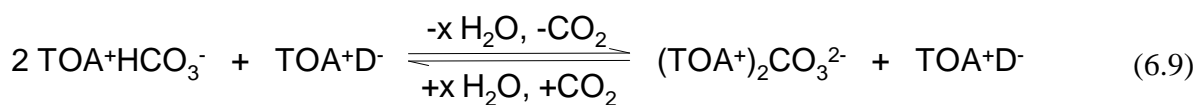


Fig. 6.10. A₀/A versus % CO₂ plots of M3_TOA (left) and M3_PBO (right) at RH values of 100 % (A), 80 % (B), 60 % (C), 40 % (D), 20 % (E) and 0 % (F).

The complete removal of water of solvation from the membranes (e.g. storage over P₂O₅) leads to insensitivity towards CO₂ and enhances the basicity of the buffer in the TOA-OH-containing sensor according to eq. 6.9.



6.4.5 Use of other neutral organic bases

Like phosphazene bases tertiary amines are neutral organic bases with a tertiary nitrogen as basic position. Due to the structural analogy to PBO a similar behaviour of tert. amines within solid state pCO₂ sensors should be expected. In general the basicity of tert. amines is well below that of PBO (${}^{\text{MeCN}}K_{\text{HB}}(\text{PBO}) \sim 26.5$, ${}^{\text{MeCN}}K_{\text{HB}}(\text{Et}_3\text{N}) \sim 18.5^{5,6}$ and ${}^{\text{MeCN}}K_{\text{HB}}(\text{Bu}_3\text{N}) \sim 18.1^7$). It decreases slightly with increasing length of the alkyl residues since the lipophilic side chains destabilise the positive charge of the protonated nitrogen. The tested amines trioctylamine and tributylamine are not capable to initially deprotonate the pH indicator. Sensor films prepared with triethylamine showed the blue colour of the basic form of XB directly after the evaporation of the solvent but turned to the acidic yellow form again within one minute. This is due to the high vapour pressure of triethylamine (70 hPa at 20 °C) which causes the fast evaporation of the base from the thin sensor layer. Like triethylamine all neutral bases discussed so far are more or less volatile. Another tested amine suitable as organic base was triethanolamine. It has a very low vapour pressure ($5 \cdot 10^{-5}$ hPa at 40 °C) due to the hydroxyl groups which can interact via hydrogen bonds. Triethanolamine is significantly less basic (pKa ~ 7.8) than triethylamine (pKa ~ 10.8). This proves that the capability to initially deprotonate the indicator can not only be explained by the basicity of the base. In contrast to the sterically demanding trioctylamine and tributylamine, triethylamine and triethanolamine can form a very close ion pair with the indicator. Thus the charges of the ions are better shielded from the non-polar environment. In the case of triethanolamine the hydroxyl groups further stabilise the ions especially at high buffer contents. But the formation of a close ion pair also makes the protonation of the dye more difficult and therewith may result in a lower sensitivity towards CO₂.

6.4.6 Possible Utilisation of PBO-containing pCO₂ sensors as humidity sensors

The investigated solid state pCO₂ sensor containing PBO as neutral organic base shows characteristics which seem to make it also applicable as humidity sensor. The sensor dynamic covers the whole RH range from 100 % to 0 % (Figs. 6.8 and 6.9). However, a crucial precondition for this application is to keep the pCO₂ constant throughout the measurement. The examined system with XB used as pH indicator is extremely sensitive towards pCO₂ because of the high pKa value of the dye. Small changes in the pCO₂ therefore cause

substantial errors in the measured RH. This can be reduced by using an indicator with a lower pK_a like m-cresol purple (pK_a ~ 8.3). PBO, however, is slightly volatile which causes a change in the sensor properties after a while. At a low RH the effect is even more pronounced since here the main part of the base is existent in its neutral form. Thus PBO-containing sensors are not suitable for gas phase measurements but are limited to the detection of dissolved CO₂. The use of triethanolamine as neutral base within a humidity sensor seems more convenient. However, this application was not further investigated within the scope of this work.

6.5 Conclusion

The neutral organic phosphazene base investigated in this study proved to be perfectly suitable for the application as a buffer substance within solid state optical pCO₂ sensors. Although sensors incorporating PBO are not superior in respect of their sensitivity towards pCO₂, results comparable to TOA-OH-containing sensors were obtained. Both sensor types showed similar t_{90} values. The response and recovery times at a change from 0 to 10 % CO₂ were 6 s/390 s and 4 s/458 s for M3_TOA and M3_PBO, respectively. The fact that PBO bears no fixed positive charge results in a strong cross-sensitivity of the sensor towards the RH of the analyte gas. Furthermore the neutral form of PBO is slightly volatile. On this account this sensor is only applicable for the detection of dissolved CO₂ but not for pCO₂ measurements in the gas phase. A cross-sensitivity towards RH has no relevance for the practical use of sensor films with TOA-OH in gas phase measurements. Here the sensor response is only influenced at RH values below 20%. In a surrounding with a constant pCO₂ like ambient air it is conceivable to apply membranes containing neutral, non-volatile organic bases as humidity sensors.

6.6 References

- [1] Weigl B. H., Wolfbeis O. S., *Sensitivity studies on optical carbon dioxide sensors based on ion pairing*. Sens. Actuators B (1995), 28, 151 - 156.
- [2] Mills A., Chang Q., McMurray N., *Equilibrium studies on colorimetric plastic film sensors for carbon dioxide*. Anal. Chem. (1992), 64, 1383 - 1389.

- [3] Waldner A., Barnard S. M., *Optical carbon dioxide sensors*. US Pat. 6 969 857 (2002).
- [4] Brinz T. et al., *Optical sensor*. US Pat. 6 682 935B2 (2004).
- [5] Schwesinger R. et al., *Extremely strong, uncharged auxiliary bases; monomeric and polymer-supported polyaminophosphazenes (P2-P5)*. Liebigs Ann. (1996), 1055 - 1081.
- [6] http://www.sigmaaldrich.com/Brands/Fluka___Riedel_Home/Literature/ChemFiles/Vol_3_No_1/Phosphazene_Bases.html
- [7] Galezowski W., Grzeskowiak I., Jarczewski A., *Kinetic study of the reactions of various types of C-acids with amine bases in acetonitrile. An unusual effect of common BH⁺ cation on the rate constants*. Can. J. Chem./Rev. Can. Chim. (1999), 77, 1042 - 1049.

7. Summary

This thesis describes the development and characterisation of optical chemical sensor materials optimised for the determination of pH, pCO₂ and pO₂ distributions in marine systems via time-resolved luminescence imaging. A new measurement concept for time-resolved mapping of the parameter combinations pH/pO₂ and pCO₂/pO₂ with luminescent dual sensors is introduced. Application examples of planar optodes for imaging of pH and pH/pO₂ in natural marine sediments are shown and discussed.

Chapter 1 gives a short introduction into the importance of pH, pCO₂ and pO₂ in marine biogeochemistry, followed by an overview of existing sensors for the three parameters in general and in particular of sensors typically used for studies in marine systems. Furthermore, referencing methods for measurements with luminescent optical chemical sensors are described.

The measuring instruments applied in this work are described in detail in Chapter 2. Modifications made to the imaging set-up are presented and the newly build integrated light source modules based on Luxeon™ V Star chip LEDs are characterised with respect to the intensity and homogeneity of the excitation light field and the resulting irradiance at the optode surface.

A set of novel luminescent pH sensor materials with a dynamic range optimised to the predominant pH range in marine systems (pH 7.2 - pH 9.2) is presented in Chapter 3. They are based on two new lipophilic carboxyfluorescein derivatives DHFA and DHFAE applied as pH indicators and immobilised in a polyurethane-type hydrogel matrix. Ratiometric dual wavelength referencing is possible with DHFAE-containing sensors and both indicators are suitable for DLR measurements using polyacrylonitrile-derived nanoparticles incorporating Ru(dpp)₃ as reference standard. The sensors are characterised as to their stability and cross-sensitivity towards IS and temperature. A DHFAE-based DLR sensor foil is successfully applied to visualise pH gradients and dynamical pH changes during a 24 h day/night cycle in a natural marine sediment sample via time-resolved imaging of pH.

In Chapter 4, a novel three-window measurement scheme for time-resolved, internally referenced imaging of pH and pO₂ with planar, dual optodes is introduced. The dual hybrid membrane examined is composed of a single polyurethane-type hydrogel layer incorporating DHFA as pH indicator and the Pt(PFPP) complex as oxygen indicator. In principle, the three-window scheme allows the detection of the pH signal as a dual signal dependent on pH and

pO_2 and the pO_2 signal as a pure signal only dependent on pO_2 . A generally applicable procedure to generate a two-dimensional function describing the pH signal in dependence of pH and pO_2 is introduced. Since the hybrid membrane concept leads to an additional influence of pH on the measured pO_2 signal an iteration procedure is necessary to calculate the pH and pO_2 values from the measured raw data of the dual sensor. The sensor stability and the IS and temperature effect are investigated for the DHFA/Pt(PFPP) dual sensor. The working range of the dual sensor (pH 7 - pH 9 and 0 - 400 hPa pO_2) meets the requirements for an application in marine systems. It was used for the mapping of pH and pO_2 in a marine sandy sediment sample as a proof of principle.

In Chapter 5, a luminescent planar dual optode for the intrinsically referenced mapping of pCO_2 and pO_2 is described. Imaging measurements and their evaluation are performed according to the method introduced in chapter 4. Again the sensor chemistry for both analytes (HPTS/TOA-OH as pCO_2 -sensing system and $Ru(dpp)_3$ as oxygen indicator) is dissolved in a single layer polymer matrix, which on one hand reduces the long-term stability of the sensor but on the other hand results in a high sensor precision due to the homogeneous distribution of the indicators. Due to a second silicone layer the planar dual optode can be applied for the detection of dissolved gases. The optimal working range of the sensor is 0 - 10 hPa pCO_2 and 0 - 250 hPa pO_2 . An iterative evaluation is necessary for the recovery of pCO_2 and pO_2 from a dual sensor measurement at CO_2 partial pressures near 0 hPa, however, at $pCO_2 > 2.5$ hPa this interfering effect is negligible. The dynamic range of the pCO_2 -sensing part of the dual sensor is suitable for the detection of most processes in marine systems, which alter the pCO_2 such as aerobic or anaerobic respiration. However, its sensitivity is too low for the detection of pCO_2 changes during photosynthesis (0 - 0.6 hPa pCO_2).

In Chapter 6, the influence of the nature of the lipophilic buffer substance on the properties of solid state optical pCO_2 sensors is investigated in order to increase the sensor sensitivity. Although sensors incorporating the neutral organic phosphazene base PBO are not superior in respect of their sensitivity towards pCO_2 , results comparable to TOA-OH-containing sensors are obtained. The fact that PBO bears no fixed positive charge results in a strong cross-sensitivity towards the RH of the analyte gas.

8. Abbreviations, Acronyms and Symbols

A	Absorbance intensity
A_{em}	Luminescence intensity integral (image) recorded after the excitation light pulse
A_{ex}	Luminescence intensity integral (image) recorded during the excitation light pulse
ASW	Artificial seawater
c	Molar concentration
CCD	Charge coupled device
CHFOE	2'-chloro-7'-hexylfluorescein octadecyl ester
CTA	Hexadecyltrimethylammonium
D4	Polyurethane-based hydrogel
DHCF	5(6)-Carboxy-2',7'-dihexylfluorescein
DHFA	2',7'-Dihexyl-5(6)-N-octadecyl-carboxamidofluorescein
DHFAE	2',7'-Dihexyl-5(6)-N-octadecyl-carboxamidofluorescein ethyl ester
DIC	Dissolved inorganic carbon
DLR	Dual lifetime referencing
DMF	N,N-Dimethylformamide
DMSO	Dimethyl sulfoxide
DTMA	Dodecyltrimethylammonium
EC49	Ethyl cellulose (49 % ethoxyl content)
Φ	Phase shift
F	Fluorescence intensity

fd	Frequency domain
f_{mod}	Modulation frequency
f_x	Activity coefficient of species x
HPTS	8-Hydroxypyrene-1,3,6-trisulfonic acid sodium salt
I	Luminescence intensity
IS	Ionic strength
K_{sv}	Stern-Volmer constant
λ	Wavelength
LED	Light emitting diode
$\lambda_{\text{em.}}$	Wavelength of the emission maximum
$\lambda_{\text{exc.}}$	Wavelength of the excitation maximum
LIX	Liquid ion-exchanger
M	mol/L
MFC	Mass flow controller
NMR	Magnetic nuclear resonance
PAH	Polycyclic aromatic hydrocarbons
PBO	Phosphazene base P ₁ -t-Oct
pCO ₂	Carbon dioxide partial pressure
PHEMA	Poly(2-hydroxyethyl methacrylate)
pixel	(photosensitive) Picture elements
pKa	negative decadic logarithm of an acid dissociation constant
PMMA	Poly(methyl methacrylate)
PMT	Photomultiplier tube
pO ₂	Oxygen partial pressure

ppm	Parts per million
Pt(PFPP)	Platinum(II) meso-tetrakis-(pentafluorophenyl)-porphyrin
PTFE	Polytetrafluoroethylene
PVC	Polyvinyl chloride
QY	Quantum yield
R	Intensity integral (image) ratio
RET	Resonance energy transfer
RH	Relative humidity
RLD	Rapid lifetime determination
Ru(dpp) ₃	Ruthenium(II) tris-(4,7-diphenyl-1,10-phenanthroline)
Ru(phen) ₃	Ruthenium(II) tris-(1,10-phenanthroline)
S	Salinity
SNAFL	Seminaphthofluorescein
SNARF	Seminaphthorhodafluor
τ	Luminescence lifetime
T	Temperature
t ₉₀	Response time (time required for a 90 % signal change)
td	Time domain
TOA	Tetraoctylammonium
TRIS	Tris-(hydroxymethyl)aminomethane
TTL	Transistor-transistor logic
UV	Ultraviolet
VIS	Visible spectrum
XB	p-Xylenol blue

9. Curriculum Vitae

Name:	Schröder	
Vorname:	Claudia Regina	
Geburtsdatum:	06.01.1970	
Geburtsort:	Pirmasens (Rheinland-Pfalz)	
Nationalität:	deutsch	
Schulbildung:	1976 - 1980	Grundschule Heßheim
	1980 - 1983	Staatliche Realschule Frankenthal
	1983 - 1986	Realschule Pegnitz
	07/1986	Abschluss: Mittlere Reife
	1991 - 1993	Berufsoberschule Miesbach
	07/1993	Abschluss: Fachgebundene Hochschulreife
Berufsausbildung:	1986 - 1988	Berufsfachschule für Diätetik, Hof Abschluss: Diätassistentin (Staatl. Prüfung)
Berufliche Tätigkeit:	10/1988 - 02/1990	Diätassistentin, Heilbad Bad Neustadt/Saale
	02/1990 - 08/1991	Diätassistentin, Höhenklinik Bischofsgrün
	09/1993 - 10/1994	Telefonistin, DPD Nürnberg
Studium:	11/1994 - 10/1996	Grundstudium Chemie (Diplom), Universität Regensburg
	11/1996 - 03/1999	Hauptstudium Chemie (Diplom), Universität Regensburg
	03/1999	Diplomprüfung
	06/1999 - 05/2000	Diplomarbeit am Institut für Analytische Chemie, Chemo- und Biosensorik, Universität Regensburg Titel: <i>Immobilisierung und Charakterisierung redoxaktiver Indikatorfarbstoffe als Basis für die Entwicklung optischer Redoxsensoren</i>

05/2000 Abschluss: Diplom Chemikerin

10/2000 - 10/2006 Promotion am Institut für Analytische
Chemie, Chemo- und Biosensorik,
Universität Regensburg

Titel: *Luminescent Planar Single and
Dual Optodes for Time-Resolved Imaging
of pH, pCO₂ and pO₂ in Marine Systems*

10. List of Publications

Diploma Thesis

Immobilisierung und Charakterisierung redoxaktiver Indikatorfarbstoffe als Basis für die Entwicklung optischer Redoxsensoren, Institute for Analytical Chemistry, Chemo- and Biosensors, University of Regensburg (2000)

Papers

1. Schroeder C. R., Klimant I., *The influence of the lipophilic base in solid state optical $p\text{CO}_2$ sensors: a comparative study*. Sens. Actuators B (2005), 107, 572 - 579.
2. Schroeder C. R., Weidgans B. M., Klimant I., *pH Fluorosensors for use in marine systems*. Analyst (2005), 130, 907 - 916.
3. Stahl H., Glud A., Schroeder C. R., Klimant I., Tengberg A., Glud R. N., *Time-resolved pH imaging in marine sediments with a luminescent planar optode*. Limnol. Oceanogr.: Methods (2006), in press.
4. Schroeder C. R., Polerecky L., Klimant I., *Time-resolved pH/ $p\text{O}_2$ Mapping with Luminescent Hybrid Sensors*. Anal. Chem. (2006), accepted.
5. Schroeder C. R., Neurauter G., Wolfbeis O. S., Klimant I., *Luminescent Dual Sensor for Time-resolved Imaging of $p\text{CO}_2$ and $p\text{O}_2$ in Aquatic Systems*. Microchim. Acta (2006), submitted.
6. Borisov S. M., Neurauter G., Schroeder C. R., Wolfbeis O. S., *Modified Dual Lifetime Referencing Method for Simultaneous Optical Determination and Sensing of Two Analytes*. Appl. Spectrosc. (2006), 60, in press.

Poster Presentations

1. Schröder C., Klimant I., *Use of neutral bases for solid-state optical pCO₂ sensors.* Europt(r)ode VI, Manchester, UK (2002)
2. Schröder C., Arain S., Weidgans B., Klimant I., *Novel fluorescein derivatives for pH measurements in the neutral and basic pH range.* 8th Conference on Methods and Applications of Fluorescence (MAF), Prague, Czech Republic (2003)
3. Polerecký L., Franke U., E. Precht, Schröder C., Grunwald B., Holst G., de Beer D., Klimant I., *Use of planar optodes in marine microbiology – overview of most recent applications.* Europt(r)ode VII, Madrid, Spain (2004)
4. Schröder C., Polerecký L., Franke U., Klimant I., *pO₂/pH and pO₂/pCO₂ hybrid optodes for 2D-sensing in marine systems.* Europt(r)ode VII, Madrid, Spain (2004)

11. Appendix

11.1. Partial pressure - concentration conversion table for carbon dioxide and oxygen

The concentrations of carbon dioxide and oxygen can be calculated from the partial pressures by means of Henry's Law with the Henry constants $K_H(\text{CO}_2)^1 = 2.85 \cdot 10^{-5} \text{ mol L}^{-1} \text{ hPa}^{-1}$ and $K_H(\text{O}_2)^2 = 1.24 \cdot 10^{-6} \text{ mol L}^{-1} \text{ hPa}^{-1}$ ($T = 25^\circ\text{C}$)

$$\text{Henry's Law:} \quad c(X) = K_H(X) \cdot p_X$$

where c_X represents the concentration in mol L^{-1} and p_X the partial pressure in hPa of carbon dioxide or oxygen, respectively:

$p\text{CO}_2$ [hPa]	$c(\text{CO}_2)$ [$\mu\text{mol L}^{-1}$]	$p\text{O}_2$ [hPa]	$c(\text{O}_2)$ [$\mu\text{mol L}^{-1}$]
0	0	0	0
1	28.46	5	6.22
2	56.93	10	12.44
3	85.39	20	24.87
4	113.85	30	37.31
5	142.32	40	49.74
6	170.78	50	62.18
8	227.71	100	124.35
10	284.63	150	186.53
12	341.56	200	248.70
14	398.48	300	373.06
16	455.41	400	497.41
18	512.34	500	621.76
20	569.26	600	746.11

11.2. List of Suppliers

Company	Location	Homepage
Aldrich	Taufkirchen, Germany	www.sigmaaldrich.com
Bruker BioSpin	Rheinstetten, Germany	www.bruker-biospin.de
Büchi	Flawil, Switzerland	www.buchi.com
Cardiotech	Wilmington, MA, USA	www.cardiotech-inc.com
Carl Roth	Karlsruhe, Germany	www.carl-roth.de
Coesfeld	Dortmund, Germany	www.coesfeld.com
Edmund Industrie Optik	Karlsruhe, Germany	www.edmundoptics.com
Fluka	Buchs, Switzerland	www.sigmaaldrich.com
Frontier Scientific	Carnforth, UK	www.frontiersci.com
Gilson	Bad Camberg, Germany	www.gilson.com
Goodfellow	Bad Nauheim, Germany	www.goodfellow.com
Hamamatsu Photonics Deutschland	Herrsching, Germany	sales.hamamatsu.com
Heraeus	Hanau, Germany	www.heraeus.de
Hitachi	Düsseldorf, Germany	www.hitachi.de
Linde	Höllriegelskreuth, Germany	www.linde-gas.de
Linos Photonics	München, Germany	www.linos-photonics.com
Lumileds	San Jose, CA, USA	www.lumileds.com
Mallinckrodt Backer	Deventer, Netherlands	www.mallbaker.com
Merck	Darmstadt, Germany	www.merck.de
MKS Instruments Deutschland	München, Germany	www.mksinst.com
Nichia	Nürnberg, Germany	www.nichia.com
PCO	Kelheim, Germany	www.pco.de
PreSens	Regensburg, Germany	www.presens.de
Radiometer Danmark	Bronshøj, Denmark	www.radiometer.dk
Research Systems	Boulder, CO, USA	www.itvis.com
Schott	Mainz, Germany	www.schott.com
Scott Specialty Gases	Breda, Netherlands	www.scottgas.com
Serva	Heidelberg, Germany	www.servade.com
SLM-Aminco	Rochester, NY, USA	www.thermo.com

Stanford Research Systems	Sunnyvale, CA, USA	www.thinksrs.com
Thermo Electron	Bremen, Germany	www.thermo.com
Wacker-Chemie	München, Germany	www.wacker.com
WTW	Weilheim, Germany	www.wtw.com

11.3. Source code examples of the VBA applications used for the evaluation of the dual sensor measurements

11.3.1. Extraction of the image data matrix from the IDL raw data file

Sub imagematrix()

For k = 1 To 480 'number of image rows/blocks of data

 m = 8 'begin column for image matrix

 p = (k - 1) * 107 'auxiliary variable: skips already read-out image rows

 For i = 1 To 27 'auxiliary variable: position and number of data points per image row

 s = p + i

 For n = 1 To 6

 Wert = Cells(s, n).Value

 Cells(k, m) = Wert

 m = m + 1

 Next n

 Next i

Next k

Range("H1:FN480").Select

 Selection.Copy

 Sheets("Spalte 1-162").Select

 Range("A1").Select

 ActiveSheet.Paste

End Sub

11.3.2. Number of iteration steps required for the evaluation of the pH-pO₂ dual sensor measurements (Chapter 4.3.4.4)

Sub pH_pO2iteration_test()

'Parameters for the correction of the pO₂ measurement

'Parameters: DeltatauO2

DtauB1 = Cells(4, 7).Value

DtauB2 = Cells(5, 7).Value

Dtauxo = Cells(6, 7).Value

Dtaudx = Cells(7, 7).Value

'Parameters: tauO2mean

tau0 = Cells(9, 7).Value

f1 = Cells(10, 7).Value

Ksv = Cells(11, 7).Value

delta_t = Cells(13, 7).Value

'Parameters for the correction of the pH measurement

'Parameters: C1

C1a = Cells(18, 7).Value

C1b = Cells(19, 7).Value

C1c = Cells(20, 7).Value

'Parameters: C2

C2a = Cells(22, 7).Value

C2b = Cells(23, 7).Value

C2c = Cells(24, 7).Value

'Parameters: pHmean

pHA1 = Cells(26, 7).Value

pHA2 = Cells(27, 7).Value

pHxo = Cells(28, 7).Value

pHdx = Cells(29, 7).Value

'=====

'Start

For n = 2 To 26

RpH = Cells(n, 1).Value

RpO2 = Cells(n, 2).Value

i = 5

'initial condition pH is set to 8.0

pH = Cells(n, 9).Value

DtaupO2 = ((DtauB1 - DtauB2) / (1 + Exp((pH - Dtauxo) / Dtaudx))) + DtauB2

taupO2corr = (delta_t / Log(RpO2)) + DtaupO2

pO2 = (1 / Ksv) * ((f1 / ((taupO2corr / tau0) + f1 - 1)) - 1)

Cells(n, 10).Value = pO2

For m = 1 To 5

q = 2 * i + 1

o = 2 * i

r = 2 * (i + 1)

C1 = C1a + C1b * pO2 + C1c * (pO2) ^ 2

C2 = C2a + C2b * pO2 + C2c * (pO2) ^ 2

RpHcorr = (RpH - C1) / C2

'Test 1

Bug1 = ((pHA1 - pHA2) / (RpHcorr - pHA2)) - 1

If Bug1 <= 0 Then

MsgBox "Bug1"

GoTo NeueStartwerte

End If

$$\text{pH} = \text{pHxo} + \text{pHdx} * \text{Log}(((\text{pHA1} - \text{pHA2}) / (\text{RpHcorr} - \text{pHA2})) - 1)$$

Cells(n, q).Value = pH

$$\text{DtaupO2} = ((\text{DtauB1} - \text{DtauB2}) / (1 + \text{Exp}((\text{pH} - \text{Dtauxo}) / \text{Dtaudx}))) + \text{DtauB2}$$

$$\text{taupO2corr} = (\text{delta}_t / \text{Log}(\text{RpO2})) + \text{DtaupO2}$$

$$\text{pO2} = (1 / \text{Ksv}) * ((\text{f1} / ((\text{taupO2corr} / \text{tau0}) + \text{f1} - 1)) - 1)$$

Cells(n, r).Value = pO2

i = i + 1

Next m

NeueStartwerte:

Next n

End Sub

11.3.3. Evaluation of the pH-pO₂ dual sensor images of a natural sediment sample (Chapter 4.3.5)

Sub pH_pO2image_iteration()

'Parameters for the correction of the pO₂ measurement

'Parameters: DeltatauO2

DtauB1 = Cells(4, 125).Value

DtauB2 = Cells(5, 125).Value

Dtauxo = Cells(6, 125).Value

Dtaudx = Cells(7, 125).Value

'Parameters: tauO2mean

tau0 = Cells(9, 125).Value

f1 = Cells(10, 125).Value

Ksv = Cells(11, 125).Value

delta_t = Cells(13, 125).Value

'Parameters for the correction of the pH measurement

'Parameters: C1

C1a = Cells(18, 125).Value

C1b = Cells(19, 125).Value

C1c = Cells(20, 125).Value

'Parameters: C2

C2a = Cells(22, 125).Value

C2b = Cells(23, 125).Value

C2c = Cells(24, 125).Value

'Parameters: pHmean

pHA1 = Cells(26, 125).Value

pHA2 = Cells(27, 125).Value

pHxo = Cells(28, 125).Value

pHdx = Cells(29, 125).Value

'=====

'Start

For k = 1 To 60

j = 1 + k

l = 62 + k

p = 127 + k

o = 189 + k

For n = 1 To 90

RpH = Cells(n, j).Value

RpO2 = Cells(n, l).Value

m = 0

'initial condition pH is set to 8.0

pH = Cells(n, 126).Value

$$D\tau_{pO_2} = ((D\tau_{B1} - D\tau_{B2}) / (1 + \exp((pH - D\tau_{oxo}) / D\tau_{dx}))) + D\tau_{B2}$$

$$\tau_{pO_2\text{corr}} = (\Delta t / \log(R_{pO_2})) + D\tau_{pO_2}$$

$$pO_2 = (1 / K_{sv}) * ((f_1 / ((\tau_{pO_2\text{corr}} / \tau_0) + f_1 - 1)) - 1)$$

Cells(n, 127).Value = pO2

Do

m = m + 1

$$C_1 = C_{1a} + C_{1b} * pO_2 + C_{1c} * (pO_2)^2$$

$$C_2 = C_{2a} + C_{2b} * pO_2 + C_{2c} * (pO_2)^2$$

$$R_{pH\text{corr}} = (R_{pH} - C_1) / C_2$$

'Test 1

$$\text{Bug1} = ((pHA_1 - pHA_2) / (R_{pH\text{corr}} - pHA_2)) - 1$$

If Bug1 <= 0 Then

'MsgBox "Bug1"

Cells(n, p).Value = 0

Cells(n, o).Value = 0

GoTo NeueStartwerte

End If

$$pH = pH_{xo} + pH_{dx} * \log(((pHA_1 - pHA_2) / (R_{pH\text{corr}} - pHA_2)) - 1)$$

Cells(n, p).Value = pH

$$D\tau_{pO_2} = ((D\tau_{B1} - D\tau_{B2}) / (1 + \exp((pH - D\tau_{oxo}) / D\tau_{dx}))) + D\tau_{B2}$$

$$\tau_{pO_2\text{corr}} = (\Delta t / \log(R_{pO_2})) + D\tau_{pO_2}$$

$$pO_2 = (1 / K_{sv}) * ((f_1 / ((\tau_{pO_2\text{corr}} / \tau_0) + f_1 - 1)) - 1)$$

Cells(n, o).Value = pO2

pO2diff = Cells(n, 127).Value - Cells(n, o).Value

Cells(n, 127).Value = pO2

If m > 120 Then

MsgBox "infinite loop!"

Exit Sub

End If

Loop Until Abs(pO2diff) <= 0.05

NeueStartwerte:

Next n

Next k

End Sub

11.3.4. Number of iteration steps required for the evaluation of the pCO₂-pO₂ dual sensor measurements (Chapter 5.3.4)

Sub pCO2_pO2iteration_test()

'Parameters for the correction of the pO₂ measurement

'Parameters: B0

B0a = Cells(4, 7).Value

B0b = Cells(5, 7).Value

B0c = Cells(6, 7).Value

'Parameters: B1

B1a = Cells(8, 7).Value

B1b = Cells(9, 7).Value

B1c = Cells(10, 7).Value

B2 = Cells(12, 7).Value

'Parameters for the correction of the pCO₂ measurement

'Parameters: C1

C1a = Cells(17, 7).Value

C1b = Cells(18, 7).Value

C1c = Cells(19, 7).Value

Parameters: C2

C2a = Cells(21, 7).Value

C2b = Cells(22, 7).Value

C2c = Cells(23, 7).Value

alfa = Cells(25, 7).Value

'Start

For n = 2 To 16

RpCO2 = Cells(n, 1).Value

RpO2 = Cells(n, 2).Value

i = 5

pCO2 = Cells(n, 9).Value

B0 = (B0a / (1 + B0b * pCO2)) + B0c

B1 = (B1a / (1 + B1b * pCO2)) + B1c

pO2 = (-B1 + Sqr((B1 ^ 2) - 4 * B0 * B2 + 4 * RpO2 * B2)) / (2 * B2)

Cells(n, 10).Value = pO2

For m = 1 To 5

q = 2 * i + 1

o = 2 * i

r = 2 * (i + 1)

C1 = C1a + C1b * pO2 + C1c * (pO2) ^ 2

C2 = C2a + C2b * pO2 + C2c * (pO2) ^ 2

'Test 1

Bug1 = RpCO2 - C1

```
If Bug1 = 0 Then
MsgBox "Bug1"
GoTo NeueStartwerte
End If
```

```
pCO2 = (1 / alfa) * ((C2 / (RpCO2 - C1)) - 1)
Cells(n, q).Value = pCO2
```

```
'Test 2
Bug2 = 1 + B0b * pCO2
If Bug2 = 0 Then
MsgBox "Bug2"
GoTo NeueStartwerte
End If
```

```
'Test 3
Bug3 = 1 + B1b * pCO2
If Bug3 = 0 Then
MsgBox "Bug3"
GoTo NeueStartwerte
End If
```

```
B0 = (B0a / (1 + B0b * pCO2)) + B0c
B1 = (B1a / (1 + B1b * pCO2)) + B1c
```

```
'Test 4
Bug4 = B1 ^ 2 - 4 * B2 * B0 + 4 * RpO2 * B2
If Bug4 < 0 Then
MsgBox "Bug4"
GoTo NeueStartwerte
End If
```

```
pO2 = (-B1 + Sqr((B1 ^ 2) - 4 * B0 * B2 + 4 * RpO2 * B2)) / (2 * B2)
Cells(n, r).Value = pO2
```

$i = i + 1$

Next m

NeueStartwerte:

Next n

End Sub

11.4. References

- [1] Butler J. N., *Carbon Dioxide Equilibria and Their Applications*. CRC Press, Boca Raton (1991).
- [2] www.ocean.washington.edu/courses/oc521/Chpt11.pdf

